



PLEASE CHECK THE APPROPRIATE BLOCK BELOW:

AO # M98-03-6549

☐ 1 copies are being forwarded. Indicate whether Statement A, B, C, D, E, F, or X applies.

☒ DISTRIBUTION STATEMENT A:  
APPROVED FOR PUBLIC RELEASE: DISTRIBUTION IS UNLIMITED

☐ DISTRIBUTION STATEMENT B:  
DISTRIBUTION AUTHORIZED TO U.S. GOVERNMENT AGENCIES ONLY; (Indicate Reason and Date). OTHER REQUESTS FOR THIS DOCUMENT SHALL BE REFERRED TO (Indicate Controlling DoD Office).

☐ DISTRIBUTION STATEMENT C:  
DISTRIBUTION AUTHORIZED TO U.S. GOVERNMENT AGENCIES AND THEIR CONTRACTORS; (Indicate Reason and Date). OTHER REQUESTS FOR THIS DOCUMENT SHALL BE REFERRED TO (Indicate Controlling DoD Office).

☐ DISTRIBUTION STATEMENT D:  
DISTRIBUTION AUTHORIZED TO DoD AND U.S. DoD CONTRACTORS ONLY; (Indicate Reason and Date). OTHER REQUESTS SHALL BE REFERRED TO (Indicate Controlling DoD Office).

☐ DISTRIBUTION STATEMENT E:  
DISTRIBUTION AUTHORIZED TO DoD COMPONENTS ONLY; (Indicate Reason and Date). OTHER REQUESTS SHALL BE REFERRED TO (Indicate Controlling DoD Office).

☐ DISTRIBUTION STATEMENT F:  
FURTHER DISSEMINATION ONLY AS DIRECTED BY (Indicate Controlling DoD Office and Date) or HIGHER DoD AUTHORITY.

☐ DISTRIBUTION STATEMENT X:  
DISTRIBUTION AUTHORIZED TO U.S. GOVERNMENT AGENCIES AND PRIVATE INDIVIDUALS OR ENTERPRISES ELIGIBLE TO OBTAIN EXPORT-CONTROLLED TECHNICAL DATA IN ACCORDANCE WITH DoD DIRECTIVE 5230.25, WITHHOLDING OF UNCLASSIFIED TECHNICAL DATA FROM PUBLIC DISCLOSURE, 6 Nov 1984 (Indicate date of determination). CONTROLLING DoD OFFICE IS (Indicate Controlling DoD Office).

☐ This document was previously forwarded to DTIC on \_\_\_\_\_ (date) and the AD number is \_\_\_\_\_.

☐ In accordance with provisions of DoD instructions, the document requested is not supplied because:

☐ It will be published at a later date. (Enter approximate date, if known).

☐ Other. (Give Reason)

DoD Directive 5230.24, "Distribution Statements on Technical Documents," 18 Mar 87, contains seven distribution statements, as described briefly above. Technical Documents must be assigned distribution statements.

per Tel/corr - w/ Joyce 12/5/97

SM/SGT MARK CHARLES

Print or Type Name

DSN 785-2259 EXT. 2005

Telephone Number

Joyce J. Chiras  
Authorized Signature/Date

# Numerical Techniques for Electromagnetic Applications in Microelectronic and Radar Imaging Systems

by

Jerome J. Akerson

Submitted to the Department of Electrical Engineering and Computer Science  
on October 31, 1997, in partial fulfillment of the  
requirements for the degree of  
Doctor of Philosophy

## Abstract

In this thesis, the application of numerical techniques to electromagnetic problems in microelectronic and radar imaging systems are investigated. In particular the following problems are studied: (1) Dielectric rib waveguide discontinuities are analyzed with the Finite Difference Time Domain (FDTD) method. The application of Berenger's Perfectly Matched Layer to multi-layered dielectrics is analyzed and the specific conditions needed to successfully match the multiple dielectric layers are determined and justified. An FDTD method to find the fundamental mode's spatial distribution is used to excite the discontinuity problem. It is shown that the computational domain can be reduced by twenty percent over Gaussian excitations. The effects of rib waveguide bend discontinuities and the effects of the rib geometry to the bend loss are presented. (2) An Impedance Boundary Condition (IBC) for two dimensional FDTD simulations containing thin, good conductor sheets is developed. The IBC uses a recursive convolution scheme based on approximating the conductor's impedance as a sum of exponentials. The effects of FDTD parameters such as grid size and time step on simulation accuracy are presented. The IBC is shown to accurately model the conductor loss over a wide frequency range. The verification is performed by comparing the quality factors of rectangular resonant structures determined by the FDTD simulation and analytical methods. (3) Phase unwrapping techniques for the inversion of terrain height using Synthetic Aperture Radar Interferometry (InSAR) data are analyzed. The weighted least squares and branch cut phase unwrapping techniques are specifically studied. An optimal branch cut method and a hybrid least squares/branch cut method are presented and used to unwrap the phase of both simulated and real SAR interferograms. When used to invert terrain height, these new SAR phase unwrapping methods offer over fifty percent reduction in root mean square (rms) height error compared to the straight least squares method and over thirty-five percent reduction in rms height error compared to the weighted least squares method based on coherence data weighting schemes.

Thesis Supervisor: Professor Jin Au Kong

Thesis Supervisor: Dr. Y. Eric Yang

19971208 001

# Numerical Techniques for Electromagnetic Applications in Microelectronic and Radar Imaging Systems

by

Jerome J. Akerson

B.S. Electrical and Computer Engineering,  
University of California, Davis, 1984

M.S. Electrical Engineering and Computer Science,  
Massachusetts Institute of Technology, Cambridge, 1990

Submitted to the Department of Electrical Engineering and Computer Science  
in partial fulfillment of the requirements for the degree of

Doctor of Philosophy

at the

Massachusetts Institute of Technology

February 1998

© Jerome J. Akerson, 1998. All rights reserved.

The author hereby grants to MIT permission to reproduce and distribute publicly paper and electronic copies of this thesis document in whole or in part, and to grant others the right to do so.

Author \_\_\_\_\_

Department of Electrical Engineering and Computer Science  
October 31, 1997

Certified by \_\_\_\_\_

Professor Jin Au Kong  
Thesis Supervisor

Certified by \_\_\_\_\_

Dr. Y. Eric Yang  
Thesis Supervisor

Accepted by \_\_\_\_\_

Professor Arthur C. Smith  
Chairman, Department Committee on Graduate Students



# Numerical Techniques for Electromagnetic Applications in Microelectronic and Radar Imaging Systems

by

Jerome J. Akerson

Submitted to the Department of Electrical Engineering and Computer Science  
on October 31, 1997, in partial fulfillment of the  
requirements for the degree of  
Doctor of Philosophy

## Abstract

In this thesis, the application of numerical techniques to electromagnetic problems in microelectronic and radar imaging systems are investigated. In particular the following problems are studied: (1) Dielectric rib waveguide discontinuities are analyzed with the Finite Difference Time Domain (FDTD) method. The application of Berenger's Perfectly Matched Layer to multi-layered dielectrics is analyzed and the specific conditions needed to successfully match the multiple dielectric layers are determined and justified. An FDTD method to find the fundamental mode's spatial distribution is used to excite the discontinuity problem. It is shown that the computational domain can be reduced by twenty percent over Gaussian excitations. The effects of rib waveguide bend discontinuities and the effects of the rib geometry to the bend loss are presented. (2) An Impedance Boundary Condition (IBC) for two dimensional FDTD simulations containing thin, good conductor sheets is developed. The IBC uses a recursive convolution scheme based on approximating the conductor's impedance as a sum of exponentials. The effects of FDTD parameters such as grid size and time step on simulation accuracy are presented. The IBC is shown to accurately model the conductor loss over a wide frequency range. The verification is performed by comparing the quality factors of rectangular resonant structures determined by the FDTD simulation and analytical methods. (3) Phase unwrapping techniques for the inversion of terrain height using Synthetic Aperture Radar Interferometry (InSAR) data are analyzed. The weighted least squares and branch cut phase unwrapping techniques are specifically studied. An optimal branch cut method and a hybrid least squares/branch cut method are presented and used to unwrap the phase of both simulated and real SAR interferograms. When used to invert terrain height, these new SAR phase unwrapping methods offer over fifty percent reduction in root mean square (rms) height error compared to the straight least squares method and over thirty-five percent reduction in rms height error compared to the weighted least squares method based on coherence data weighting schemes.

Thesis Supervisor: Professor Jin Au Kong

Thesis Supervisor: Dr. Y. Eric Yang

## Acknowledgments

Along the way, many people supported my effort and contributed to my success.

I would like to thank Professor Kong for letting me study in his group and giving me the opportunity to learn so much. His kindness, generosity and support will never be forgotten.

I must thank Col Litwhiler of the United States Air Force Academy for his confidence and a special thanks to Majors Rich Schooff and Ralph Tolle for their support and help when things did not go as planned.

Words cannot express my appreciation for Dr. Eric Yang who spent many hours with me and this document and guided me through this ordeal called a PhD.

I would also like to thank Professor Staelin for always taking time out of his busy schedule to help me when asked.

I would like to acknowledge the help Yan Zhang gave me with the SAR interferometry, especially the program to generate simulated interferograms; and to Sean Shih for the VAX help. More importantly, thanks for their friendship and support.

Marilyn Pierce has been a tremendous help at every stage of my MIT experience. Whenever I needed help with department requirements or Air Force paper work she always took the time to help me out. I am greatly indebted to her.

I could not have endured if not for the friendship of Frank Mullen who has listened to me and shared his views on life throughout the years.

Near the end, it was the support and friendship of Mike Davis that kept me sane and allowed me to finish this thesis. Thanks.

Finally, I must acknowledge the hardship that my family has endured while I worked at MIT. It was an the incredibly long journey and often it felt like it would never end. My family encouraged me throughout process. To Debby, my wife, and our children, Lindsay, Jarrod, and Stacy thank you for your love and support.

To Debby with love, respect and admiration.



# Contents

<b>1</b>	<b>Introduction</b>	<b>21</b>
1.1	Technical Discussion . . . . .	23
1.1.1	Analysis of Dielectric Waveguide Discontinuities . . . . .	23
1.1.2	Modeling of Thin Finite Conductivity Sheets . . . . .	26
1.1.3	Phase Unwrapping . . . . .	29
1.2	Description of Thesis . . . . .	33
<b>2</b>	<b>Finite Difference Time Domain Method</b>	<b>35</b>
2.1	Introduction . . . . .	35
2.2	Maxwell's Equations in Cartesian Coordinates . . . . .	36
2.3	Difference Equations in Free Space . . . . .	37
2.3.1	Central Difference Approximation . . . . .	37
2.3.2	Yee Grid and FDTD Nomenclature . . . . .	37
2.3.3	Difference Equations . . . . .	39
2.4	Difference Equations in Lossy Dielectric Media . . . . .	42
2.4.1	Maxwell's Equations in Lossy Dielectric Media . . . . .	42
2.4.2	Difference Equations . . . . .	45
2.5	Treatment of Dielectric Interfaces . . . . .	46
2.6	Perfect Conductors . . . . .	48
2.7	Accuracy, Numerical Dispersion, and Stability . . . . .	50
2.7.1	Accuracy and Numerical Dispersion . . . . .	50
2.7.2	Stability . . . . .	51
2.8	Implementation of Sources and Excitations . . . . .	52

2.9	Treatment of Computational Boundaries . . . . .	54
2.9.1	One Way Wave Equation . . . . .	55
2.9.2	Absorbing Boundary Layer . . . . .	58
2.10	Berenger's Perfectly Matched Layer . . . . .	59
2.10.1	PML Reflection Coefficient Analysis . . . . .	62
2.10.2	PML Propagation Characteristics . . . . .	65
2.10.3	PML and FDTD Simulations . . . . .	66
2.10.4	PML and Multilayer Dielectrics . . . . .	67
2.10.5	PML Coefficients in FDTD . . . . .	74
2.11	Considerations and Overview of FDTD Algorithm . . . . .	77
2.12	Summary . . . . .	78
<b>3</b>	<b>Analysis of Waveguide Discontinuities</b>	<b>79</b>
3.1	Introduction . . . . .	79
3.2	Implementation of Dielectric Rib Waveguide in FDTD . . . . .	80
3.3	Approximate Analytic Solution . . . . .	81
3.4	Excitation . . . . .	84
3.5	Template Excitation . . . . .	86
3.5.1	Template Construction . . . . .	86
3.5.2	Verification of Computational Domain Reduction . . . . .	89
3.6	Absorbing Boundary Condition Demonstration . . . . .	91
3.7	Measurements . . . . .	95
3.7.1	Power measurements . . . . .	95
3.7.2	S Parameters . . . . .	96
3.8	Discontinuity Analysis . . . . .	97
3.9	Analysis of Rib Geometry on Turn Loss . . . . .	99
3.10	Discussion . . . . .	104
<b>4</b>	<b>IBC for Thin Finite Conducting Sheets in FDTD</b>	<b>107</b>
4.1	Introduction . . . . .	107
4.2	Derivation of Impedance Boundary Condition . . . . .	110

4.3	Recursive Convolution . . . . .	112
4.4	Implementation of IBC in FDTD . . . . .	114
4.4.1	Impedance Equations - Piecewise Constant Assumption . . . .	114
4.4.2	Impedance Equations - Piecewise Linear Assumption . . . . .	116
4.5	Extension of IBC to Two Dimensions . . . . .	116
4.6	FDTD Simulation Parameters and IBC Accuracy . . . . .	118
4.6.1	1D FDTD Simulation Configuration . . . . .	119
4.6.2	Transmissivity Error Measurements . . . . .	121
4.6.3	Optimum Settings . . . . .	123
4.7	Verification of IBC in Two Dimensions . . . . .	130
4.7.1	Calculation of Quality Factor . . . . .	130
4.7.2	Measurement of Quality Factor in FDTD Simulations . . . . .	134
4.7.3	2D Simulations and Results . . . . .	135
4.8	Discussion . . . . .	137
<b>5</b>	<b>Phase Unwrapping of SAR Interferometry</b>	<b>139</b>
5.1	Introduction . . . . .	139
5.2	Least Squares Phase Unwrapping Technique . . . . .	143
5.3	Weighted Least Squares Phase Unwrapping . . . . .	146
5.3.1	Weighted Least Squares . . . . .	146
5.3.2	Determining Weights . . . . .	147
5.3.3	Picard Iteration method . . . . .	148
5.4	Branch Cut Method . . . . .	151
5.4.1	Minimum Branch Cut Algorithm . . . . .	154
5.4.2	Branch Cut Limitations . . . . .	156
5.5	Local optimum branch cut method . . . . .	158
5.6	Hybrid method . . . . .	159
5.7	Comparison of Algorithms on Simulated Data . . . . .	159
5.7.1	Generation of Simulated SAR Interferogram . . . . .	160
5.7.2	Addition of noise . . . . .	162

5.7.3	Application and Analysis of Techniques on Simulated Data . .	163
5.8	Height Inversion . . . . .	164
5.9	Application and Analysis of Techniques on Real Data . . . . .	168
5.9.1	ERS -1 Data . . . . .	168
5.9.2	Registration Process . . . . .	169
5.9.3	Forshortening . . . . .	172
5.9.4	SAR/DEM Registration . . . . .	173
5.9.5	Determination of data weights . . . . .	176
5.9.6	Results . . . . .	179
5.10	Summary . . . . .	194
<b>6</b>	<b>Conclusion</b>	<b>199</b>
6.1	Analysis of Dielectric Waveguide Discontinuities . . . . .	200
6.2	Modeling of Thin Finite Conductivity Sheets . . . . .	201
6.3	Phase Unwrapping of SAR Interferograms . . . . .	202
6.4	Outlook . . . . .	203
<b>A</b>	<b>Mur FDTD Equations</b>	<b>205</b>
A.1	1st Order Mur FDTD Equations . . . . .	205
A.2	2nd Order Mur FDTD Equations . . . . .	207
<b>B</b>	<b>FDTD PML Difference Equations</b>	<b>213</b>
<b>C</b>	<b>Transportation Problem</b>	<b>219</b>
C.1	Introduction . . . . .	219
C.2	Maximum Flow Through a Network . . . . .	221
C.3	Transportation and the Maximum Flow Problem . . . . .	223
C.4	Application to Branch Cut Connections . . . . .	225



# List of Figures

1-1	Dielectric rib waveguide configuration in a 3D FDTD simulation. . . .	25
1-2	Replacement of thin conductor with Impedance Boundary Condition	27
1-3	SAR interferogram . . . . .	29
1-4	Digital Elevation Model (DEM) of Alaskan mountain. . . . .	30
2-1	Yee's FDTD grid. . . . .	38
2-2	Graphical representations used to construct FDTD difference equations. Solid lines represent integer grid lines. . . . .	40
2-3	Individual field locations on the Yee grid. . . . .	47
2-4	Assignment of permittivity values for multiple dielectric media in FDTD simulations. . . . .	49
2-5	Normalized phase velocity versus angle of propagation for 2D FDTD; $\frac{\lambda}{20}$ : (solid line), $\frac{\lambda}{10}$ : (dashed line), and $\frac{\lambda}{5}$ : (large-dashed line). . . . .	51
2-6	2D Yee grid: dashed line represents the edges of the computational domain. . . . .	54
2-7	2D Yee grid with an absorbing boundary layer used to truncate the computational domain. . . . .	58
2-8	Geometry for PML reflection coefficient analysis. . . . .	63
2-9	Configuration for multi-dielectric layer PML. . . . .	68
2-10	Configuration for multi-dielectric reflection coefficient analysis. . . . .	70
2-11	Test setup for PML instability demonstration. Field measured at point A.	72

2-12	Field $E_z$ measurements at PML/PML interface (Point A in Figure 2-11) with dependent(top) and independent(lower) PML matching conditions. . . . .	73
2-13	Fourier transform of field inside rib using dependent (top) and independent (bottom) PML conductivity matching condition. . . . .	75
2-14	Fundamental mode spatial field distribution using dependent (top) and independent (bottom) PML conductivity matching condition. . . . .	76
3-1	Schematic of dielectric rib waveguide cross section. Parameters are $rw$ : rib width, $rh$ : rib height, $fh$ : film height, and $(xc, zc)$ : center reference point. . . . .	81
3-2	Rectangular dielectric waveguide used with Marcatili method. . . . .	82
3-3	Normalized dispersion curves of first three modes, $E_{1,1}^z$ , (diamond) $E_{2,1}^z$ , (triangle) and $E_{1,2}^z$ (star), as derived by the Marcatili method. . . . .	85
3-4	Spectrum of field in dielectric waveguide using two dimensional FDTD code with $k_y = 600 m^{-1}$ . . . . .	88
3-5	Mode template for $E_{1,1}^z$ of square dielectric waveguide using two dimensional FDTD code. . . . .	89
3-6	Validation of mode dispersion curve. Diamonds represent the Marcatili calculation and the triangles represent the numerically derived results. . . . .	90
3-7	Configuration for numerical template analysis. . . . .	92
3-8	$S_{11}$ as measured at the Input Reference Plane for an analytical Gaussian excitation at Source Planes A (diamonds), B (triangles), and C (stars). . . . .	93
3-9	$S_{21}$ as measured at the Output Reference Plane for an analytical Gaussian excitation at Source Planes A (diamonds), B (triangles), and C (stars). . . . .	93
3-10	$S_{11}$ as measured at the Input Reference Plane for an numeric template excitation at Source Planes A (diamonds), and B (triangles). . . . .	94

3-11	$S_{21}$ as measured at the Output Reference Plane for an numeric template excitation at Source Planes A (diamonds), and B (triangles). . .	94
3-12	Time domain snap shots of FDTD simulation with 1st order Mur (left) and PML (right). . . . .	95
3-13	Configuration of bends tested, from left to right, 90° bend, 90° bend with bevel, and 45° bend. . . . .	97
3-14	Mode template for $E_{1,1}^z$ of dielectric rib waveguide using two dimensional FDTD code. . . . .	98
3-15	$S_{21}$ rib waveguide through three different types of turns: 90° bend (diamond), 90° bend with bevel (triangle), 45° bend (star). . . . .	99
3-16	Time domain snap shots of propagation through a 90° bend at 173, 233, 293, and 323 time steps. (Clockwise starting at upper left.) . . .	100
3-17	Time domain snap shots of propagation through a 45° bend at 173, 233, 293, and 323 time steps. (Clockwise starting at upper left.) . . .	101
3-18	Mode template for $E_{1,1}^z$ of dielectric rib waveguide with film height: 6 mm, rib height: 4 mm and rib width: 10 mm. . . . .	102
3-19	Mode template for $E_{1,1}^z$ of dielectric rib waveguide with film height: 5 mm, rib height: 5 mm and rib width: 10 mm. . . . .	102
3-20	Mode template for $E_{1,1}^z$ of dielectric rib waveguide with film height: 4 mm, rib height: 6 mm and rib width: 10 mm. . . . .	103
3-21	Mode template for $E_{1,1}^z$ of dielectric rib waveguide with film height: 3 mm, rib height: 7 mm and rib width: 10 mm. . . . .	103
3-22	Mode template for $E_{1,1}^z$ of dielectric rib waveguide with film height: 0 mm, rib height: 10 mm and rib width: 10 mm. . . . .	103
3-23	$S_{21}$ through 45° bend of dielectric rib waveguide. Starting from top curve to bottom curve the film height to rib height ratios are 0.0, 0.43, 0.67, 1.0, and 1.5. . . . .	104
4-1	1D transmission line model used for IBC formulation. . . . .	110
4-2	2D configuration used for IBC equations of a rectangular resonator. .	118

4-3	1D configuration for IBC error analysis. . . . .	119
4-4	Transmissivity FDTD (dashed) vs. Analytic (solid) for a $35\mu m$ thick sheet of copper with $\sigma = 5.8 \times 10^7 \Omega^{-1}m^{-1}$ ; $P = 20$ , $\Delta = .005 m$ , $CFL = 2.0$ , and $\beta = 50$ . . . . .	120
4-5	Error vs. CFL for a $35\mu m$ thick conductor for two different FDTD configurations: (1) $\sigma = 5.8 \times 10^4 \Omega^{-1}m^{-1}$ , $P = 3$ , $\Delta = .005 m$ (diamond) and (2) $\sigma = 5.8 \times 10^7 \Omega^{-1}m^{-1}$ , $P = 125$ , $\Delta = .00125 m$ (triangle). . .	122
4-6	Error vs. expansion terms for a $35\mu m$ thick conductor with $\sigma = 5.8 \times 10^4 \Omega^{-1}m^{-1}$ ; $\Delta = .005 m$ (diamond), $\Delta = .0025 m$ (triangle), $\Delta = .00125 m$ (star). . . . .	124
4-7	Error vs. expansion terms for a $35\mu m$ thick conductor with $\sigma = 5.8 \times 10^5 \Omega^{-1}m^{-1}$ ; $\Delta = .005 m$ (diamond), $\Delta = .0025 m$ (triangle), $\Delta = .00125 m$ (star). . . . .	124
4-8	Error vs. expansion terms for a $35\mu m$ thick conductor with $\sigma = 5.8 \times 10^6 \Omega^{-1}m^{-1}$ ; $\Delta = .005 m$ (diamond), $\Delta = .0025 m$ (triangle), $\Delta = .00125 m$ (star). . . . .	125
4-9	Error vs. expansion terms for a $35\mu m$ thick conductor with $\sigma = 5.8 \times 10^7 \Omega^{-1}m^{-1}$ ; $\Delta = .005 m$ (diamond), $\Delta = .0025 m$ (triangle), $\Delta = .00125 m$ (star). . . . .	125
4-10	Error vs. expansion terms for a $35\mu m$ thick conductor with $\sigma = 5.8 \times 10^8 \Omega^{-1}m^{-1}$ ; $\Delta = .005 m$ (diamond), $\Delta = .0025 m$ (triangle), $\Delta = .00125 m$ (star). . . . .	126
4-11	Error vs. expansion terms for a $35\mu m$ thick conductor with $\sigma = 5.8 \times 10^9 \Omega^{-1}m^{-1}$ ; $\Delta = .005 m$ (diamond), $\Delta = .0025 m$ (triangle), $\Delta = .00125 m$ (star). . . . .	126
4-12	Piecewise linear error vs. expansion terms for a $35\mu m$ thick conductor with $\sigma = 5.8 \times 10^7 \Omega^{-1}m^{-1}$ ; $\Delta = .005 m$ (solid), $\Delta = .0025 m$ (dash), $\Delta = .00125 m$ (dash-dot). . . . .	128

4-13	Piecewise constant error vs. expansion terms for a $35\mu m$ thick conductor with $\sigma = 5.8 \times 10^7 \Omega^{-1}m^{-1}$ ; $\Delta = .005 m$ (solid), $\Delta = .0025 m$ (dash), $\Delta = .00125 m$ (dash-dot). . . . .	128
4-14	Comparison of error behavior of piecewise constant IBC and piecewise linear IBC for a $35\mu m$ thick conductor with $\sigma = 5.8 \times 10^7 \Omega^{-1}m^{-1}$ ; $\Delta = .005 m$ (solid), $\Delta = .0025 m$ (dash), $\Delta = .00125 m$ (dash-dot). . .	129
4-15	Magnitude of piecewise constant IBC term, $ e^{A_m \Delta t} - 1 $ , vs. expansion terms for a $35\mu m$ thick conductor with $\sigma = 5.8 \times 10^7 \Omega^{-1}m^{-1}$ ; $\Delta t = \frac{.005 m}{2c}$ (solid), $\Delta t = \frac{.0025 m}{2c}$ (dash), $\Delta t = \frac{.00125 m}{2c}$ (dash-dot). . . . .	129
4-16	Piecewise constant error vs. expansion terms for various conductor thicknesses with $\Delta = .005 m$ and $\sigma = 5.8 \times 10^7 \Omega^{-1}m^{-1}$ ; $l = 17.5\mu m$ (solid), $l = 35\mu m$ (dash), $l = 70\mu m$ (dash-dot). . . . .	130
4-17	Test structure for IBC validation. . . . .	132
4-18	2D resonator quality factor percent error versus conductivity exponent, $x$ in $5.8 \times 10^x \Omega^{-1}m^{-1}$ ; $3.03 GHz$ (solid), $6.06 GHz$ (dash), $9.60 GHz$ (dash-dot), $12.10 GHz$ (dash-dot-dot). . . . .	137
5-1	Pole connection ambiguity. . . . .	156
5-2	Effect of missing one residue in nearest neighbor search. . . . .	156
5-3	Effect of erroneous residue placed on boundary. . . . .	157
5-4	Effect of too few image residues on the image boundary. . . . .	158
5-5	Simulated SAR interferogram without noise. . . . .	161
5-6	Simulated SAR interferogram with $\Delta\psi = 55^\circ$ rms noise. . . . .	162
5-7	Least squares unwrapping phase error versus phase noise, mean (diamond), standard deviation (triangle). . . . .	165
5-8	Weighted least squares unwrapping phase error versus phase noise, mean (diamond), standard deviation (triangle). . . . .	165
5-9	Branch cut unwrapping phase error versus phase noise, mean (diamond), standard deviation (triangle). . . . .	166

5-10	Weighted least squares unwrapping phase error standard deviation versus iteration number: $\Delta\psi = 35^\circ$ , (diamond); $\Delta\psi = 45^\circ$ , (triangle); $\Delta\psi = 55^\circ$ , ( <i>star</i> ). . . . .	166
5-11	SAR set up for terrain height inversion. . . . .	167
5-12	Forshortening diagram. . . . .	172
5-13	DEM subset: shaded square indicates subset used for registration. . .	174
5-14	Gray scale image of Alaskan DEM terrain used for registration. . . .	174
5-15	ERS-1 SAR interferogram: black rectangle represents the subset used for registration (ERS-1 Data Set 1). . . . .	175
5-16	Weighting mask based on coherence map, (ERS-1 Data Set 1). . . . .	176
5-17	Weighting mask based on coherence map with $c_{thr} = 0.8$ , (ERS-1 Data Set 1). . . . .	177
5-18	Weighting mask based on coherence map with $c_{thr} = 0.5$ , (ERS-1 Data Set 1). . . . .	177
5-19	Weighting mask based on coherence map with $c_{thr} = 0.2$ . (ERS-1 Data Set 1). . . . .	178
5-20	Weighting mask based on residues (ERS-1 Data Set 1). . . . .	178
5-21	Least square error plot (ERS-1 Data Set 1). . . . .	180
5-22	Weighted least square error plot using coherence mask (ERS-1 Data Set 1).180	
5-23	Weighted least square error plot with residue mask (ERS-1 Data Set 1).181	
5-24	Branch cut error plot (ERS-1 Data Set 1). . . . .	181
5-25	Histogram of least square height errors (ERS-1 Data Set 1). Standard deviation: 38.60 m. . . . .	182
5-26	Histogram of weighted least square height errors using coherence mask (ERS-1 Data Set 1). Standard deviation: 29.47 m. . . . .	182
5-27	Histogram of weighted least square height errors using residue mask (ERS-1 Data Set 1). Standard deviation: 18.26 m. . . . .	183
5-28	Histogram of branch cut height errors (ERS-1 Data Set 1). Standard deviation: 15.15 m. . . . .	183

5-29	Comparison of $h_{rms}$ error versus $c_{thr}$ setting of height inverted with weighted least squares with coherence weighting on ERS-1 Data Set 1.	184
5-30	Comparison of height error versus iteration on ERS-1 Data Set 1. . .	185
5-31	ERS-1 Data Set 2. . . . .	185
5-32	Coherence data for ERS-1 Data Set 2. . . . .	186
5-33	Weighting mask based on residues for ERS-1 Data Set 2. . . . .	186
5-34	Comparison of nearest neighbor (top), local optimum (center) and global optimum (bottom) branch cut phase unwrapping for ERS-1 Data Set 2. . . . .	189
5-35	Height error histogram for straight least squares method applied to ERS-1 Data Set 2. Standard deviation: 74.85 <i>m</i> . . . . .	190
5-36	Height error histogram for weighted least squares method with coherence weighting applied to ERS-1 Data Set 2. Standard deviation: 39.18 <i>m</i> . . . . .	190
5-37	Height error histogram for weighted least squares method with residue weighting applied to ERS-1 Data Set 2. Standard deviation: 20.91 <i>m</i> . . . . .	191
5-38	Height error histogram for global optimum branch cut method applied to ERS-1 Data Set 2. Standard deviation: 22.30 <i>m</i> . . . . .	191
5-39	Height error histogram for local optimum branch cut method applied to ERS-1 Data Set 2. Standard deviation: 22.40 <i>m</i> . . . . .	192
5-40	ERS-1 Data Set 3. . . . .	192
5-41	Coherence data for ERS-1 Data Set 3. . . . .	193
5-42	Weighting mask based on residues for ERS-1 Data Set 3. . . . .	193
5-43	Height error for hybrid weighted least squares method applied to ERS-1 Data Set 3. Standard deviation: 39.33 <i>m</i> . . . . .	194
5-44	Height error histogram for hybrid weighted least squares method applied to ERS-1 Data Set 3. Standard deviation: 39.33 <i>m</i> . . . . .	195
5-45	Height error for global optimum branch cut method applied to ERS-1 Data Set 3. Standard deviation: 39.07 <i>m</i> . . . . .	195

5-46	Height error histogram for global optimum branch cut method applied to ERS-1 Data Set 3. Standard deviation: 39.07 <i>m</i> . . . . .	196
C-1	Transportation network. . . . .	220
C-2	Transportation as a maximum flow network. . . . .	224



# List of Tables

2.1	Maximum conductivities to match PML to rib structure. . . . .	74
4.1	Comparison of $Q_{FDTD}$ and analytic $Q$ at 3.03 GHz . . . . .	135
4.2	Comparison of $Q_{FDTD}$ and analytic $Q$ at 6.06 GHz . . . . .	136
4.3	Comparison of $Q_{FDTD}$ and analytic $Q$ at 9.6 GHz . . . . .	136
4.4	Comparison of $Q_{FDTD}$ and analytic $Q$ at 12.1 GHz . . . . .	136
5.1	Algorithm for weight assignments based on coherence data. . . . .	149
5.2	Algorithm for weight assignment based on residue identification. . . .	159
5.3	SAR parameters for simulated SAR interferogram. . . . .	161
5.4	$N_p$ settings for rms phase noise. . . . .	163
5.5	Number of residues in simulated SAR interferograms. . . . .	164
5.6	ERS SAR parameters. . . . .	168
5.7	DEM parameters. . . . .	169
5.8	Registration definitions . . . . .	170
5.9	Registration steps. . . . .	172
5.10	Comparison of rms height error and CPU times for the phase unwrapping methods. LS: least squares, W-LS: weighted least squares and BC: branch cut. . . . .	187

# Chapter 1

## Introduction

Numerical modeling of electromagnetic phenomena is a popular pursuit for many scientists and engineers. One of the most popular time domain numerical techniques is the Finite Difference Time Domain Method or FDTD. The FDTD method attempts to model the interaction between electric and magnetic fields by describing the universe at discrete locations at discrete times. The physics are defined by a set of difference equations that describe the relationships between field quantities at the various locations at different times. If space and time are divided into small enough intervals the difference equations adequately approximate the electromagnetic interactions.

The key to electromagnetic interactions is the media and the FDTD method can model most materials quite accurately. However, computer resources always constrain the types of problems that can be simulated within a reasonable amount of time. In fact, FDTD's most serious limitation is that it requires large amounts of computer memory.

The computer resources needed to simulate an electromagnetic problem are usually directly related to the smallest wavelength of the simulation. However, a very small wavelength may imply small structures, and a small simulation volume may offset the high density of sample points. The resource problem is most pronounced when a small portion of the simulation contains a dense material that greatly shortens the

wavelength. In this case, the dense material drives the spatial interval and in turn the memory required. Another factor that greatly influences the memory requirements is the treatment of the simulation volume's physical boundaries. Modeling open space implies no physical boundaries; however, a simulation volume of infinite extend is, of course, impossible. Many techniques have been developed to simulate open space with a closed simulation volume; however, they are problem specific. It is the engineer's job to make the appropriate approximations to simulate a given problem within the computer resource constraints.

Discretization of space, time and Maxwell's equations is clearly a numerical technique that can be applied to many types of electromagnetic problems. Other numerical techniques involve the analysis of the measurements of electromagnetic phenomena such as analyzing radar data. Extracting useful information from radar measurements in the presence of noise is a continuing topic of great interest. The use of multiple passes of a satellite based synthetic aperture radar (SAR) to perform interferometry is a very useful tool to image the earth's terrain height. Noise in the system and decorrelation of the two passes add greatly to the height errors in an inverted height image. Reducing these errors is of great interest in the remote sensing community.

In this thesis, the application of numerical techniques to electromagnetic problems in microelectronic and radar imaging systems are investigated. In particular the following problems are studied: (1) Dielectric rib waveguide discontinuities are analyzed with the Finite Difference Time Domain (FDTD) method. Berenger's Perfectly Matched Layer application to multi-layered dielectrics is analyzed and the specific conditions needed to successfully match the multiple dielectric layers are determined and justified. An FDTD method to find the fundamental mode's spatial distribution is used to excite the discontinuity problem. The effects of this type of excitation on computational domain reduction is presented. These numerical techniques are used to study the effect of bend discontinuities in the rib waveguide. (2) A new Impedance Boundary Condition (IBC) is analyzed and developed for two dimensional

FDTD simulations containing thin, good conductor sheets. The need for a very large computational domain is overcome by the replacement of the good conductor with an impedance boundary condition that accurately models the conductor loss over a wide frequency range. The IBC uses a recursive convolution scheme. The two dimensional IBC is verified by comparing the quality factors of rectangular resonant structures determined by the FDTD simulation and those calculated with analytical methods. (3) Phase unwrapping techniques for the inversion of terrain height using Synthetic Aperture Radar Interferometry (InSAR) data are analyzed. The weighted least squares and branch cut phase unwrapping techniques are specifically studied. An optimal branch cut method and a hybrid least squares/branch cut method are presented and used to unwrap the phase of both simulated and real SAR interferograms. These new SAR phase unwrapping methods are compared to straight least squares unwrapping and other weighted least squares schemes.

## 1.1 Technical Discussion

### 1.1.1 Analysis of Dielectric Waveguide Discontinuities

Dielectric waveguides are commonly used as interconnects in millimeter-wave and sub-millimeter wave integrated circuit technologies [75]-[100]. As frequencies increase, conductor losses diminish the utility of microstrip and coplanar interconnect structures. Furthermore, to maintain single mode operation the structure size must decrease which further increases the loss through these metal guides. Dielectric waveguides avoid these losses; however, when these interconnects contain discontinuities such as bends, these discontinuities introduce loss through the waveguide. Since the propagating modes of this type of structure are characterized by very complex field distributions that do not have exact analytic solutions, a numerical approach is appropriate to investigate these structures. In this thesis an FDTD implementation is used to analyze the effects of waveguide discontinuities on the fundamental mode's

propagation through the waveguide.

The main difficulty of using the FDTD method on this type of problem is computer resources. With multiple dielectric media, the most dense material determines the spatial interval of the discretization. And, the open nature commonly found in many dielectric guiding structures creates the need for special treatment on the edges of the simulation volume.

The first analysis of dielectric waveguides focused on finding dispersion curves and field distributions in two dimensional cross sections of the guides using frequency domain techniques [75, 76, 77, 78]. More recent work has concentrated on using integral equations to solve the two-dimensional problem [82, 99], while others have used frequency methods like Beam Propagation Method or the discretization of the scalar wave equation [81, 83]. Much of the dielectric waveguide discontinuities work has been limited to two dimensional dielectric slab waveguides as in [94].

Three dimensional single frequency analysis has been done on structures such as directional couplers [80], tapered rib waveguides [89], Y-junctions [92], and step discontinuities [84].

Multi-frequency analysis of three dimensional structures using FDTD has been done on the transitions from rectangular waveguides and microstrip to dielectric waveguides [85, 96, 100], but little has been done with dielectric bends. One work reports a full three dimensional look at a bend in a rectangular dielectric guide limited to a single frequency [93].

Figure 1-1 is a graphical representation of a dielectric rib waveguide and the essential elements of a FDTD simulation. Unless bounded with a perfect conductor, the walls of the simulation volume must contain some absorbing boundary condition. The problem is excited by an excitation plane and the power is measured at two reference planes.

When using FDTD to study any waveguide, depending on the excitation used, it can take some distance for the fundamental mode to develop as the evanescent modes

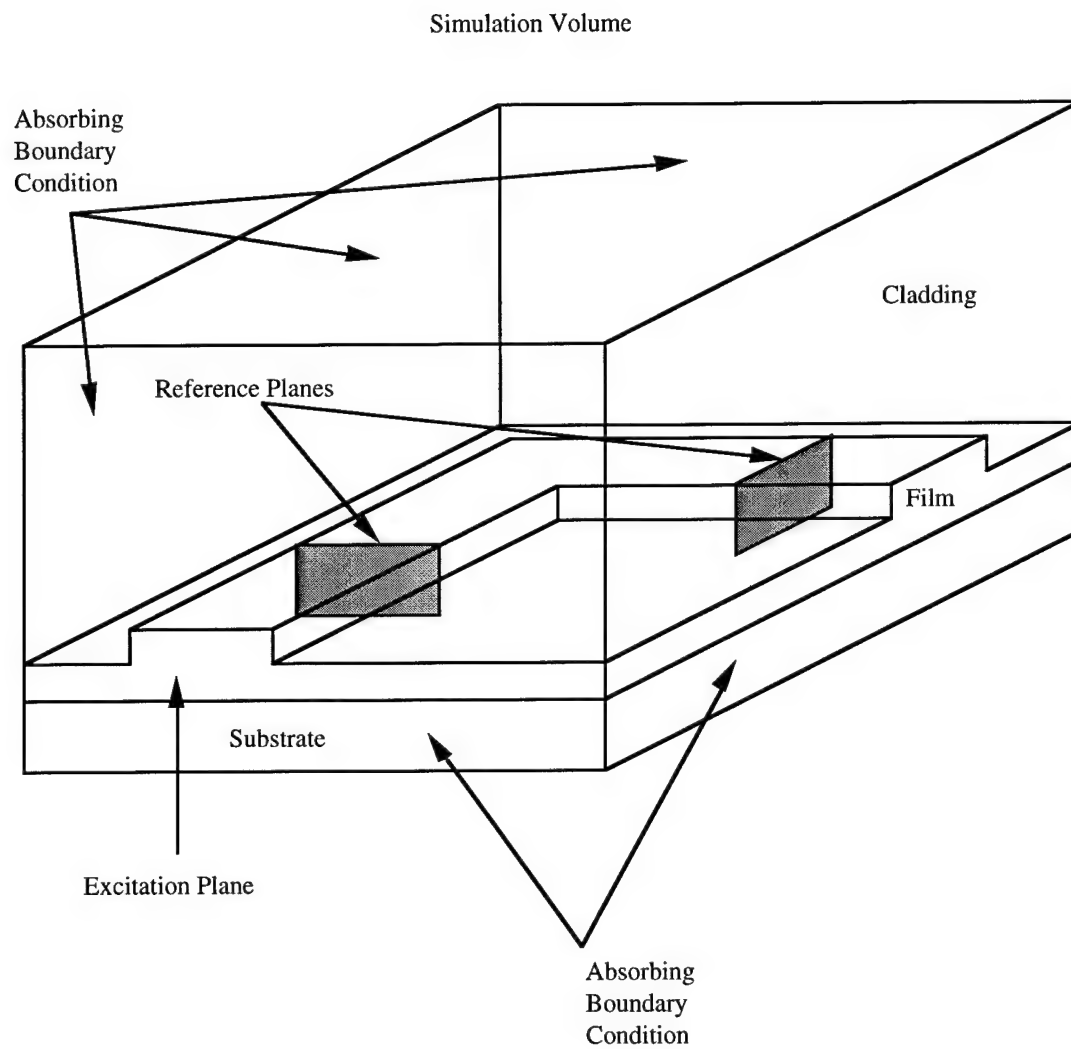


Figure 1-1: Dielectric rib waveguide configuration in a 3D FDTD simulation.

decay away and radiating modes leave the simulation volume. In order to more efficiently launch the fundamental mode, in this work the mode's spatial distribution is determined up front. A two dimensional FDTD method is used to construct a mode template [131, 133]. The three dimensional FDTD code is collapsed in the direction of propagation by replacing the spatial difference equation with an equation based on an assumed propagation constant and the corresponding phase difference between adjacent spatial grid points. A two dimensional simulation of the waveguide cross section produces the corresponding temporal frequencies of the propagating modes. The lowest frequency is the fundamental mode and the spatial distribution is found by performing a Fourier transform at each space point on the two dimensional grid at the fundamental mode frequency. With this source condition, the computational domain can be reduced from the commonly used spatial Gaussian source condition by allowing shorter distances between excitation and the discontinuity and thus the waveguide can be studied with fewer computer resources.

Unlike metallic waveguides, the dielectric rib waveguide is an open structure and analyzing them with the Finite Difference Time Domain method requires absorbing boundary conditions (ABC) that simulate open space. In this work the new Perfectly Matched Layer [46] is used. A careful examination of its application to multi-layer dielectrics is given and the results are used to implement the ABC for the study of waveguide discontinuities.

### 1.1.2 Modeling of Thin Finite Conductivity Sheets

In FDTD simulations involving highly conductive materials, such as the metal case of a computer system, the tangential electric fields are typically set to zero on the surface of the material. This Perfect Electric Conductor (PEC) assumption ignores any loss associated with the less than infinite conductivity. The errors that result from this approximation are considered against the large cost of discretizing the lossy material. Since the wavelength of a highly conductive material is very small, the simulation

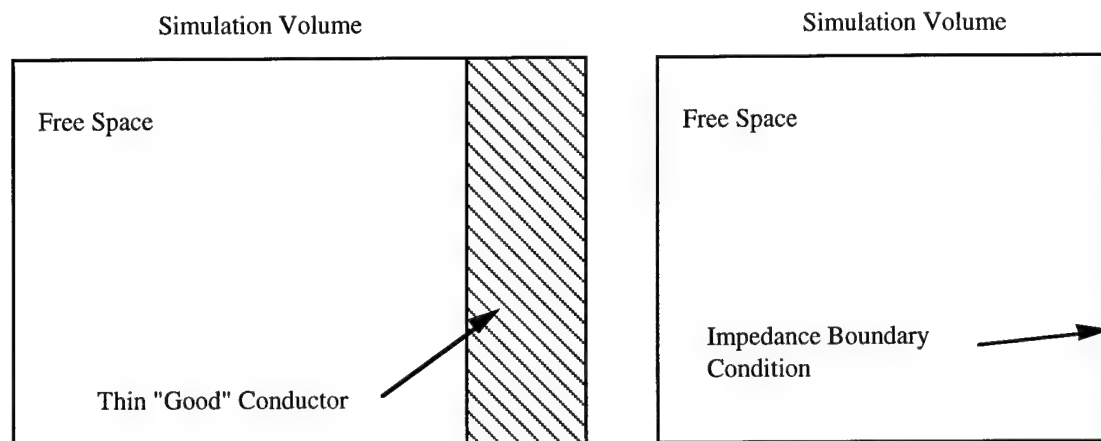


Figure 1-2: Replacement of thin conductor with Impedance Boundary Condition

volume must be divided into a very fine grid in order to capture the loss mechanism within the conductor. When a uniform grid is used (called the *brute force* method) computer resources are wasted by having to finely divide the other less dense materials (*e.g.* free space). In these materials the fine grid is not necessary to capture the physics of the problem. The computational size can be reduced with a sub-gridding scheme where the conducting material uses a much smaller grid than the rest of the computational domain [9, 10, 12]. With this technique care must be given to reduce reflections caused by the change in lattice grid size. For very good conductors; however, the grid size must be so small that even sub-gridding is not a viable option. To overcome the resource problem, the surface of the highly conductive material can be replaced with an Impedance Boundary Condition (IBC) [126]-[130]. Figure 1-2 represents how the conductive material is replaced with a boundary condition that incorporates the physics of the conductor layer. An IBC is only appropriate when the simulation volume of interest is on one side of the the conductive material. However, IBCs have the added complication that they are usually frequency dependent and are not directly applicable to the the standard frequency independent FDTD equations. In this case, the FDTD equations must be modified to incorporate the dispersive nature of the surface [109] -[120]. Typical frequency domain equations relating the



electric fields and magnetic fields become convolution equations in time. Since a convolution has a large memory overhead, if the convolution integral can be approximated by a sum of exponentials, then recursive convolution can be implemented and the memory requirements reduced.

Similar to an IBC, another approach [117] uses a *synthetic* conductivity and the normal FDTD difference equations for lossy media. A synthetic conductivity is derived by comparing the numerical impedance of the difference equations and the actual impedance of a good conductor at specified frequency. In this way the derived synthetic conductivity is inserted into the FDTD equations at the boundary; thus being a surface boundary condition similar to an IBC. The advantage to this method is that no *new* equations are needed; however, it's major disadvantage is that it is only appropriate at a single frequency.

An Impedance Boundary Condition that incorporates frequency dependence was developed for thin dielectric coatings over PEC surfaces [127]. The IBC formulation starts with the analytically derived expression for the impedance in the frequency domain. The expression is expanded in a Taylor series about the wave number. Next the frequency domain is transformed to the time domain by replacing  $-i\omega$  with  $\partial/\partial t$ . The resulting partial differential equation is fourth order in time and first order in space. The difference equations do model the frequency characteristics fairly well; however, the equations are quite complicated and rely on many past values of the surface electric field. Furthermore, the condition is limited to normal incidence; thus, limited to 1D structures. This work is extended to include non-normal incidence [129]; however, the modified IBC is only good for a single incidence angle.

Like the IBC of [127], Tassoudji [128] starts with a frequency domain expression for the impedance of one dimensional structures. Here the structure is a thin sheet of highly conducting material. The frequency domain equation is transformed to the Laplace domain and the subsequent expression is approximated by a sum of first-order rational functions. This approximation is critical to the IBC's practicality to

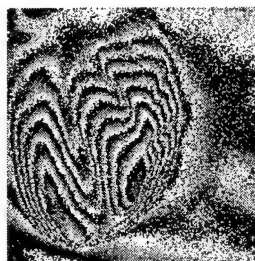


Figure 1-3: SAR interferogram

FDTD. The first-order rational functions are exponentials in time and thus a recursive convolution scheme is implemented. The benefit of this scheme is the wide range of frequencies for which it is valid.

In this thesis, the IBC for thin finite conducting sheets of [128] is examined and extended to two dimensions. Guidelines for the number of expansion terms needed are derived in order to give users an *a priori* estimate of the resources required to perform a given simulation. The new 2D IBC is validated through the measurements of the *quality* factor of rectangular resonant cavities at different frequencies and conductivity values.

### 1.1.3 Phase Unwrapping

Airborne and spaceborne Synthetic Aperture Radar (SAR) platforms have been used for many years to study the earth's surface [144]-[159]. When two radars on a single platform or two passes of a single radar map the same area, an interferogram can be produced from the difference in phase measured by each radar or pass. An interferogram is a pictorial representation of the phase differences measured at each pixel as shown in Figure 1-3

Since the measured phase differences lie between  $-\pi$  and  $\pi$ , the phase is said to be *wrapped*. A SAR interferogram contains *fringes*. These fringes are the locations on the interferogram where a  $2\pi$  discontinuity exists. The interferogram resembles a

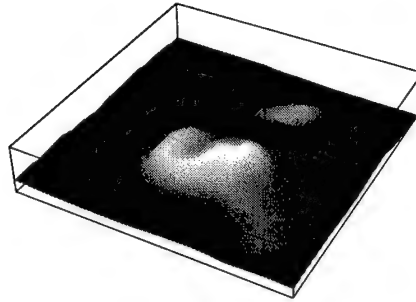


Figure 1-4: Digital Elevation Model (DEM) of Alaskan mountain.

topographical contour map where a line of constant elevation corresponds to a fringe. When no noise is present, the fringes can easily be located and the data adjusted by adding multiples of  $2\pi$  to produce an *unwrapped* phase image. However, real data contain noise and phase unwrapping can be a complicated process.

Successful phase unwrapping is the key to the extraction of DEM (digital elevation model) from an interferometric SAR phase image. Figure 1-4 is the DEM associated with the terrain that produced the ERS-1 SAR interferogram of Figure 1-3.

Although some new phase unwrapping techniques have been introduced recently based on the principle of maximum entropy [164] and multiresolution [165] that may lead to better phase unwrapping algorithms, there are really two basic approaches to unwrapping phase data. The first is based on finding an unwrapped solution such that the solution's first-order partial derivatives in the  $x$  and  $y$  directions match (or closely match) the wrapped first-order partial derivatives or gradients of the phase data. Typically noise is handled by unwrapping the *best* data first in local schemes or weighting the data in global schemes. The second approach integrates along the data and adds or subtracts  $2\pi$  when a fringe is crossed. The noise is considered by searching for phase inconsistencies, in the form of *residues*. The residues are connected to form branch cuts and phase is unwrapped by adjusting the integration path or by modifying the fringe information.

There are local and global techniques to phase unwrapping algorithms based on the gradients of the measured data. The local algorithms usually locate one or more areas on the image that are considered *good* data. Finding these points may use noise floor data and signal-to-noise ratio [168] or use coherence data [166],[178]. Unwrapping usually begins with these *good* areas. The algorithms move from pixel to pixel and add or subtract  $2\pi$  based on some criteria. One method follows the least-gradient path with the assumption that the smallest gradient points to the best data [180],[178] and the adjustments are made to match the solution gradient to the wrapped measured gradient. Other methods use more neighbors to decide the value to add to the unwrapped pixel [161],[169]. Here all the gradients of the adjacent unwrapped pixels are examined and the phase of the unwrapped pixel is predicted based on these gradients. Then an integer number of  $2\pi$  is added to bring the unwrapped pixel closest to the predicted phase. In this way it is possible to have phase differences larger than  $\pi$ , so this method can accommodate *real* discontinuities due to terrain features. All of these local techniques have the added complication of growing separate unwrapped regions that must be joined to produce the final product. Since the *best* pixels are unwrapped first, the likelihood of errors propagating through the image is reduced.

Global gradient algorithms are based on least squares and weighted least squares methods [170]. In this way, the technique attempts to find a solution that minimizes the differences between all of the solution's gradients and the wrapped data's gradients. The least squares approach is very desirable because of the speed at which all the data can be unwrapped; but, the method does not treat noisy data very well [170]. The weighted least squares method allows the user to favor the *good* data by applying a set of weights to the data based on some knowledge of the data's noise content. These methods were applied to a single SAR interferogram [160]; however, no details of the weighting criteria were presented. [162] used a weighting least squares on a simulated interferogram with a shear, where the shear discontinuity was masked out and a new multi-grid iteration scheme was used to solve the weighted partial differential

equation. [171] applied a weighted least squares technique to a speckle interferogram using a weighting scheme based on masking out the phase inconsistencies or residues.

The branch cut method also has local and global approaches. So far, only local approaches have been reported in SAR interferometry. The branch cut method and SAR interferometry phase unwrapping was first reported in [173]. Applied to the interferogram derived from two passes of Seasat, the residue connections were based on a *nearest neighbor* approach. This approach works well with a low density of residues; however, it breaks down with a high density of residues [173]. Once two residues are connected they are removed and no longer considered for connection to any other residues. This method is very likely to leave an uncompensated residue. The phase is then unwrapped by integrating along a path that never crosses a branch cut. This approach was briefly reported in [160] as part of an overview of SAR phase unwrapping techniques. The reported disadvantage to the branch cut method is the propagation of global errors from uncompensated residues. A modification to the basic branch cut method in SAR interferometry involves connecting and removing residue pairs that are only 1 or 2 pixels apart [163]. The remaining residues are handled separately and considered part of *real* discontinuities that exist as a result of terrain features.

The branch cut method has also been applied to speckle interferometry, used to measure very small surface deformations on structures. In this application, a nearest neighbor (local) connection algorithm was used and reported in [174]. The first global branch cut method is used to unwrap a speckle interferogram. All residues are considered before making any branch cuts. In this way, the algorithm is based on minimizing the total branch cut length[175].

Finding efficient, accurate and automatic phase unwrapping algorithms is an interesting topic and is becoming more important as more processing occurs on the SAR platform. In this thesis, the least squares global approaches are investigated and applied to SAR interferometry. Specifically, a hybrid method that uses a weighting

mask based on branch cut residues is examined and compared to weighting schemes based on coherence data. Also, *optimum* branch cut algorithms are applied to SAR interferograms and the techniques are compared to the least squares method. Data from both simulated and real SAR interferograms are used.

## 1.2 Description of Thesis

This thesis is divided into six chapters. Chapters 1 and 6 are the introduction and conclusion and require no description.

Chapter 2 provides a detailed look at the Finite Difference Time Domain Method as a numerical technique to solving electromagnetic problems. The discretization of Maxwell's equations and the treatment of both lossless and lossy materials are described. Special attention is given to Absorbing Boundary Conditions and specifically the relatively new perfectly matched layer and the it's application to multilayer dielectric media in preparation for it's use in Chapter 3.

Chapter 3 is dedicated to the use of the numerical FDTD technique to study dielectric rib waveguides. The perfectly matched layer of Chapter 2 is used as the absorbing boundary. The application of a mode template to efficiently launch the guide's fundamental mode is described. This numerical technique is compared to analytical methods for deriving dispersion characteristics of dielectric waveguides. A numerical study of the benefit of this technique is conducted. Afterwards, these methods are used to analyze various bend discontinuities found in dielectric waveguide structures.

In Chapter 4 a new Impedance Boundary Condition is extended for use in two dimensional FDTD simulations. The IBC is described in great detail and studied in one dimensional simulations. The influence of FDTD parameters and the number of IBC expansion terms on the accuracy of the IBC based on the reflection of a wave from a thin finite conducting sheet is presented. The IBC is extended to two dimensions

and verified through the study of resonant structures. The *quality factor* of many rectangular resonant structures is found using FDTD and compared to analytical results.

Numerical techniques of phase unwrapping of synthetic aperture radar interferograms are investigated in Chapter 5. The foundations of global phase unwrapping are described, specifically least squares and optimal branch cut unwrapping. New modifications to these techniques are applied to both simulated and real interferograms. After the application of these techniques to the real SAR data, the phase is used to invert terrain height and the height is compared to ground truth.

There are three appendices included in this thesis. Appendix A lists the first and second order Mur absorbing boundary condition FDTD equations. Appendix B describes the methods used to determine the coefficients used in the PML FDTD equations. Appendix C gives a detailed review of the transportation problem found in linear programming that was used to build an optimum branch cut connection algorithm in Chapter 5.

## Chapter 2

# Finite Difference Time Domain Method

### 2.1 Introduction

The Finite Difference Time Domain Method is one of the most popular numerical methods for solving electromagnetic problems in the time domain. K. S. Yee [1] proposed a discretizing scheme for Maxwell's equations that staggers the electric and magnetic fields in space and time in such a way that the difference equations are second order accurate. But, more importantly, it is possible to analyze very complicated structures over multiple frequencies with a single simulation. FDTD's basic limitation is its need for large computer resources to represent the simulation volume. The impact of this limitation has been lessened with the recent advances in computer technology. The FDTD method has been widely used to solve electromagnetic problems [2]-[28]. The purpose of this chapter is to describe the FDTD method used in this thesis.



## 2.2 Maxwell's Equations in Cartesian Coordinates

Maxwell's curl equations form the basis of the FDTD difference equations. Starting with

$$\nabla \times \bar{E}(\bar{r}, t) = -\frac{\partial}{\partial t} \bar{B}(\bar{r}, t), \quad (2.1)$$

and

$$\nabla \times \bar{H}(\bar{r}, t) = \frac{\partial}{\partial t} \bar{D}(\bar{r}, t) + \bar{J}(\bar{r}, t), \quad (2.2)$$

with the constitutive relations

$$\bar{D} = \epsilon \bar{E}, \quad (2.3)$$

and

$$\bar{B} = \mu \bar{H}, \quad (2.4)$$

the first step is to separate the equations into their individual components. The electric field component equations are

$$\frac{\partial}{\partial t} \epsilon E_x = \frac{\partial}{\partial y} H_z - \frac{\partial}{\partial z} H_y - J_x, \quad (2.5)$$

$$\frac{\partial}{\partial t} \epsilon E_y = \frac{\partial}{\partial z} H_x - \frac{\partial}{\partial x} H_z - J_y, \quad (2.6)$$

and

$$\frac{\partial}{\partial t} \epsilon E_z = \frac{\partial}{\partial x} H_y - \frac{\partial}{\partial y} H_x - J_z, \quad (2.7)$$

while the magnetic field equations are

$$\frac{\partial}{\partial t} \mu H_x = \frac{\partial}{\partial z} E_y - \frac{\partial}{\partial y} E_z, \quad (2.8)$$

$$\frac{\partial}{\partial t} \mu H_y = \frac{\partial}{\partial x} E_z - \frac{\partial}{\partial z} E_x, \quad (2.9)$$

and

$$\frac{\partial}{\partial t} \mu H_z = \frac{\partial}{\partial y} E_x - \frac{\partial}{\partial x} E_y. \quad (2.10)$$

## 2.3 Difference Equations in Free Space

### 2.3.1 Central Difference Approximation

The FDTD difference equations are constructed from a central difference approximation of the partial derivatives in equations (2.5) through (2.10).

Given a function  $f(x)$ , the continuous variable  $x$  is divided into discrete points separated by  $\Delta$  such that  $x = i\Delta$  where  $i$  is any integer. The partial derivative may be approximated by

$$\left. \frac{\partial}{\partial x} f(x) \right|_{x=i\Delta} \approx \frac{f((i + \frac{1}{2})\Delta) - f((i - \frac{1}{2})\Delta)}{\Delta} \quad (2.11)$$

This central difference approximation is second-order accurate (*i.e.* the error  $\sim \Delta^2$ ). Thus, theoretically, the error can be made as small as desired for well behaved functions if the grid size,  $\Delta$ , is made small enough.

### 2.3.2 Yee Grid and FDTD Nomenclature

Yee [1] introduced a spatial arrangement of the six field quantities shown in Figure 2-1, that places the electric field unknowns along the edges of a discretized grid and the magnetic field unknowns on the faces of the grid. The electric and magnetic fields are staggered both in time and space by  $\frac{\Delta t}{2}$  and  $\frac{\Delta x}{2}$ ,  $\frac{\Delta y}{2}$ , and  $\frac{\Delta z}{2}$ , respectively. This staggered approach allows the difference equations to be local in both time and space. By local we mean that an unknown is a function of itself and its nearest neighbors (local in space) at the most recent time step (local in time). Thus only one set of unknowns at each location must be stored in memory at a given time. The set of all discrete cells is called the *computational domain*.

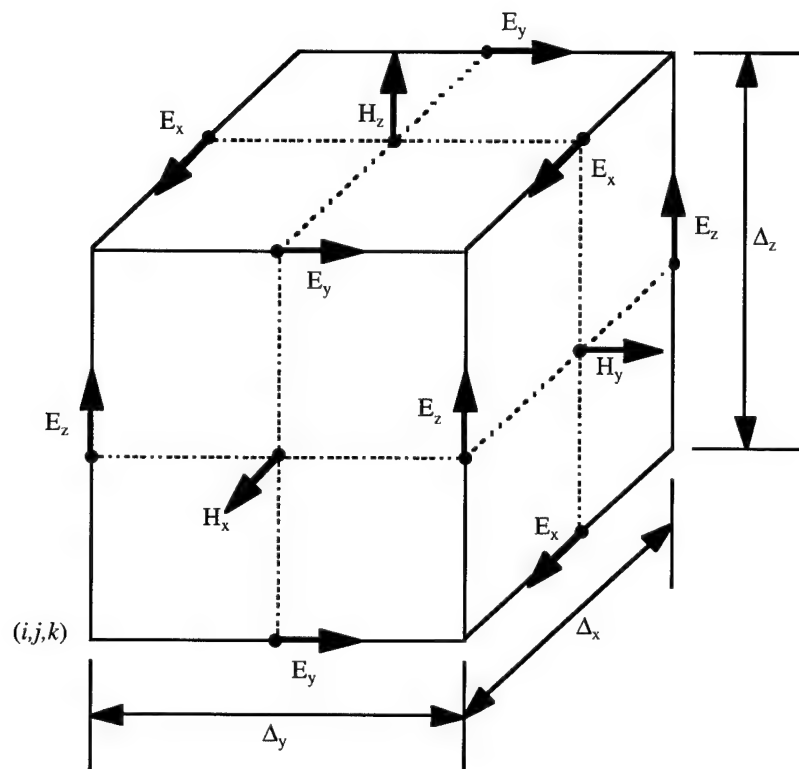


Figure 2-1: Yee's FDTD grid.

The continuous coordinates  $(x, y, z, t)$  become discrete coordinates  $(i\Delta x, j\Delta y, k\Delta z, n\Delta t)$  or simply  $(i, j, k, n)$  where  $i, j$ , and  $k$  represent the space coordinate indices and  $n$  represents the time coordinate index and  $\Delta x, \Delta y, \Delta z$  and  $\Delta t$  are the spatial and temporal intervals between sampled points. These intervals are referred to as the grid size (spatial) and time step (temporal). When uniform gridding is used, the grid spacings are all set to a single value,  $\Delta$ . The most common FDTD nomenclature uses a subscript to represent the field component direction, a superscript to represent the time index, and three arguments to represent the space indices.

For example,  $E_z^{n+1}(i, j, k + \frac{1}{2})$  represents the  $z$  component of the electric field sampled at  $t = (n + 1)\Delta t$  seconds and sampled in space at  $x = i\Delta x$ ,  $y = j\Delta y$ , and  $z = (k + \frac{1}{2})\Delta z$  meters.

### 2.3.3 Difference Equations

Figure 2-2 shows the spatial arrangement of the individual field components used to construct the difference equations. A field equation includes its past value plus a linear combination of the four nearest fields that lie in the plane perpendicular to the field component. The free space difference equations are depicted in equations 2.12-2.17.

$$\begin{aligned}
 E_x^{n+1}(i + \frac{1}{2}, j, k) &= E_x^n(i + \frac{1}{2}, j, k) \\
 &+ \frac{\Delta t}{\epsilon_0 \Delta y} \left( H_z^{n+\frac{1}{2}}(i + \frac{1}{2}, j + \frac{1}{2}, k) - H_z^{n+\frac{1}{2}}(i + \frac{1}{2}, j - \frac{1}{2}, k) \right) \\
 &- \frac{\Delta t}{\epsilon_0 \Delta z} \left( H_y^{n+\frac{1}{2}}(i + \frac{1}{2}, j, k + \frac{1}{2}) - H_y^{n+\frac{1}{2}}(i + \frac{1}{2}, j, k - \frac{1}{2}) \right)
 \end{aligned} \tag{2.12}$$

$$E_y^{n+1}(i, j + \frac{1}{2}, k) = E_y^n(i, j + \frac{1}{2}, k) \tag{2.13}$$

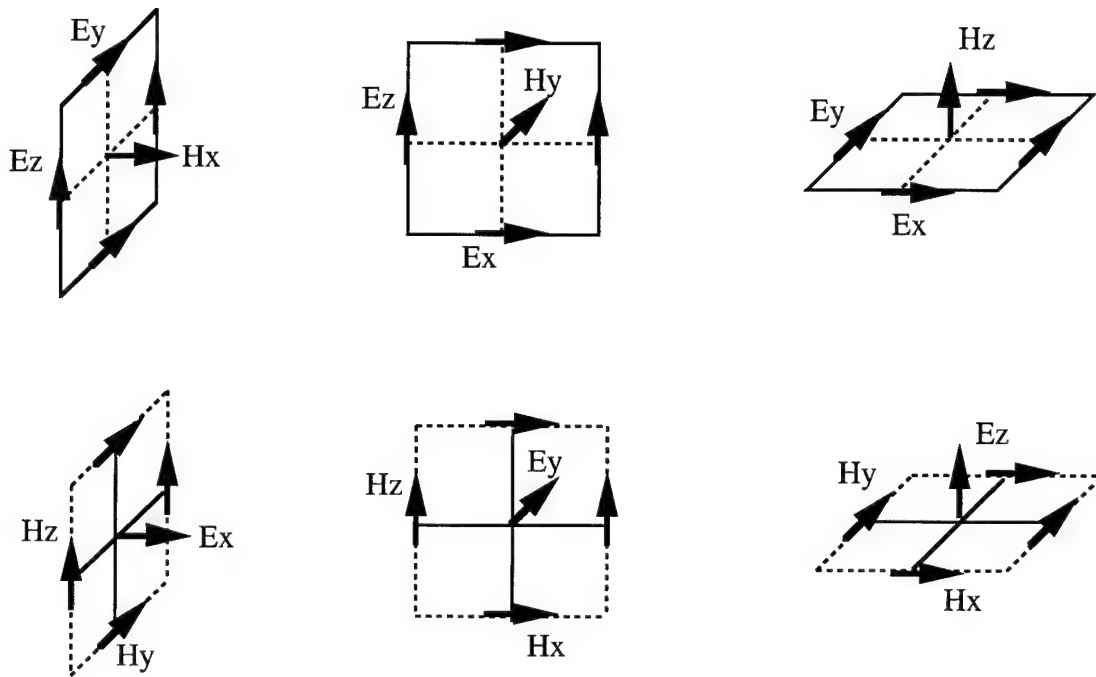


Figure 2-2: Graphical representations used to construct FDTD difference equations. Solid lines represent integer grid lines.

$$\begin{aligned}
& + \frac{\Delta t}{\epsilon_0 \Delta z} \left( H_x^{n+\frac{1}{2}}(i, j + \frac{1}{2}, k + \frac{1}{2}) - H_x^{n+\frac{1}{2}}(i, j + \frac{1}{2}, k - \frac{1}{2}) \right) \\
& - \frac{\Delta t}{\epsilon_0 \Delta x} \left( H_z^{n+\frac{1}{2}}(i + \frac{1}{2}, j + \frac{1}{2}, k) - H_z^{n+\frac{1}{2}}(i - \frac{1}{2}, j + \frac{1}{2}, k) \right)
\end{aligned}$$

$$\begin{aligned}
E_z^{n+1}(i, j, k + \frac{1}{2}) &= E_z^n(i, j, k + \frac{1}{2}) \\
& + \frac{\Delta t}{\epsilon_0 \Delta x} \left( H_y^{n+\frac{1}{2}}(i + \frac{1}{2}, j, k + \frac{1}{2}) - H_y^{n+\frac{1}{2}}(i - \frac{1}{2}, j, k + \frac{1}{2}) \right) \\
& - \frac{\Delta t}{\epsilon_0 \Delta y} \left( H_x^{n+\frac{1}{2}}(i, j + \frac{1}{2}, k + \frac{1}{2}) - H_x^{n+\frac{1}{2}}(i, j - \frac{1}{2}, k + \frac{1}{2}) \right)
\end{aligned} \tag{2.14}$$

$$\begin{aligned}
H_x^{n+\frac{1}{2}}(i, j + \frac{1}{2}, k + \frac{1}{2}) &= H_x^{n-\frac{1}{2}}(i, j + \frac{1}{2}, k + \frac{1}{2}) \\
& + \frac{\Delta t}{\mu_0 \Delta z} \left( E_y^n(i, j + \frac{1}{2}, k + 1) - E_y^n(i, j + \frac{1}{2}, k) \right) \\
& - \frac{\Delta t}{\mu_0 \Delta y} \left( E_z^n(i, j + 1, k + \frac{1}{2}) - E_z^n(i, j, k + \frac{1}{2}) \right)
\end{aligned} \tag{2.15}$$

$$\begin{aligned}
H_y^{n+\frac{1}{2}}(i + \frac{1}{2}, j, k + \frac{1}{2}) &= H_y^{n-\frac{1}{2}}(i + \frac{1}{2}, j, k + \frac{1}{2}) \\
& - \frac{\Delta t}{\mu_0 \Delta z} \left( E_x^n(i + \frac{1}{2}, j, k + 1) - E_x^n(i + \frac{1}{2}, j, k - 1) \right) \\
& + \frac{\Delta t}{\mu_0 \Delta x} \left( E_z^n(i + 1, j, k + \frac{1}{2}) - E_z^n(i - 1, j, k + \frac{1}{2}) \right)
\end{aligned} \tag{2.16}$$

$$\begin{aligned}
H_z^{n+\frac{1}{2}}(i + \frac{1}{2}, j + \frac{1}{2}, k) &= H_z^{n-\frac{1}{2}}(i + \frac{1}{2}, j + \frac{1}{2}, k) \\
& + \frac{\Delta t}{\mu_0 \Delta y} \left( E_x^n(i + \frac{1}{2}, j + 1, k) - E_x^n(i + \frac{1}{2}, j, k) \right) \\
& - \frac{\Delta t}{\mu_0 \Delta x} \left( E_y^n(i + 1, j + \frac{1}{2}, k) - E_y^n(i, j + \frac{1}{2}, k) \right)
\end{aligned} \tag{2.17}$$

As shown, the temporal discretization places the electric and magnetic fields half a time step away from each other. With this configuration, the method first calculates the electric field (2.12-2.14), then advances the time by half a time step and calculates the magnetic field (2.15-2.17). This technique is called *leap frogging*.

## 2.4 Difference Equations in Lossy Dielectric Media

In this section, we describe the inclusion of lossy media and the scattered versus total field FDTD formulation.

### 2.4.1 Maxwell's Equations in Lossy Dielectric Media

The framework for FDTD equations and algorithm used in this thesis were based on those in Kunz and Luebber [14] and modified where necessary. We begin with Maxwell's curl equations for source free lossy medium:

$$\frac{\partial}{\partial t} \bar{H} = -\frac{1}{\mu} \nabla \times \bar{E} - \frac{\sigma^m}{\mu} \bar{H} \quad (2.18)$$

and

$$\frac{\partial}{\partial t} \bar{E} = \frac{1}{\epsilon} \nabla \times \bar{H} + \frac{\sigma^e}{\epsilon} \bar{E}. \quad (2.19)$$

When equations (2.18) and (2.19) are discretized, we have a total field formulation; however, it is more convenient to use a scattered field formulation. The main benefit of a scattered field formulation is that an incident field can be analytically specified throughout the computational domain. In this way a plane wave can be specified without needing to provide a source sufficiently far away to generate a plane wave at the scatterer. This reduces the size of the computational domain and provides a convenient way to insert plane waves radiating at different angles. Also, it is more

general than a total field formulation *i.e.* a scattered field code becomes a total field code when the incident field is set to zero.

The basic assumption is that Maxwell's equations are linear in the simulation volume. Thus, outside any scatterers both the incident and total fields satisfy Maxwell's equations for free space and inside any scatterer the total field satisfies Maxwell's equations for the lossy medium. Of course, the linearity assumption does not hold for all media but does apply to the media used in this thesis. So we have

$$\bar{E}^t = \bar{E}^i + \bar{E}^s, \quad (2.20)$$

and

$$\bar{H}^t = \bar{H}^i + \bar{H}^s, \quad (2.21)$$

where the superscripts  $t$ ,  $i$ , and  $s$  stand for total, incident, and scattered respectively. The incident fields satisfy the free space equations:

$$\nabla \times \bar{E}^i = -\mu_0 \frac{\partial}{\partial t} \bar{H}^i \quad (2.22)$$

and

$$\nabla \times \bar{H}^i = \epsilon_0 \frac{\partial}{\partial t} \bar{E}^i \quad (2.23)$$

and the total fields satisfy equations (2.18) and (2.19). Substitution of (2.20) and (2.21) into (2.18) and (2.19) and subtracting the incident field equations (2.22) and (2.23) we find the scattered field equations for inside the scatters,

$$\nabla \times \bar{E}^s = -\mu \frac{\partial}{\partial t} \bar{H}^s - \sigma^m \bar{H}^s - \left[ (\mu - \mu_0) \frac{\partial}{\partial t} \bar{H}^i + \sigma^m \bar{H}^i \right] \quad (2.24)$$

and

$$\nabla \times \bar{H}^s = -\mu \frac{\partial}{\partial t} \bar{E}^s + \sigma^e \bar{E}^s + \left[ (\epsilon - \epsilon_0) \frac{\partial}{\partial t} \bar{E}^i + \sigma^e \bar{E}^i \right]. \quad (2.25)$$

Outside the scatter, since the total fields also satisfy (2.22) and (2.23), substitution



and subtraction of the incident fields yield

$$\nabla \times \bar{E}^s = -\mu_0 \frac{\partial}{\partial t} \bar{H}^s \quad (2.26)$$

and

$$\nabla \times \bar{H}^s = \epsilon_0 \frac{\partial}{\partial t} \bar{E}^s. \quad (2.27)$$

Equations (2.24), (2.25), (2.26), and (2.27) are the foundation for the FDTD difference equations. Since equations (2.26) and (2.27) are just special cases of (2.24) and (2.25) with  $\mu = \mu_0$ ,  $\epsilon = \epsilon_0$ ,  $\sigma^e = 0$  and  $\sigma^m = 0$  only (2.24) and (2.25) are needed to generate the FDTD equations. The equations for each field component are

$$\epsilon \frac{\partial}{\partial t} E_x^s + \sigma^e E_x^s = \left[ \frac{\partial}{\partial y} H_z^s - \frac{\partial}{\partial z} H_y^s \right] + \left[ (\epsilon - \epsilon_0) \frac{\partial}{\partial t} E_x^i + \sigma^e E_x^i \right], \quad (2.28)$$

$$\epsilon \frac{\partial}{\partial t} E_y^s + \sigma^e E_y^s = - \left[ \frac{\partial}{\partial x} H_z^s - \frac{\partial}{\partial z} H_x^s \right] + \left[ (\epsilon - \epsilon_0) \frac{\partial}{\partial t} E_y^i + \sigma^e E_y^i \right], \quad (2.29)$$

$$\epsilon \frac{\partial}{\partial t} E_z^s + \sigma^e E_z^s = \left[ \frac{\partial}{\partial x} H_y^s - \frac{\partial}{\partial y} H_x^s \right] + \left[ (\epsilon - \epsilon_0) \frac{\partial}{\partial t} E_z^i + \sigma^e E_z^i \right], \quad (2.30)$$

$$\mu \frac{\partial}{\partial t} H_x^s + \sigma^m H_x^s = - \left[ \frac{\partial}{\partial y} E_z^s - \frac{\partial}{\partial z} E_y^s \right] - \left[ (\mu - \mu_0) \frac{\partial}{\partial t} H_x^i + \sigma^m H_x^i \right], \quad (2.31)$$

$$\mu \frac{\partial}{\partial t} H_y^s + \sigma^m H_y^s = \left[ \frac{\partial}{\partial x} E_z^s - \frac{\partial}{\partial z} E_x^s \right] - \left[ (\mu - \mu_0) \frac{\partial}{\partial t} H_y^i + \sigma^m H_y^i \right], \quad (2.32)$$

and

$$\mu \frac{\partial}{\partial t} H_z^s + \sigma^m H_z^s = - \left[ \frac{\partial}{\partial x} E_y^s - \frac{\partial}{\partial y} E_x^s \right] - \left[ (\mu - \mu_0) \frac{\partial}{\partial t} H_z^i + \sigma^m H_z^i \right]. \quad (2.33)$$

For completeness, the most general equations are shown above. Because in this work no magnetic materials are used, only equations (2.28)-(2.30) need to be discretized. The magnetic fields can be updated with the free space difference equations (2.15)-(2.17).

### 2.4.2 Difference Equations

The electric field difference equations for lossy dielectric media are shown below. The equations are constructed with computer coding in mind. The coefficients  $C_1 - C_4$  are calculated up front and stored in computer memory and called during the simulation. Also, the coefficients are a function of the medium,  $m$ . One of the tasks at the beginning of the FDTD simulation is to build the structure under test by specifying which materials are at each cell location; such that  $m$  is a function of the field component and location. The electric field equations are

$$\begin{aligned}
 E_x^{s^{n+1}}(i + \tfrac{1}{2}, j, k) &= C_1^e(m) E_x^{s^n}(i + \tfrac{1}{2}, j, k) \\
 &- C_2^e(m) E_x^{i^n}(i + \tfrac{1}{2}, j, k) \\
 &- C_3^e(m) \text{der}\{E_x^{i^n}(i + \tfrac{1}{2}, j, k)\} \\
 &+ C_4^{ey}(m) \left[ H_z^{s^{n+\frac{1}{2}}}(i + \tfrac{1}{2}, j + \tfrac{1}{2}, k) - H_z^{s^{n+\frac{1}{2}}}(i + \tfrac{1}{2}, j - \tfrac{1}{2}, k) \right] \\
 &- C_4^{ez}(m) \left[ H_y^{s^{n+\frac{1}{2}}}(i + \tfrac{1}{2}, j, k + \tfrac{1}{2}) - H_y^{s^{n+\frac{1}{2}}}(i + \tfrac{1}{2}, j, k - \tfrac{1}{2}), \right]
 \end{aligned} \tag{2.34}$$

$$\begin{aligned}
 E_y^{s^{n+1}}(i, j + \tfrac{1}{2}, k) &= C_1^e(m) E_y^{s^n}(i, j + \tfrac{1}{2}, k) \\
 &- C_2^e(m) E_y^{i^n}(i, j + \tfrac{1}{2}, k) \\
 &- C_3^e(m) \text{der}\{E_y^{i^n}(i, j + \tfrac{1}{2}, k)\} \\
 &+ C_4^{ez}(m) \left[ H_x^{s^{n+\frac{1}{2}}}(i, j + \tfrac{1}{2}, k + \tfrac{1}{2}) - H_x^{s^{n+\frac{1}{2}}}(i, j + \tfrac{1}{2}, k - \tfrac{1}{2}) \right] \\
 &- C_4^{ex}(m) \left[ H_z^{s^{n+\frac{1}{2}}}(i + \tfrac{1}{2}, j + \tfrac{1}{2}, k) - H_z^{s^{n+\frac{1}{2}}}(i - \tfrac{1}{2}, j + \tfrac{1}{2}, k), \right]
 \end{aligned} \tag{2.35}$$

and

$$E_z^{s^{n+1}}(i + \tfrac{1}{2}, j, k) = C_1^e(m) E_z^{s^n}(i + \tfrac{1}{2}, j, k) \tag{2.36}$$

$$\begin{aligned}
& - C_2^e(m) E_z^{i,n}(i + \frac{1}{2}, j, k) \\
& - C_3^e(m) \text{der}\{E_z^{i,n}(i + \frac{1}{2}, j, k)\} \\
& + C_4^{ex}(m) \left[ H_y^{s,n+\frac{1}{2}}(i + \frac{1}{2}, j, k + \frac{1}{2}) - H_y^{s,n+\frac{1}{2}}(i - \frac{1}{2}, j, k + \frac{1}{2}) \right] \\
& - C_4^{ey}(m) \left[ H_x^{s,n+\frac{1}{2}}(i, j + \frac{1}{2}, k + \frac{1}{2}) - H_x^{s,n+\frac{1}{2}}(i, j - \frac{1}{2}, k + \frac{1}{2}) \right].
\end{aligned}$$

where

$$C_1^e(m) = \frac{\epsilon}{\epsilon + \sigma^e \Delta t}, \quad (2.37)$$

$$C_2^e(m) = \frac{\sigma^e \Delta t}{\epsilon + \sigma^e \Delta t}, \quad (2.38)$$

$$C_3^e(m) = \frac{(\epsilon - \epsilon_0) \Delta t}{\epsilon + \sigma^e \Delta t}, \quad (2.39)$$

$$C_4^{e\alpha}(m) = \frac{\Delta t}{\Delta\alpha(\epsilon + \sigma^e \Delta t)} \quad \alpha = x, y, z,$$

and  $\text{der}\{\}$  represents a discretized analytic expression for the time derivative of the analytically specified incident field.

## 2.5 Treatment of Dielectric Interfaces

Figure 2-3 represents the placement of the electric and magnetic fields in a Yee grid cell. A single cell represented by the indices  $(i, j, k)$  has its lower left front corner positioned at  $(i\Delta x, j\Delta y, k\Delta z)$ . Although a cell only has one each of the six field quantities associated with it, a cell has 12 electric and 6 magnetic field quantities adjacent to it as Figure 2-3 shows. This configuration is key to the construction of multiple dielectric media structures within the simulation volume.

When more than one material is used in the simulation volume permittivity becomes a function of position. In general, the permeability is also a function of position, but throughout this thesis only non-magnetic materials are used. Although there are

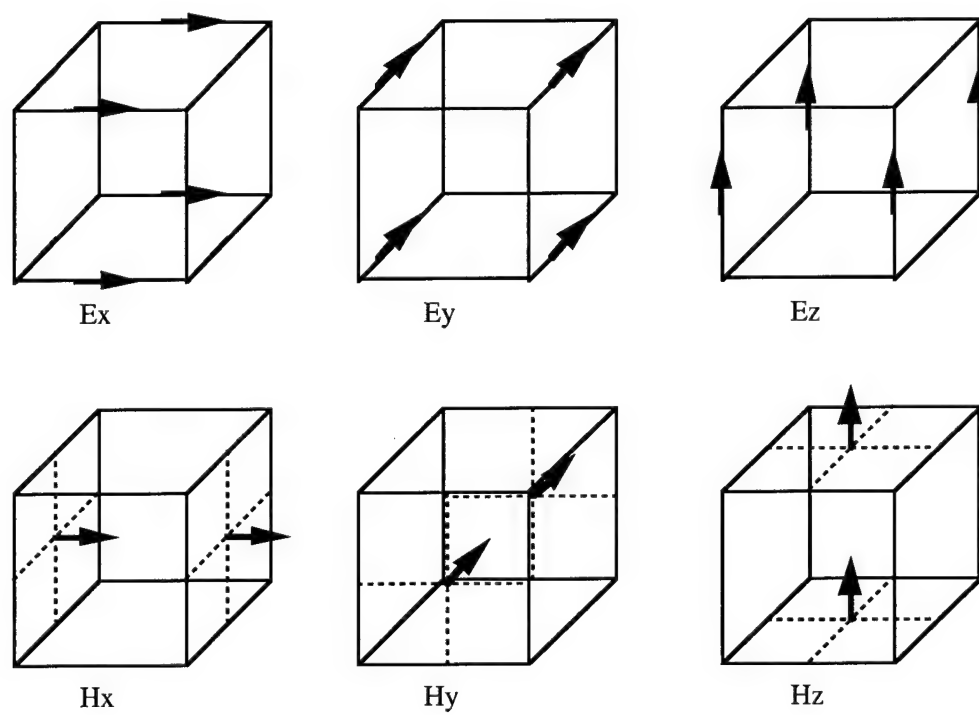


Figure 2-3: Individual field locations on the Yee grid.

many possible ways to fill the simulation volume with different media, the typical method places dielectric media wholly within a cell such that the media interfaces are located along the faces of the Yee grid. In this way the continuity of the tangential electric fields is inherently enforced. The construction of a multi-dielectric structure consists of assigning a permittivity to each of the electric field component positions within the computational domain. The permittivities are based on the physical dimensions of the structure. For those electric field components that lie completely within a dielectric medium with permittivity  $\epsilon_1$  the permittivity is set to  $\epsilon_1$ . However for those electric field components that lie on the planar interface between two media with  $\epsilon_1$  and  $\epsilon_2$ , an average of the two dielectric's permittivities is used:  $\frac{\epsilon_1 + \epsilon_2}{2}$ . Finally, for those electric field components that lie along a line that lies at the intersection of four dielectric media with  $\epsilon_1$ ,  $\epsilon_2$ ,  $\epsilon_3$ , and  $\epsilon_4$ , an average of the four permittivities is used:  $\frac{\epsilon_1 + \epsilon_2 + \epsilon_3 + \epsilon_4}{4}$ . Figure 2-4 is a diagram that shows the proper assignment of the permittivity values for a FDTD simulation with multiple dielectric type.

## 2.6 Perfect Conductors

When perfect conductors are present in the simulation volume the the total electric field must be zero inside the conductor, so the tangential electric fields on the surface must be zero to satisfy the boundary conditions. If an analytic plane wave excitation is used then we set

$$\bar{E}^s = -\bar{E}^i \quad (2.40)$$

inside the conductor.

If a total field formulation is used (*i.e.*  $\bar{E}^i = 0$ ), then the tangential fields are explicitly set to zero on the surface of the conductor.

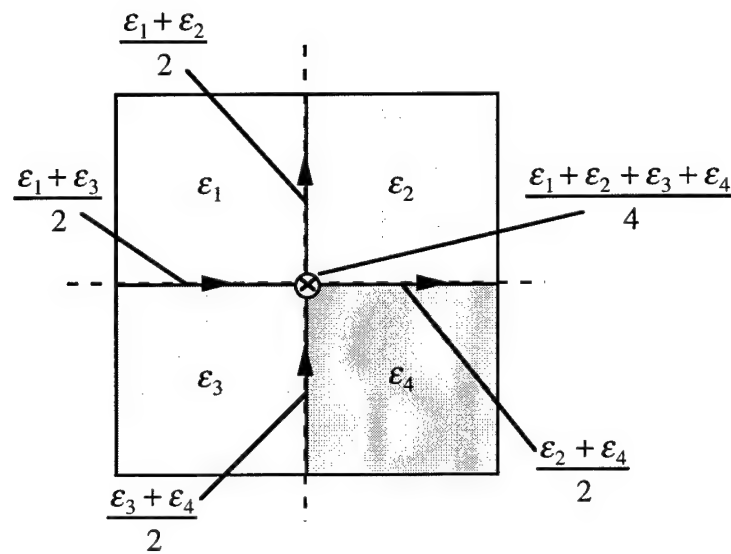


Figure 2-4: Assignment of permittivity values for multiple dielectric media in FDTD simulations.

## 2.7 Accuracy, Numerical Dispersion, and Stability

Since the FDTD method is based on central differencing, the smaller the grid size the more accurately the difference equations will approximate the partial derivatives. However, decreasing the grid size will increase the memory required and the run time of the simulation so, the question is how accurate do we want to be?

### 2.7.1 Accuracy and Numerical Dispersion

The measure of accuracy used to determine the grid size is derived from the numerical dispersion relation of the FDTD grid [14]. In free space a plane wave satisfies the following dispersion relation:

$$k_x^2 + k_y^2 + k_z^2 = \omega^2 \epsilon_0 \mu_0, \quad (2.41)$$

where

$$\epsilon_0 \mu_0 = \frac{1}{c_0^2}.$$

The phase velocity in any direction is a constant,

$$v_{ph} = \frac{\omega}{k} = c_0. \quad (2.42)$$

The difference between the numerical dispersion and the analytical dispersion is the measure of the accuracy. The dispersion relation of the FDTD grid with a uniform grid spacing is given by

$$\sin^2 \frac{\omega \Delta t}{\Delta} = \left( \frac{c_0 \Delta t}{\Delta} \right)^2 \left\{ \sin^2 \frac{k_x \Delta}{2} + \sin^2 \frac{k_y \Delta}{2} + \sin^2 \frac{k_z \Delta}{2} \right\}. \quad (2.43)$$

Instead of being constant the FDTD dispersion relation is a function of the grid spacing,  $\Delta$ , the angle of propagation, and the ratio,  $\frac{c_0 \Delta t}{\Delta}$ , called the *stability factor*. As expected, when  $\Delta t \rightarrow 0$  and  $\Delta \rightarrow 0$ , equation (2.43) approaches (2.41) showing

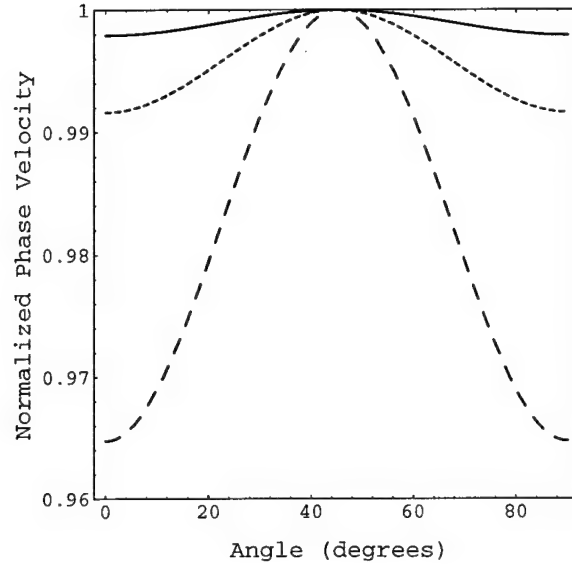


Figure 2-5: Normalized phase velocity versus angle of propagation for 2D FDTD;  $\frac{\lambda}{20}$  : (solid line),  $\frac{\lambda}{10}$  : (dashed line), and  $\frac{\lambda}{5}$  : (large-dashed line).

again that with a small enough grid arbitrarily good accuracy can be achieved with FDTD. Figure 2-5 is a plot of the normalized phase velocity versus the angle that the  $k$  vector makes with the  $x$  axis, for a 2D FDTD algorithm. Each curve represents a different grid size in terms of the wavelength,  $\lambda$ . The solid line represents  $\frac{\lambda}{20}$ , the dashed line represents  $\frac{\lambda}{10}$  and the large-dashed line represents  $\frac{\lambda}{5}$ . Linear dispersion equates to a normalized phase velocity of 1 and any deviation from 1 represents error. The FDTD guideline is to keep the dispersion error to less than one percent, so the grid size should satisfy

$$\Delta \leq \frac{\lambda}{10}. \quad (2.44)$$

### 2.7.2 Stability

Once the grid size has been determined to provide a reasonable amount of accuracy, numerical stability places an upper bound on the time step. Stability can be guaran-



teed if for all possible wave numbers the frequency,  $\omega$ , in (2.41) remains real valued. Thus, the stability condition for a non-uniform cartesian grid is

$$c\Delta t \leq \frac{1}{\sqrt{\frac{1}{(\Delta x)^2} + \frac{1}{(\Delta y)^2} + \frac{1}{(\Delta z)^2}}}, \quad (2.45)$$

and for a uniform grid is

$$\Delta t \leq \frac{\Delta}{\sqrt{3}c} \quad (2.46)$$

where  $c$  is the speed of light. The constraint from (2.45), is known as the Courant stability condition and must be enforced at all times within all materials.

Many FDTD codes will allow the user to specify the grid spacing then automatically sets the time step to the maximum allowed under the stability condition of equation 2.46; however, sometimes the user may desire a smaller time step. To accommodate a smaller time step we write

$$\Delta t \leq \frac{\Delta}{CFL c} \quad (2.47)$$

where  $CFL$  is a real number the can be used to adjust the time step, keeping in mind that there is a lower limit and that limit depends on the dimension of the simulation.

## 2.8 Implementation of Sources and Excitations

There are many ways to excite an FDTD simulation. Whether the excitation is an analytic plane wave, current source, or boundary condition, a Gaussian pulse is used for the basic temporal excitation. The continuous Gaussian pulse excitation is

$$g(t) = e^{-(t-t_o)^2/T^2}. \quad (2.48)$$

The Gaussian pulse is desirable because it's spectrum is also Gaussian as shown below.

$$\begin{aligned} G(\omega) &= \int_{-\infty}^{\infty} g(t)e^{i\omega t} dt \\ &= T\sqrt{\pi}e^{i\omega t_o}e^{-\omega^2 T^2/4}. \end{aligned} \quad (2.49)$$

Thus a Gaussian pulse may be used to excite several frequencies in a single simulation. In FDTD, since the Gaussian pulse must be truncated (*i.e.* the signal cannot extend to  $\pm\infty$ ), care must be given to prevent unwanted high frequency components from entering the simulation from the waveform's truncation. This is accomplished by linking  $t_o$  and  $T$ . Discretizing (2.48),  $t \rightarrow n\Delta t$  and  $t_o \rightarrow \beta\Delta t$ , where  $\Delta t$  is the time step and  $n$  and  $\beta$  are integers. The unwanted frequencies can essentially be eliminated by choosing  $T$  large enough to damp out the effects of the truncation. Typically,

$$T = t_o/4, \quad (2.50)$$

so that the attenuation of the step is  $e^{-16}$  or 140 dB. So, the pulse width of the signal, determined by  $t_o = \beta\Delta t$ , must be chosen to ensure the desired bandwidth and  $T$  is automatically set to suppress the undesired high frequencies.

The pulse width of the excitation is approximately  $2\beta\Delta t$  and therefore the spectral content is  $\frac{1}{2\beta\Delta t}$ . When needed, a modulated Gaussian pulse is used to shift the spectrum to a desired frequency as shown below.

$$g(t) = \cos(\omega_o t)e^{-(t-t_o)^2/T^2} \quad (2.51)$$

There are three ways to insert the temporal excitation into the simulation. The first way is to use the analytic plane wave excitation,  $E^i$ , in equations (2.35)-(2.37). The second way is to add electric current density components to the discretized Ampere's Law. For a current source in the  $\hat{z}$  direction the cross sectional area is assumed to be  $\Delta x\Delta y$  and a length of  $\Delta z$  [20]. In this way if a finer grid is used

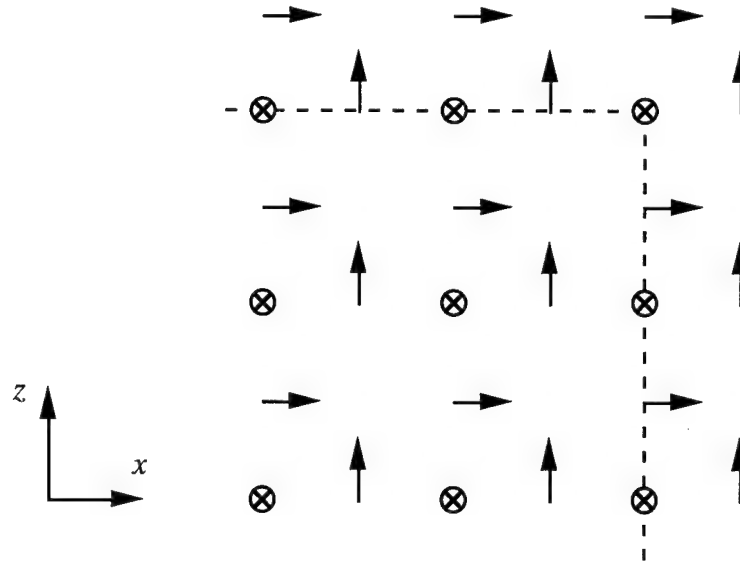


Figure 2-6: 2D Yee grid: dashed line represents the edges of the computational domain.

for the same physical dimensions then the current density component must be scaled down in order to excite with the same current density. The last way to excite the problem is with a boundary condition *i.e.* define an electric field component as a function of time at some location within the simulation volume.

## 2.9 Treatment of Computational Boundaries

Figure 2-6 represents a two dimensional Yee grid for a TE polarized wave with fields  $E_y$ ,  $H_x$  and  $H_z$ . The dashed lines in Figure 2-6 represent the truncation of the computational boundary along two edges to the domain's grid lattice. Since the magnetic field quantities above and to the right of the dashed lines do not exist, the electric field components that lie along the boundaries cannot be updated with the standard difference equations.

When the edges are perfect conductors, the tangential electric fields can be set to zero and therefore the boundaries pose no difficulty. However, these boundary

conditions apply to a narrow range of electromagnetic problems.

If left alone, the edges of the computational domain would act as an open circuit and reflect the outgoing waves that impinge upon the boundary. With a large enough domain, measurements can be taken before they are corrupted by the non-physical reflections from the boundary. Unfortunately this technique, called *time gating*, may require too much computer memory to be viable. Many approaches have been used to terminate the FDTD computational domain [29]-[45].

### 2.9.1 One Way Wave Equation

The most common treatment of the boundaries is based on the one way wave equation made popular by Mur [29]. The concept is simple: construct equations that allow only outgoing waves. In free space the solutions of the electric field will satisfy the wave equation:

$$\left( \frac{\partial^2}{\partial x^2} + \frac{\partial^2}{\partial y^2} + \frac{\partial^2}{\partial z^2} - \frac{1}{c_0^2} \frac{\partial^2}{\partial t^2} \right) \bar{E} = 0. \quad (2.52)$$

Consider a boundary at  $x = 0$  and a computational domain that lies to the right of the boundary, a plane wave traveling in free space is given by

$$W(\bar{r}, t) = \text{Re} \left\{ W_0 e^{i(k_x x + k_y y + k_z z - \omega t)} \right\} \quad (2.53)$$

where  $W$  represents a field component and

$$k_x = \pm \left( k_0^2 - k_y^2 - k_z^2 \right)^{\frac{1}{2}} \quad (2.54)$$

with

$$\text{Re} \left\{ \left( k_0^2 - k_y^2 - k_z^2 \right)^{\frac{1}{2}} \right\} \geq 0 \quad (2.55)$$

and

$$k_0^2 = \frac{\omega^2}{c_0^2}. \quad (2.56)$$

Allowing only outgoing waves, then

$$k_x = - \left( k_0^2 - k_y^2 - k_z^2 \right)^{\frac{1}{2}}. \quad (2.57)$$

The next step is to convert (2.57) to the time domain

$$\left\{ \frac{\partial}{\partial x} - \frac{1}{c_0} \left( 1 - (c_0 v_y)^2 - (c_0 v_z)^2 \right)^{\frac{1}{2}} \frac{\partial}{\partial t} \right\} W = 0 \quad (2.58)$$

where  $v_y$  and  $v_z$  are the phase velocities in the  $y$  and  $z$  directions defined by

$$v_y = \frac{k_y}{\omega}$$

and

$$v_z = \frac{k_z}{\omega}.$$

The essence of the Mur boundary conditions lies in the approximation to

$$\left( 1 - (c_0 v_y)^2 - (c_0 v_z)^2 \right)^{\frac{1}{2}}. \quad (2.59)$$

If  $((c_0 v_y)^2 - (c_0 v_z)^2) \ll 1$ , then we can expand (2.59) as follows:

$$\begin{aligned} & \left( 1 - (c_0 v_y)^2 - (c_0 v_z)^2 \right)^{\frac{1}{2}} \\ &= 1 - \frac{1}{2} ((c_0 v_y)^2 + (c_0 v_z)^2) \\ &+ O(((c_0 v_y)^2 + (c_0 v_z)^2)) \end{aligned}$$

The first order Mur uses the first term in the expansion. This is equivalent to assuming normal incidence at the boundary. The partial differential equation is

$$\left( \frac{\partial}{\partial x} - \frac{1}{c_0} \frac{\partial}{\partial t} \right) W \Big|_{x=0} = 0 \quad (2.60)$$

The first order Mur difference equation derived from (2.60) is

$$\begin{aligned} W^{n+1}(0, j, k) &= W^n(1, j, k) \\ &+ \frac{c_0 \Delta t - \Delta x}{c_0 \Delta t + \Delta x} [W^{n+1}(1, j, k) - W^n(0, j, k)]. \end{aligned} \quad (2.61)$$

All six first order Mur absorbing boundary conditions can be found in Appendix A.

The second order Mur improves the approximation by using the first two terms in the expansion so that the partial differential equation is

$$\left\{ \frac{1}{c_0} \frac{\partial}{\partial x} \frac{\partial}{\partial t} - \frac{1}{c_0^2} \frac{\partial^2}{\partial t^2} + \frac{1}{2} \left( \frac{\partial^2}{\partial y^2} + \frac{\partial^2}{\partial z^2} \right) \right\} W|_{x=0} = 0 \quad (2.62)$$

the difference equation becomes

$$\begin{aligned} W^{n+1}(0, j, k) &= -W^{n-1}(1, j, k) \\ &+ \frac{c_0 \Delta t - \Delta x}{c_0 \Delta t + \Delta x} [W^{n+1}(1, j, k) + W^n(1, j, k)] \\ &+ \frac{2\Delta x}{c_0 \Delta t + \Delta x} [W^n(0, j, k) + W^n(1, j, k)] \\ &+ \frac{\Delta x (c_0 \Delta t)^2}{2(\Delta z)^2 (c_0 \Delta t + \Delta x)} [W^n(0, j, k+1) - 2W^n(0, j, k) + W^n(0, j, k-1) \\ &\quad + W^n(1, j, k+1) - 2W^n(1, j, k) + W^n(1, j, k-1)] \\ &+ \frac{\Delta x (c_0 \Delta t)^2}{2(\Delta y)^2 (c_0 \Delta t + \Delta x)} [W^n(0, j + \frac{3}{2}, k) - 2W^n(0, j + \frac{1}{2}, k) + W^n(0, j - \frac{1}{2}, k) \\ &\quad + W^n(1, j + \frac{3}{2}, k) - 2W^n(1, j + \frac{1}{2}, k) + W^n(1, j - \frac{1}{2}, k)]. \end{aligned} \quad (2.63)$$

All twelve second order Mur absorbing boundary conditions can be found in Appendix A.

### Coding Considerations

Since the Mur ABC equations require values older than the most recent time step, the Mur equations are not local in time and additional memory locations are neces-

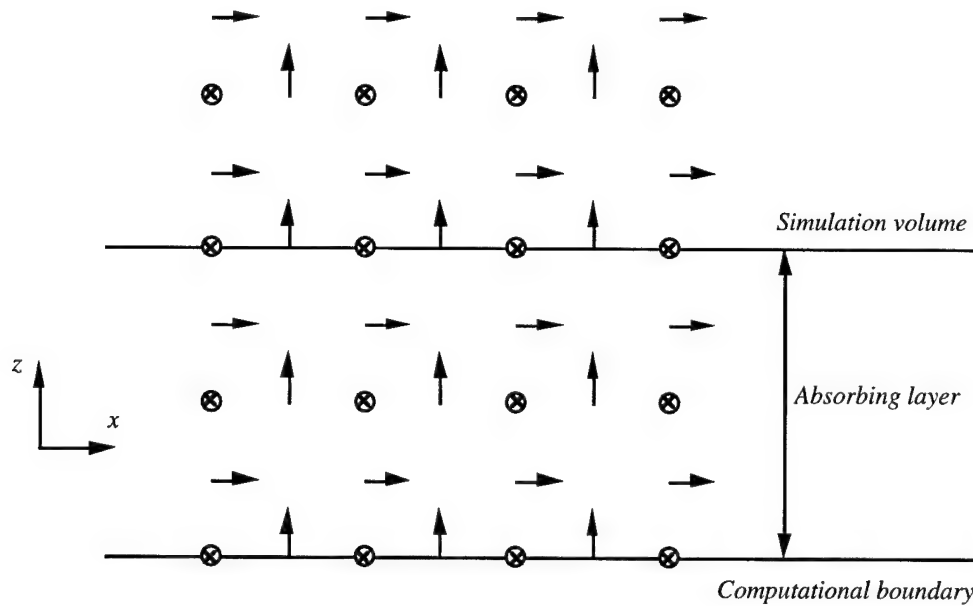


Figure 2-7: 2D Yee grid with an absorbing boundary layer used to truncate the computational domain.

sary for each tangential electric field on the boundary. In the first order case, the boundary value plus its nearest neighbor in the normal direction must be saved at each time step for a total of two extra memory locations per tangential field component. In the second order case, two past time steps must be saved for a total of four additional memory locations per tangential field component. Although higher order equations can be constructed, the additional accuracy does not usually justify the added complexity and memory required.

For efficient implementation, the coefficients found in the Mur equations are calculated once at the beginning of the program and stored for use in the difference equations.

### 2.9.2 Absorbing Boundary Layer

In addition to ABCs based on one way wave equation, an absorbing layer can be used to absorb the waves. A layer is constructed within the computational domain but

outside the simulation volume. The idea is to construct a layer with a loss mechanism that will allow the waves to propagate into the absorbing layer with little reflection and damp out the waves so that they will not reflect back into the simulation volume.

Holland [8] showed that an absorber can be built to match an isotropic lossless media with another media with both electric and magnetic conductivities as long as the absorbing media has the same permittivity and permeability as the media to be matched and

$$\frac{\sigma^m}{\sigma^e} = \frac{\mu}{\epsilon}. \quad (2.64)$$

With (2.64) set, the impedance of the absorbing layer matches the impedance of the medium inside the simulation volume; however, this type of ABC is only good at normal incidence.

## 2.10 Berenger's Perfectly Matched Layer

In 1994, Jean-Pierre Berenger introduced a novel approach [46] to the absorbing layer problem, and the technique has been the subject of much research [47]- [74]. Berenger essentially built an artificial electromagnetic absorbing layer around the FDTD computational domain that offers very small reflections and dissipates the electromagnetic energy as the waves travel through the layer.

Berenger's goal was to remove the angle dependence of Holland's ABC [8] while maintaining the reflectionless property. Berenger modified Maxwell's equations by splitting each field component into two subcomponents, one for each of the other two directions as shown below:

$$E_x = E_{xy} + E_{xz}, \quad (2.65)$$

$$E_y = E_{yx} + E_{yz}, \quad (2.66)$$

$$E_z = E_{zx} + E_{zy}, \quad (2.67)$$

$$H_x = H_{xy} + H_{xz}, \quad (2.68)$$



$$H_y = H_{yx} + H_{yz}, \quad (2.69)$$

and

$$H_z = H_{zx} + H_{zy}. \quad (2.70)$$

He further added anisotropic electric and magnetic conductivities. Although Berenger originally introduced his absorbing boundary for two dimensional problems, it was quickly expanded to three and the 12 equations are

$$\mu \frac{\partial}{\partial t} H_{xy} + \sigma_y^m H_{xy} = -\frac{\partial}{\partial y} (E_{zx} + E_{zy}), \quad (2.71)$$

$$\mu \frac{\partial}{\partial t} H_{xz} + \sigma_z^m H_{xz} = \frac{\partial}{\partial z} (E_{yx} + E_{yz}), \quad (2.72)$$

$$\mu \frac{\partial}{\partial t} H_{yx} + \sigma_x^m H_{yx} = \frac{\partial}{\partial x} (E_{zx} + E_{zy}), \quad (2.73)$$

$$\mu \frac{\partial}{\partial t} H_{yz} + \sigma_z^m H_{yz} = -\frac{\partial}{\partial z} (E_{xy} + E_{xz}), \quad (2.74)$$

$$\mu \frac{\partial}{\partial t} H_{zx} + \sigma_x^m H_{zx} = -\frac{\partial}{\partial x} (E_{yx} + E_{yz}), \quad (2.75)$$

$$\mu \frac{\partial}{\partial t} H_{zy} + \sigma_y^m H_{zy} = \frac{\partial}{\partial y} (E_{xy} + E_{xz}), \quad (2.76)$$

$$\epsilon \frac{\partial}{\partial t} E_{xy} + \sigma_y^e E_{xy} = \frac{\partial}{\partial y} (H_{zx} + H_{zy}), \quad (2.77)$$

$$\epsilon \frac{\partial}{\partial t} E_{xz} + \sigma_z^e E_{xz} = -\frac{\partial}{\partial z} (H_{yx} + H_{yz}), \quad (2.78)$$

$$\epsilon \frac{\partial}{\partial t} E_{yx} + \sigma_x^e E_{yx} = -\frac{\partial}{\partial x} (H_{zx} + H_{zy}), \quad (2.79)$$

$$\epsilon \frac{\partial}{\partial t} E_{yz} + \sigma_z^e E_{yz} = \frac{\partial}{\partial z} (H_{xy} + H_{xz}), \quad (2.80)$$

$$\epsilon \frac{\partial}{\partial t} E_{zx} + \sigma_x^e E_{zx} = \frac{\partial}{\partial x} (H_{yx} + H_{yz}), \quad (2.81)$$

and

$$\epsilon \frac{\partial}{\partial t} E_{zy} + \sigma_y^e E_{zy} = -\frac{\partial}{\partial y} (H_{xy} + H_{xz}). \quad (2.82)$$

The key to understanding the PML and why it works so well is the fact that if  $\sigma_x^e = \sigma_y^e = \sigma_z^e = \sigma^e$  and  $\sigma_x^m = \sigma_y^m = \sigma_z^m = \sigma^m$ , using equations (2.65)-(2.70), the PML equations (2.71)-(2.82) reduce to Maxwell's equations of a lossy medium (2.18) and (2.19). In other words, Maxwell's equations are a special case of the more general PML equations.

For a TE polarized wave traveling in two dimensional space, the twelve PML equations reduce to six:

$$\epsilon \frac{\partial}{\partial t} E_{yx} + \sigma_x^e E_{yx} = -\frac{\partial}{\partial x} (H_{zx} + H_{zy}) \quad (2.83)$$

$$\epsilon \frac{\partial}{\partial t} E_{yz} + \sigma_z^e E_{yz} = \frac{\partial}{\partial z} (H_{xy} + H_{xz}) \quad (2.84)$$

$$\mu \frac{\partial}{\partial t} H_{xy} + \sigma_y^m H_{xy} = 0 \quad (2.85)$$

$$\mu \frac{\partial}{\partial t} H_{xz} + \sigma_z^m H_{xz} = \frac{\partial}{\partial z} (E_{yx} + E_{yz}) \quad (2.86)$$

$$\mu \frac{\partial}{\partial t} H_{zx} + \sigma_x^m H_{zx} = -\frac{\partial}{\partial x} (E_{yx} + E_{yz}) \quad (2.87)$$

$$\mu \frac{\partial}{\partial t} H_{zy} + \sigma_y^m H_{zy} = 0 \quad (2.88)$$

Since the  $y$  direction collapses and  $\sigma_y^m = 0$ , a plane wave solution yields

$$E_{yx} = \frac{k_x}{\omega \epsilon \alpha_x^e} H_z, \quad (2.89)$$

$$E_{yz} = -\frac{k_z}{\omega \epsilon \alpha_z^e} H_x, \quad (2.90)$$

$$H_x = -\frac{k_z}{\omega\mu\alpha_z^m} (E_{yx} + E_{yz}), \quad (2.91)$$

and

$$H_z = \frac{k_x}{\omega\mu\alpha_x^m} (E_{yx} + E_{yz}), \quad (2.92)$$

where

$$\alpha_x^m = \left(1 + i\frac{\sigma_x^m}{\omega\mu}\right), \quad (2.93)$$

$$\alpha_z^m = \left(1 + i\frac{\sigma_z^m}{\omega\mu}\right), \quad (2.94)$$

$$\alpha_x^e = \left(1 + i\frac{\sigma_x^e}{\omega\epsilon}\right), \quad (2.95)$$

and

$$\alpha_z^e = \left(1 + i\frac{\sigma_z^e}{\omega\epsilon}\right). \quad (2.96)$$

Substituting (2.89) and (2.90) into (2.91) and (2.92) gives

$$E_{yx} = \frac{k_x^2}{\omega^2\epsilon\mu\alpha_x^e\alpha_x^m} (E_{yx} + E_{yz}), \quad (2.97)$$

and

$$E_{yz} = \frac{k_z^2}{\omega^2\epsilon\mu\alpha_z^e\alpha_z^m} (E_{yx} + E_{yz}). \quad (2.98)$$

Solving for one split field, the PML dispersion relation is given by

$$\frac{k_x^2}{\alpha_x^e\alpha_x^m} + \frac{k_z^2}{\alpha_z^e\alpha_z^m} = \omega^2\epsilon\mu. \quad (2.99)$$

### 2.10.1 PML Reflection Coefficient Analysis

Berenger and Cai *et al* [51] offer analytical derivations of the PML conditions for matching. The following is another that offers insight into the PML mechanism. Consider two PML media with non-zero values of permittivity, permeability and conductivity; one PML medium occupies Region 0 and the other Region  $t$ . A TE

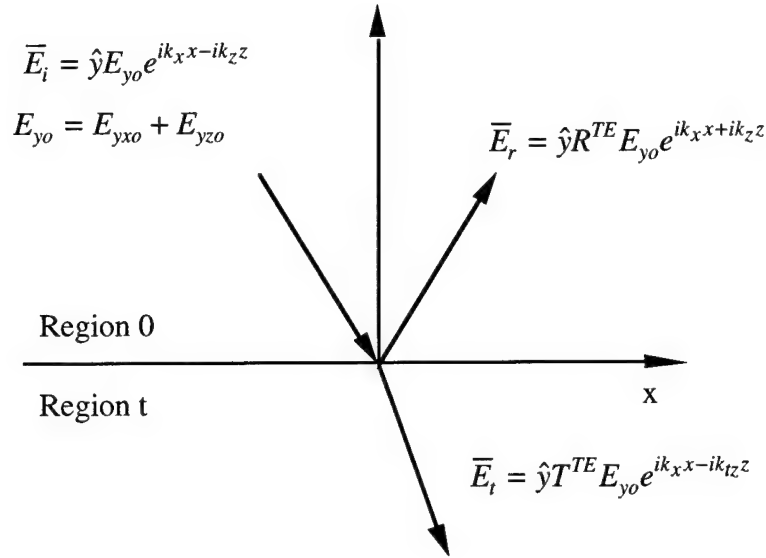


Figure 2-8: Geometry for PML reflection coefficient analysis.

polarized incident wave with  $\vec{k} = k_x \hat{x} - k_z \hat{z}$ , strikes the boundary from above. The electric fields are assumed [137] to be of the form

$$\vec{E}_i = \hat{y} (E_{yxo} + E_{yzo}) e^{ik_x x - ik_z z}, \quad (2.100)$$

$$\vec{E}_r = \hat{y} R^{TE} (E_{yxo} + E_{yzo}) e^{ik_x x + ik_z z}, \quad (2.101)$$

and

$$\vec{E}_t = \hat{y} T^{TE} (E_{yxo} + E_{yzo}) e^{ik_x x - ik_t z}. \quad (2.102)$$

Using (2.91) and (2.92) to determine the magnetic fields and imposing the boundary conditions at  $z = 0$  the reflection coefficient is

$$R^{TE} = \frac{1 - p_{0t}^{TE}}{1 + p_{0t}^{TE}}. \quad (2.103)$$

The reflection characteristics can be found in the term

$$p_{0t}^{TE} = \frac{k_{tz}\alpha_z^m}{k_z\alpha_{tz}^m}. \quad (2.104)$$

From the PML dispersion relations for each PML medium (2.104) becomes

$$p_{0t}^{TE} = \sqrt{\frac{\alpha_z^m \alpha_{tz}^e \alpha_x^e \alpha_x^m (\alpha_{tx}^e \alpha_{tx}^m k_t^2 - k_{xi}^2)}{\alpha_{tz}^m \alpha_z^e \alpha_{tx}^e \alpha_{tx}^m (\alpha_x^e \alpha_x^m k^2 - k_{xi}^2)}} \quad (2.105)$$

For the interface to be reflectionless at all angles, the  $k$  dependence must be removed.

This is possible if

$$\alpha_{tx}^e \alpha_{tx}^m k_t = \alpha_x^e \alpha_x^m k, \quad (2.106)$$

which is true if  $\epsilon_t = \epsilon$ ,  $\mu_t = \mu$  and  $\alpha_{tx}^e \alpha_{tx}^m = \alpha_x^e \alpha_x^m$  the angle dependence is removed leaving

$$p_{0t}^{TE} = \sqrt{\frac{\alpha_z^m \alpha_{tz}^e}{\alpha_z^e \alpha_{tz}^m}}. \quad (2.107)$$

Finally if  $p_{0t}^{TE} = 1$ , the interface will be reflectionless which is satisfied by  $\alpha_z^m \alpha_{tz}^e$  must equal  $\alpha_z^e \alpha_{tz}^m$ . In terms of the media parameters, to match (*i.e.* reflectionless at all angles) the PML medium in Region 0 with  $(\epsilon, \mu, \sigma_x^e, \sigma_x^m, \sigma_z^e, \sigma_z^m)$  with the PML media in Region  $t$ , Region  $t$ 's parameters must be

$$\epsilon_t = \epsilon, \quad (2.108)$$

$$\epsilon_t = \epsilon, \quad (2.109)$$

$$\sigma_{tx}^e = \sigma_x^e, \quad (2.110)$$

$$\sigma_{tx}^m = \sigma_x^m, \quad (2.111)$$

$$\sigma_{tz}^m = \frac{\mu}{\epsilon} \sigma_{tz}^e, \quad (2.112)$$

and

$$\sigma_z^m = \frac{\mu}{\epsilon} \sigma_z^e. \quad (2.113)$$

The last condition (2.113) is imposed on Region 0. Thus, the electric and magnetic conductivities in Region 0 can not be arbitrary. However, a lossless medium with  $\epsilon$ ,  $\mu$ , does satisfy (2.113), and the corresponding matching parameters in Region  $t$  are

$$\epsilon_t = \epsilon, \quad (2.114)$$

$$\mu_t = \mu, \quad (2.115)$$

$$\sigma_{tx}^e = 0, \quad (2.116)$$

$$\sigma_{tx}^m = 0, \quad (2.117)$$

and

$$\sigma_{tz}^m = \frac{\mu}{\epsilon} \sigma_{tz}^e. \quad (2.118)$$

For infinite half-spaces, the selection of  $\sigma_{tx}^e$  is arbitrary. In FDTD simulations, however, the selection of  $\sigma_{tx}^e$  is not arbitrary and will be discussed in a future section.

### 2.10.2 PML Propagation Characteristics

Again consider the transmission from a lossless dielectric in Region 0 into its matched PML in Region  $t$ . From the dispersion relation in Region  $t$ ,

$$\frac{k_{tx}^2}{\alpha_{tx}^e \alpha_{tx}^m} + \frac{k_{tz}^2}{\alpha_{tz}^e \alpha_{tz}^m} = k_t^2, \quad (2.119)$$

and the incident  $k$  vector  $x$ -component,  $k_{ix}$ , the dispersion relation in Region  $t$ , simplifies to

$$k_{ix}^2 + \frac{k_{tz}^2}{\alpha_{tz}^e \alpha_{tz}^e} = k_t^2. \quad (2.120)$$

Therefore, the  $z$  component of the  $k$  vectors are related by  $k_{tz} = \alpha_{tz}^e k_{iz}$  or

$$k_{tz} = k_{iz} + i \frac{\sigma_{tz}^e}{\omega \epsilon} k_{iz}. \quad (2.121)$$

When the wave enters the PML, it propagates in the same direction as the incident wave and is attenuated in the direction normal to the interface. In terms of the incident angle, (2.121) becomes

$$k_{tz} = k_{iz} + i \sigma_{tz}^e \eta_t \cos \theta. \quad (2.122)$$

The imaginary part of the  $k_{tz}$  is a function of the incident angle, providing the most damping in the normal direction and no damping in the tangential direction. If the incident wave is evanescent ( $k_{iz}$  purely imaginary), then the PML provides no additional damping.

### 2.10.3 PML and FDTD Simulations

So far, only infinite half-spaces have been considered. An infinite half-space is not appropriate for FDTD simulations since the computational domain must be truncated at some point. Berenger proposed truncating the PML with a Perfect Electric Conductor (PEC) *i.e.* setting all tangential fields to zero at the outer boundary. Thus a wave will travel through the PML, reflect off of the PEC, travel through the PML again, and re-enter the simulation volume. However, the wave will be attenuated by the loss mechanism (2.121) in the PML. The user will select a PML thickness, a PML conductivity, and a conductivity profile to achieve the desired low reflection coefficient. Even though analytic analysis shows that a constant conductivity profile is sufficient for a zero reflection at the boundary, numerical reflections will occur at any interface that contains conductivity discontinuities[60]. To reduce these numerical reflections, Berenger proposed grading the conductivity from a low value of zero at the boundary to some maximum value at the PEC wall. The most common conductivity

profile is given by

$$\sigma_{\rho}^e(\rho) = \sigma_{\rho max}^e \left( \frac{\rho}{d} \right)^n \quad (2.123)$$

where  $\rho$  is the normal coordinate variable,  $d$  is the thickness of the PML, and  $n$  is the conductivity grading factor so that  $n = 0$  is a constant profile,  $n = 1$  is a linear profile,  $n = 2$  is a parabolic profile, etc. If the PML starts at  $\rho = 0$  and ends at  $\rho = d$  then the expression for the reflection coefficient is given by

$$R(\theta) = e^{-2 \int_0^d \sigma_{\rho}^e(\rho) \eta \cos \theta d\rho}, \quad (2.124)$$

and after the integration

$$R(\theta) = e^{\frac{-2\eta d \sigma_{\rho max}^e}{n+1} \cos \theta}. \quad (2.125)$$

So for practical FDTD applications the reflection coefficient is still a function of the incident angle; however, the low grazing angle waves will be absorbed by the PML that terminates the simulation volume at the edges perpendicular to the normal PML layer. Also, it appears that the reflection coefficient can be made arbitrarily small with a large enough conductivity, but as mentioned, numerical reflections occur with large changes in conductivity between FDTD cells and prevents arbitrarily small reflection coefficients.

Berenger proposed that one way to select the conductivity is to set the reflection coefficient at normal incidence to some desired value. Setting  $\theta = 0$  and solving for  $\sigma_{\rho max}^e$ , the conductivity is determined by

$$\sigma_{\rho max}^e = -\frac{(n+1) \ln R(0)}{2d\eta}. \quad (2.126)$$

#### 2.10.4 PML and Multilayer Dielectrics

When applying Berenger's PML to multilayer dielectrics, as in the case of microstrip and dielectric waveguides, special care must be taken when determining the conduc-



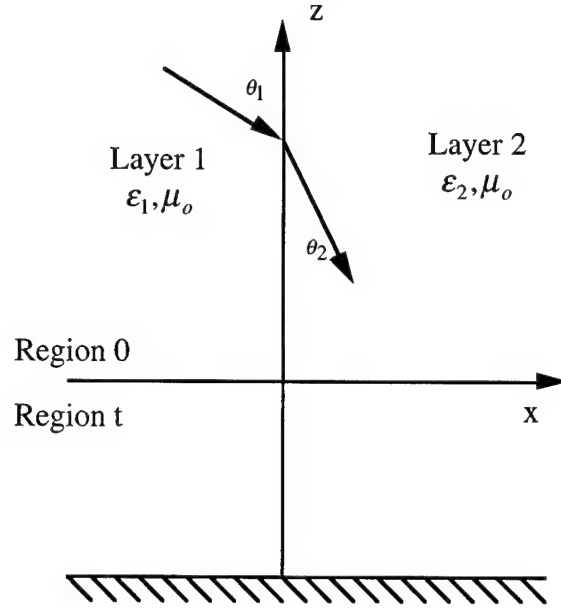


Figure 2-9: Configuration for multi-dielectric layer PML.

tivities for each layer. For a single layer (*i.e.* no layer) the conductivity is calculated based on the desired reflection coefficient at normal incidence.

Now consider two lossless dielectrics with permittivities,  $\epsilon_1$  and  $\epsilon_2$ , and permeability,  $\mu_o$ , in Region 0 with their interface at  $x = 0$ . Layer 1 is located at  $x < 0$  and layer 2 is located at  $x > 0$ . The layers are terminated with a PML in Region  $t$  with two conductivities,  $\sigma_{t1}$  and  $\sigma_{t2}$ . See Figure 2-9. Given the same PML thickness, profile, and desired reflection coefficient, if computed independently, the conductivities are

$$\sigma_{1tz\max}^e = -\frac{(n+1)\ln R(0)}{2d\eta_1} \quad (2.127)$$

and

$$\sigma_{2tz\max}^e = -\frac{(n+1)\ln R(0)}{2d\eta_2}. \quad (2.128)$$

In this way, the conductivity ratio between the two PML terminating layers is

$$\frac{\sigma_{2tz\max}^e}{\sigma_{1tz\max}^e} = \sqrt{\frac{\epsilon_2}{\epsilon_1}}. \quad (2.129)$$

However, if the ratio of the reflection coefficients is examined; given by

$$\frac{R_{0t1}(\theta)}{R_{0t2}(\theta)} = e^{\frac{-2d\sqrt{\mu_0}(\frac{\sigma_{1\max}^e \cos \theta_1}{\sqrt{\epsilon_1}} - \frac{\sigma_{2\max}^e \cos \theta_2}{\sqrt{\epsilon_2}})}{n+1}}. \quad (2.130)$$

Substitution of (2.129) into (2.130) leads to

$$\frac{R_{0t1}(\theta)}{R_{0t2}(\theta)} = e^{-\frac{2d\sigma_{1\max}^e \eta_1}{n+1}(\cos \theta_1 - \cos \theta_2)}. \quad (2.131)$$

The reflection coefficients will be equal only when  $\theta_1 = \theta_2$  which is true only at grazing incidence or when there is no boundary at  $x = 0$ . Both cases are uninteresting. On the other hand, if phase matching in Region 0 is applied  $x = 0$  *i.e.*  $k_1 \cos \theta_1 = k_2 \cos \theta_2$ , substitution leads to

$$\frac{R_{0t1}(\theta)}{R_{0t2}(\theta)} = e^{\frac{-2d\sqrt{\mu_0}(\frac{\sigma_{1\max}^e}{\sqrt{\epsilon_1}} - \frac{\sigma_{2\max}^e \sqrt{\epsilon_1}}{\epsilon_2}) \cos \theta_1}{n+1}}. \quad (2.132)$$

In order for the reflection coefficients along  $z = 0$  to be continuous, *i.e.*

$$\frac{R_{0t1}(\theta)}{R_{0t2}(\theta)} = 1, \quad (2.133)$$

the conductivities between adjacent dielectric layers must satisfy

$$\sigma_{2\max}^e = \frac{\epsilon_2}{\epsilon_1} \sigma_{1\max}^e. \quad (2.134)$$

Further insight into this condition can be seen from examining the reflection coefficients in the direction tangential to the dielectric-PML interface, at the layer 1/layer 2 interface at  $x = 0$ . The reflection coefficient at the dielectric interface,  $R_{12}^{TE}(z > 0)$ ,

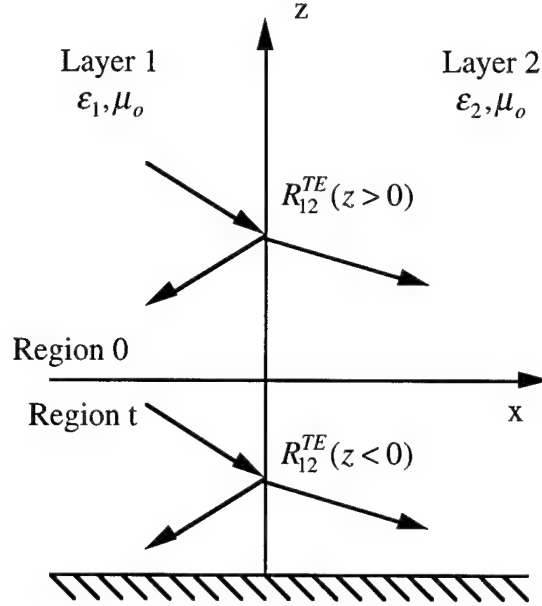


Figure 2-10: Configuration for multi-dielectric reflection coefficient analysis.

should equal the reflection coefficient at the matching PML layer interface,  $R_{12}^{TE}(z < 0)$ , for the PML to truly simulate open space. From the original analysis of the PML, the reflection coefficient between any two PML media is

$$R_{12}^{TE} = \frac{1 - p_{12}^{TE}}{1 + p_{12}^{TE}} \quad (2.135)$$

where

$$p_{12}^{TE} = \sqrt{\frac{\alpha_{1x}^m \alpha_{2x}^e \alpha_{1z}^e \alpha_{1z}^m (\alpha_{2z}^e \alpha_{2z}^m k_2^2 - k_z^2)}{\alpha_{2x}^m \alpha_{1x}^e \alpha_{2z}^e \alpha_{2z}^m (\alpha_{1z}^e \alpha_{1z}^m k_1^2 - k_z^2)}}. \quad (2.136)$$

After the setting the material parameters and PML matching conditions between Regions 0 and  $t$ , (2.136) becomes

$$p_{12}^{TE}(z > 0) = \sqrt{\frac{k_2^2 - k_z^2}{k_1^2 - k_z^2}} \quad (2.137)$$

and

$$p_{12}^{TE}(z < 0) = \sqrt{\frac{\alpha_{1tz}^e \alpha_{1tz}^m (\alpha_{2tz}^e \alpha_{2tz}^m k_{2t}^2 - k_{zt}^2)}{\alpha_{2tz}^e \alpha_{2tz}^m (\alpha_{1tz}^e \alpha_{1tz}^m k_{1t}^2 - k_{zt}^2)}}. \quad (2.138)$$

Phase matching at the  $x = 0$  interface says  $k_{1z} = k_{2z} = k_z$  and  $k_{1tz} = k_{2tz} = k_{tz}$ . The PML matching conditions along with the PML dispersion relation imply  $k_{1t} = k_1$ ,  $k_{2t} = k_2$ ,  $\alpha_{1tz}^e = \alpha_{1tz}^m$ ,  $\alpha_{2tz}^e = \alpha_{2tz}^m$ ,  $k_{1tz} = \alpha_{1tz}^e k_z$  and  $k_{2tz} = \alpha_{2tz}^e k_z$ . Substitution of these relationships into (2.138) reveal

$$p_{12}^{TE}(z < 0) = \sqrt{\frac{k_2^2 - \frac{\alpha_{1tz}^e \alpha_{1tz}^e}{\alpha_{2tz}^e \alpha_{2tz}^e} k_z^2}{k_1^2 - k_z^2}}. \quad (2.139)$$

Equations (2.138) and (2.138) are equivalent if an additional PML condition is met:

$$\alpha_{1tz}^e = \alpha_{2tz}^e. \quad (2.140)$$

This additional condition is equivalent to (2.64). Ensuring that the reflection coefficients be continuous at the intersection of the four different media leads directly to

$$\sigma_{2max}^e = \frac{\epsilon_2}{\epsilon_1} \sigma_{1max}^e. \quad (2.141)$$

Enforcing this ratio is equivalent to saying the loss tangents within each PML layer must be equal. Bahr *et al* in [50] arrived at the same conclusion by demanding that there be equal decay in the normal direction in each of the layers with phase matching in mind.

Failure to impose this condition can lead to instabilities at the PML/PML interface due to the generation of other waves necessary to match the boundary conditions. In the next chapter, the generation of mode templates for dielectric waveguides is discussed. When generating these templates many time steps are required to capture the necessary frequency resolution. When a large permittivity contrast between exists between two layers in a multi-layer dielectric structure, the independent PML

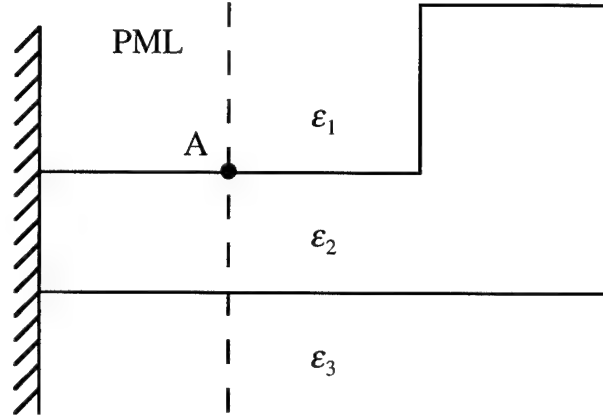


Figure 2-11: Test setup for PML instability demonstration. Field measured at point A.

matching condition (2.129) produces instabilities.

For example, the fundamental mode spatial distribution is calculated from a 2D FDTD simulation of a dielectric rib built with Gallium Arsenide with  $\epsilon_2 = 11.8\epsilon_0$  on top of a substrate  $\epsilon_3 = 10.0\epsilon_0$  surrounded with free space cladding,  $\epsilon_1 = \epsilon_0$ . See Figure 2-11. The grid size is  $\Delta = .002m$  and the time step is set to the 3D Courant limit. The simulation volume is  $57 \times 41$ .

Figure 2-12 represents  $E_z$  versus time step at Point A in Figure 2-11 within the FDTD simulation volume with two different PML matching conditions. Both simulations use an eight layer PML with  $n = 2$  and  $R(0) = 10^{-5}$  to terminate the computational domain. The conductivities of each layer were calculated using the dependent matching conditions of equation 2.134 and independent matching conditions of equation 2.129. Table 2.1 provides the conductivity values. The two graphs clearly show the effects of using the independent matching condition. The independent construction of the PML conductivities produces solutions that grow and take over the simulation after 3000 time steps.

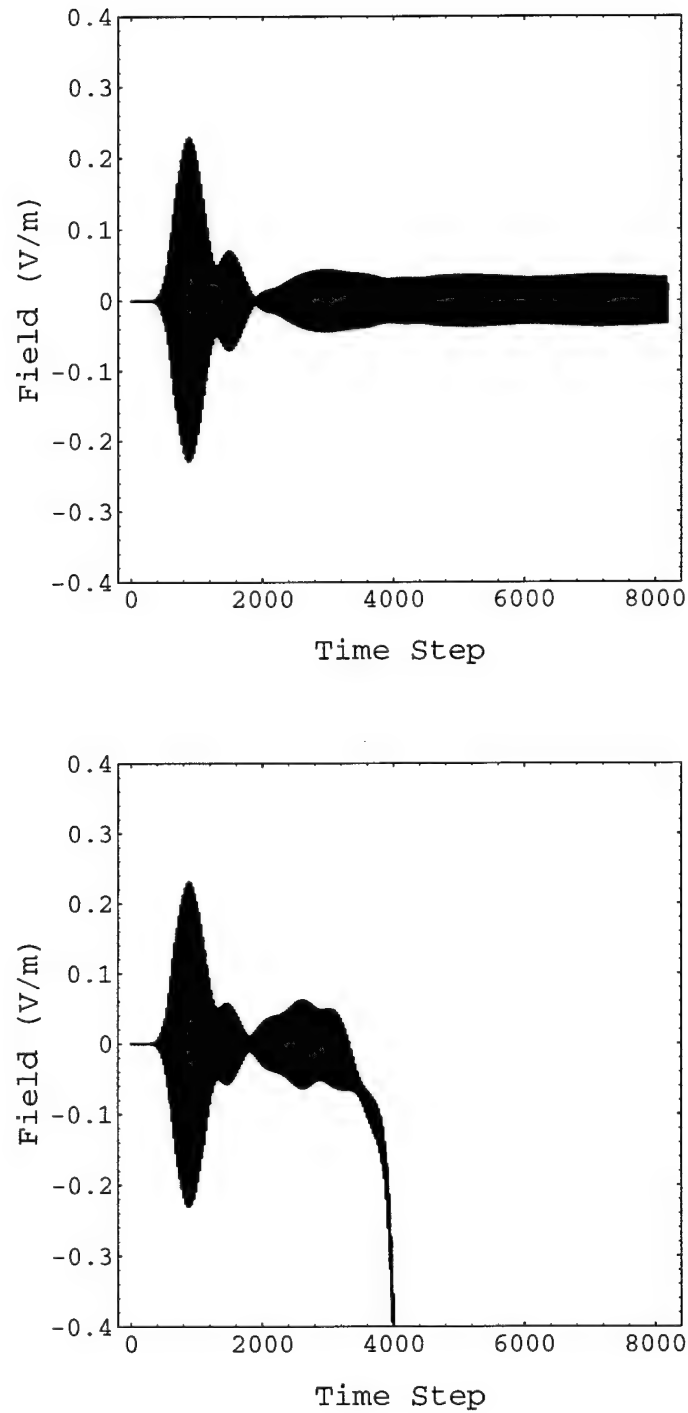


Figure 2-12: Field  $E_z$  measurements at PML/PML interface (Point A in Figure 2-11) with dependent(top) and independent(lower) PML matching conditions.

Layer	Permittivity	$\sigma_{max}^e \Omega^{-1} m^{-1}$	
		Dependent	Independent
Cladding	$1.0\epsilon_0$	11.45	11.45
Film	$11.8\epsilon_0$	135.11	39.33
Substrate	$10.0\epsilon_0$	114.50	36.21

Table 2.1: Maximum conductivities to match PML to rib structure.

The simulations were constructed to excite the fundamental mode of the rib waveguide by fixing the propagation constant at  $600 m^{-1}$  and exciting the problem with a wide ( $\beta = 256$ ) Gaussian pulse modulated at the corresponding mode temporal frequency of  $f_0 = 8.1 GHz$ . Figure 2-13 represents the temporal frequency content inside the rib waveguide due to the modulated Gaussian pulse with a fixed propagation constant with the dependent(top) and independent(lower) PML matching conditions. The lower spectrum shows the effects of the independent PML matching conditions. The singularities at the PML/PML interfaces act as sources and place energy in frequencies other than the fundamental mode. These sources make it difficult to determine the fundamental mode spatial arrangement as shown in Figure 2-14. The lower plot has unwanted spikes in the mode's spatial distribution at the PML/PML interfaces as seen on the left and right sides of the computational domain.

### 2.10.5 PML Coefficients in FDTD

The PML difference equations use an explicit exponential form as proposed by Berenger. For example, the  $E_{xy}$  equation used in the PML region of the computational domain is given by

$$\begin{aligned}
 E_{xy}^{n+1}(i + \tfrac{1}{2}, j, k) &= C_1^{ye}(i + \tfrac{1}{2}, j, k) E_{xy}^n(i + \tfrac{1}{2}, j, k) \\
 &- C_2^{ye}(i + \tfrac{1}{2}, j, k) \left[ H_z^{n+\frac{1}{2}}(i + \tfrac{1}{2}, j + \tfrac{1}{2}, k) - H_z^{n+\frac{1}{2}}(i + \tfrac{1}{2}, j - \tfrac{1}{2}, k) \right]
 \end{aligned} \tag{2.142}$$

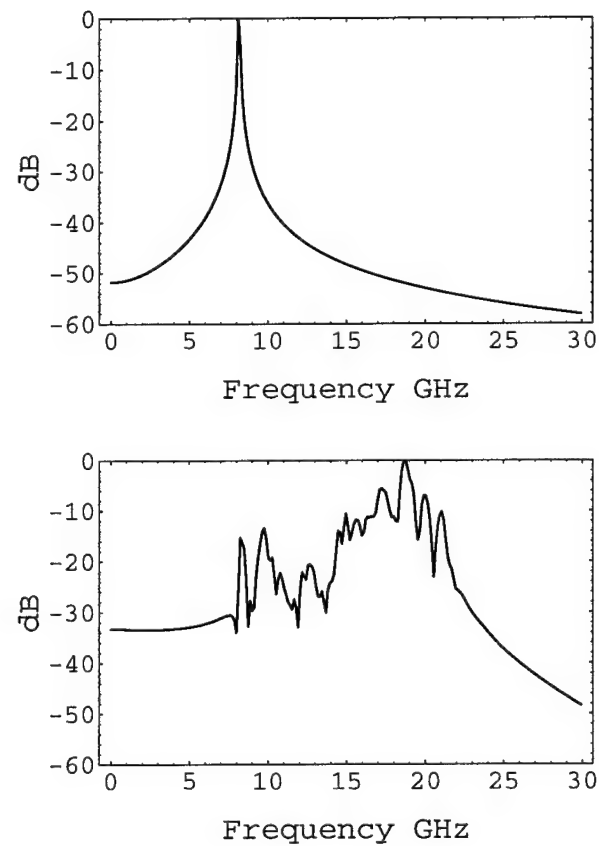


Figure 2-13: Fourier transform of field inside rib using dependent (top) and independent (bottom) PML conductivity matching condition.



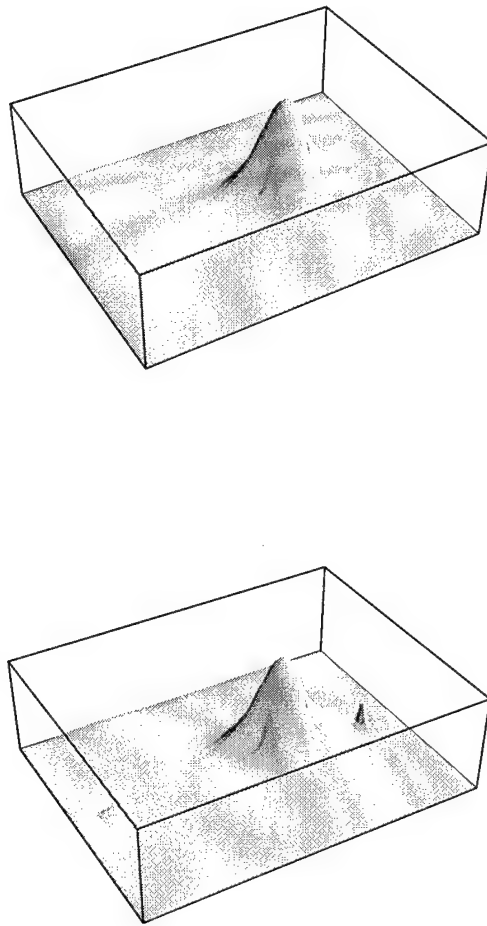


Figure 2-14: Fundamental mode spatial field distribution using dependent (top) and independent (bottom) PML conductivity matching condition.

where the two constants,  $C_1^{ye}$  and  $C_2^{ye}$  are given by

$$C_1^{ye}(i + \frac{1}{2}, j, k) = e^{-\sigma_y^e(i + \frac{1}{2}, j, k)\Delta t / \epsilon(i + \frac{1}{2}, j, k)} \quad (2.143)$$

and

$$C_2^{ye}(i + \frac{1}{2}, j, k) = \frac{(1 - C_1^{ye}(i + \frac{1}{2}, j, k))}{\sigma_y^e(i + \frac{1}{2}, j, k)\Delta y} \quad (2.144)$$

The remainder of the PML FDTD difference equations along with a very detailed description of the PML coefficients is found in Appendix B

## 2.11 Considerations and Overview of FDTD Algorithm

The FDTD method is a very versatile method for solving electromagnetic problems. The discretization of Maxwell's equations has a built in error that is proportional to the square of the grid size ( $\Delta^2$ ). In addition, the difference equations introduce non-physical numerical dispersion. The dispersion error can be kept to less than one percent if the grid size is less than one tenth of a wavelength. When there is more than one material in the simulation volume, it is the most dense material that determines the grid size. This means that the less dense material is essentially over sampled. If two grid sizes are used, then numerical reflections may result [14]. Also, the FDTD method must model curved surfaces with a staircase. When the other errors are kept small, the grid size is typically sufficiently fine that the staircase is a good approximation to a curved surface. Finally, there will always be some reflections from the boundaries of the computational domain no matter which ABC is used and must be considered when constructing the problem.

The basic steps to the FDTD algorithm are listed below.

1. Build geometry.

2. Initialize variables and calculate coefficients.
3. Calculate electric fields.
4. Impose source condition.
5. Advance time by half step.
6. Calculate magnetic fields.
7. Advance time by half step.
8. Save desired values.
9. Repeat time marching until steady state is achieved.
10. Perform post-processing on saved data.

## 2.12 Summary

In this chapter the Finite Difference Time Domain method for solving Maxwell's equations has been presented. The method is simply a finite difference approximation to the partial derivatives found in Maxwell's curl equations. Electromagnetic wave interactions with fairly complicated structures can be modeled and multiple frequencies can be tested by controlling the pulse width of the excitation.

Difference equations suitable for coding were presented for free space, lossy dielectric media, Mur absorbing boundaries, and the Perfectly Matched Layer.

The artificial PML conductivities used to absorb the outgoing waves in a multiple dielectric layer simulation must not be assigned independently from Berenger's proposed method of normal incidence; instead, once one of the layer's conductivities is calculated the others must be constructed so that the loss tangents in each layer are equal. With this done, there will be no reflection coefficient singularities in both the normal and tangential directions and the PML will simulate open space to the maximum extent possible under the discretization scheme.

## Chapter 3

# FDTD Analysis of Dielectric Rib Waveguide Discontinuities

### 3.1 Introduction

Dielectric waveguides are commonly used as interconnects in millimeter-wave and sub-millimeter wave integrated circuit technologies [75]-[100]. These interconnects contain discontinuities such as bends that can introduce high loss through the waveguide. Since the propagating modes of this type of structure are characterized by very complex field distributions, with no exact analytic solutions, a numerical approach is appropriate to investigate these structures. In this chapter, a full three dimensional FDTD implementation is used to analyze the effects of waveguide discontinuities on the fundamental mode's propagation through the waveguide.

When using FDTD to study any waveguide, depending on the excitation used, it may take time for the desired mode (*e.g.* the fundamental) to develop as the evanescent modes decay away and radiating modes leave the simulation volume. In order to launch the fundamental mode more efficiently, in this work the mode's spatial distribution is determined up front. A two dimensional FDTD method is used to construct a mode template [131, 133]. The three dimensional FDTD code is collapsed in the

direction of propagation by replacing the spatial difference equation with an equation based on an assumed propagation constant and the corresponding phase difference between adjacent spatial grid points. A two dimensional simulation of the waveguide cross section produces the corresponding temporal frequencies of the propagating modes. The lowest frequency is the fundamental mode and the spatial distribution is found by performing a Fourier transform at each space point on the two dimensional grid at the fundamental mode frequency. With this source condition, the computational domain can be reduced from the commonly used spatial Gaussian source condition by allowing shorter distances between excitation and the discontinuity.

The FDTD method has been used to study metallic waveguides and metallic planar structures [101]-[108]. Unlike metallic waveguides the dielectric rib waveguide is an open structure and analyzing them with the Finite Difference Time Domain method requires absorbing boundary conditions that simulate open space. The perfectly matched layer (PML) described and analyzed in Chapter 2 is used to terminate the simulation volume unless otherwise stated.

With mode template excitations and PML absorbing boundary conditions, the dielectric rib waveguide is studied. Different waveguide bends are examined along with the effects of the rib geometry.

## 3.2 Implementation of Dielectric Rib Waveguide in FDTD

Various dielectric rib waveguides are constructed and analyzed in this chapter. The input parameters are the rib width ( $rw$ ), rib height ( $rh$ ), film height ( $fh$ ) and the center reference point ( $xc, zc$ ) as shown in Figure 3-1. The simulation model of a waveguide is constructed by carefully assigning a permittivity at each electric field location as described in Section 2.5. The initial propagation is in the  $+\hat{y}$  direction.

The Berenger perfectly matched layer described in Section 2.10 is used to termi-

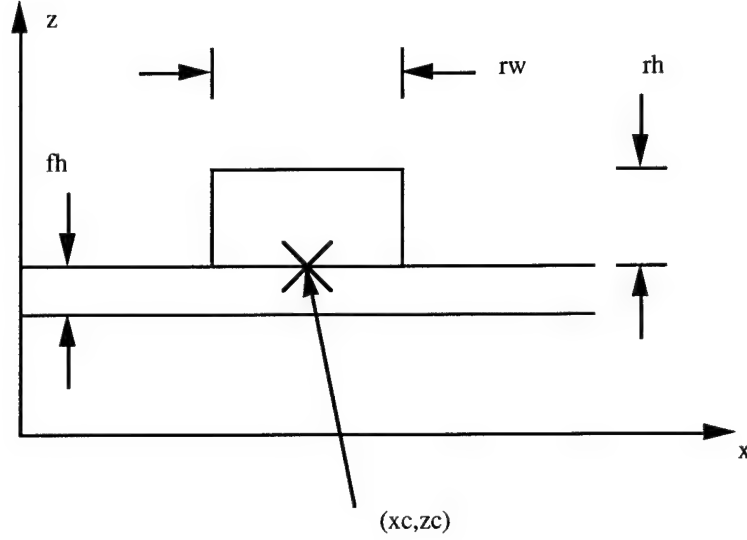


Figure 3-1: Schematic of dielectric rib waveguide cross section. Parameters are  $rw$  : rib width,  $rh$  : rib height,  $fh$  : film height, and  $(xc, zc)$  : center reference point.

nate the FDTD computational domain for all three dimensional simulations unless otherwise stated. The PML consists of 8 discretized layers using a quadratic conductivity profile (*i.e.*  $n = 2$ ) with the maximum conductivity derived by setting  $R(0) = 10^{-5}$  with free space permittivity,  $\epsilon_0$ . The conductivities for the other dielectric layers are calculated with equation (2.134).

To analyze waveguide discontinuities, the  $S$  parameters are calculated from the FDTD simulation measurements of the time-domain waveforms. Multiple frequencies are analyzed within a single FDTD simulation. The methods are described in Section 3.7.1.

### 3.3 Approximate Analytic Solution

The study of dielectric waveguide modes and their propagation characteristics have been studied since the late sixties, except for the dielectric slab and circular dielectric waveguides, exact analytical solutions do not exist and numerical techniques are

necessary when complex structures are used.

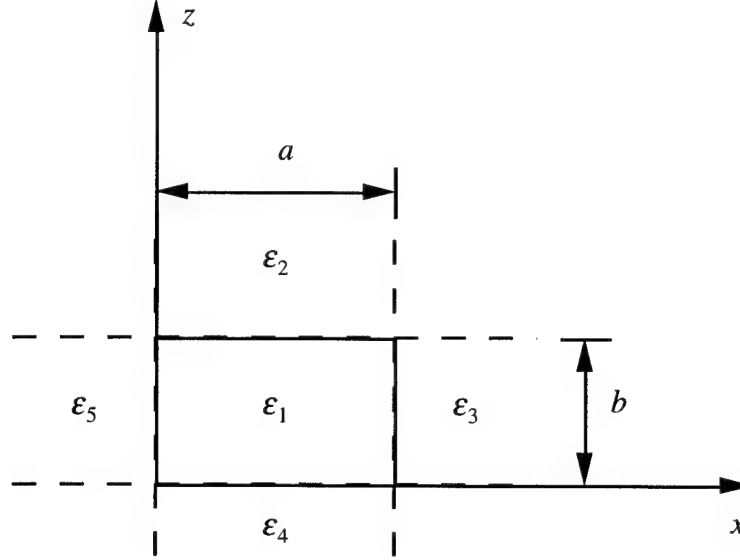


Figure 3-2: Rectangular dielectric waveguide used with Marcattili method.

In 1969, Marcattili introduced an approximate analytical solution for the guided modes of a rectangular dielectric waveguide that is still used today. Figure 3-2 represents the cross-section of a rectangular dielectric waveguide with permittivity,  $\epsilon_1$ , surrounded by four different dielectric media,  $\epsilon_{2,3,4,5}$  with dispersion relations:  $k_l^2 = \omega^2 \mu \epsilon_l$ ,  $l = 1 - 5$ . As summarized in [142], Marcattili derived an approximate solution by applying the boundary conditions to the edges of the guide only. He assumed sinusoidal variations along the  $x$  and  $z$  directions inside the guide and exponential decay outside of the guide.

For the  $E_{s,q}^z$  modes the governing equations are

$$k_x a = s\pi - \tan^{-1}(k_x \xi_3) - \tan^{-1}(k_x \xi_5), \quad (3.1)$$

and

$$k_z b = q\pi - \tan^{-1}\left(\frac{\epsilon_2 k_z \zeta_2}{\epsilon_1}\right) - \tan^{-1}\left(\frac{\epsilon_4 k_z \zeta_4}{\epsilon_1}\right), \quad (3.2)$$

where

$$\xi_{3,5} = \left[ \left( \frac{\pi}{\chi_{3,5}} \right)^2 - k_x^2 \right]^{-\frac{1}{2}}, \quad (3.3)$$

$$\zeta_{2,4} = \left[ \left( \frac{\pi}{\chi_{2,4}} \right)^2 - k_z^2 \right]^{-\frac{1}{2}}, \quad (3.4)$$

and

$$\chi_l = \pi \left( k_1^2 - k_l^2 \right)^{\frac{1}{2}} \quad l = 2 - 5. \quad (3.5)$$

Phase matching at  $z = 0$  and  $z = b$  implies  $k_x = k_{x1} = k_{x2} = k_{x4}$  and similarly at  $x = 0$  and  $x = a$  implies  $k_z = k_{z1} = k_{z3} = k_{z5}$ . Propagation is in the  $y$  direction with a propagation constant given by

$$\beta = k_y = \left( k_1^2 - k_x^2 - k_z^2 \right)^{\frac{1}{2}}. \quad (3.6)$$

For the dielectric waveguide surrounded by the same dielectric such as free space,  $\epsilon_2 = \epsilon_3 = \epsilon_4 = \epsilon_5 = \epsilon_0$ , the equations simplify to

$$k_x a = s\pi - 2 \tan^{-1}(k_x \xi), \quad (3.7)$$

and

$$k_z b = q\pi - 2 \tan^{-1} \left( \frac{\epsilon_0 k_z \zeta}{\epsilon_1} \right), \quad (3.8)$$

with

$$\xi_{3,5} = \xi = \left[ \left( \frac{\pi}{\chi} \right)^2 - k_x^2 \right]^{-\frac{1}{2}}, \quad (3.9)$$

$$\zeta_{2,4} = \zeta = \left[ \left( \frac{\pi}{\chi} \right)^2 - k_z^2 \right]^{-\frac{1}{2}}, \quad (3.10)$$

and

$$\chi_{2,3,4,5} = \chi = \pi \left( k_1^2 - k_0^2 \right)^{\frac{1}{2}}. \quad (3.11)$$



At a given frequency,  $\omega$ ,  $\chi$  can be found with equations (3.7) and (3.11). Substitution of  $\chi$  into (3.9) and (3.10) give  $\xi$  and  $\zeta$ . Graphical techniques or Newton's method can be used to find the discrete set of  $k_x$  and  $k_z$  using (3.7) and (3.8) that correspond to a given mode number and  $\omega$ . However, the Marcatili Method is only good when most of the mode's energy is confined to the core dielectric region and is not reliable near cutoff [76].

Dispersion curves for dielectric waveguides are often displayed in terms of normalized variables. The normalized propagation constant is defined by

$$\Lambda = \frac{\left(\frac{\lambda_0}{\lambda}\right)^2 - 1}{\left(\frac{\epsilon_1}{\epsilon_0}\right) - 1} \quad (3.12)$$

and the normalized waveguide height is

$$u = \frac{2b}{\lambda_0} \left(\frac{\epsilon_1}{\epsilon_0} - 1\right)^{\frac{1}{2}} \quad (3.13)$$

where  $\lambda = \frac{2\pi}{\beta}$  and  $\lambda_0 = \frac{2\pi}{k_0}$ .

In order to validate the upcoming FDTD mode construction procedure, a square dielectric waveguide is examined. The waveguide has a permittivity of  $2.8\epsilon_0$  surrounded by a cladding of free space. The structure measures 1 cm on a side. Using equations (3.7)-(3.11), the dispersion curves were constructed for the  $E_{1,1}^z$ ,  $E_{2,1}^z$ , and  $E_{1,2}^z$  modes. Figure 3-3 represents the normalized curves using (3.12) and (3.13). The results of the fundamental mode will be used to compare with the FDTD method.

### 3.4 Excitation

The excitation consists of a source plane of distributed  $\hat{z}$  directed current sources at the interface between the simulation volume and the PML that forms the front of the computational domain. This excitation technique has advantages over the an electric field boundary condition; a major one being that the PML can absorb waves reflected

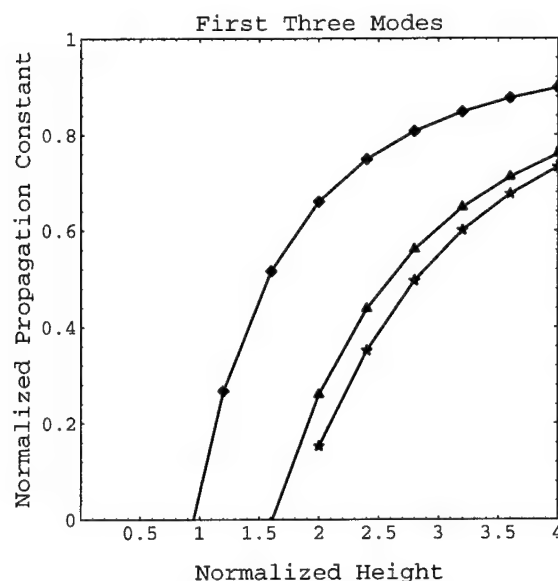


Figure 3-3: Normalized dispersion curves of first three modes,  $E_{1,1}^z$ , (diamond)  $E_{2,1}^z$ , (triangle) and  $E_{1,2}^z$  (star), as derived by the Marcatili method.

from the waveguide discontinuities [50]. When Mur boundary conditions are used one of the faces has a dual role: first as an excitation plane and then as an absorbing boundary. After the excitation is completely launched, the source is essentially turned off and the absorbing boundary condition is turned on [106]. Using this method, a larger computational domain is necessary so that the ABC can be turned on after the excitation but before any reflections from the discontinuity reach the source edge. The magnitude of the individual current sources are derived up front with a template calculation described in Section 3.5. The temporal excitation is that of a modulated Gaussian as described in Section 2.8.

### 3.5 Improvement to the FDTD Method with a Better Excitation

Although the recent strides in computer technology have placed more memory and computing power in the hands of engineers, reducing computational domain requirements is always desirable. The reduction in the domain leads to faster simulations and the ability to simulate larger problems. In this section the construction of a mode template is described and tested to show how the computational domain can be reduced.

#### 3.5.1 Template Construction

When performing discontinuity analysis, it is desirable to launch a known mode. However, complicated structures like the rib waveguide have modes that have complicated spatial distributions. These modes can not be expressed analytically; therefore, a sufficient length of section of computational domain after the source plane and before the discontinuity is needed to allow the fundamental mode to set up.

A numerical approach has been used with closed and partially closed structures to find what is called a *mode template* [131, 133]. The template is the spatial arrangement of the field in the plane perpendicular to the direction of propagation. In this section, the numerical technique of templates is extended to open structures.

To construct a mode template, the three dimensional FDTD algorithm is converted to a two dimensional algorithm where the propagating direction is replaced by equations that incorporate the assumed known phase difference between planes perpendicular to the propagating direction.

The first step is to assume a propagation constant,  $k_y$ . Then the  $y$  dependence in the difference equations is modified by

$$F(i, j, k) - F(i, j - 1, k) \rightarrow F(i, j, k)(1 - e^{-ik_y\Delta y}) \quad (3.14)$$

and

$$F(i, j+1, k) - F(i, j, k) \rightarrow F(i, j, k)(e^{ik_y \Delta y} - 1). \quad (3.15)$$

With the new algorithm and a propagation constant, a two dimensional simulation is run and the time domain waveform is saved. The Fourier transform is taken of the steady state portion of signal. The first half of the signal is discarded. The peaks in the Fourier transform correspond the mode frequencies associated with the selected propagation constant.

The rationale behind this template construction can be seen in the following analysis. We assume that the steady state of a component of the electric field can be expressed as the sum of propagating modes:

$$E_\alpha(x, y, z, t) = \sum_n \phi_n(x, z) e^{ik_y y} e^{-i\omega_n t}, \quad \alpha = x, y, z. \quad (3.16)$$

The Fourier transform of the electric field is

$$\tilde{E}_\alpha(x, y, z, \omega) = \int_{-\infty}^{\infty} E_\alpha(x, y, z, t) e^{i\omega t} dt, \quad \alpha = x, y, z. \quad (3.17)$$

Substitution of (3.16) into (3.17) yields

$$\begin{aligned} \tilde{E}_\alpha(x, y, z, \omega) &= \int_{-\infty}^{\infty} \sum_n \phi_n(x, z) e^{ik_y y} e^{-i\omega_n t} e^{i\omega t} dt \\ &= \sum_n \phi_n(x, z) e^{ik_y y} \int_{-\infty}^{\infty} e^{-i\omega_n t} e^{i\omega t} dt \\ &= \sum_n \phi_n(x, z) e^{ik_y y} 2\pi \delta(\omega - \omega_n) \\ &\quad \alpha = x, y, z. \end{aligned} \quad (3.18)$$

The delta functions in (3.18) implies that peaks in the spectrum will correspond to the mode frequencies.

Once the mode frequency is determined, the Fourier transform of each  $(x, z)$  location is performed to form the template. Then the template is modulated near  $\omega_n$

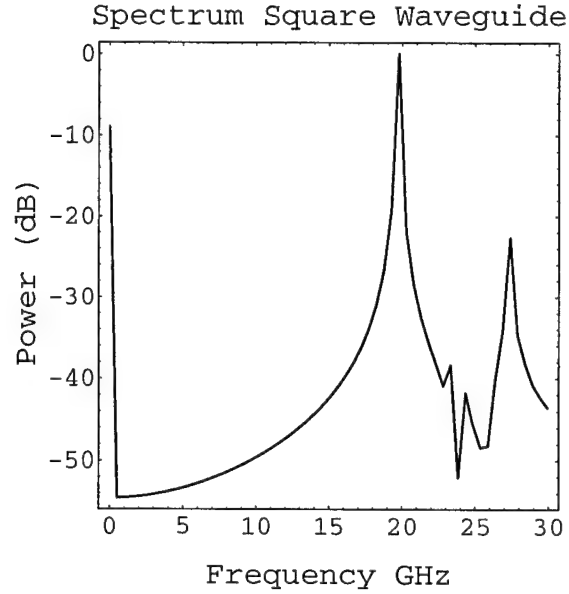


Figure 3-4: Spectrum of field in dielectric waveguide using two dimensional FDTD code with  $k_y = 600 \text{ m}^{-1}$

to excite the simulation.

To validate this procedure the same structure of Section 3.3 is used. The FDTD grid spacing is set to  $0.01 \text{ cm}$  and the time step set to the Courant limit for three dimensional space (2.45). The computational domain measured  $37 \times 41$ , bounded with a first order Mur absorbing boundary condition. The spatial excitation was a two dimensional Gaussian centered inside the waveguide. The temporal excitation was a narrow Gaussian pulse with  $\beta = 16$  as described in Section 2.8. The excitation entered the simulation volume through current sources at the desired polarization in this case  $E_z$ . 8192 time steps were performed and the last 4096 were used for the Fourier transform.

The spectrum of the response to the excitation is shown in Figure 3-4. The first peak represents the temporal frequency of the fundamental mode that corresponds to the pre-determined propagation constant. The Fourier transform is taken at the mode frequency to produce the mode template in Figure 3-5.

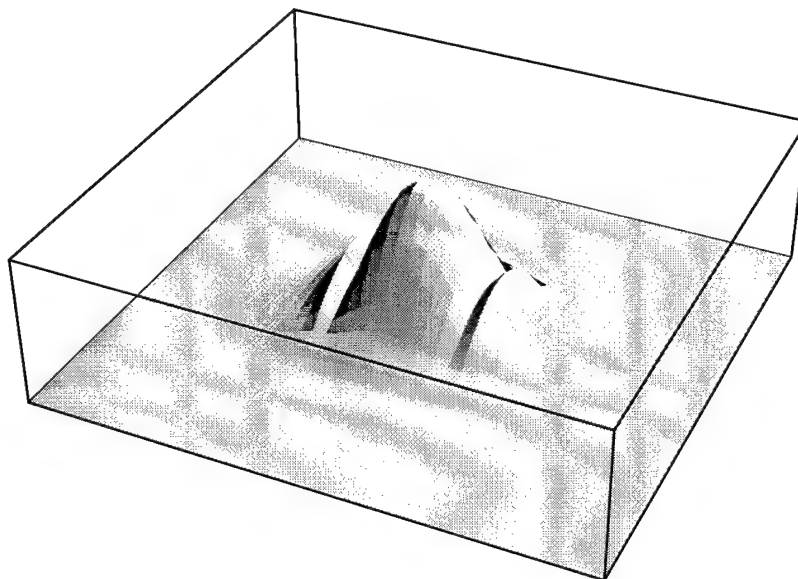


Figure 3-5: Mode template for  $E_{1,1}^z$  of square dielectric waveguide using two dimensional FDTD code.

The fundamental mode frequencies at different propagation constants were numerically derived with the FDTD 2D code and plotted against the analytic curve in Figure 3-6. The results show good agreement at the frequency range of interest. The deviation at the higher frequencies is due to the numerical dispersion error introduced by the discretization of Maxwell's equations and can be removed with a smaller grid size.

### 3.5.2 Verification of Computational Domain Reduction

Even though the numerical templates lead to accurate fundamental mode dispersion curves, there is no guarantee that the computational domain can be reduced. In order to show this reduction several FDTD simulations were conducted on a waveguide with permittivity  $\epsilon = 2.8\epsilon_0$ , on top of a substrate with permittivity  $\epsilon = 2.2\epsilon_0$ , surrounded above with a cladding of free space. The substrate is mounted on a ground plane.

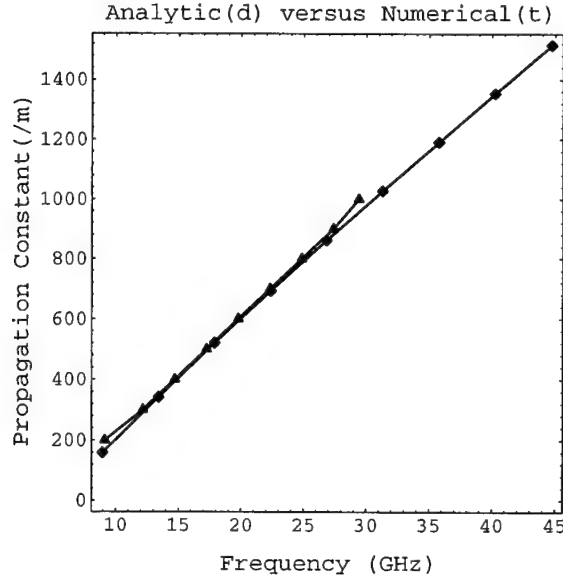


Figure 3-6: Validation of mode dispersion curve. Diamonds represent the Marcattili calculation and the triangles represent the numerically derived results.

The basic FDTD simulation volume is  $57 \times 62 \times 41$  surrounded by an 8 layer PML. The grid spacing is uniform with  $\Delta = .001m$  and the time step is set at the 3D Courant limit. A modulated Gaussian pulse with  $f = 20GHz$  and  $\beta = 128$  is used with either a numerical template or a 2D Gaussian pulse centered in the waveguide with widths equal to the width and height of the waveguide. The center point is set to (18,15) with waveguide dimensions  $rh = 10\Delta$ ,  $rw = 10\Delta$ , and  $fh = 0$ . The center of the perpendicular section of the waveguide is at  $j = 45$  with an input reference plane at  $j = 22$  and an output reference plane at  $i = 41$ . The computational domain is varied in  $y$  dimension while keeping the distances between the reference planes and the discontinuity constant. Two larger domains of  $57 \times 82 \times 41$  and  $57 \times 92 \times 41$  were tested; Figure 3-7 represents a top view of the configuration.

Figure 3-8 and Figure 3-9 represent  $S_{11}$  and  $S_{21}$  calculated at each of the three computational domain sizes with the Gaussian excitation. A detailed description of the  $S$  parameters,  $S_{11}$  and  $S_{21}$ , can be found in Section 3.7.1. Figure 3-10 and Figure 3-

11 represent  $S_{11}$  and  $S_{21}$  calculated at the two smallest computational domain sizes using a numerical mode template to excite the problem. The extra section of twenty grid spaces was definitely not needed when using the mode template by the fact that the results are nearly identical. On the other hand, the Gaussian results are very different between the small and middle sized domains. Since the middle and large domains are nearly identical, the mode did settle to an acceptable level with the addition of the twenty grid spaces in the  $y$  dimension. Thus, using a mode template in this simulation reduced the computational domain by over 20%. In what would normally take two hours, the computational domain reduction means a CPU savings of over 20 minutes. If only one simulation is necessary, since finding the template takes approximately five minutes, the savings is not really that significant; however, when many simulations are necessary the savings can be substantial. (All simulations were run on a DEC3000 Server Model 800 with a 200 MHz 21064 Alpha CPU.)

### 3.6 Absorbing Boundary Condition Demonstration

Before the PML's introduction and its subsequent application to multi-layered dielectrics, a first order Mur ABC was usually used to terminate the FDTD computational domain when multiple dielectric media are adjacent to the domain edges. The second order Mur cannot be used because of discontinuities at dielectric/dielectric interfaces. Figure 3-12 shows the time domain response at the 503rd time step of a simulation to analyze the effects of the  $45^\circ$  bend in a dielectric rib waveguide with  $rw = 10\text{ mm}$ ,  $rh = 6\text{ mm}$ , and  $fh = 4\text{ mm}$ . The cladding is free space and the permittivities of the substrate and film are  $2.2\epsilon_0$  and  $2.8\epsilon_0$  respectively. In open space the excitation should have exited the simulation volume before the 300th time step. Figure 3-12 clearly shows the benefit of using the PML over the first order Mur ABC.



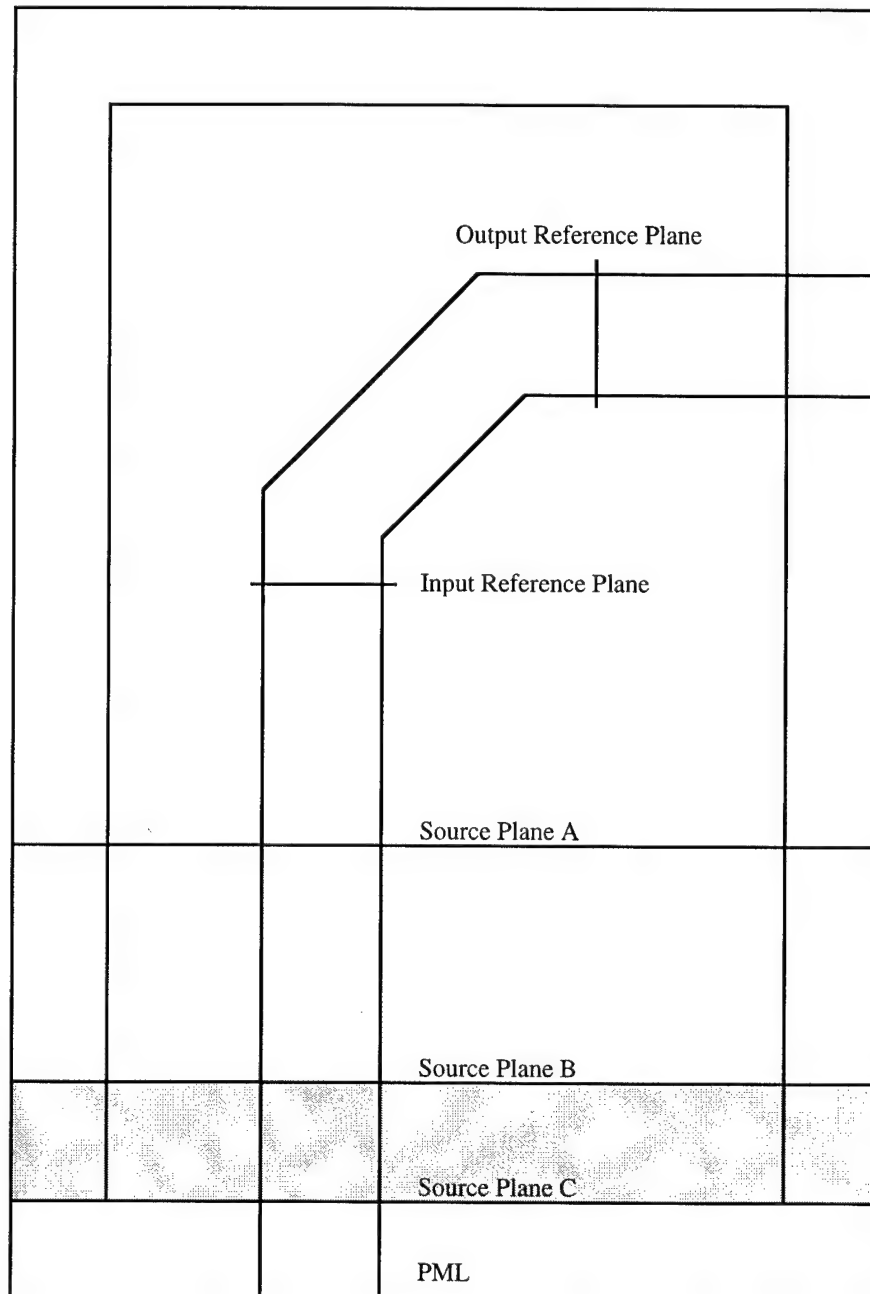


Figure 3-7: Configuration for numerical template analysis.

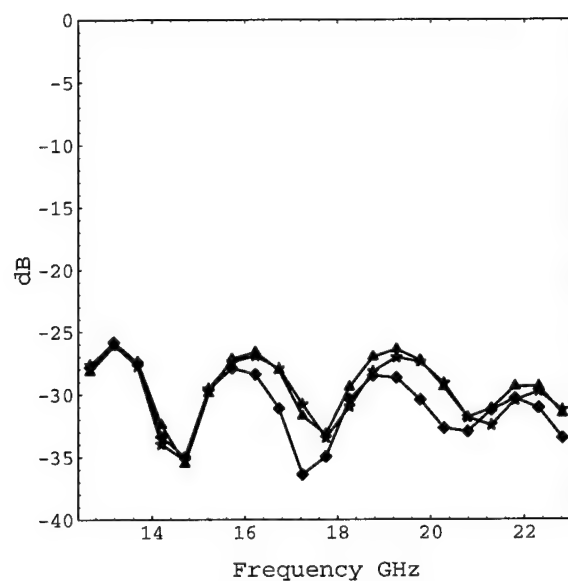


Figure 3-8:  $S_{11}$  as measured at the Input Reference Plane for an analytical Gaussian excitation at Source Planes A (diamonds), B (triangles), and C (stars).

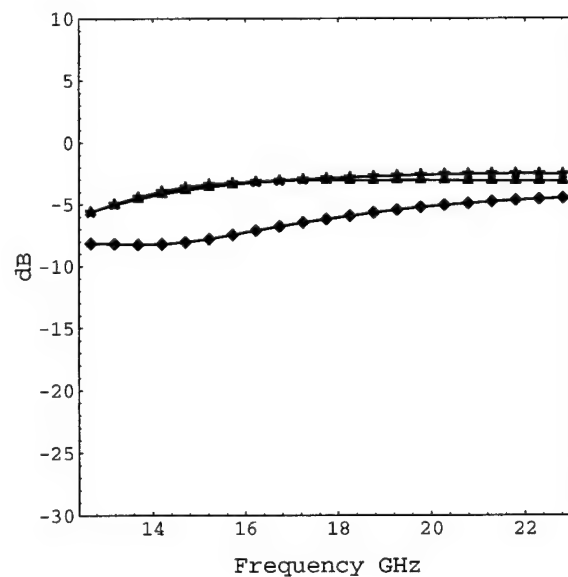


Figure 3-9:  $S_{21}$  as measured at the Output Reference Plane for an analytical Gaussian excitation at Source Planes A (diamonds), B (triangles), and C (stars).

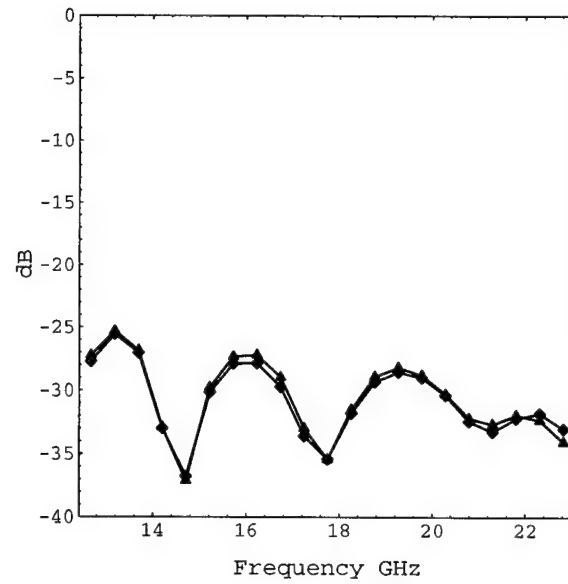


Figure 3-10:  $S_{11}$  as measured at the Input Reference Plane for an numeric template excitation at Source Planes A (diamonds), and B (triangles).

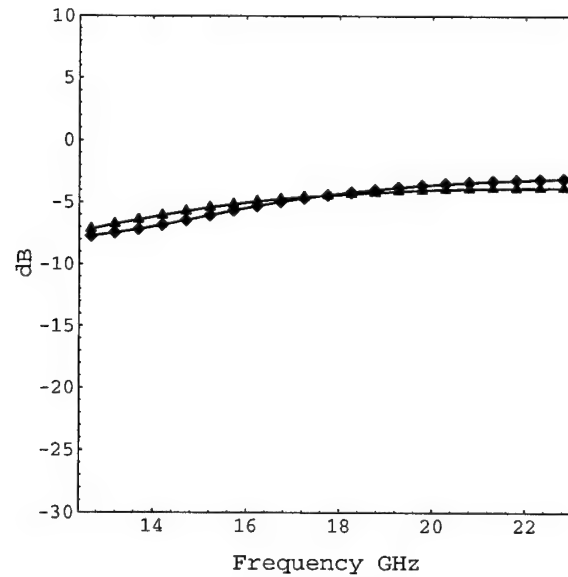


Figure 3-11:  $S_{21}$  as measured at the Output Reference Plane for an numeric template excitation at Source Planes A (diamonds), and B (triangles).

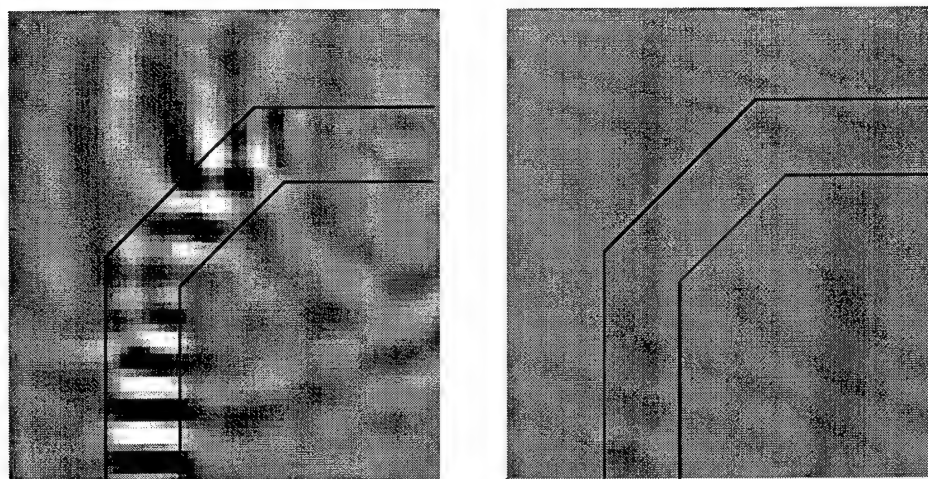


Figure 3-12: Time domain snap shots of FDTD simulation with 1st order Mur (left) and PML (right).

## 3.7 Measurements

Since the FDTD is a time domain simulation tool, the easiest measurements involve the placement of software probes that store the desired field quantities at each time step. When frequency measurements are needed, a sufficient number of time steps are necessary to achieve the desired frequency resolution. The frequency domain information is obtained with a Fast Fourier Transform (FFT) of the time domain data.

### 3.7.1 Power measurements

To analyze waveguide discontinuities, the  $S$  parameters are found. From the FDTD measurements of the time-domain waveforms, the  $S$  parameters may be calculated. The first step is to insert two reference planes in the simulation volume: one before the discontinuity and the other after the discontinuity. In those planes, the field components are saved at each time step. Next, the Fourier transform of each field

component at each location is taken to find the complex time harmonic field quantities. Then the power is calculated at by integrating the normal component of the Poynting vector over the surface of the reference plane and taking one half of the real part [137] such that

$$Power = \frac{1}{2} \text{Re} \left\{ \int \int \bar{\mathbf{E}} \times \bar{\mathbf{H}}^* d\bar{\mathbf{S}} \right\}, \quad (3.19)$$

where  $\bar{\mathbf{S}} = \bar{\mathbf{E}} \times \bar{\mathbf{H}}^*$  or

$$S_x = E_y H_z^* - E_z H_y^*, \quad (3.20)$$

$$S_y = E_z H_x^* - E_x H_z^*, \quad (3.21)$$

and

$$S_z = E_x H_y^* - E_y H_x^*. \quad (3.22)$$

For example, in the dielectric rib waveguide simulation, the propagation is in the  $\hat{y}$  direction so the power transmitted through the input reference plane is given by

$$Power_{input\ plane} = \frac{1}{2} \Delta x \Delta z \text{Re} \left\{ \sum_x \sum_z E_z H_x^* - E_x H_z^* \right\}. \quad (3.23)$$

### 3.7.2 S Parameters

The scattering parameters can be derived from the power calculations. However, first the incident and reflected waves must be separated. This is done by running two simulations: one with a straight section of waveguide with no discontinuity (producing a pure incident wave) and the other with the discontinuity (producing an incident plus a reflected wave). The waves can be separated by subtracting the incident wave calculated in the first simulation from the incident plus reflected waves calculated in the second simulation. The  $S$  parameters can be determined from

$$S_{11} = 10 \log \left( \frac{P_r}{P_i} \right) \quad (3.24)$$

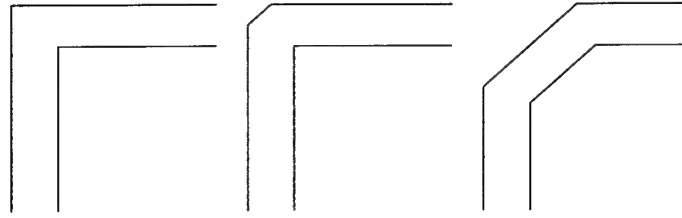


Figure 3-13: Configuration of bends tested, from left to right, 90° bend, 90° bend with bevel, and 45° bend.

and

$$S_{21} = 10 \log \left( \frac{P_t}{P_i} \right) \quad (3.25)$$

where  $P_i$ ,  $P_r$ , and  $P_t$  represent the incident, reflected and transmitted power.

### 3.8 Discontinuity Analysis

In this section the effects of various types of bends in a dielectric rib waveguide are investigated. The different bends are shown in Figure 3-13. The FDTD simulation uses a uniform grid size set to 1 mm, with the time step set to the 3D Courant limit. The simulation's duration is 1024 time steps and the subsequent FFTs use the data with  $1 \times$  padding.

The waveguide is constructed with a film layer and rib of permittivity  $\epsilon = 2.8\epsilon_0$ , on top of a substrate with permittivity  $\epsilon = 2.2\epsilon_0$ , surrounded above with a cladding of free space. The substrate is mounted on a ground plane. The basic FDTD simulation volume is  $57 \times 62 \times 41$  surrounded by an 8 layer PML. modulated Gaussian pulse with  $f = 18.8 \text{ GHz}$  and  $\beta = 128$  is used with a numerical template (Figure 3-14). The center point is set to (18,20) with waveguide dimensions  $rh = 6\Delta$ ,  $rw = 10\Delta$ , and  $fh = 4\Delta$ . The center of the perpendicular section of waveguide is at  $j = 45$  with an input reference plane at  $j = 22$  and an output reference plane at  $i = 41$ . The loss through these three types of bends can be seen by examining  $S_{21}$  in Figure 3-15.

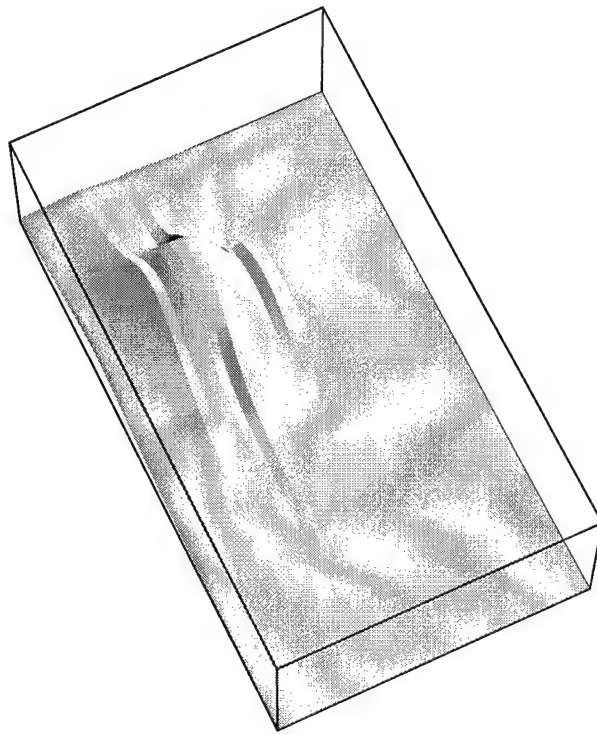


Figure 3-14: Mode template for  $E_{1,1}^z$  of dielectric rib waveguide using two dimensional FDTD code.

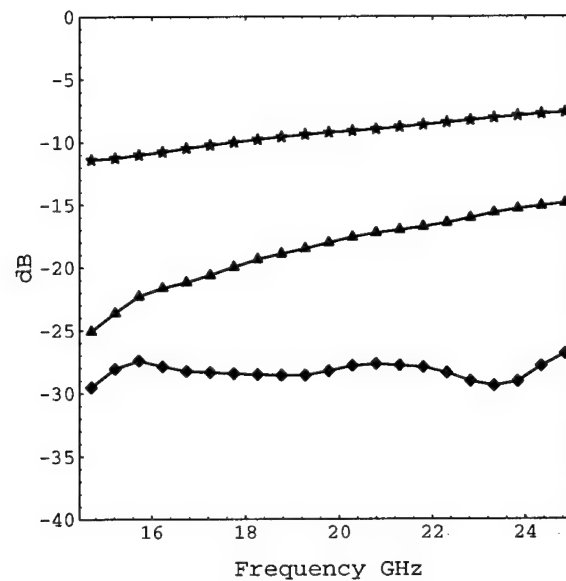


Figure 3-15:  $S_{21}$  rib waveguide through three different types of turns: 90° bend (diamond), 90° bend with bevel (triangle), 45° bend (star).

None of the turns do a very good job guiding the energy around the turn. The 45° bend offers the best performance with 10 dB of loss. One of the advantages of using the FDTD method in this type of analysis is that snap shots can be taken and the progress of the wave can be visually tracked. Figures 3-16 and 3-17 show how the wave travels through the guide. We can see that the 90° bend loses most of its energy in radiated out the back of the turn while the 45° bend does guide energy around the turn although a lot is still radiated out through the back.

### 3.9 Analysis of Rib Geometry on Turn Loss

The effects of the film height to rib height ratio ( $fh$  and  $rf$  in Figure 3-1) are investigated in this section. Figures 3-18 through 3-22 show the mode templates for the five guides tested. Each guide is excited with modulated Gaussian pulse. The guides were 10 mm wide and a 45° bend was used as the discontinuity tested. The results



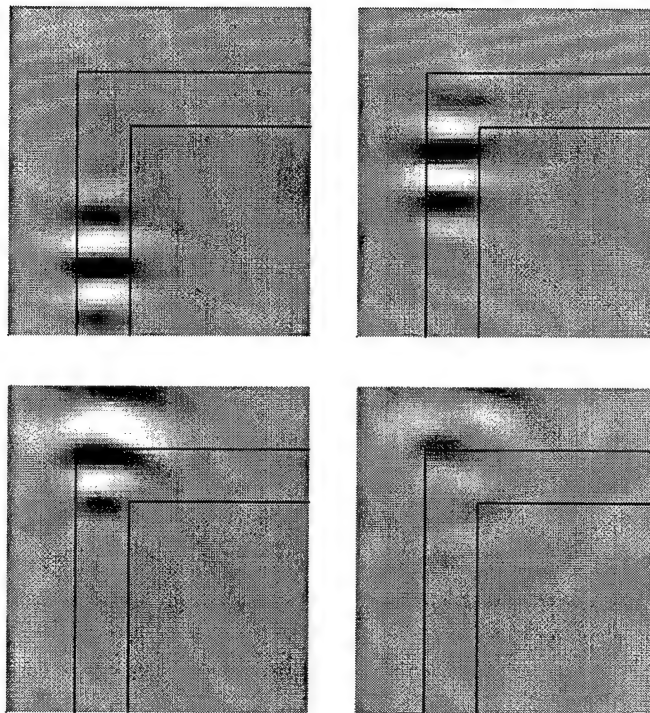


Figure 3-16: Time domain snap shots of propagation through a  $90^\circ$  bend at 173, 233, 293, and 323 time steps. (Clockwise starting at upper left.)

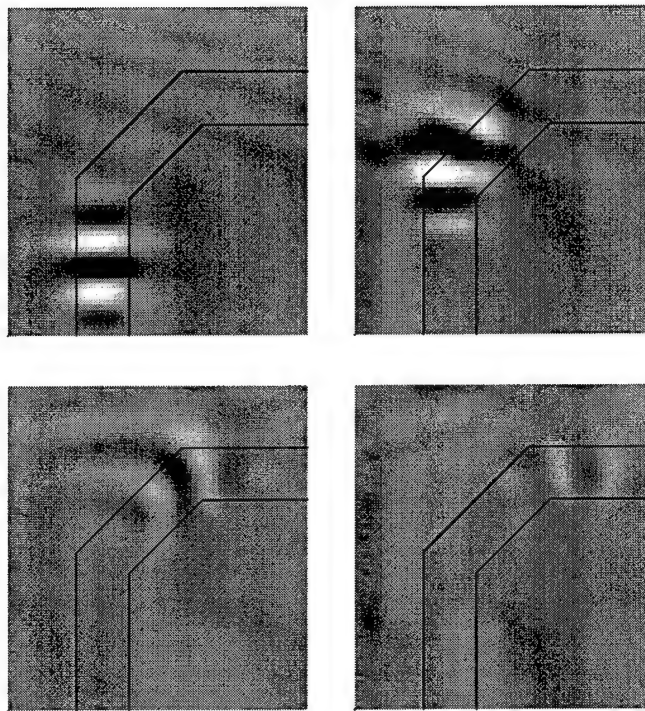


Figure 3-17: Time domain snap shots of propagation through a  $45^\circ$  bend at 173, 233, 293, and 323 time steps. (Clockwise starting at upper left.)

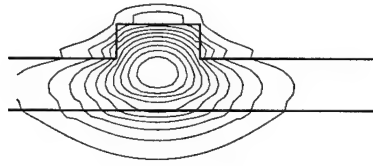


Figure 3-18: Mode template for  $E_{1,1}^z$  of dielectric rib waveguide with film height:  $6\text{ mm}$ , rib height:  $4\text{ mm}$  and rib width:  $10\text{ mm}$ .

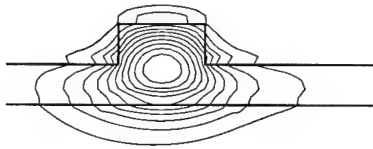


Figure 3-19: Mode template for  $E_{1,1}^z$  of dielectric rib waveguide with film height:  $5\text{ mm}$ , rib height:  $5\text{ mm}$  and rib width:  $10\text{ mm}$ .

show that the smaller film height to rib height ratio the better the bend will guide the energy. Over  $10\text{ dB}$  of improvement can be seen when the ratio is decreased from 1.5 to 0. In other words, a rectangular waveguide on top of a substrate has better performance than a rib guide. And, as the film thickness is reduced compared to the film height the better the performance. Better performance is attributed to the open nature of the film layer. As the rib height decreases relative to the film height, the guide approaches a dielectric slab waveguide that would offer no guidance in the transverse direction.

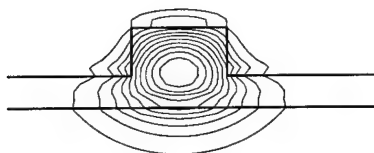


Figure 3-20: Mode template for  $E_{1,1}^z$  of dielectric rib waveguide with film height:  $4\text{ mm}$ , rib height:  $6\text{ mm}$  and rib width:  $10\text{ mm}$ .

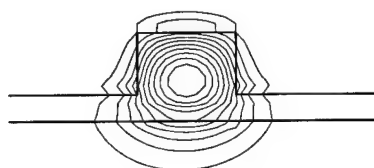


Figure 3-21: Mode template for  $E_{1,1}^z$  of dielectric rib waveguide with film height:  $3\text{ mm}$ , rib height:  $7\text{ mm}$  and rib width:  $10\text{ mm}$ .

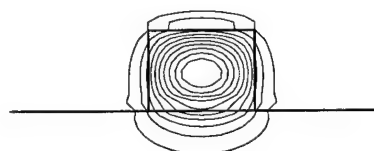


Figure 3-22: Mode template for  $E_{1,1}^z$  of dielectric rib waveguide with film height:  $0\text{ mm}$ , rib height:  $10\text{ mm}$  and rib width:  $10\text{ mm}$ .

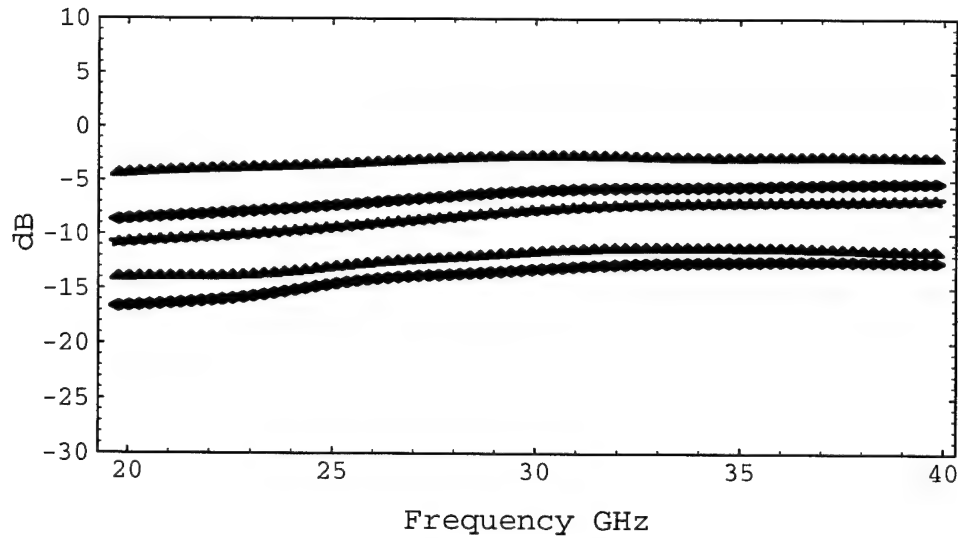


Figure 3-23:  $S_{21}$  through  $45^\circ$  bend of dielectric rib waveguide. Starting from top curve to bottom curve the film height to rib height ratios are 0.0, 0.43, 0.67, 1.0, and 1.5.

### 3.10 Discussion

The Finite Difference Time Domain numerical technique is an excellent tool to study the dielectric rib waveguide. The openness of the structure can be simulated with the Berenger Perfectly Matched Layer if each dielectric layer is matched considering all the layers within the simulation volume. The computation domain can be reduced if the fundamental mode's spatial distribution is calculated first and used to excite the mode. The better excitation means that shorter distances between the excitation plane and the discontinuity are needed for the mode to settle. A twenty percent reduction was shown in Section 3.5.2. This reduction implies bigger problems can be simulated within the same time as those simulations using other excitation techniques, or the same simulations can be run in shorter times.

Although the dielectric rib waveguide provides very low loss for high frequency signals compared to microstrip or coplanar structures, the rib waveguide bend does introduce a significant amount of loss. As the abruptness on the turn is lessened, the

rib guides more energy around turn; however, gradual turns require more space on an integrated circuit. With the improvements to the FDTD method presented in this chapter, rib bend structures can be studied to improve their loss characteristics.



## Chapter 4

# Impedance Boundary Condition for Thin Finite Conducting Sheets in FDTD

### 4.1 Introduction

In FDTD simulations involving highly conductive materials, such as the metal case of a computer system, the tangential electric fields are typically set to zero on the surface of the material. This Perfect Electric Conductor (PEC) assumption ignores any loss associated with the less than infinite conductivity. The errors that result from this approximation are considered against the large cost of discretizing the lossy material. Since the wavelength of a highly conductive material is very small, in order to capture the loss mechanism within the conductor the simulation volume must be divided into a very fine grid. When the *brute force* method is used, computer resources are wasted by having to finely divide the the other less dense materials (*e.g.* free space). In these materials the fine grid is not necessary to capture the physics of the problem. The computational size can be reduced with a sub-gridding scheme where the conducting material uses much smaller grid than the rest of the computational domain [9, 10, 12].



For very good conductors; however, the grid size is so small that even sub-gridding is not a viable option. To overcome the resource problem, the surface of the highly conductive material can be replaced with an Impedance Boundary Condition (IBC) [126]-[130]. An IBC is only appropriate when the simulation volume of interest is on one side of the conductive material. However, IBCs have the added complication that they are usually frequency dependent and are not directly applicable to the standard frequency independent FDTD equations. In this case the FDTD equations must be modified to incorporate the dispersive nature of the surface [109]-[120]. Typical frequency domain equations relating the electric fields and magnetic fields become convolution equations in time. Convolutions have a large computational and memory overhead, but if the convolution integral can be approximated by a sum of exponentials then recursive convolution can be implemented and the memory requirements reduced.

A *synthetic* conductivity has been used with normal FDTD difference equations for lossy media to model good conductors [117]. The synthetic conductivity is derived by comparing the numerical impedance of the difference equations and the actual impedance of a good conductor at specified frequency. In this way the derived synthetic conductivity is inserted into the FDTD equations at the boundary only; thus being a surface boundary condition similar to an IBC. The advantage to this method is that no *new* equations are needed; however, it's major disadvantage is that it is good at a single frequency.

An Impedance Boundary Condition that incorporates the frequency dependence was developed for thin dielectric coatings over PEC surfaces [127]. The IBC starts with the analytically derived expression for the impedance in the frequency domain. The expression is expanded in a Taylor series about the wave number,  $k$ , and transformed to the time domain. The resulting partial differential equation is fourth order in time and first order in space. The difference equations do model the frequency characteristics fairly well; however, the equations are quite complicated and rely on

many past values of the surface electric field. Furthermore, the condition is good at normal incidence only thus limited to 1D structures. This work is extended to include non-normal incidence [129]; however, the modified IBC is only good for a single incidence angle.

Like the IBC of [127], Tassoudji [128] starts with a frequency domain expression for the impedance. This time for a thin sheet of a very good conductor. The frequency domain equation is transformed to the Laplace domain and the subsequent expression is approximated by a sum of first-order rational functions. This approximation is critical to the IBC's usefulness in FDTD simulations. The first-order rational functions are exponentials in time and thus a recursive convolution scheme is implemented. This FDTD IBC scheme has been applied to one-dimensional (1D) FDTD simulation of a plane wave reflecting from  $35\mu m$  thick copper plate with conductivity of  $\sigma = 5.8 \times 10^7 \Omega^{-1}m^{-1}$ . Compared with the analytic solution, the results have shown excellent agreement up to 30 GHz. The benefit of this scheme is that it is good over a wide range of frequencies.

The same approach was applied to lossy dielectric portions of a FDTD computational domain with an IBC where the frequency domain impedance expression was approximated by a rational function using *Mathematica* and then expanded using partial fraction expansion. In this way, like [128] a recursive convolution can be used.

In this chapter the IBC for thin finite conducting sheets of [128] is examined and extended to two dimensions. In order for this IBC to be a practical FDTD tool, this extension is very important. Also, guidelines for the number of expansion terms are needed in order to give users an *a priori* estimate of the resources required to perform a given simulation.

This chapter describes the 1D Impedance Boundary Condition for thin finite conducting sheets and recursive convolution. Then the accuracy of the 1D IBC is examined and quantified. Finally, the IBC is extended to two dimensions and validated through the measurements of the *quality* factor of rectangular resonant cavities at

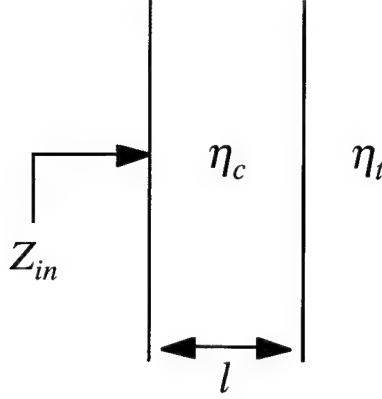


Figure 4-1: 1D transmission line model used for IBC formulation.

different frequencies and conductivity values.

## 4.2 Derivation of Impedance Boundary Condition

To construct an impedance boundary condition we start with the impedance equation that relates the tangential components of the electric and magnetic field at an interface between two different media,

$$\bar{E}_{\text{tan}}(\omega) = Z(\omega) \left[ \hat{n} \times \bar{H}_{\text{tan}}(\omega) \right], \quad (4.1)$$

where  $\bar{E}_{\text{tan}}$  and  $\bar{H}_{\text{tan}}$  are the tangential components of the electric and magnetic fields and  $\hat{n}$  is the normal unit vector pointing out at the interface [128]. For a conducting media with properties  $\epsilon$ ,  $\mu_o$  and  $\sigma$  representing the permittivity, permeability, and conductivity respectively, if the media is a *good* conductor such that  $1 \ll \frac{\sigma}{\omega\epsilon}$  then the permittivity of the conductor can be approximated by

$$\epsilon_c \approx i \frac{\sigma}{\omega}. \quad (4.2)$$

In one dimensional simulations, since propagation is normal to the surface, the

surface impedance of a thin good conductor can be modeled as a transmission line with thickness  $l$  and an intrinsic impedance  $\eta_c = \sqrt{\frac{\mu_o}{\epsilon_c}}$ . From transmission line theory, if a transmission line is terminated with impedance  $\eta_t$  then the impedance seen at distance  $l$  from the termination is

$$Z_{in} = \eta_c \frac{\eta_t - \eta_c \tanh(ik_cl)}{\eta_c - \eta_t \tanh(ik_cl)}. \quad (4.3)$$

When the termination impedance is free space *i.e.*  $\eta_t = \eta_o \gg \eta_c$ , then input impedance can be approximated by

$$Z_{in} \approx \eta_c \coth(ik_cl). \quad (4.4)$$

In order to utilize this impedance condition, it is necessary to transform equation into the Laplace domain. The Laplace transform of (4.4) is

$$Z_{in}(s) = \sqrt{\frac{\mu_o s}{\sigma}} \coth \left( \sqrt{\frac{\mu_o s}{\sigma}} \sigma l \right). \quad (4.5)$$

Using power series expansions for cosh and sinh [141],

$$\cosh z = \prod_{k=1}^{\infty} \left[ 1 + \frac{4z^2}{(2k-1)^2 \pi^2} \right] \quad (4.6)$$

and

$$\sinh z = z \prod_{k=1}^{\infty} \left[ 1 + \frac{z^2}{k^2 \pi^2} \right], \quad (4.7)$$

the input impedance (4.5) can be represented by quotient of two infinite products:

$$Z_{in}(s) = \frac{1}{\sigma l} \frac{\prod_{m=1}^{\infty} \left[ 1 + \frac{4\mu_o \sigma l^2}{(2m-1)^2 \pi^2 s} \right]}{\prod_{m=1}^{\infty} \left[ 1 + \frac{\mu_o \sigma l^2}{m^2 \pi^2 s} \right]}. \quad (4.8)$$

To use this relationship within the FDTD framework the impedance condition (4.3) must be transformed into the time domain,

$$\bar{E}_{\text{tan}}(t) = \int_0^t Z(t - \tau) [\hat{n} \times \bar{H}_{\text{tan}}(\tau)] d\tau. \quad (4.9)$$

A simple expression for  $\bar{E}_{\text{tan}}(t)$  must be found that can be converted to update equations that do not explicitly use the convolution integral of (4.9). This can be accomplished by approximating (4.8) with  $P$  terms in the denominator and  $P - 1$  terms in the numerator. The quotient can be expressed as a sum of quotients using partial fraction expansion and then transformed into the time domain. The result is a sum of exponentials,

$$Z(t) \approx \sum_{m=1}^P C_m e^{A_m t}, \quad (4.10)$$

where  $A_m$  is the  $m$ th pole and  $C_m$  in the  $m$ th residue of (4.8), given by

$$A_m = -\frac{m^2 \pi^2}{\mu_o \sigma l^2} \quad (4.11)$$

and

$$C_m = \left( 1 + \frac{\mu_o \sigma l^2}{m^2 \pi^2} s \right) Z_{\text{in}}(s) \Big|_{s=A_m}. \quad (4.12)$$

### 4.3 Recursive Convolution

Recursive convolution is possible when one of the operands is an exponential function. Since we have expressed the impedance of (4.9) at a sum of exponentials recursive convolution can be used. As in [130], we begin with the following convolution integral,

$$y(t) = \int_0^t a e^{-b(t-\tau)} x(\tau) d\tau, \quad (4.13)$$

and discretize it so that

$$y(n\Delta t) = \sum_{k=0}^{n-1} \int_{k\Delta t}^{(k+1)\Delta t} a e^{-b(n\Delta t - \tau)} x(\tau) d\tau. \quad (4.14)$$

Assuming that  $x(t)$  is constant over the interval (*i.e.* piecewise constant), the integration over  $\tau$  yields

$$y(n\Delta t) = \frac{a}{b} \sum_{k=0}^{n-1} x(k\Delta t) e^{-b(n-k)\Delta t} (e^{b\Delta t} - 1). \quad (4.15)$$

Remove the  $n$ th term from the summation,

$$\begin{aligned} y(n\Delta t) &= \frac{a}{b} \sum_{k=0}^{n-2} x(k\Delta t) e^{-b(n-k)\Delta t} (e^{b\Delta t} - 1) \\ &\quad + \frac{a}{b} x(n\Delta t) e^{-b(n-n)\Delta t} (e^{b\Delta t} - 1), \end{aligned} \quad (4.16)$$

and rewrite the sum over  $n-2$  so that

$$\begin{aligned} &\sum_{k=0}^{n-2} x(k\Delta t) e^{-b(n-k)\Delta t} (e^{b\Delta t} - 1) \\ &= \sum_{k=0}^{n-2} x(k\Delta t) e^{-b(n-k-1)\Delta t} e^{-b\Delta t} (e^{b\Delta t} - 1) \\ &= e^{-b\Delta t} \sum_{k=0}^{n-2} x(k\Delta t) e^{-b(n-k-1)\Delta t} (e^{b\Delta t} - 1) \\ &= e^{-b\Delta t} y((n-1)\Delta t). \end{aligned} \quad (4.17)$$

The result is the basis for a recursive convolution equation:

$$\begin{aligned} y(n\Delta t) &= e^{-b\Delta t} y((n-1)\Delta t) \\ &\quad + \frac{a}{b} x(n\Delta t) (1 - e^{-b\Delta t}). \end{aligned} \quad (4.18)$$

In the derivation above we assume  $x(t)$  could be approximated as  $x(n\Delta t)$  over the interval  $[n\Delta t, (n+1)\Delta t]$ . If we assume a piecewise linear approximation instead of

piecewise constant,  $x(t)$  is approximated as

$$x(t) \simeq x(n\Delta t) + \frac{t}{\Delta t}(x((n+1)\Delta t) - x(n\Delta t)) \quad (4.19)$$

so that

$$y(n\Delta t) = \sum_{k=0}^{n-1} \int_{k\Delta t}^{(k+1)\Delta t} ae^{-b(n\Delta t-\tau)} \left[ x(n\Delta t) + \frac{\tau - k\Delta t}{\Delta t}(x((n+1)\Delta t) - x(n\Delta t)) \right] d\tau \quad (4.20)$$

and the recursion formula becomes

$$\begin{aligned} y(n\Delta t) &= e^{-b\Delta t}y((n-1)\Delta t) \\ &+ \frac{a}{b}\{x(n\Delta t)\left[1 + \frac{1}{\Delta tb}(e^{-b\Delta t} - 1)\right] \\ &+ x((n-1)\Delta t)\left[\frac{1}{\Delta tb} - e^{-b\Delta t}\left(1 + \frac{1}{\Delta tb}\right)\right]\}. \end{aligned} \quad (4.21)$$

## 4.4 Implementation of Impedance Boundary Condition in FDTD

Now that we have the form of the recursive convolution integrals we can construct FDTD IBC update equations.

### 4.4.1 Impedance Equations - Piecewise Constant Assumption

The derivation of the previous section can be used to construct the FDTD update equations if we let

$$y(n\Delta t) \rightarrow \bar{G}_m^n, \quad (4.22)$$

$$x((n-1)\Delta t) \rightarrow \hat{n} \times \bar{H}_{tan}^{n-\frac{1}{2}}, \quad (4.23)$$

and

$$ae^{-bn\Delta t} \rightarrow C_me^{A_m n\Delta t}. \quad (4.24)$$

Substitution into (4.19) gives

$$\bar{G}_m^n = \bar{G}_m^{n-1}e^{A_m\Delta t} \quad (4.25)$$

$$+ (\hat{n} \times \bar{H}_{tan}^{n-\frac{1}{2}}) \frac{C_m}{A_m} (e^{A_m\Delta t} - 1) \quad (4.26)$$

The tangential electric field update equation at the conductor surface is

$$\bar{E}_{tan}^n = \sum_{m=1}^P \bar{G}_m^n \quad (4.27)$$

The impedance equation relates the electric and magnetic fields at the same position and at the same time. However, in this work, we use the tangential electric field on the surface accompanied by the tangential magnetic field half a grid space away and we take a time average of the electric field so that the update equation becomes

$$\bar{E}_{tan}^n = -\bar{E}_{tan}^{n-1} + 2 \sum_{m=1}^P \bar{G}_m^{n-\frac{1}{2}}. \quad (4.28)$$

The tangential electric field on the surface at the current time step,  $n$ , is a function of last tangential electric field and the last sum,  $\bar{G}_m$ . Compared to the full convolution, memory requirements are low since this method requires only  $2P$  variables for the poles and residues and  $P$  variables for each grid point on the surface containing a tangential electric field.



### 4.4.2 Impedance Equations - Piecewise Linear Assumption

When more accuracy is desired the piecewise linear assumption can be used so that the tangential electric fields update equation is still (4.28) but now

$$\begin{aligned}\bar{G}_m^n &= \bar{G}_m^{n-1} e^{A_m \Delta t} \\ &+ (\hat{n} \times \bar{H}_{tan}^{n-\frac{1}{2}}) \frac{C_m}{A_m} \left[ \frac{1}{A_m \Delta t} (e^{A_m \Delta t} - 1) - 1 \right] \\ &+ (\hat{n} \times \bar{H}_{tan}^{n-\frac{3}{2}}) \frac{C_m}{A_m} \left[ \frac{1}{A_m \Delta t} + e^{A_m \Delta t} \left( 1 - \frac{1}{A_m \Delta t} \right) \right].\end{aligned}\tag{4.29}$$

Improved accuracy is obtained at the expense of a more complicated equation and an additional memory location for each tangential electric field component on the surface.

## 4.5 Extension of IBC to Two Dimensions

The use of the transmission line to model the impedance of a thin finite conducting sheet is completely justified in 1D simulations since propagation is fixed in the normal direction. On the other hand, since the angle of incidence is not restricted to normal incidence in 2D simulations, we must verify that the model is still valid.

Consider phase matching at the surface of the conductor, located at  $z = 0$ , where  $k_i$  is the wave number on the free space side with incidence angle  $\theta_i$  and  $k_c$  is the wave number in the conductor with a transmission angle of  $\theta_c$ . The incident components of the  $k$  vector are  $k_{ix} = k_0 \sin \theta_i$  and  $k_{iz} = k_0 \cos \theta_i$  and the conductor wave number is  $k_c = k_0 \sqrt{1 + i \frac{\sigma}{\omega \epsilon_0}}$ .

Since phase matching says  $k_{ix} = k_{cx}$ , we know  $k_{cz}^2 = k_c^2 - k_{ix}^2$ . Solving for  $k_{cz}$ ,

$$k_{cz}^2 = k_0^2 \left( \cos^2 \theta_i + i \frac{\sigma}{\omega \epsilon_0} \right),\tag{4.30}$$

and using the good conductor approximation, we find

$$k_{cz} \simeq k_0 \sqrt{\frac{\sigma}{2\omega\epsilon_0}} (1 + i). \quad (4.31)$$

The angle in the conductor is given by

$$\tan \theta_c = \frac{k_{cx}}{\text{Re}\{k_{cz}\}} = \sin \theta_i \sqrt{\frac{2\omega\epsilon_0}{\sigma}}. \quad (4.32)$$

Since  $\sqrt{\frac{\sigma}{\omega\epsilon_0}}$  is very large, the propagation direction will, for all practical purposes, be normal to the surface regardless of the incidence angle. Therefore, we expect the transmission line model to apply even in the two dimensional case.

Figure 4-2 is a schematic of a 2D rectangular resonator with finite conducting walls. The relationships between the tangential electric and magnetic walls and the surface normal are shown and are used to construct IBC equations for each of the four walls. If the computational domain is  $N_x \times N_z$ , the piecewise constant equations are

$$\begin{aligned} E_y^n(0, k) &= -E_y^{n-1}(0, k) \\ &+ 2 \sum_{m=1}^P \left[ G_m^{n-1} e^{A_m \Delta t} - H_z^{n-\frac{1}{2}}\left(\frac{1}{2}, k\right) \frac{C_m}{A_m} (e^{A_m \Delta t} - 1) \right], \end{aligned} \quad (4.33)$$

for the left wall;

$$\begin{aligned} E_y^n(N_x, k) &= -E_y^{n-1}(N_x, k) \\ &+ 2 \sum_{m=1}^P \left[ G_m^{n-1} e^{A_m \Delta t} + H_z^{n-\frac{1}{2}}\left(N_x - \frac{1}{2}, k\right) \frac{C_m}{A_m} (e^{A_m \Delta t} - 1) \right], \end{aligned} \quad (4.34)$$

for the right wall;

$$E_y^n(i, 0) = -E_y^{n-1}(0, k) \quad (4.35)$$

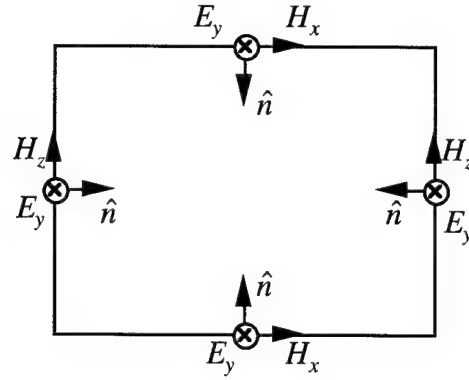


Figure 4-2: 2D configuration used for IBC equations of a rectangular resonator.

$$+ 2 \sum_{m=1}^P \left[ G_m^{n-1} e^{A_m \Delta t} + H_x^{n-\frac{1}{2}}(i, \frac{1}{2}) \frac{C_m}{A_m} (e^{A_m \Delta t} - 1) \right],$$

for the lower wall; and

$$\begin{aligned} E_y^n(i, N_z) &= -E_y^{n-1}(i, N_z) \\ &+ 2 \sum_{m=1}^P \left[ G_m^{n-1} e^{A_m \Delta t} - H_x^{n-\frac{1}{2}}(i, N_z - \frac{1}{2}, k) \frac{C_m}{A_m} (e^{A_m \Delta t} - 1) \right] \end{aligned} \quad (4.36)$$

for the upper wall.

The piece linear equations can easily be constructed by modifying equations (4.34) through (4.37) keeping equation (4.30) in mind.

## 4.6 Effects of FDTD Simulation Parameters on IBC Accuracy

In this section a numerical study of the effects of the FDTD simulation parameters such as grid spacing, time step, and the number of expansions terms is presented.

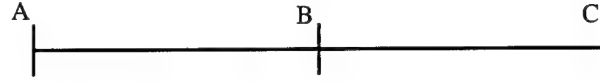


Figure 4-3: 1D configuration for IBC error analysis.

### 4.6.1 1D FDTD Simulation Configuration

Figure 4-3 is a representation of the 1D FDTD simulation set up used to analyze the effects of FDTD parameters on the IBC accuracy. An unmodulated Gaussian pulse is used to excite the problem at one end of the computational domain, point **A**, with the boundary condition  $E_x^n(k=0) = g(n)$ . The IBC is placed at point **B** and a first order Mur boundary condition is placed at the other end of the computational domain, point **C**. The propagation direction is  $z$  and a TEM wave,  $(E_x, H_y)$  is launched toward the IBC. The computational domain is  $3000\Delta$  long with **B** in the middle at  $z = 1500\Delta$  or more simply  $k = 1500$ . As described in Chapter 2, the time step is set to

$$\Delta t = \frac{\Delta}{CFL c}$$

where  $c$  is the speed of light and  $CFL$  a real number greater than or equal to the Courant limit. The normal 1D FDTD algorithm requires  $CFL \geq 1$  for stability. Two simulations are run for any given test set up. The first simulation does not include the IBC at  $k = 1500$ . Instead the field is allowed to freely propagate to the right and the field is measured at  $k = 1499$  and saved at all time steps to be used as the incident field when calculating the reflection coefficient of the IBC. The second simulation also measures the electric field at  $k = 1499$ ; however this time, the IBC is in place at  $k = 1500$ . Here the stored field includes both the incident and reflected waves. By using this total field and the stored incident field the reflection coefficient is calculated up to  $10\text{GHz}$ . Even though the reflection coefficient would be a sufficient

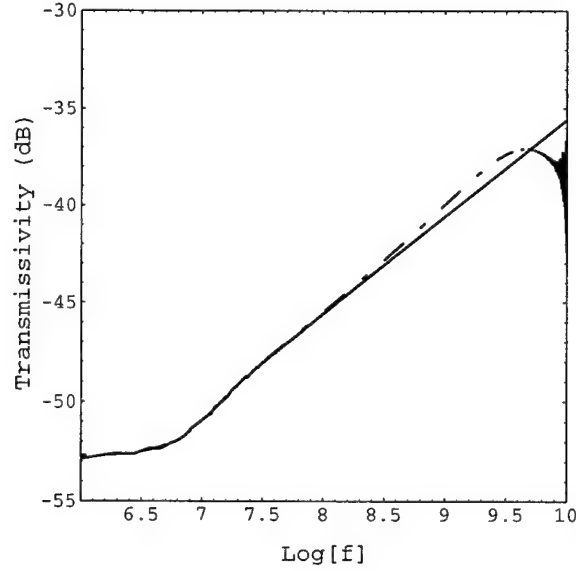


Figure 4-4: Transmissivity FDTD (dashed) vs. Analytic (solid) for a  $35\text{ }\mu\text{m}$  thick sheet of copper with  $\sigma = 5.8 \times 10^7\text{ }\Omega^{-1}\text{m}^{-1}$ ;  $P = 20$ ,  $\Delta = .005\text{ m}$ ,  $CFL = 2.0$ , and  $\beta = 50$ .

measure of the IBC, the transmissivity is calculated from the reflection coefficient via

$$t(f) = 10 \log[1 - |R(f)|^2]. \quad (4.37)$$

The transmissivity has the nice property that it increases with increasing frequency in this application.

The frequency content of the incident pulse is controlled through the selection of  $\beta$  from Chapter 2 once the time step is determined by  $\Delta$  and  $CFL$ . Figure 4-4 is a plot of the transmissivity measured from a  $35\text{ }\mu\text{m}$  thick sheet of copper with  $\sigma = 5.8 \times 10^7\text{ }\Omega^{-1}\text{m}^{-1}$ . The IBC is within  $1\text{ dB}$  up to  $3\text{ GHz}$  with only 20 expansion terms. In the next section the FDTD parameters are varied and the effects studied.

### 4.6.2 Transmissivity Error Measurements

The error analysis is based on a direct comparison between the FDTD transmissivity results versus the analytical transmissivity calculation using

$$e = \sqrt{\frac{\sum_{i=1}^N [t_a(f_i) - t_{FDTD}(f_i)]^2}{N}}, \quad (4.38)$$

where  $t_{FDTD}(f_i)$  is the transmissivity calculated from the FDTD simulation and  $t_a(f_i)$  is the equivalent analytical calculation at frequency,  $f_i$ .

The first FDTD parameter examined is the time step. In [128], the time step was fixed relative to the grid spacing with  $CFL = 2.0$ . However, the FDTD stability criteria places the lower limit at  $CFL = 1.0$ . A larger time step can reduce the run time and improve the frequency resolution in any post simulation processing. Typically, FDTD codes allow the users to set the grid spacing while the code automatically sets the time step at the Courant limit, so it's important to know if the IBC requires a time step smaller than the Courant stability limit in order to bound the error. Figure 4-5 shows the results from a numerical experiment with two very different simulation configurations. The conductivities are different,  $5.8 \times 10^4 \Omega^{-1}m^{-1}$  versus  $5.8 \times 10^7 \Omega^{-1}m^{-1}$ ; the number of expansion terms are different,  $P = 3$  versus  $P = 125$ ; and finally the grid spacing is different,  $\Delta = .005 m$  versus  $\Delta = .00125 m$ . Both simulations used a sheet thickness of  $35 \mu m$  and the  $\beta$  is adjusted at each simulation to ensure the same frequency content in the excitation. Also, all simulations were run for 8192 times steps and the Fourier transforms were taken with padding at 16 times the original length. The error is calculated with (4.38). The results show that in order to keep the error low the IBC definitely has a stricter time step constraint than the FDTD Courant stability limit. In fact, both 1D experimental configurations had the same  $CFL$  limit. The results show that  $CFL \geq 1.82$  is necessary to bound the error. This does not mean the algorithm is unstable when  $CFL$  is set to the Courant limit it just means the accuracy is very poor. Furthermore, it is important to note

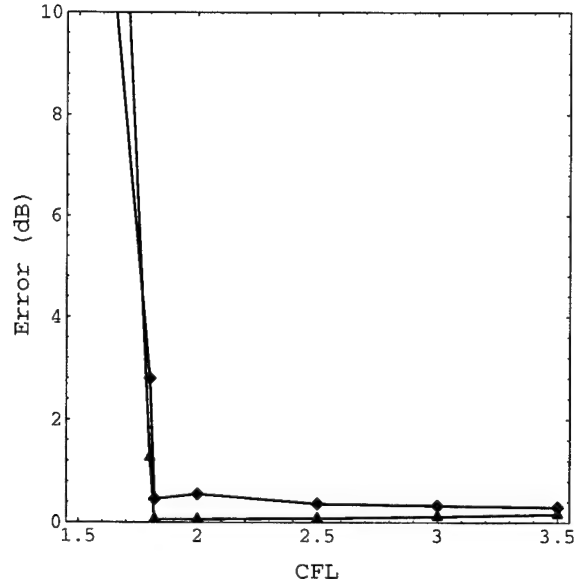


Figure 4-5: Error vs. CFL for a  $35\mu m$  thick conductor for two different FDTD configurations: (1)  $\sigma = 5.8 \times 10^4 \Omega^{-1}m^{-1}$ ,  $P = 3$ ,  $\Delta = .005 m$  (diamond) and (2)  $\sigma = 5.8 \times 10^7 \Omega^{-1}m^{-1}$ ,  $P = 125$ ,  $\Delta = .00125 m$  (triangle).

that the  $CFL$  is even larger than the 3D FDTD Courant limit of  $\sqrt{3}$  for a uniform grid.

Next the effects of grid size and number of expansion terms are studied. Figures 4-6 through 4-11 are plots of the transmissivity error of equation (4.38) versus the number of expansion terms at three different grid spacings,  $\Delta = .005 m$ ,  $\Delta/2$ , and  $\Delta/4$ . All simulations used a conductor thickness of  $35\mu m$  and the  $\beta$ 's were 50, 100, and 200 respectively. Figure 4-9 are the results with copper,  $\sigma = 5.8 \times 10^7$ , while Figure 4-6, Figure 4-7, and Figure 4-8 are the results for a conductivities three orders of magnitude less than copper and Figure 4-10 and Figure 4-11 are the results for a conductivities 2 orders of magnitude greater than copper.

The results show the general trend that smaller grid size will reduce the error. This, of course, makes sense. The FDTD algorithm is more accurate with a smaller grid size. Also, the impedance in the FDTD IBC is approximated by electric and

magnetic fields that are half a grid space apart, so the closer the grid space the more accurately the IBC scheme will approximate the actual impedance. However, the numerical results also show that the number of expansion terms plays a big role in the accuracy of the IBC algorithm and more terms does not necessarily mean more accuracy. For example, in Figure 4-6 we see that the error levels out at about 20 expansion terms. Interestingly, the optimum setting for  $P$  is about 5. Although the differences in error are less than  $.2\text{ dB}$  and  $.1\text{ dB}$  for  $\Delta = .005\text{ m}$  and  $\Delta = .00125\text{ m}$  respectively, these errors would accumulate in simulations where multiple reflections from the surface occur.

The optimum number of expansion terms is a function of conductivity and grid spacing. As Figure 4-9 indicates, the best values for  $P$  are approximately 50, 80, and 120 for a conductivity of  $\sigma = 5.8 \times 10^7$  and a grid spacing of  $\Delta = .005\text{ m}$ ,  $\Delta = .0025\text{ m}$ , and  $\Delta = .00125\text{ m}$  respectively. Whereas for low and high conductivities the effect of grid spacing is much reduced.

The results clearly show that as the conductivity increases the number of terms need to accurately approximate the impedance increases. In fact for the largest conductivity shown,  $\sigma = 5.8 \times 10^9$ , the IBC requires more than 250 terms to keep the error below  $1\text{ dB}$ .

### 4.6.3 Optimum Settings

The fact that there is an *optimum* number of terms for the piecewise constant IBC seems to go against intuition. If additional terms more accurately model the impedance then why doesn't the error decrease as the number of expansion terms increase?

We begin with a look at the error results for the piecewise linear IBC for copper with  $\sigma = 5.8 \times 10^7\text{ }\Omega^{-1}\text{m}^{-1}$  at three different grid spacings, as shown in Figure 4-12 versus the piecewise constant error in Figure 4-13. The two plots are combined in Figure 4-14. The results show that there is no optimum number of expansion terms (at least up to 300 terms) when using the piecewise linear IBC. Next, we look at the



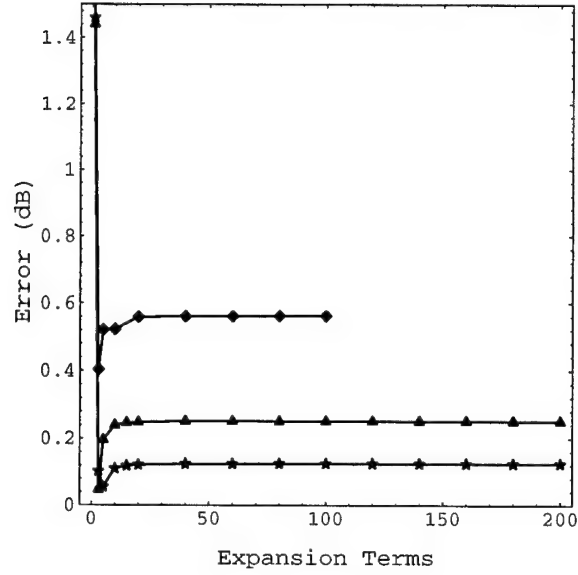


Figure 4-6: Error vs. expansion terms for a  $35\mu m$  thick conductor with  $\sigma = 5.8 \times 10^4 \Omega^{-1}m^{-1}$ ;  $\Delta = .005 m$  (diamond),  $\Delta = .0025 m$  (triangle),  $\Delta = .00125 m$  (star).

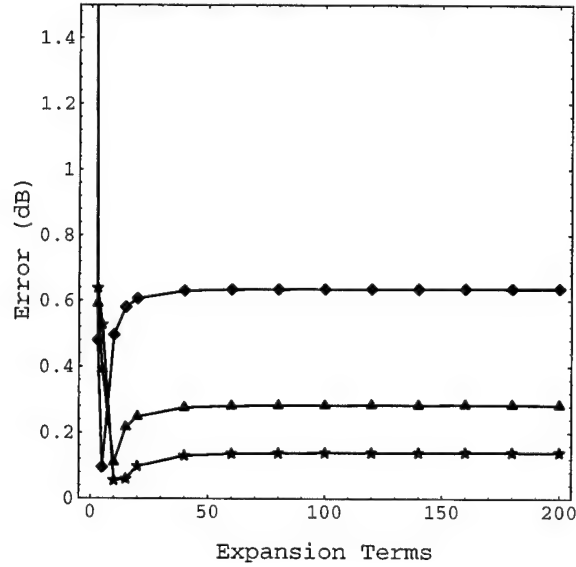


Figure 4-7: Error vs. expansion terms for a  $35\mu m$  thick conductor with  $\sigma = 5.8 \times 10^5 \Omega^{-1}m^{-1}$ ;  $\Delta = .005 m$  (diamond),  $\Delta = .0025 m$  (triangle),  $\Delta = .00125 m$  (star).

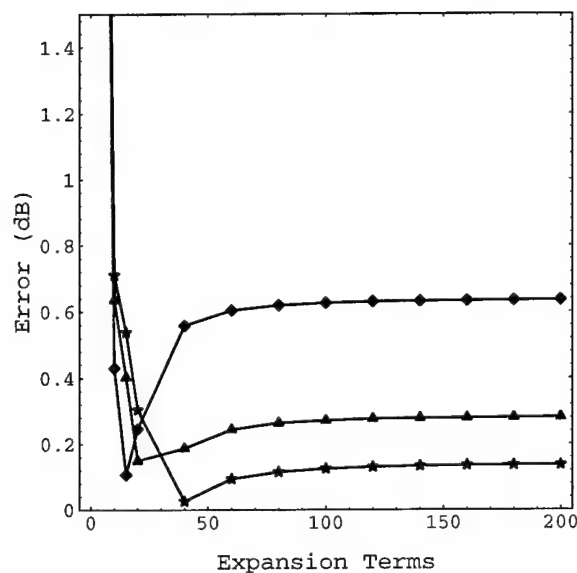


Figure 4-8: Error vs. expansion terms for a  $35 \mu m$  thick conductor with  $\sigma = 5.8 \times 10^6 \Omega^{-1}m^{-1}$ ;  $\Delta = .005 m$  (diamond),  $\Delta = .0025 m$  (triangle),  $\Delta = .00125 m$  (star).

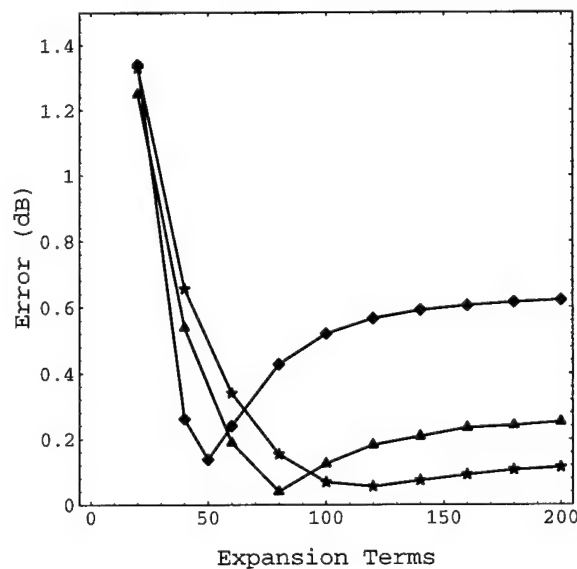


Figure 4-9: Error vs. expansion terms for a  $35 \mu m$  thick conductor with  $\sigma = 5.8 \times 10^7 \Omega^{-1}m^{-1}$ ;  $\Delta = .005 m$  (diamond),  $\Delta = .0025 m$  (triangle),  $\Delta = .00125 m$  (star).

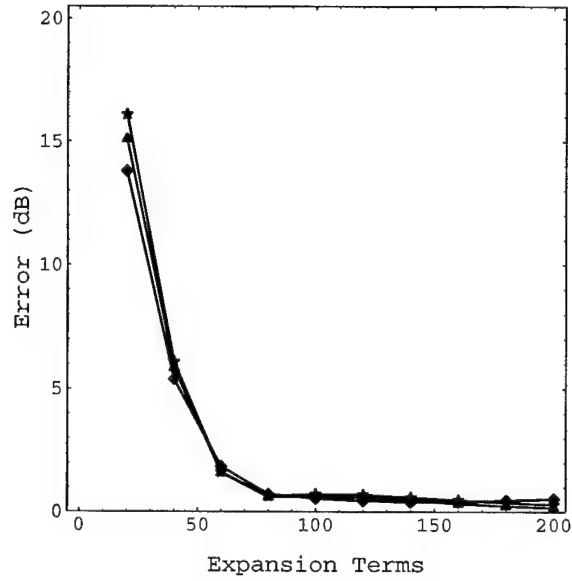


Figure 4-10: Error vs. expansion terms for a  $35 \mu m$  thick conductor with  $\sigma = 5.8 \times 10^8 \Omega^{-1}m^{-1}$ ;  $\Delta = .005 m$  (diamond),  $\Delta = .0025 m$  (triangle),  $\Delta = .00125 m$  (star).

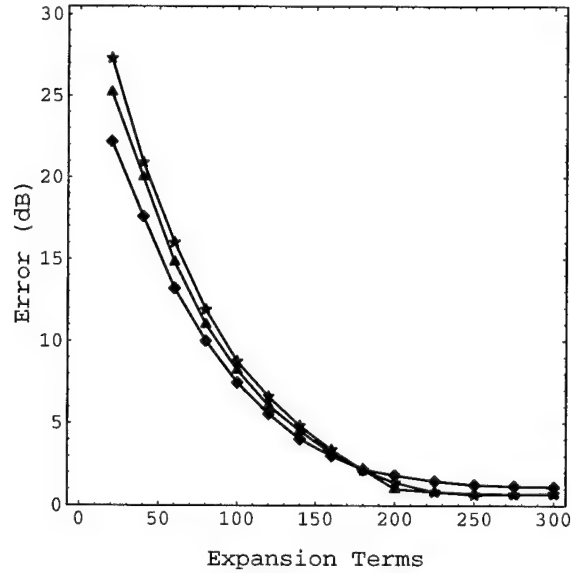


Figure 4-11: Error vs. expansion terms for a  $35 \mu m$  thick conductor with  $\sigma = 5.8 \times 10^9 \Omega^{-1}m^{-1}$ ;  $\Delta = .005 m$  (diamond),  $\Delta = .0025 m$  (triangle),  $\Delta = .00125 m$  (star).

magnitude of main term in the piecewise constant IBC formulation,  $e^{A_m \Delta t} - 1$ , and plot it versus expansion number at the three time steps of Figure 4-12 as shown in Figure 4-15. Figure 4-15 shows that we should expect a leveling off of the error since the IBC term levels off rather quickly. Since the exponential term is proportional to the square of the expansion term number, it follows that the influence of the term will quickly decrease. Furthermore, the other factors in the exponential term should show similar results. As the conductivity decreases the number of strong influential terms decreases (Figures 4-6 through 4-11). As the conductor thickness increases the number of influential terms also increases (Figure 4-16).

There are essentially two approximations that contribute to the transmissivity error. The first is from the approximation of the impedance by a sum of exponentials, and the other is from the approximation to the convolution integral. The two convolution approximations used are piecewise constant and piecewise linear. When few expansion terms are used, the impedance error is the dominant error. As the number of terms increases, the impedance error decreases. In fact, it should approach zero as  $m \rightarrow \infty$ . Therefore, as  $m$  becomes sufficiently large, the convolution integral approximation error will dominate the overall error and increasing  $m$  will not improve the error. This is clearly evident in Figure 4-14 as seen by the leveling of the error curves at some small but finite error as  $m$  increases. The optimum settings evident in the piecewise constant must result from the combination of the two types of errors, and the piecewise linear error is evidently sufficiently small such that it does not produce an optimum setting.

Depending on the problem being considered, a non-optimum number of expansion terms may not lead to significant error since the errors are still small. However, if the problem includes many reflections from the IBC as in resonant cavities, the optimum number of terms should be considered when using the piecewise constant formulation.

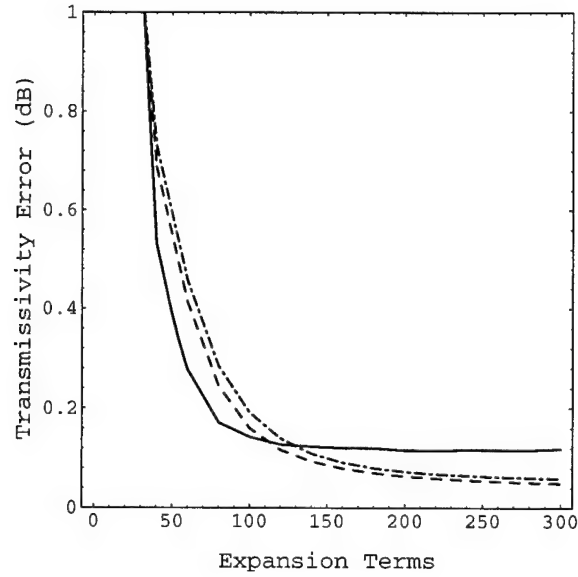


Figure 4-12: Piecewise linear error vs. expansion terms for a  $35\text{ }\mu\text{m}$  thick conductor with  $\sigma = 5.8 \times 10^7\text{ }\Omega^{-1}\text{m}^{-1}$ ;  $\Delta = .005\text{ m}$  (solid),  $\Delta = .0025\text{ m}$  (dash),  $\Delta = .00125\text{ m}$  (dash-dot).

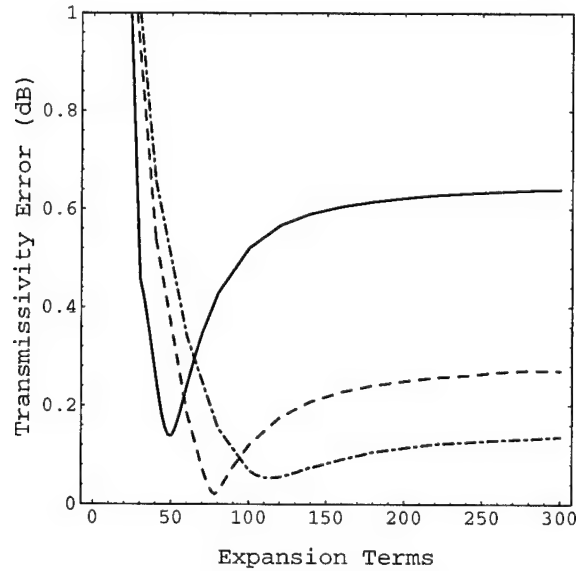


Figure 4-13: Piecewise constant error vs. expansion terms for a  $35\text{ }\mu\text{m}$  thick conductor with  $\sigma = 5.8 \times 10^7\text{ }\Omega^{-1}\text{m}^{-1}$ ;  $\Delta = .005\text{ m}$  (solid),  $\Delta = .0025\text{ m}$  (dash),  $\Delta = .00125\text{ m}$  (dash-dot).

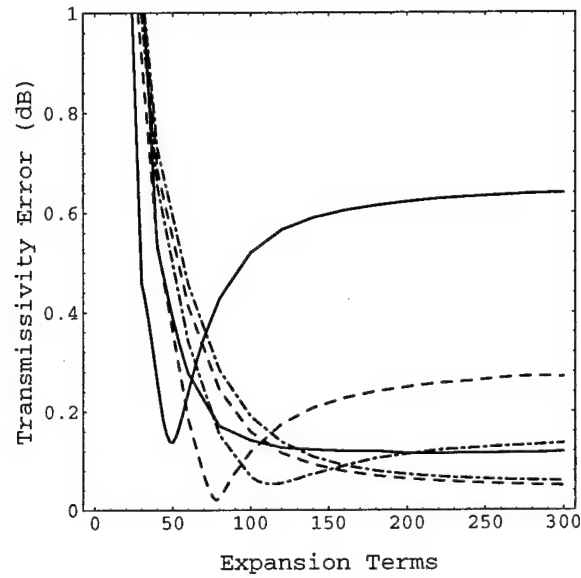


Figure 4-14: Comparison of error behavior of piecewise constant IBC and piecewise linear IBC for a  $35 \mu m$  thick conductor with  $\sigma = 5.8 \times 10^7 \Omega^{-1}m^{-1}$ ;  $\Delta = .005 m$  (solid),  $\Delta = .0025 m$  (dash),  $\Delta = .00125 m$  (dash-dot).

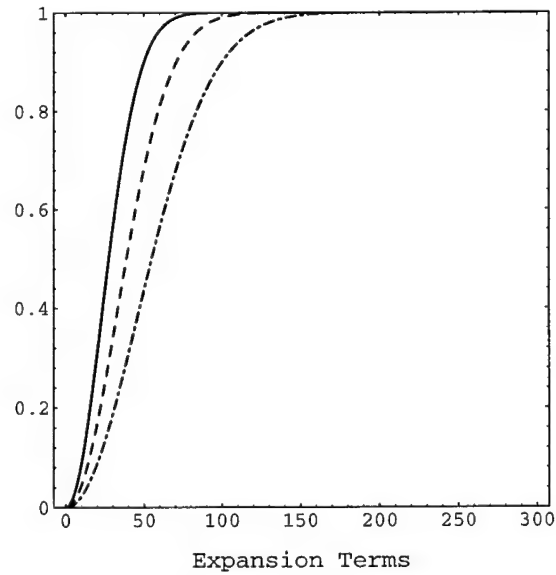


Figure 4-15: Magnitude of piecewise constant IBC term,  $|e^{A_m \Delta t} - 1|$ , vs. expansion terms for a  $35 \mu m$  thick conductor with  $\sigma = 5.8 \times 10^7 \Omega^{-1}m^{-1}$ ;  $\Delta t = \frac{.005 m}{2c}$  (solid),  $\Delta t = \frac{.0025 m}{2c}$  (dash),  $\Delta t = \frac{.00125 m}{2c}$  (dash-dot).

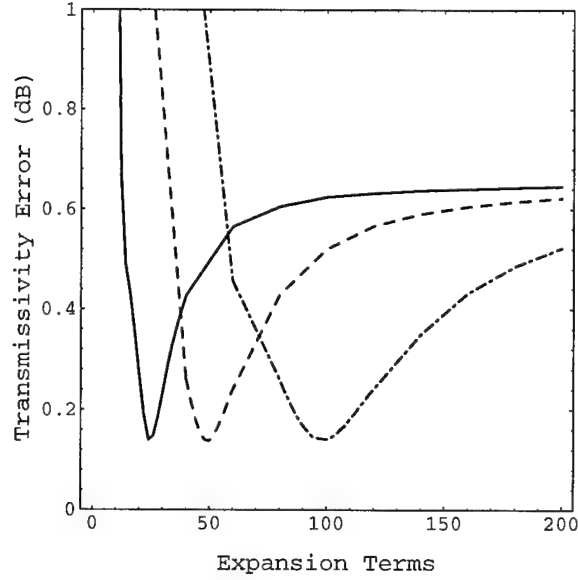


Figure 4-16: Piecewise constant error vs. expansion terms for various conductor thicknesses with  $\Delta = .005 m$  and  $\sigma = 5.8 \times 10^7 \Omega^{-1} m^{-1}$ ;  $l = 17.5 \mu m$  (solid),  $l = 35 \mu m$  (dash),  $l = 70 \mu m$  (dash-dot).

## 4.7 Verification of IBC in Two Dimensions

Measurement of the quality factor of resonant structures is used to verify the multi-dimensional IBC. This method is desirable for two reasons. First, it is the very small but finite loss that a good conductor exhibits that causes errors in FDTD simulations where good conductors are represented by perfect conductors. Second, the measurement is based on many reflections from the cavity's surfaces and should give a good indication of the accuracy and thus the benefit of this type of IBC.

### 4.7.1 Calculation of Quality Factor

An analytical approximation for the quality factor of a resonant cavity is used for the comparison against the FDTD IBC. Using the nomenclature and derivation found in [138], the essential ideas follow.

The quality factor of  $Q$  is a measure of the loss of a resonant cavity. Let  $w_{T_n}(t)$

represent the total electromagnetic energy of a mode  $n$  within a resonant cavity. The energy can be approximated by

$$w_{T_n}(t) = w_{T_n}(0)e^{\frac{-\omega_n t}{Q_n}} \quad (4.39)$$

where  $\omega_n$  is the resonant frequency in radians of the  $n$ th mode. So using the definition in [138], the quality factor is the average number of radians it takes for the total electromagnetic energy to decay to  $\frac{1}{e}$  of its original value. The higher the  $Q$  the lower the loss. The quality factor can be determine from the average power dissipated within the structure and the average electromagnetic energy stored within the structure given by

$$Q_n = \frac{\omega_n \times \text{energy stored in } n\text{th mode}}{\text{average power dissipated in } n\text{th mode}} = \frac{\omega_n w_{T_n}}{\langle P_n \rangle}. \quad (4.40)$$

The power lost in the resonant structures used in this chapter are a result of the current flowing through the walls of the cavity. So to calculate the  $Q$  of the resonant structure under test we must calculate the following two integrals:

$$w_{T_n} = \frac{1}{2} \int_V \epsilon_0 |\bar{E}_n|^2 dv \quad (4.41)$$

and

$$P_n = \frac{1}{2} \int_V \bar{E}_n \cdot \bar{J}_n^* dv. \quad (4.42)$$

As in [138], since we're dealing with very large conductivities perturbation methods can be used. The current can be approximated by the current generated in a perfect conductor. So the power calculation of (4.42) becomes

$$P_n \simeq \frac{1}{2} \int_V \frac{|\bar{J}_n^0|^2}{\sigma} dv, \quad (4.43)$$

where  $\bar{J}_n^0$  represents the current in a resonator with PEC walls. Again using the *good* conductor approximation, most of the current flows within one skin depth of the



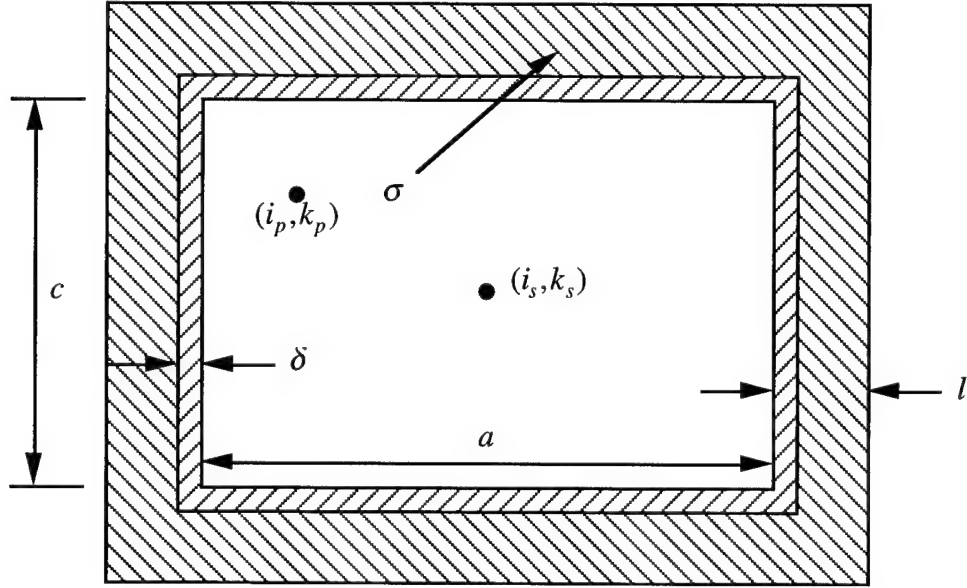


Figure 4-17: Test structure for IBC validation.

conductor, where the skin depth,  $\delta$  is defined by

$$\delta = \sqrt{\frac{2}{\omega_n \mu_0 \sigma}}, \quad (4.44)$$

and the current can be approximated by assuming that the current is equivalent to the surface current of a perfect conductor uniformly distributed over a single skin depth, so equation 4.43 becomes

$$P_n \simeq \frac{1}{2\sigma\delta} \int_A |\bar{J}_{sn}^0|^2 da, \quad (4.45)$$

where  $A$  is the inside surface of the resonator and  $\bar{J}_{sn}^0$  is the surface current due to the  $n$ th mode in a PEC resonator. Figure 4-17 is a schematic of the test structure used to validate the two dimensional IBC. The test structure is a rectangular resonating cavity made with a good conductor with conductivity,  $\sigma$ , with dimensions (in meters)  $a$  in the  $x$  direction and  $c$  in the  $z$  direction. The thickness of the thin conducting sheet is  $l$  m and the skin depth is  $\delta$  m. (The figure is not drawn to scale  $l \ll a, c$ .)

The cavity is excited with  $TE$  modes by using a line source located at  $(i_s, k_s)$  on a discretized FDTD grid and the response is measured with a software probe at  $(i_p, k_p)$  that records  $E_y(i_p, k_p)$  at each time step.

For the power and energy calculations we assume infinite extent in the  $y$  direction and therefore the energy and power units are all described per meter.

With Figure 4-17 in mind the power dissipated per meter is given by

$$\begin{aligned} P_n &= 2 \frac{1}{2\sigma\delta} \int_0^a |\hat{z} \times \bar{H}_n^0(z=0)|^2 dx \\ &+ 2 \frac{1}{2\sigma\delta} \int_0^c |\hat{x} \times \bar{H}_n^0(x=0)|^2 dz. \end{aligned} \quad (4.46)$$

Given a TE excitation ( $E_y$ ), the mode can be described by

$$E_y(x, z) = E_o \sin k_x x \sin k_z z, \quad (4.47)$$

where  $k_x = \frac{m\pi}{a}$ , and  $k_z = \frac{p\pi}{c}$ . The magnetic fields can be found from Maxwell's equations and (4.47). They are

$$H_x(x, z) = i \frac{k_z}{\omega\mu_o} E_o \sin k_x x \cos k_z z \quad (4.48)$$

and

$$H_z(x, z) = -i \frac{k_x}{\omega\mu_o} E_o \cos k_x x \sin k_z z. \quad (4.49)$$

Using (4.48) and (4.49) in (4.46) the power becomes

$$\begin{aligned} P_{m,p} &= \frac{|E_o|^2}{2\sigma\delta\omega_{m,p}^2\mu_o^2} [ak_z^2 + ck_x^2] \\ &= \frac{|E_o|^2\pi^2}{2\sigma\delta\omega_{m,p}^2\mu_o^2 a^2 c^2} [m^2 a^3 + p^2 c^3]. \end{aligned} \quad (4.50)$$

The total electromagnetic energy is calculated from (4.41) and (4.47), resulting in

$$w_{t_{m,p}} = \frac{ac}{8} \epsilon_0 |E_0|^2. \quad (4.51)$$

Substitution of (4.50) and (4.51) into (4.40) yields

$$Q_{m,p} = \frac{\epsilon_0 \sigma \delta \omega_{m,p}^3 \mu_0^2 a^3 c^3}{4\pi^2 [m^2 a^3 + p^2 c^3]}, \quad (4.52)$$

substituting  $\omega_{m,p}^2 \epsilon_0 \mu_0 = k_{m,p}^2 = k_x^2 + k_z^2 = \pi^2 \left( \frac{1}{a^2} + \frac{1}{c^2} \right)$  we arrive at

$$Q_{m,p} = \frac{(a^2 m^2 + c^2 p^2) ac}{2\delta [m^2 a^3 + p^2 c^3]}. \quad (4.53)$$

The quality factor of a good conductor resonator is a function of the mode number, skin depth, and the physical dimensions of the resonator.

### 4.7.2 Measurement of Quality Factor in FDTD Simulations

There are two ways to measure the quality factor in a FDTD simulation. The first is to take the Fourier transform of the electric field measured by the software probe. By measuring the half-power bandwidth about the resonator's resonant frequencies, the quality factor can be derived [138], [140]. However, this method will require millions of time steps for very high  $Q$  structures. A more practical method relies on exciting a single mode and measuring the decay in the mode's field strength measured by the software probe. In the lossy resonator, the resonant frequencies are better described in the  $s$  domain,  $s_{m,p} = -i\omega_{m,p} - \alpha_{m,p}$ . Since the energy is proportional to the magnitude of the electric field squared, equation (4.39) can be rewritten as

$$w_{T_{m,p}}(t) = w_{T_{m,p}}(t=0) e^{-2\alpha_{m,p}t}, \quad (4.54)$$

MSiemans	$l/\delta$	$Q_{FDTD}$	$Q$	% error
.058	.92	801.5	922.0	-13.1
.58	2.92	2950.4	2915.5	+1.2
5.8	9.22	9220.3	9219.7	0.0
58.0	29.16	30365.7	29155.2	+3.8
580	92.20	100939.0	92196.8	+9.4

Table 4.1: Comparison of  $Q_{FDTD}$  and analytic  $Q$  at 3.03 GHz

and the quality factor becomes

$$Q_{m,p} = \frac{\omega_{m,p}}{2\alpha_{m,p}}. \quad (4.55)$$

If a single mode is excited in the FDTD simulation,  $\alpha_{m,p}$  can be calculate from two peaks in the stored electric field, given by

$$\alpha_{m,p} = -\frac{\ln[E_y^{n_2}/E_y^{n_1}]}{(n_2 - n_1)\Delta t} \quad (4.56)$$

### 4.7.3 2D Simulations and Results

The impedance boundary condition is extended to two-dimensions. Using the test structure in Figure 4-17 the dimensions of the structure are changed to vary the frequency. The current source is placed at the center of the structure and the probe is off center. A modulated gaussian pulse, modulated at the  $TE_{1,1}$  resonant frequency with  $\beta = 4096$ , is used as the temporal excitation. The software probe stores the electric field at each time step. Equation (4.56) is used to measure  $\alpha_{1,1}$  and equation (4.55) is used to measure  $Q_{FDTD}$ . The simulated results are compared to the analytically derived values of  $Q$ . Tables 4.1- 4.4 show the results. Each table represents a different frequency and each table spans four orders of magnitude of conductivity. The tabular results are shown graphically in Figure 4-18.

MSiemans	$l/\delta$	$Q_{FDTD}$	$Q$	% error
.058	1.30	693.5	652.0	+6.4
.58	4.12	2019.6	2061.6	-2.0
5.8	13.04	6521.0	6519.3	0.0
58.0	41.23	20855.4	20615.8	+1.2
580	130.39	63140.3	65193.0	-3.1

Table 4.2: Comparison of  $Q_{FDTD}$  and analytic  $Q$  at 6.06 GHz

MSiemans	$l/\delta$	$Q_{FDTD}$	$Q$	% error
.058	1.64	518.8	455.4	+13.9
.58	5.18	1399.0	1440.2	-2.9
5.8	16.40	4574.4	4554.2	+0.4
58.0	51.85	14502.5	14401.7	+0.7
580	163.95	45889.3	45542.1	+0.8

Table 4.3: Comparison of  $Q_{FDTD}$  and analytic  $Q$  at 9.6 GHz

MSiemans	$l/\delta$	$Q_{FDTD}$	$Q$	% error
.058	1.84	501.0	461.0	+8.7
.58	5.83	1401.8	1457.8	-3.8
5.8	18.44	4642.0	4609.8	+0.7
58.0	58.31	14430.6	14577.6	-1.0
580	184.39	44324.1	46098.4	-3.8

Table 4.4: Comparison of  $Q_{FDTD}$  and analytic  $Q$  at 12.1 GHz

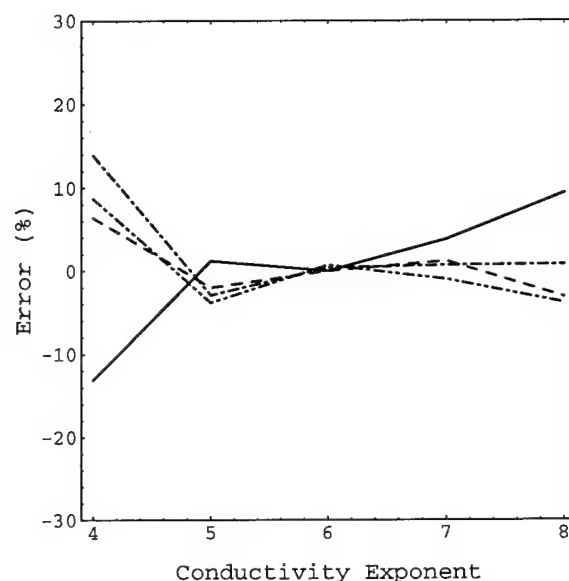


Figure 4-18: 2D resonator quality factor percent error versus conductivity exponent,  $x$  in  $5.8 \times 10^x \Omega^{-1}m^{-1}$ ; 3.03 GHz (solid), 6.06 GHz (dash), 9.60 GHz (dash-dot), 12.10 GHz (dash-dot-dot).

## 4.8 Discussion

The conductivity range studied in this chapter spanned four orders of magnitude from  $10^4$  to  $10^8 \Omega^{-1}m^{-1}$ . (Some work at  $10^9$  was done in Section 4.6.2.) Even the lowest conductivity used would be considered a good conductor at the frequencies tested as defined by  $1 \ll \frac{\sigma}{\omega\epsilon}$ . The conductivities, in  $\Omega^{-1}m^{-1}$ , of the most popular signal conductors, silver, copper, gold and aluminum are  $6.14 \times 10^7$ ,  $5.80 \times 10^7$ ,  $4.10 \times 10^7$ , and  $3.54 \times 10^7$  and the conductivity of steel is  $3.54 \times 10^7$  which all easily fall within the range of conductivities tested.

When a piecewise constant approximation is used for the magnetic field, the amount of computer resources (as measured by number of expansion terms) is directly proportional to the conductivity. Lower conductivities result in larger pole magnitudes and lesser sensitivity to increase number of terms. The piecewise constant approximation produces an error that cannot be overcome by more expansion

terms. In fact, the errors from the impedance approximation and the magnetic field approximation combine to produce an optimum number of expansion terms.

With a piecewise linear approximation, the error due to the magnetic field is greatly reduced and an optimum number of terms is not evident. The more terms used the more accurate the IBC; however, the error levels off at 200 terms in the test of the copper sheet in Section 4.6.3.

When extended to two dimensions, except for the lowest conductivity of  $\sigma = 5.8 \times 10^4 \Omega^{-1}m^{-1}$  the impedance boundary condition works incredibly well over the wide range of skin depths studied,  $3 \rightarrow 185$ . The IBC is an excellent model for thin sheets of good conductors with finite conductivity. The IBC offers the advantage of working over a wide range of frequencies with very little computational overhead. For typical conductors, like copper, 125 terms per tangential electric field component are needed with errors in  $Q$  less than 5%.

## Chapter 5

# Phase Unwrapping of Synthetic Aperture Radar (SAR) Interferometry

### 5.1 Introduction

Airborne and spaceborne Synthetic Aperture Radar (SAR) platforms have been used for many years to study the earth's surface [144]-[159]. When two radars on a single platform or two passes of a single radar map the same area, an interferogram can be produced from the difference in phase measured by each radar or pass. An interferogram is a pictorial representation of the phase differences measured at each pixel.

Since the measured phase differences lie between  $-\pi$  and  $\pi$ , the phase is said to be *wrapped*. A SAR interferogram contains *fringes*. These fringes are the locations on the interferogram where a  $2\pi$  discontinuity exists. The interferogram resembles a topographical contour map where a line of constant elevation corresponds to a fringe. When no noise is present, the fringes can easily be located and the data adjusted by adding multiples of  $2\pi$  to produce an *unwrapped* phase image. However, real-



world data are always contaminated with noise, hence there is a need to develop sophisticated phase unwrapping algorithms.

Successful phase unwrapping is the key to the extraction of DEM (digital elevation model) from an interferometric SAR phase image. There are local and global methods to unwrap phase data. Local methods unwrap a pixel based only on its nearest neighboring pixels; whereas global methods consider the whole set of pixels to be unwrapped. Phase unwrapping has been a topic of much research [160] -[175].

Local or global aside, there are really two basic approaches to unwrapping phase data. The first is based on finding an unwrapped solution such that the solution's first-order partial derivatives in the  $x$  and  $y$  directions match (or closely match) the wrapped first-order partial derivatives or gradients of the phase data. Typically noise is handled by unwrapping the *best* data first in local schemes, or in global schemes, like the least squares method, the data is weighted to favor the *best* data. The second approach moves along the data and adds or subtracts  $2\pi$  when a fringe is crossed. The fringes are found with a *fringe detection* scheme [155]. With this method, one way to handle the noise is to form branch cuts. This way the image is searched for phase inconsistencies, in the form of *residues*. The residues are connected to form branch cuts and phase is unwrapped by adjusting the integration path or by modifying the fringe information.

There are local and global techniques to phase unwrapping algorithms based on the gradients of measured data. The local algorithms usually locate one or more areas on the image that are considered *good* data. To find these points one may use noise floor data and signal-to-noise ratio [168] or use coherence data [178], [166]. Unwrapping usually begins with these *good* areas. The algorithms move from pixel to pixel and add or subtract  $2\pi$  based on some criteria. One method follows the least-gradient path with the assumption that the smallest gradient points to the best data [178], [180] and the adjustments are made to match the solution gradient to the wrapped measured gradient. Other methods use more neighbors to decide the value to add to

the unwrapped pixel [161], [169]. Here all the gradients of the adjacent unwrapped pixels are examined and the phase of the unwrapped pixel is predicted based on these gradients. Then an integer number of  $2\pi$  is added to bring the unwrapped pixel closest to the predicted phase. In this way it is possible to have phase differences larger than  $\pi$ , so this method can accommodate *real* discontinuities due to terrain features. All of these local approaches have the added complication of growing separate unwrapped regions that must be joined to produce the final product. Since the *best* pixels are unwrapped first, the likelihood of errors propagating through the image is reduced.

Global gradient algorithms are based on least squares and weighted least squares methods [170]. In this way, the technique attempts to find a solution that minimizes the differences between all of the solution's gradients and the wrapped data's gradients. The least squares approach is very desirable because of the speed at which all the data can be unwrapped, but, the method cannot treat noisy data very well [170]. The weighted least squares allows the user to favor the *good* data by applying a set of weights to the data based on some knowledge of the data's noise content. These methods have been applied to a single SAR interferogram in [160]; however, no details of the weighting criteria was presented. Others have used a weighted least squares method to unwrap a simulated interferogram with a shear [162], where the shear discontinuity was masked out and a multi-grid iteration scheme was used to solve the weighted partial differential equation. A weighted least squares technique has been used to unwrap speckle interferograms using a weighting scheme based on masking out the phase inconsistencies or residues [171].

The branch cut method also has local and global approaches. So far only local approaches have been reported in SAR interferometry. The branch cut method and SAR interferometry phase unwrapping was first reported in [173]. Applied to the interferogram derived from two passes of Seasat, the residue connection was based on a *nearest neighbor* approach. This technique works well with a low density of residues; however, it breaks down with a high density of residues [173]. Once two residues are

connected they are removed and no longer considered for connection to any other residues. This method is very likely to leave an uncompensated residue. The phase is then unwrapped by integrating along a path that never crosses a branch cut. This approach was briefly reported in [160] as part of an overview of SAR phase unwrapping techniques. It was reported that the main disadvantage to the branch cut method is the propagation of global errors from uncompensated residues. A modification to the basic branch cut method in SAR interferometry involves connecting and removing residue pairs that are only 1 or 2 pixels apart [163]. The remaining residues are handled separately and considered part of *real* discontinuities that exist as a result of terrain features.

The branch cut method has also been applied to speckle interferometry, used to measure very small surface deformations on structures. In this application, a nearest neighbor (local) connection algorithm was used and reported in [174]. The first global branch cut method is used to unwrap a speckle interferogram. All residues are considered before making any branch cuts. In this way, the algorithm is based on minimizing the total branch-cut length [175].

Finding efficient, accurate and automatic phase unwrapping algorithms is an interesting topic and is becoming more important as more processing occurs on the SAR platform. Although some new phase unwrapping techniques have been briefly introduced recently based on the principle of maximum entropy [164] and multiresolution [165], they have not been used as yet on SAR data. In this chapter, the weighted least squares approach is investigated and applied to SAR interferometry. Specifically, the a hybrid method that uses branch cut residues to weight the data is presented and compared to weighting schemes based on coherence data. Also, *optimum* global and local branch cut algorithms are presented and applied to SAR interferograms. Data from both simulated and real SAR interferograms are used.

## 5.2 Least Squares Phase Unwrapping Technique

The least squares approach attempts to minimize the difference between the wrapped derivatives of the measured data and the derivatives of the solution. It turns out that through a little manipulation the least squares problem can be constructed to form a discretized Poisson equation where the source term is calculated from the wrapped data. The equation can be solved with the discrete cosine transform (DCT) offering a fast and fully automatic algorithm.

Consider an  $M \times N$  matrix of wrapped phase values. The  $(i, j)$ th element of the wrapped phase matrix will be represented by  $\phi_{i,j}^w$ . The goal is to find the actual (unwrapped) phase,  $\phi_{i,j}$ , based on the measured wrapped phase.

First, a wrapping operator,  $W \{ \}$ , must be defined such that

$$W \{x\} = x + k2\pi, \quad (5.1)$$

where  $k$  is any integer that satisfies

$$-\pi \leq x + k2\pi \leq \pi. \quad (5.2)$$

The wrapped phase values may be described in terms of the unwrapped phase values by

$$\phi_{i,j}^w = W \{ \phi_{i,j} + n_{i,j} \} \quad (5.3)$$

where  $n_{i,j}$  is the noise associated with pixel  $(i, j)$ . The least squares method uses the first order wrapped differences of the data given by

$$\Delta_{i,j}^x = \begin{cases} W \{ \phi_{i+1,j}^w - \phi_{i,j}^w \} & 0 \leq i \leq M-2; 0 \leq j \leq N-1 \\ 0 & \text{otherwise} \end{cases}, \quad (5.4)$$

and

$$\Delta_{i,j}^y = \begin{cases} W \{ \phi_{i,j+1}^w - \phi_{i,j}^w \} & 0 \leq i \leq M-1; 0 \leq j \leq N-2 \\ 0 & \text{otherwise} \end{cases}. \quad (5.5)$$

The solution  $\phi_{i,j}$  is the set of all  $\phi_{i,j}$  such that the sum of all the squares of the differences between the solution phase differences,  $\phi_{i+1,j} - \phi_{i,j}$  and  $\phi_{i,j+1} - \phi_{i,j}$ , and the measured phase differences,  $\Delta_{i,j}^x$  and  $\Delta_{i,j}^y$ , is a minimum. In other words,  $\phi_{i,j}$  is the least squares solution to

$$\sum_{i=0}^{M-2} \sum_{j=0}^{N-1} (\phi_{i+1,j} - \phi_{i,j} - \Delta_{i,j}^x)^2 + \sum_{i=0}^{M-1} \sum_{j=0}^{N-2} (\phi_{i,j+1} - \phi_{i,j} - \Delta_{i,j}^y)^2. \quad (5.6)$$

Equation (5.6) can be formulated as a discretized Poisson equation with the wrapped data as the basis of the source term. In continuous space the Poisson equation is

$$\frac{\partial^2}{\partial x^2} \phi(x, y) + \frac{\partial^2}{\partial y^2} \phi(x, y) = \rho(x, y) \quad (5.7)$$

where  $\phi(x, y)$  is the continuous phase function and  $\rho(x, y)$  is a continuous source term. The discretize form, given the sampled phase values, is

$$(\phi_{i+1,j} - 2\phi_{i,j} + \phi_{i-1,j}) + (\phi_{i,j+1} - 2\phi_{i,j} + \phi_{i,j-1}) = \rho_{i,j} \quad (5.8)$$

where

$$\rho_{i,j} = (\Delta_{i,j}^x - \Delta_{i-1,j}^x) + (\Delta_{i,j}^y - \Delta_{i,j-1}^y). \quad (5.9)$$

For those source values that lie on the edge of the domain the phase differences are set to zero as (5.4) and (5.5) indicate. Essentially a Neumann boundary condition is imposed. Now that a discrete Poisson equation has been constructed the solution can be found with the use of the Discrete Cosine Transform (DCT). Using cosine series expansions for the unknowns leads to a very simple solution technique. The DCT

and Inverse DCT pair,  $x_{i,j} \Leftrightarrow C_{m,n}$ , are defined as

$$C_{m,n} = \begin{cases} \sum_{i=0}^{M-1} \sum_{j=0}^{N-1} 4x_{i,j} \cos \left[ \frac{\pi}{2M} m(2i+1) \right] \cos \left[ \frac{\pi}{2N} n(2j+1) \right] & 0 \leq m \leq M-1; \quad 0 \leq n \leq N-1; \\ 0 & \text{otherwise} \end{cases}, \quad (5.10)$$

and

$$x_{i,j} = \begin{cases} \frac{1}{MN} \sum_{m=0}^{M-1} \sum_{n=0}^{N-1} 4w_1(m)w_2(n)C_{m,n} \cos \left[ \frac{\pi}{2M} m(2i+1) \right] \cos \left[ \frac{\pi}{2N} n(2j+1) \right] & 0 \leq i \leq M-1; \quad 0 \leq j \leq N-1; \\ 0 & \text{otherwise} \end{cases}, \quad (5.11)$$

where

$$\begin{aligned} w_1 &= 1/2, \quad m = 0, \\ w_1 &= 1, \quad 1 \leq m \leq M-1, \\ w_2 &= 1/2, \quad n = 0, \\ w_2 &= 1, \quad 1 \leq n \leq N-1, \end{aligned} \quad (5.12)$$

Substituting the cosine expansions into (5.8) leads to

$$\hat{\phi}_{i,j} = \frac{\hat{\rho}_{i,j}}{2 \left( \cos \frac{\pi i}{M} + \cos \frac{\pi j}{N} \right)}, \quad (5.13)$$

where  $\hat{\phi}_{i,j}$  and  $\hat{\rho}_{i,j}$  are the discrete cosine transforms of  $\phi_{i,j}$  and  $\rho_{i,j}$ .

The solution may be found by performing a 2D DCT on the source term, modifying the transformed source term by using the right hand side of (5.13), and performing an inverse DCT on the modified source term to arrive at the solution  $\phi_{i,j}$ . Very fast DCT algorithms have been developed based on the Fast Fourier Transform [143] and can be used to unwrap phase very quickly.

The disadvantage to the least squares method is that it does not consider the integrity of the data. If only a small localized portion of the interferogram is corrupted by noise, the entire unwrapped image is effected [170]. In other words, a local error

will propagate throughout the image.

## 5.3 Weighted Least Squares Phase Unwrapping Technique

The least squares solution to phase unwrapping assumes that the noise associated with each pixel is Gaussian and independent [143]. The assumptions will not always apply to the noise in a SAR interferogram. Applying a weighting scheme attempts to incorporate the knowledge of the interferogram's pixel integrity when unwrapping the phase.

### 5.3.1 Weighted Least Squares

If we suspect that a measured phase value is corrupted with noise or otherwise unreliable, as assumed in real data, we can weight that phase value,  $\phi_{i,j}^w$  by  $w_{i,j}$  where

$$0.0 \leq w_{i,j} \leq 1.0. \quad (5.14)$$

The *best* values are assigned weights of one or close to one whereas the *worst* data are assigned weights near zero. Although the weighted least squares problem cannot directly be solved with the Discrete Cosine Transform, Ghiglia *et al.* [170] showed how an iterative approach can be constructed to take advantage of the DCT. Instead of a source term based solely on the measured data, a new source term built with a weighted sum of the measured data's first derivatives and the current iteration's first derivative is used.

The first order differences of the data are weighted by  $f_{i,j}^{x,y}$  such that

$$f_{i,j}^x = \min(w_{i+1,j}^2, w_{i,j}^2) \quad (5.15)$$

and

$$f_{i,j}^y = \min(w_{i,j+1}^2, w_{i,j}^2). \quad (5.16)$$

The portion of the source term based on the data,  $\rho_{i,j}^d$ , is given by

$$\rho_{i,j}^d = (f_{i,j}^x \Delta_{i,j}^x - f_{i-1,j}^x \Delta_{i-1,j}^x) + (f_{i,j}^y \Delta_{i,j}^y - f_{i,j-1}^y \Delta_{i,j-1}^y) \quad (5.17)$$

and the contribution from the current iteration's solution,  $\rho_{i,j}^{s(k)}$ , is given by

$$\begin{aligned} \rho_{i,j}^{s(k)} = & (1 - f_{i,j}^x)(\phi_{i+1,j}^{k-1} - \phi_{i,j}^{k-1}) - (1 - f_{i-1,j}^x)(\phi_{i,j}^{k-1} - \phi_{i-1,j}^{k-1}) \\ & + (1 - f_{i,j}^y)(\phi_{i,j+1}^{k-1} - \phi_{i,j}^{k-1}) - (1 - f_{i,j-1}^y)(\phi_{i,j}^{k-1} - \phi_{i,j-1}^{k-1}) \end{aligned} \quad (5.18)$$

so that the  $k$ th solution is found by solving the discretized Poisson's equation with a new source term,

$$\rho_{i,j}^k = \rho_{i,j}^d + \rho_{i,j}^{s(k-1)}. \quad (5.19)$$

Solving the weighted least squares method in this way is known as the Picard Iteration Method and is described in Section 5.3.3. The iterations are performed until a user specified number of iterations are complete. The method is still very fast since it uses the DCT and the total time depends on the number of iterations performed. Note that if all  $w_{i,j} = 1$  then the weighted least squares method becomes the least squares method of Section 5.2.

### 5.3.2 Determining Weights

When using the weighted least squares method for unwrapping interferograms, some scheme must be used to assign the weights to each pixel. In this section, weighting schemes based on coherence data are described.



### Coherence Weighting

The coherence of the image is directly related to the integrity of the data. Given the complex returns from both sensors due to the same place on the earth,  $S_1(i, j)$  and  $S_2(i, j)$ , the coherence,  $\rho$ , of pixel  $(i, j)$  is defined by

$$\rho = \frac{|S_1(i, j)S_2^*(i, j)|}{\sqrt{S_1(i, j)S_1^*(i, j)S_2(i, j)S_2^*(i, j)}} \quad (5.20)$$

The maximum value for the coherence is 1 and the minimum value is 0. Low coherence can be the result of many factors such as thermal noise and processing phase errors. In repeat-pass spaceborne systems, decorrelation can come from different atmospheric conditions during each pass, changes in the terrain between the passes, and from the different viewing positions of the passes[155]. Also the length of the baseline is a critical factor. If the baseline is too large there is a complete loss of coherence and the corresponding phase data is useless for terrain height inversion.

The coherence data is a logical choice for a weight. When coherence weighting is used,  $w_{i,j} = c_{i,j}$  where  $w_{i,j}$  is the weight assigned to pixel  $(i, j)$  and  $c_{i,j}$  is the coherence of pixel  $(i, j)$  of equation (5.20).

### Modified Coherence Weighting

A variant of the straight coherence weighting scheme is to set a coherence threshold,  $c_{thr}$ , in order to give the maximum weight to *good* data. Table 5.1 shows the algorithm used to produced modified coherence weights. Setting  $c_{thr} = 0$  is equivalent to no weighting (*i.e.* a straight least squares method) and setting  $c_{thr} = 1$  is equivalent to straight coherence weighting.

### 5.3.3 Picard Iteration method

As stated, the Picard iteration method is used to solve the weighted least squares problem. Following the description found in [170], starting with the over determined

```

Set threshold  $c_{thr}$ 
If  $c_{i,j} \geq c_{thr}$  then
     $w_{i,j} = 1$ 
else
     $w_{i,j} = c_{i,j}$ 
endif

```

Table 5.1: Algorithm for weight assignments based on coherence data.

problem given by the matrix equation

$$\overline{\overline{A}}\overline{\overline{x}} = \overline{\overline{b}}, \quad (5.21)$$

the least squares solution is found by solving

$$\overline{\overline{A}}^T \overline{\overline{A}}\overline{\overline{x}} = \overline{\overline{A}}^T \overline{\overline{b}}, \quad (5.22)$$

where  $\overline{\overline{x}}$  is the solution vector containing  $MN$  phase values and  $\overline{\overline{b}}$  is a vector containing  $N(M-1) + M(N-1)$  wrapped phase differences. Let  $\overline{\overline{P}} = \overline{\overline{A}}^T \overline{\overline{A}}$  (the discrete Laplacian),  $\overline{\overline{\rho}} = \overline{\overline{A}}^T \overline{\overline{b}}$  (the source term), and  $\overline{\overline{\phi}}$  be the phase vector; then the least squares solution of the phase unwrapping problem is given by

$$\overline{\overline{P}}\overline{\overline{\phi}} = \overline{\overline{\rho}}. \quad (5.23)$$

However, if we apply a set of weights to the wrapped phase differences  $\overline{\overline{b}}$  then (5.21) becomes

$$\overline{\overline{W}}\overline{\overline{A}}\overline{\overline{x}} = \overline{\overline{W}}\overline{\overline{b}}, \quad (5.24)$$

and the solution is found by solving

$$\overline{\overline{A}}^T \overline{\overline{W}}^T \overline{\overline{W}} \overline{\overline{A}}\overline{\overline{x}} = \overline{\overline{A}}^T \overline{\overline{W}}^T \overline{\overline{W}} \overline{\overline{b}}. \quad (5.25)$$

Defining  $\overline{\overline{Q}} = \overline{\overline{A}}^T \overline{\overline{W}}^T \overline{\overline{W}} \overline{\overline{A}}$ ,  $\overline{\overline{c}} = \overline{\overline{A}}^T \overline{\overline{W}}^T \overline{\overline{W}} \overline{\overline{b}}$ , and  $\overline{\overline{\phi}}$  as the phase vector again, the system of equations to solve is

$$\overline{\overline{Q}} \overline{\overline{\phi}} = \overline{\overline{c}}. \quad (5.26)$$

The discrete cosine transform cannot be used to solve (5.26) as written. The Picard method rewrites  $\overline{\overline{Q}}$  as the sum of the discrete Laplacian,  $\overline{\overline{P}}$ , and a difference matrix,  $\overline{\overline{D}}$  such that

$$\overline{\overline{Q}} = \overline{\overline{P}} + \overline{\overline{D}}. \quad (5.27)$$

Substitution of (5.27) into (5.26) and a little algebra, leads to

$$\overline{\overline{P}} \overline{\overline{\phi}} = \overline{\overline{c}} - \overline{\overline{D}} \overline{\overline{\phi}}. \quad (5.28)$$

Equation (5.28) can be solve iteratively using the DCT and

$$\overline{\overline{P}} \overline{\overline{\phi}}_{k+1} = \overline{\overline{c}} - \overline{\overline{D}} \overline{\overline{\phi}}_k, \quad (5.29)$$

since (5.29) is the discrete Poisson equation,

$$\overline{\overline{P}} \overline{\overline{\phi}}_{k+1} = \overline{\overline{\rho}}_k, \quad (5.30)$$

where

$$\begin{aligned} \overline{\overline{\rho}}_k &= \overline{\overline{c}} - \overline{\overline{D}} \overline{\overline{\phi}}_k \\ &= \rho_{i,j}^d + \rho_{i,j}^{s(k)} \end{aligned} \quad (5.31)$$

from equation (5.19).

A disadvantage of the Picard iteration method is that convergence is not guaranteed. The user selects the number of iterations and the algorithm terminates when that iteration number is reached.

## 5.4 Branch Cut Method

The branch cut method is very different from the least squares approach. Instead of forming a set of equations to solve, the solution is derived from integrating the fringes. This approach is intuitively appealing, but offers its own set of difficulties.

Unwrapping phase using the branch cut method begins by constructing a fringe map from the wrapped data. A fringe map records the locations of the  $2\pi$  discontinuities call *fringes*. The wrapped data is unwrapped by moving through the image and integrating the fringes. Whenever a fringe occurs,  $2\pi$  is either added or subtracted to the data depending on the value of the fringe. In the presence of noise, erroneous fringes occur and cause errors to propagate through the image. If phase inconsistencies can be found then steps can be taken to reduce the effects of the noise. Since we know that there should be an equal number of positive and negative fringes if we travel around a closed contour, we can search for phase inconsistencies by integrating the along a closed contour. If the integration is non-zero then the contour must enclose residues. The presence of residues means the unwrapped solution is path dependent. To isolate the residues, we integrate along the smallest contour possible *i.e.* between four adjacent data points. In order to remove the ambiguity of the integration path the residues of opposite sign are connected to form branch cuts. The phase fringe map is then modified by incorporating branch cuts and the phase is unwrapped in the normal fashion. There is no global error with proper treatment of the single residues. The disadvantage, however, is that manual operation is usually required to complete the branch point connections.

We begin with another operator  $\bar{d}_{i,j} \{ \}$  defined as

$$\bar{d}_{i,j} = \{ d_{i,j}^x, d_{i,j}^y \}^T, \quad (5.32)$$

where

$$d_{i,j}^x \{ \phi_{i,j}^w \} = \left[ \frac{\phi_{i,j}^w - \phi_{i-1,j}^w}{2\pi} \right], \quad (5.33)$$

and

$$d_{i,j}^y \{ \phi_{i,j}^w \} = \left[ \frac{\phi_{i,j}^w - \phi_{i,j-1}^w}{2\pi} \right]. \quad (5.34)$$

The square brackets,  $[\ ]$ , represent rounding to the nearest integer. The  $\bar{d}_{i,j} \{ \}$  operator will find any  $2\pi$  discontinuities as one moves across the wrapped data in the vertical (along rows,  $d_{i,j}^x$ ) and horizontal (along columns,  $d_{i,j}^y$ ) directions.

If no noise is present and one phase pixel value is known, then the phase at all other pixels can be determine by integrating the number of discontinuities along any path between the known pixel and the pixel of interest. To illustrate, let  $\phi_{i_o, j_o}$  be the known phase value located at  $(i_o, j_o)$ , then

$$\phi_{i,j} = \phi_{i_o, j_o} + k2\pi \quad (5.35)$$

where

$$k = \sum \bar{d}_{i,j} \cdot d\bar{s} \quad (5.36)$$

and  $s$  is any path from  $(i_o, j_o)$  to  $(i, j)$ . If  $s$  is a closed path then  $k$  should equal zero *i.e.* we should end where we begin. Otherwise, there must be noise sources located inside the closed contour  $s$ . With these noise sources or *residues*, the simple integration technique of (5.35, 5.36) will propagate errors throughout the image. Furthermore, the results will depend on the path taken. Clearly the noise must be considered such that a unique solution can be found.

Recall that the branch cut method starts by locating the  $2\pi$  phase discontinuities (or fringes) with the  $\bar{d} \{ \}$  operator. A fringe map is constructed that marks the location of the fringes. Next, the residues are found by integrating the phase differences of four adjacent phase data points using

$$res_{i,j} = d_{i+1,j}^x + d_{i+1,j+1}^y - d_{i+1,j+1}^x - d_{i,j+1}^y. \quad (5.37)$$

If  $res_{i,j} = -1$  we have a *positive* residue and if  $res_{i,j} = 1$  we have a *negative* residue.

These definitions are consistent with the Cauchy Theorem from complex mathematics. After all the residues are located, branch cuts are drawn from the positive residues to the negative residues. The branch cut represents a  $2\pi$  discontinuity. The direction of the discontinuity depends on the direction of the branch cut. For example if a branch cut is pointing down then the branch cut represents a  $+2\pi$  jump when integrating across the branch cut from left to right. Finally the fringe map is updated to reflect the branch cut information and the solution that follows is now path independent.

Although the concept is straightforward, the difficulty of the branch cut method becomes apparent when connecting branch points. Since the residues must be connected in pairs (*i.e.* positive to negative) and there is no guarantee that the interferogram will contain an even number of positive and negative residues, it is very likely that single poles will remain after a branch cut algorithm has been run. Incorrect treatment of these single poles will result in errors.

The question is, given a set of positive and negative residues, what is the best way to connect them? Since noise will create pairs of residues (one positive and one negative) the connection method must favor connections of residues close to each other. If all the residues reside completely within the edges of the SAR interferogram, the connections can be made in a fairly straight forward manner and any errors that result tend to be local in nature. However, in a SAR interferogram the data is truncated and some of the residues's corresponding matches are not included in the SAR interferometry data set. How a connection scheme deals with this problem will determine the algorithm's accuracy.

So far SAR interferometry phase unwrapping has been limited to the local nearest neighbor connection approach [173],[160]. This method can lead to uncompensated residues and has great difficulty when the residue density is high. To alleviate some of these problems a global approach can be used that considers all residues before the connections are made; in other words *optimize* the branch cut connections. In this case, *optimize* means to find the set of branch cuts that has the shortest total branch

cut length.

### 5.4.1 Minimum Branch Cut Algorithm

Given a set of positive and negative residue locations from an interferogram, the minimum branch cut algorithm optimizes the set of connections by finding the set that minimizes the total branch cut length. With a set of  $N$  residue pairs, the algorithm minimizes the quantity defined by

$$l_{tot}^{bc} = \sum_{k=1}^N l_k^{bc}. \quad (5.38)$$

The term,  $l_k^{bc}$ , is the length of the  $k$ th branch cut given by

$$l_k^{bc} = \sqrt{(i_k^n - i_k^p)^2 + (j_k^n - j_k^p)^2}, \quad (5.39)$$

where  $(i_k^p, j_k^p)$  and  $(i_k^n, j_k^n)$  are the pixel locations of the  $k$ th positive and negative residues of branch cut  $k$ .

The optimization algorithm is essentially the same as the *transportation problem* found in Graph Theory or linear programming. In the transportation problem, there are  $m$  locations demanding a commodity and there are  $n$  different transportation means to satisfy all of the demands. The problem is to minimize the total cost given that the unit cost of using the  $i$ th transportation vehicle to ship the commodity to the  $j$ th location is  $c_{i,j}$ . Appendix C gives an overview of the transport problem and how it can be used to find the optimum set of branch cuts.

Before the transport method can be used, the set of residues must be prepared. Given an interferogram, the first step is to find all the residues which we'll call *true* residues. Next, *image* (image meaning opposite in sign) residues are placed at the boundary for every *true* residue within a specified distance from the edge of the interferogram. This distance should be larger than the expected mean branch cut

length [175]. In this work about twice the mean length is used. Once all of the *image* residues are placed, the positive and negative residues are counted. If the count is unequal additional residues are added to the boundary which we will call *false* residues. There must be equal numbers of positive and negative residues in order to perform the optimization. It is important to note that the problem must be constructed so that *false* residues are never allowed to pair up with *true* residues; they can only be paired with *image* residues.

An initial cost matrix is built with the columns representing the negative residues and the rows representing the positive residues. The matrix element  $(i, j)$  is filled with distance between the  $i$ th positive residue and the  $j$ th negative residue using (5.39). (Actually the square of length is used because the transport algorithm used demands integer cost values.)

Now, the matrix is modified to take into account both the boundary *image* residues and the *false* residues. First, all matrix locations that represent connections between any *image* residue with any other opposite *image* residue or *false* residue are set to zero. In this way the algorithm can reduce certain types of errors by being able to connect any boundary residue to any other boundary residue of opposite sign. Second, to ensure no *false* boundary residues are connected to any *true* residue, sufficiently high cost must be inserted into the cost matrix at the appropriate locations. This can easily be done by placing the *false* residues at fictitious locations far away from any actual interferogram pixel.

For each column, the minimum length within the column is subtracted from every entry in the column. This step places a zero in the row of the column that represents the closest positive residues to the  $j$ th negative residue. Then for each row the minimum length within the row is subtracted from every entry in the row. This step places a zero in the column of the row that represents the closest negative residues to the  $i$ th positive residue. Now we have what Buckland [175] called the *reduced cost matrix*.



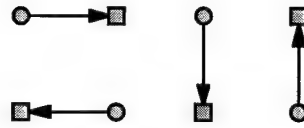


Figure 5-1: Pole connection ambiguity.

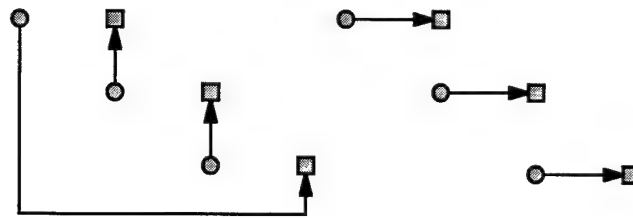


Figure 5-2: Effect of missing one residue in nearest neighbor search.

At this point, the reduced cost matrix is passed to a subroutine based on a minimum cost transport problem found in [181]. The routine will return the optimum set of branch cuts (See Appendix C).

### 5.4.2 Branch Cut Limitations

In general the residue connections are made to keep the branch cut lengths as small as possible. However, several difficulties occur even though an *optimizing* algorithm is used.

First, there is ambiguity in the residue connections. Consider a set of four residues shown in Figure 5-1 where the circles and squares represent positive and negative residues respectively. There are two equally appropriate connections based on the shortest possible paths. Where one is correct and the other is wrong and the wrong choice produces a local error. This localized phase error may look like small square discontinuities in a relatively smooth image. There is nothing that can be done to prevent this type of error.

Second, algorithms based on connecting the nearest neighbors invariably will miss

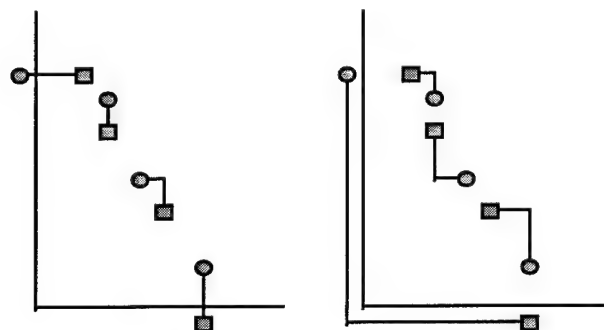


Figure 5-3: Effect of erroneous residue placed on boundary.

a residue and force a connection between two residues relatively far apart as shown in Figure 5-2. This type of error (assuming the right figure is the correct connection) produces discontinuities in the unwrapped phase proportional to the erroneous branch cut length. The minimum cost algorithm essentially eliminates this type of branch cut error.

Third, there are errors that occur owing to the treatment of the edges. With a minimum cost algorithm image residues are placed on the edges for those residues close to the edge to compensate for the fact that the residue's correct pair may have been removed by the truncation of the SAR image. An error may occur if two erroneous image residues are added as shown on the left side of Figure 5-3. Connections between *image* residues must be allowed as shown on the right side of Figure 5-3. Errors like these can cause large errors depending on the locations of the two erroneous residues. When there are areas of high residue density that extend between two edges of the interferogram, even the optimum connection may produce errors of this type.

The last error that may occur also stems from the placement of image residues at the boundary. Clearly we will not place an *image* residue on the boundary for every residue in the SAR interferogram, but some distance (threshold) from the edge must be set. If the distance is too small, errors appear as shown in the top figure in Figure 5-4. But if the distance from the edge is increased slightly more image residues are placed at the boundary and the total branch cut length is reduced.

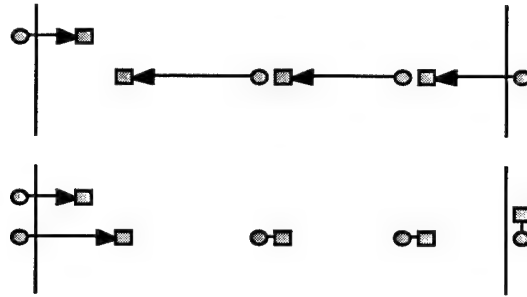


Figure 5-4: Effect of too few image residues on the image boundary.

We can never be certain that the set of branch cut connections is the *correct* set. However, since noise produces pairs of residues (positive and negative), the shortest branch cut lengths are more likely candidates for the correct connections. Also, the erroneous connections usually only produce small local errors in the unwrapped phase.

One serious limitation of the global optimum branch cut method is the CPU time necessary to find the optimal connection set. Since the solution time is directly proportional to the number of residues and proportional to the square of the number of connections, it can take anywhere from seconds to hours to find the solution.

## 5.5 Local optimum branch cut method

To overcome the potential for long solution times a local optimum technique is introduced. After *image* residues are added, a nearest neighbor connection scheme is used. Starting at the center of the image, the residue pairs that are only one pixel apart are connected and removed, then those pairs two pixels apart, then three etc. As residues are left, they are connect to the closest residue leftover. No residues are left unconnected. Then a branch cut length threshold is set. Starting with the longest branch cut that is greater than the desired threshold, a subset of the interferogram residues that includes the long branch cut is reconnected using the optimum algorithm. If a branch cut cannot be shortened in the first pass, a larger subset of residues is used. If

```

Set all  $w_{i,j} = 1$ 
If  $res_{i,j} \neq 0$  then
     $w_{i,j} = 0$ 
     $w_{i,j+1} = 0$ 
     $w_{i+1,j} = 0$ 
     $w_{i+1,j+1} = 0$ 
endif

```

Table 5.2: Algorithm for weight assignment based on residue identification.

the cut is still not shortened, the algorithm moves to the next long branch cut. The algorithm terminates when attempts have been made to fix all branch cuts longer than the threshold length.

## 5.6 Hybrid method - weighted least squares with residue weights

The residue weighting scheme is a new method based on residues found in the branch cut unwrapping method to target *bad* phase values. The idea is that if a residue exists then one or more of the four pixels surrounding the residue are bad, so let's not use them. Table 5.2 shows the algorithm used to produce weights based on residue identification.

## 5.7 Comparison of Algorithms on Simulated Data

In order to begin a comparison of the phase unwrapping algorithms, a simulated interferogram is generated. By adding noise to the simulated interferogram, applying a phase unwrapping process, and comparing against the noise-free unwrapped data, we can begin to analyze the different algorithms. Two measurements were taken: the mean phase error and the phase error standard deviation. The mean phase error is

defined as

$$\bar{\phi}(\Delta\psi) = \sum_{i=1}^M \sum_{j=1}^N \frac{[\phi(i, j, \Delta\psi) - \phi_0(i, j)]}{MN}, \quad (5.40)$$

and the phase error standard deviation is

$$\sigma_{\phi}(\Delta\psi) = \sqrt{\sum_{i=1}^M \sum_{j=1}^N \frac{[\phi(i, j, \Delta\psi) - \phi_0(i, j) - \bar{\phi}(\Delta\psi)]^2}{MN}}, \quad (5.41)$$

where  $\Delta\psi$  is the root mean square (rms) phase noise in degrees,  $\phi(i, j, \Delta\psi)$  is an unwrapped phase value of a noisy interferogram and  $\phi_0(i, j)$  is the unwrapped phase data with no noise present ( $\Delta\psi = 0$ ) used as a reference.  $M$  and  $N$  are the number of pixel rows and columns respectively.

### 5.7.1 Generation of Simulated SAR Interferogram

In this work, a simulated SAR interferogram is generated using the SAR configuration is given in Table 5.3. The interferogram is constructed by first generating a simulated mountain terrain. Then using the SAR configuration, the phase of the signal at each sensor is calculated for each pixel using

$$\phi_{i,j}^{\alpha} = 2k_0 r_{i,j}, \quad \alpha = 1, 2; \quad (5.42)$$

where  $k_0$  is the free space wave number and  $r_{i,j}$  is the distance from the sensor to the simulated terrain height for pixel  $(i, j)$ . The interferogram phase value at pixel  $(i, j)$  is found by wrapping the phase difference  $\phi_{i,j}^2 - \phi_{i,j}^1$

Figure 5-5 is a gray scale plot of the simulated SAR interferogram with no noise and Figure 5-6 is a gray scale plot of the simulated SAR interferogram with  $\Delta\psi = 55^\circ$  rms noise. These two figures represent the range of rms noise used:  $\Delta\psi = 0^\circ \rightarrow 55^\circ$ .

$B$	103.0 <i>m</i>	baseline
$\alpha$	30°	baseline angle
$\lambda$	.0567 <i>m</i>	radar wavelength
$\theta$	30°	looking angle
$H_0$	400 <i>km</i>	sensor height

Table 5.3: SAR parameters for simulated SAR interferogram.

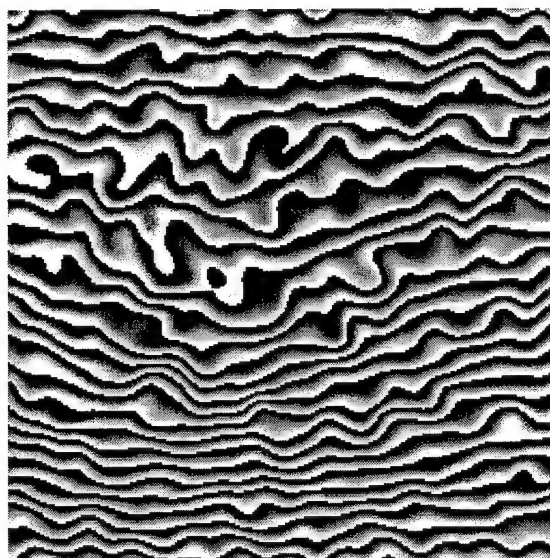


Figure 5-5: Simulated SAR interferogram without noise.

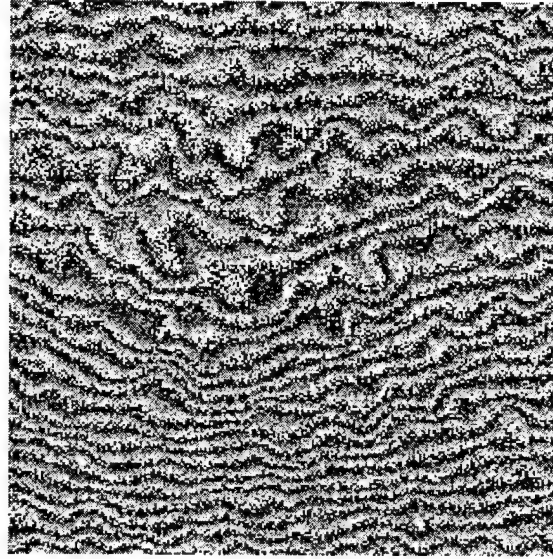


Figure 5-6: Simulated SAR interferogram with  $\Delta\psi = 55^\circ$  rms noise.

### 5.7.2 Addition of noise

The noise is added by

$$\phi(i, j) = \phi_0(i, j) + \phi_N(i, j) \quad (5.43)$$

where

$$\phi_N(i, j) = N_p \pi (1.0 - 2.0 r_n); \quad (5.44)$$

where  $N_p$  is an input noise parameter to control the amount of noise and  $r_n$  is a random variable that is uniformly distributed between 0 and 1. Therefore,

$$\bar{\phi}_N(i, j) = 0, \quad (5.45)$$

$$\sigma_{\phi_N}^2 = \frac{1}{2N_p\pi} \int_{-N_p\pi}^{+N_p\pi} \phi^2 d\phi, \quad (5.46)$$

$$= \frac{(N_p\pi)^2}{3}, \quad (5.47)$$

$\Delta\psi$	$N_p$	$\Delta\psi$	$N_p$	$\Delta\psi$	$N_p$	$\Delta\psi$	$N_p$
0	0	5	0.0481	10	0.0962	15	0.14
20	0.192	25	0.241	30	0.289	35	0.337
40	0.385	45	0.433	50	0.481	55	0.529
60	0.577	65	0.625	70	0.674	75	0.722

Table 5.4:  $N_p$  settings for rms phase noise.

$$\sigma_{\phi_N} = \frac{N_p \pi}{\sqrt{3}}, \quad (5.48)$$

$$\Delta\psi = \frac{N_p(180)}{\sqrt{3}}. \quad (5.49)$$

Table 5.4 lists the values of  $N_p$  necessary produce various values of rms phase noise,  $\Delta\psi$ .

### 5.7.3 Application and Analysis of Techniques on Simulated Data

In this section the least squares, weighted least squares and branch cut phase unwrapping techniques are applied to the simulated SAR interferogram of the last section. Figures 5-7, 5-8, and 5-9 are plots of the mean and standard deviation of the phase error for the three unwrapping techniques describe earlier in this chapter. The weights used for Figure 5-8 were base on the residue mask of Table 5.2. Table 5.7.3 lists the number of residues found in the simulated SAR interferograms for each rms noise level used. Since the additive noise does not produce many phase inconsistencies (*i.e.* residues), until the rms phase noise reaches  $\Delta\psi = 45^\circ$ , we would not expect the weighted least squares or the branch cut method to improve the error until  $\Delta\psi = 45^\circ$ . The results show that both methods greatly reduce the phase errors.

Figure 5-10 shows the standard deviation for  $\Delta\psi = 35^\circ, 45^\circ, 55^\circ$  versus the iteration number of the weighted least squares technique using the Picard iteration



Noise Level	Positive Residues	Negative Residues	Total Residues
0°	0	0	0
15°	0	0	0
25°	0	0	0
35°	17	17	34
45°	481	484	966
55°	2486	2497	4983

Table 5.5: Number of residues in simulated SAR interferograms.

method. The mean error is essentially zero for all iterations (and methods) due to the nature of noise added and not shown. However, the phase error standard deviation is greatly reduced as the iteration number increases. Fifty iterations is sufficient to reach the minimum error.

Errors in phase lead directly to errors in inverted height. These relationships, found in [146], are

$$\bar{h}(\Delta\psi) = \frac{\rho\lambda \sin \theta}{4\pi \cos(\theta - \alpha)} \bar{\phi}(\Delta\psi) \quad (5.50)$$

and

$$\sigma_h(\Delta\psi) = \frac{\rho\lambda \sin \theta}{4\pi \cos(\theta - \alpha)} \sigma_\phi(\Delta\psi) \quad (5.51)$$

Using the parameter data set in Table 5.3,  $\lambda = .0567 \text{ m}$ ,  $\theta = 30^\circ$ ,  $\alpha = 30^\circ$ , ( $B = 103 \text{ m}$ , and  $\rho = 462 \text{ km}$  equation (5.51) becomes  $\sigma_h(\Delta\psi) = 10.1\sigma_\phi(\Delta\psi) \text{ m}$ , so to keep  $\sigma_h \leq 10 \text{ m}$  then the least squares method can only tolerate approximately  $37^\circ$  of rms phase noise while both the weighted least squares and branch cut method can tolerate as much as  $55^\circ$ .

## 5.8 Height Inversion

Figure 5-11 shows the nominal configuration of an interferometric SAR set up used to invert terrain height. The phase difference between the two sensors,  $S_1$  and  $S_2$ ,

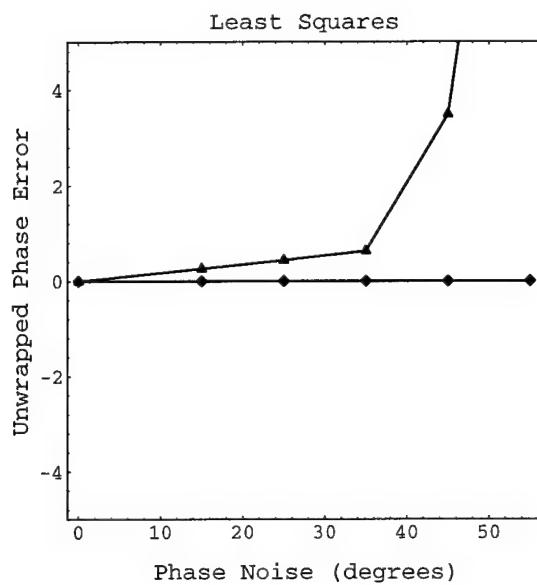


Figure 5-7: Least squares unwrapping phase error versus phase noise, mean (diamond), standard deviation (triangle).

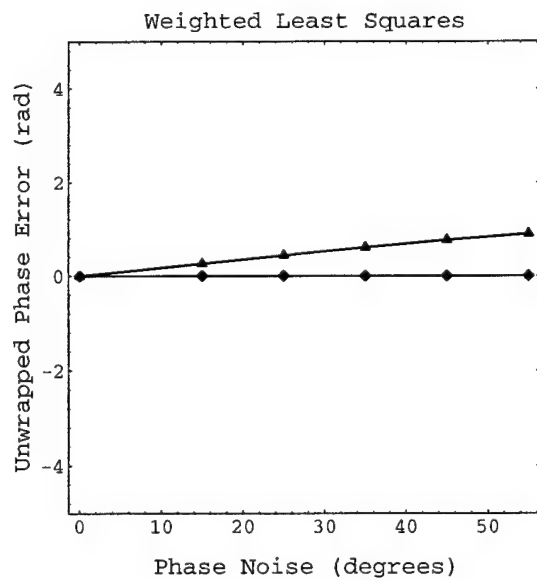


Figure 5-8: Weighted least squares unwrapping phase error versus phase noise, mean (diamond), standard deviation (triangle).

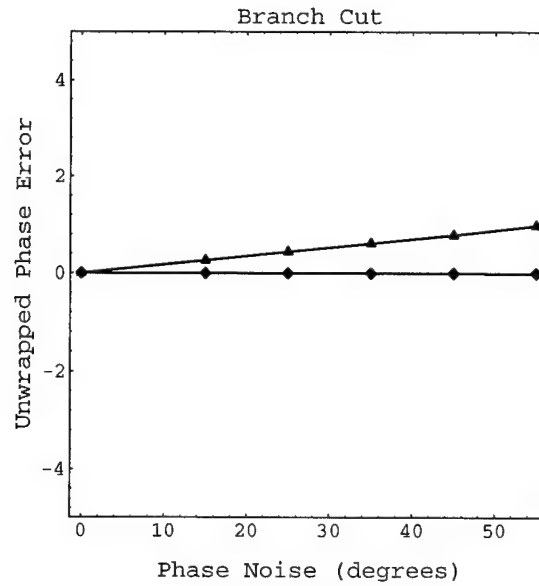


Figure 5-9: Branch cut unwrapping phase error versus phase noise, mean (diamond), standard deviation (triangle).

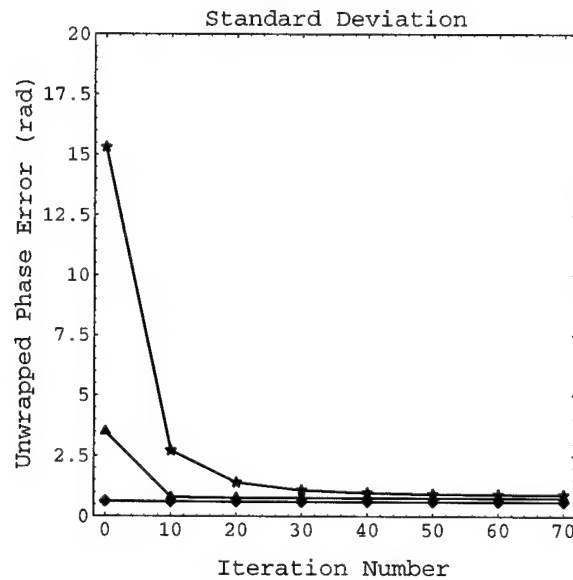


Figure 5-10: Weighted least squares unwrapping phase error standard deviation versus iteration number:  $\Delta\psi = 35^\circ$ , (diamond);  $\Delta\psi = 45^\circ$ , (triangle);  $\Delta\psi = 55^\circ$ , (star).

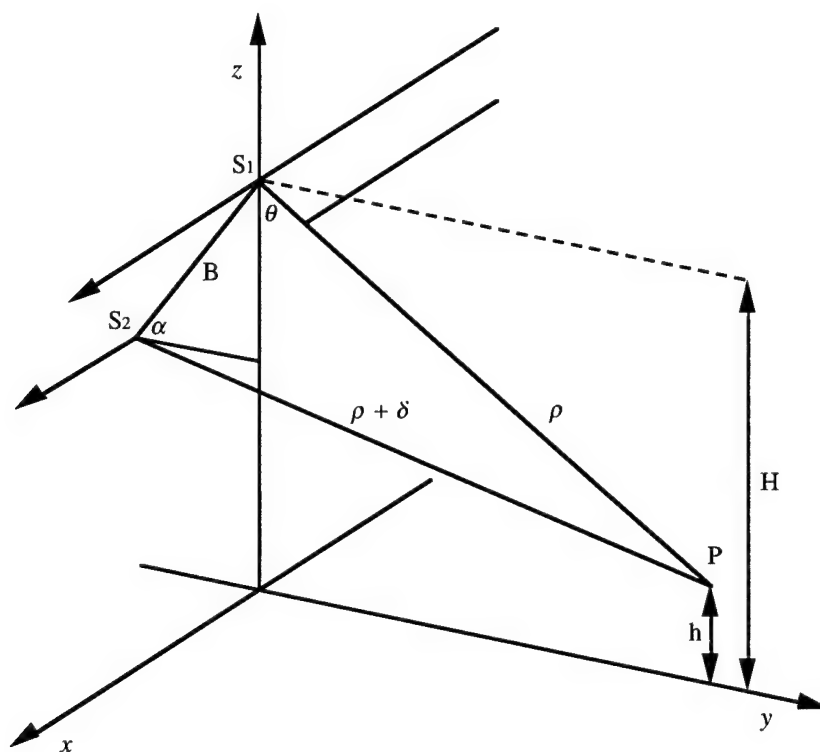


Figure 5-11: SAR set up for terrain height inversion.

can be determined from the geometry of the SAR configuration. If the separation between the two sensors, called the baseline ( $B$ ), is much smaller than the slant range ( $\rho$ ) to the target at  $P$  i.e. ( $B \ll \rho$ ), then the phase difference,  $\Delta\phi$ , is determined by (5.52). If the phase difference is known, then  $\theta$  can be found from (5.52) and the terrain height,  $h$ , determined from (5.53).

$$\Delta\phi = \frac{4\pi}{\lambda} B \sin(\theta - \alpha). \quad (5.52)$$

$$h = H - \rho \cos \theta. \quad (5.53)$$

The phase difference can be calculated from the complex radar images from the two sensors, given by

$$\phi(i, j) = \arctan S_1(i, j) S_2^*(i, j). \quad (5.54)$$

Data Size:	2304×2048
Horizontal Resolution:	19.5 meters
Vertical Resolution:	19.5 meters
Baseline:	233.5 <i>m</i>
Range:	820000 <i>m</i>
Wavelength:	0.0566 <i>m</i>
Off-nadir angle ( $\theta$ ) :	24°
$\alpha$ :	−6.5°

Table 5.6: ERS SAR parameters.

## 5.9 Application and Analysis of Techniques on Real Data

Although the results of the simulated data show that the branch cut method and the weighted least squares offer greatly improved results over the least squares method, the simulated interferograms only loosely approximate a real SAR image. In this section, the phase unwrapping techniques are applied to an actual SAR interferogram. The height is inverted and compared to the ground truth.

### 5.9.1 ERS -1 Data

An interferogram along with coherence data from the European Remote Sensing (ERS -1) satellite was obtained. The ERS data contains 2048 points in the range direction and 2304 points in the azimuthal direction. The interferogram is an image of Phillip Smith Mountains in Alaska. The SAR configuration is contained in Table 5.6. The ground truth was obtained from the U. S. Geological Survey data of Alaska, specifically the data from Phillip Smith Mountains -W. A description of the ground truth data can be found in Table 5.9.1.

Data Size:	1201×601
N-S Resolution $\hat{x}$ :	3 arc-seconds
E-W Resolution $\hat{y}$ :	6 arc-seconds
Lower Left Corner (SE):	68°N 149°W
Lower Right Corner (NE):	69°N 149°W
Upper Left Corner (SW):	68°N 150°W
Upper Right Corner (NW):	69°N 150°W
Minimum height:	370 <i>m</i>
Maximum height:	2315 <i>m</i>
Horizontal accuracy:	130 <i>m</i>
Vertical accuracy:	30 <i>m</i>

Table 5.7: DEM parameters.

### 5.9.2 Registration Process

In order to verify the phase unwrapping algorithms, the inverted height from an ERS-1 interferogram is compared to the ground truth DEM data from the U. S. Geological Survey. Since the SAR and DEM images are offset in the range and azimuthal directions, offset by a rotation angle, and differ in resolution, the SAR and DEM images must be registered before any comparisons can be made. The registration process includes all steps necessary to synchronize the two images so that a point by point compare can be done.

Throughout the registration process, the root mean square height error will be minimized to find the registration parameters. The root mean square height error is defined as

$$h_{error}^{rms} = \sum_{i=1}^M \sum_{j=1}^N \sqrt{\frac{[h_{DEM}(i, j) - h_{SAR}(i, j) - \bar{h}_{error}]^2}{MN}}, \quad (5.55)$$

where

$$\bar{h}_{error} = \sum_{i=1}^M \sum_{j=1}^N \frac{[h_{DEM}(i, j) - h_{SAR}(i, j)]}{MN}, \quad (5.56)$$

and  $h_{DEM}(i, j)$  is the DEM height interpolated from the DEM data at the  $(x, y)$  location of the SAR pixel  $(i, j)$  and  $h_{SAR}(i, j)$  is the inverted height from the unwrapped

DEM resolution along azimuth	=	$\Delta x_{DEM}$
DEM resolution along range	=	$\Delta y_{DEM}$
SAR resolution along azimuth	=	$\Delta x_{SAR}$
SAR resolution along range	=	$\Delta y_{SAR}$
$(i_d, j_d)$	=	DEM reference pixel location
$(i_s, j_s)$	=	SAR reference pixel location
$offset_x$	=	$j_d \Delta x_{DEM} - j_s \Delta x_{SAR}$
$offset_y$	=	$i_d \Delta y_{DEM} - i_s \Delta y_{SAR}$
offset angle	=	$\theta_{os}$

Table 5.8: Registration definitions

interferogram pixel located at  $(i, j)$  after registration.

Table 5.8 is a list of the parameters used in the registration process. Furthermore, the following direction standards are used. The azimuthal direction is the  $\hat{x}$  direction and the range direction is the  $\hat{y}$  direction. In addition, the interferogram data is in matrix form where  $i$  indicates the row and  $j$  indicates the column and  $i = 1, j = 1$  is located in the lower left corner of any displayed data. This means moving from column  $j$  to  $j + 1$  is the  $\hat{x}$  direction and moving from row  $i$  to  $i + 1$  is the  $\hat{y}$  direction.

The entire DEM data set measures  $601 \times 1201$  (*i.e.* rows  $\times$  columns). The  $\hat{x}$  direction contains 1201 data points separated by 3 arc-seconds and the  $\hat{y}$  direction contains 601 data points separated by 6 arc-seconds. The  $\hat{x}$  direction goes from South to North and the  $\hat{y}$  direction goes from East to West. Each row of 1201 points represents a line of constant longitude and each column of 601 points represents a line of constant latitude. As such,  $\Delta x_{DEM}$  is constant throughout the image but  $\Delta y_{DEM}$  is a function of the column number. The resolution decreases as the column number increases; however, the change is less than .005% from column to column and less than 5% over the entire image.

To begin the registration process, the height must be inverted from the SAR data and then forshortened. Forshortening adjusts the position of each pixel along the range direction to compensate for the fact that range pixels are not necessarily in

order as far as the ground dimension is concerned.

The next step is to pick out the same feature in the DEM and SAR images and label those pixels  $(i_d, j_d)$  and  $(i_s, j_s)$  respectively. In this work, the DEM reference pixel does not move while the SAR reference pixel is both changed and moved in order to minimize  $h_{error}^{rms}$ . Subsets of both data are used for this registration. The subset DEM actual image size must be greater than the subset SAR image size so that the SAR image may be shifted, rotated and compared without moving off of the DEM image. An initial guess at the angle offset,  $\theta_{os}$ , is also chosen.

With  $\theta_{os}$ ,  $(i_d, j_d)$ , and  $(i_s, j_s)$  as a starting point, the SAR reference pixel is shifted around  $(i_s, j_s)$  until a minimum  $h_{error}^{rms}$  is found. Next, small changes to  $\theta_{os}$  are made until a minimum  $h_{error}^{rms}$  is found again. Since the SAR data has a finer resolution than the DEM data, for each  $h_{error}^{rms}$  calculation, DEM height values are found by performing a two dimensional interpolation of the DEM data at the locations of the shifted and rotated SAR pixel locations [143]. A finer spatial registration is done by shifting the position of  $(i_s, j_s)$  by offsets smaller than the DEM pixel resolutions until a minimum  $h_{error}^{rms}$  is found.

To adjust for orbit errors that manifest themselves in uniform resolution errors [155], the SAR resolutions in both the range and azimuthal directions are slightly modified until a minimum  $h_{error}^{rms}$  is found. The resolutions are modified with

$$\Delta x_{SAR} = \Delta x_{SAR} \frac{1}{1 + k_x}, \quad (5.57)$$

and

$$\Delta y_{SAR} = \Delta y_{SAR} \frac{1}{1 + k_y}, \quad (5.58)$$

by shifting  $k_x$  and  $k_y$  small amounts about zero. It is important to note each time the range resolution is modified the height must be recalculated since the height inversion algorithm depends on the range resolution.

The last step is to find a height offset that can be subtracted from the SAR



1. Invert height and forshorten data.
2. Provide initial SAR range and azimuthal resolutions.
3. Provide initial DEM/SAR pixel match.
4. Provide initial offset angle.
5. Find optimum pixel match by minimizing RMS height error.
6. Find optimum angle by minimizing RMS height error.
7. Find optimum sub-pixel match by minimizing RMS height error.
8. Find optimum resolution scales.
9. Adjust SAR data to match DEM mean height.

Table 5.9: Registration steps.

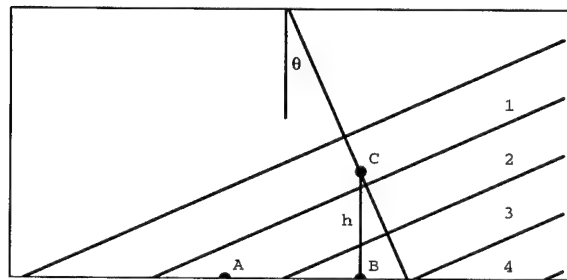


Figure 5-12: Forshortening diagram.

inverted height so that the mean heights of both data subsets are equal. A summary of registration steps is listed in Table 5.9.

### 5.9.3 Forshortening

As mentioned, forshortening adjusts the position of each pixel along the range direction to compensate for the fact that range pixels are not necessarily in order as far as the ground dimension is concerned. Figure 5-12 is a diagram that contains the necessary elements to explain the forshortening process. The horizontal axis represents the range direction and the vertical axis represents terrain height. The diagonal lines represent four range bins, labeled 1, 2, 3, and 4, at a constant azimuthal step. Any scatterer inside a range bin will return electromagnetic energy used to calculate the height for that specific azimuthal step and range distance.

Consider the three scatters, A-C, A and B are at the reference height of zero and C is at a height,  $h$  above the reference height. If the terrain is flat and includes scatters A and B, their returns will be in range bins 2 and 3 and thus converted into the proper spatial arrangement *i.e.* A is to the left of B. However, if the terrain is a hill and slanted upward including scatters A and C, the returns will be in range bins 2 and 1. In other words, scatterer C will be placed to the left of A because it was in a lower numbered range bin. The result is a mismatch between the inverted image map and the true map.

The spatial errors can be fixed by calculating the projection of the inverted height,  $g$ , along the ground using

$$g = h \tan \left( \frac{\pi}{2} - \theta \right). \quad (5.59)$$

The position of the pixel is then shifted by  $g$ . If  $g$  is positive, the pixel height is shifted to the right and if  $g$  is negative, the pixel height is shifted to the left. In this way, all pixels are shifted in the image. Equal pixel spacing is returned by interpolation at the ground range resolution of the SAR configuration.

#### 5.9.4 SAR/DEM Registration

Now that the registration process has been described, this section will provide the details of the subset of data used to compare the the phase unwrapping techniques. The registration was performed using a  $300 \times 200$  set of DEM data points taken from the northern portion of DEM image. Figure 5-13 shows the relative position and Figure 5-14 is a gray scale representation of of the DEM subset with white and black representing the highest and lowest elevations respectively. The SAR subset used for registration included  $150 \times 150$  pixels as shown in Figure 5-15. The terrain features can easily be seen in both images. This is the first set of ERS data to be unwrapped; we will refer to it as ERS-1 Data Set 1.

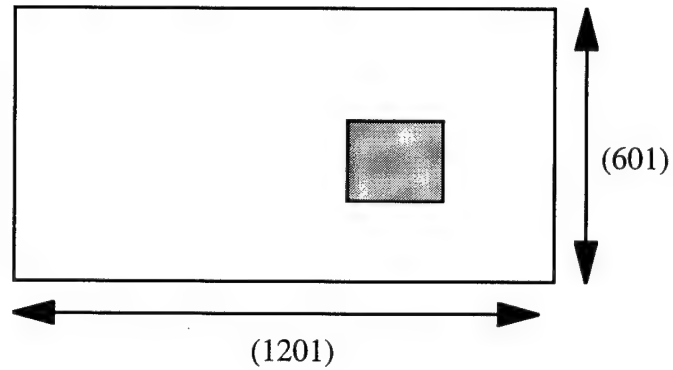


Figure 5-13: DEM subset: shaded square indicates subset used for registration.

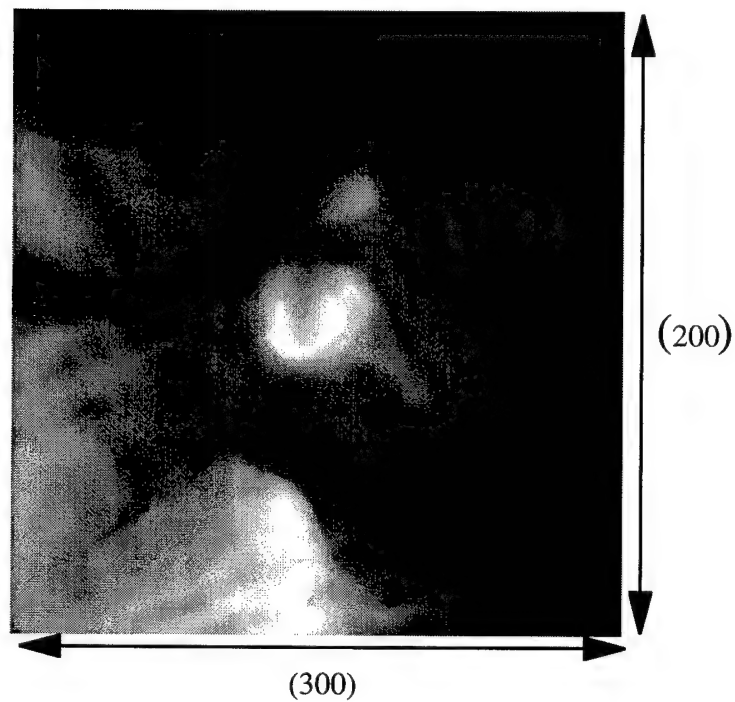


Figure 5-14: Gray scale image of Alaskan DEM terrain used for registration.

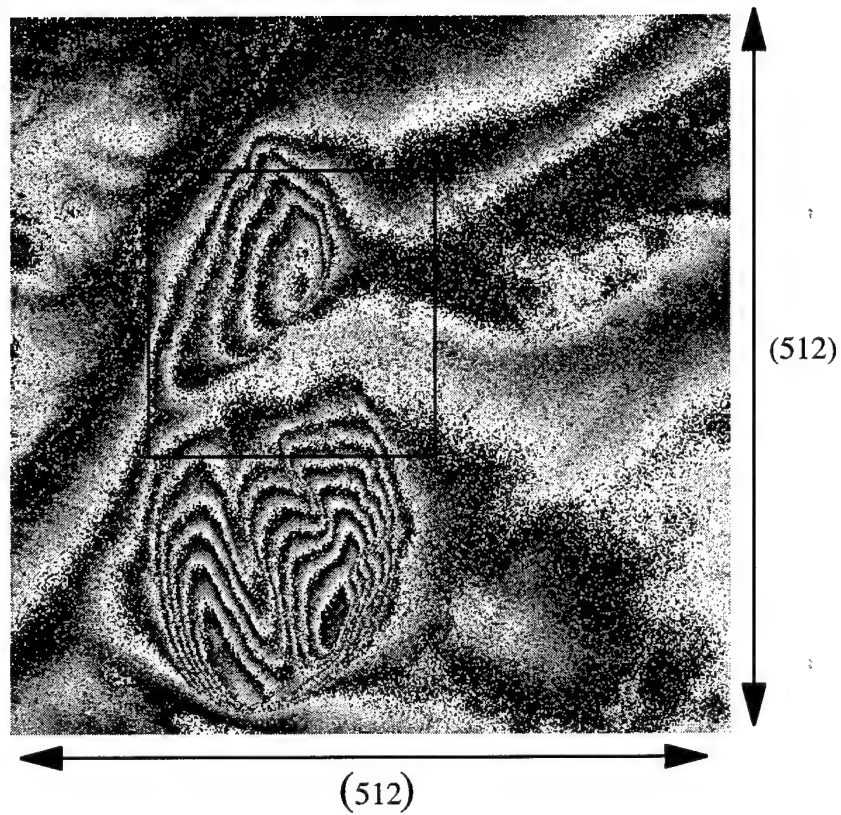


Figure 5-15: ERS-1 SAR interferogram: black rectangle represents the subset used for registration (ERS-1 Data Set 1).



Figure 5-16: Weighting mask based on coherence map, (ERS-1 Data Set 1).

### 5.9.5 Determination of data weights

The three types of weights described in Sections 5.3.2 and 5.6 were used to unwrap the real phase data with the weighted least squares method. Figures 5-16 through 5-20 represent the weights applied to the interferogram of Figure 5-15. In these gray scale pictures or *masks* white represents the largest weight of 1, black represents the smallest weight of 0, and the grays represent continuous weights between 1 and 0.

Figure 5-16 is the mask based on straight coherence data and Figures 5-17, 5-18, and 5-19 are the modified coherence masks with coherence thresholds,  $c_{thr}$ , of 0.8, 0.5, and 0.2. Setting  $c_{thr} = 0$  is equivalent to no weighting (*i.e.* a straight least square method) and setting  $c_{thr} = 1$  is equivalent to straight coherence weighting (Figure 5-16).



Figure 5-17: Weighting mask based on coherence map with  $c_{thr} = 0.8$ , (ERS-1 Data Set 1).



Figure 5-18: Weighting mask based on coherence map with  $c_{thr} = 0.5$ , (ERS-1 Data Set 1).



Figure 5-19: Weighting mask based on coherence map with  $c_{thr} = 0.2$ . (ERS-1 Data Set 1).



Figure 5-20: Weighting mask based on residues (ERS-1 Data Set 1).

### 5.9.6 Results

#### Data Set 1

This section includes a compilation of the height errors associated with four specific phase unwrapping processes. The first is based on the straight least squares method, Figure 5-21; the second and third are based on the weighted least squares method using the coherence weighting and residue weighting schemes, Figures 5-23 and 5-27 respectively; and the last is based on the global optimal branch cut method, Figure 5-24. The gray scale plots represent the errors based on location with white being the largest positive error of  $125\text{ m}$  and black being the largest negative error of  $-125\text{ m}$ .

Associated with each gray scale plot is a histogram of the pixel height errors, Figures 5-25, 5-26, 5-27, and 5-28. The spikes at zero are an artifact of the last step of the registration process (Table 5.9) that matches the mean heights of the SAR and DEM terrain images. On ERS-1 Data Set 1, the least squares methods impose a global error in the inverted terrain height as indicated by the peak in the error to the left of the  $0\text{ m}$  error mark on the horizontal axis. The unweighted least squares unwrapping process produced a peak at  $40\text{ m}$ , while the coherence and residue weighting schemes produced peaks at  $25\text{ m}$  and  $8\text{ m}$  respectively. The optimal branch cut method produces local errors indicated by the symmetric error histogram about the  $0\text{ m}$  error mark.

Using a weighting least squares method reduces the global error of the unweighted least squares method. The new residue weighting scheme offered much better improvement over the weighting based on coherence data. Figure 5-29 represents the  $h_{rms}$  error for the inverted height based on the weighted least squares method using the modified coherence weighting scheme on ERS-1 Data Set 1. Over a twenty percent reduction in the  $h_{rms}$  error was realized over the no-weight least squares method ( $c_{thr} = 0$  when using this method. Figure 5-30 compares the branch cut method and the weighted least squares method versus iterations of the Picard iteration method.



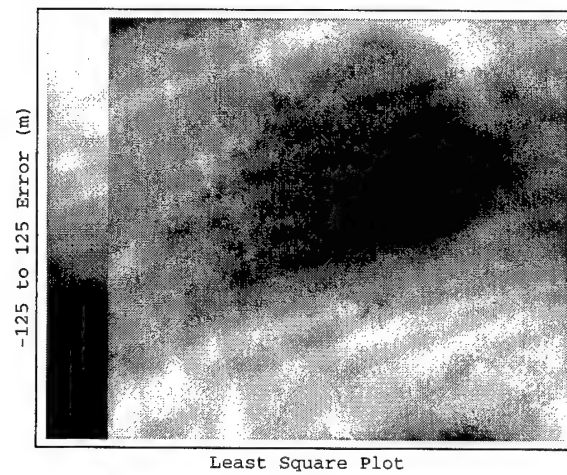


Figure 5-21: Least square error plot (ERS-1 Data Set 1).

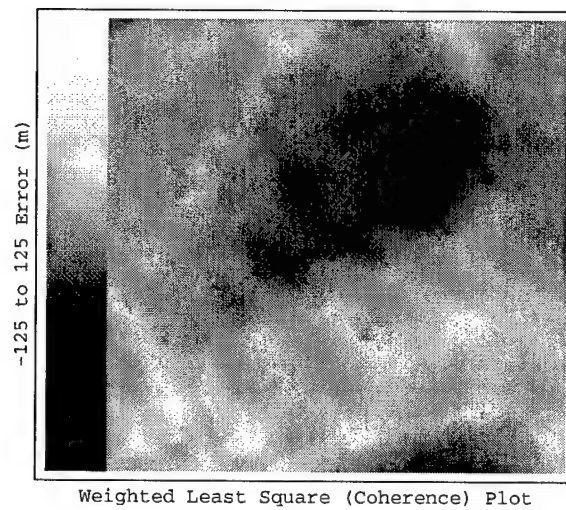


Figure 5-22: Weighted least square error plot using coherence mask (ERS-1 Data Set 1).

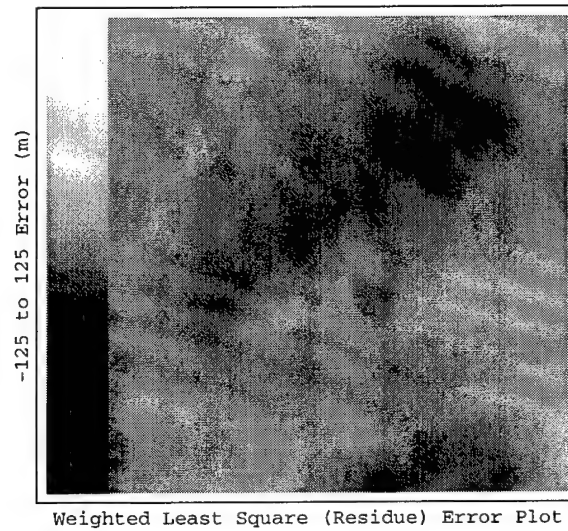


Figure 5-23: Weighted least square error plot with residue mask (ERS-1 Data Set 1).

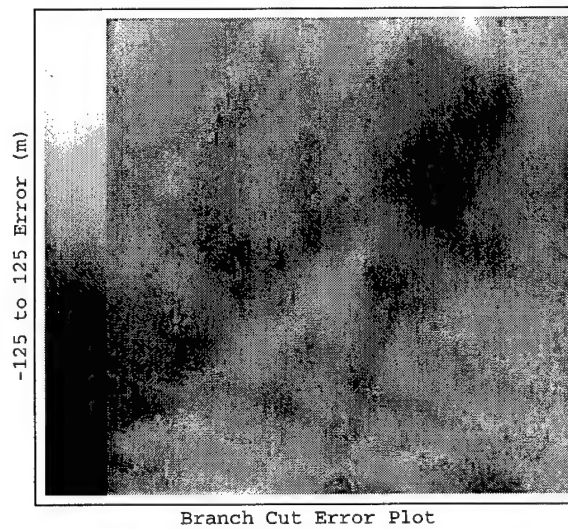


Figure 5-24: Branch cut error plot (ERS-1 Data Set 1).

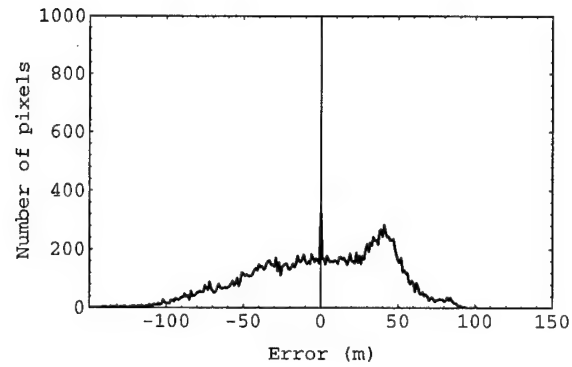


Figure 5-25: Histogram of least square height errors (ERS-1 Data Set 1). Standard deviation: 38.60 *m*.

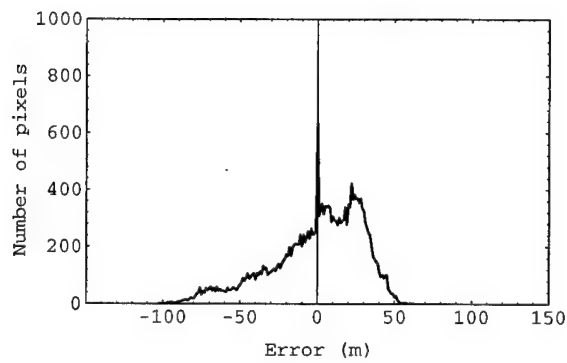


Figure 5-26: Histogram of weighted least square height errors using coherence mask (ERS-1 Data Set 1). Standard deviation: 29.47 *m*.

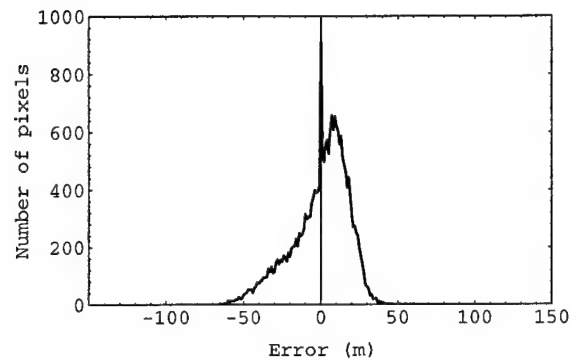


Figure 5-27: Histogram of weighted least square height errors using residue mask (ERS-1 Data Set 1). Standard deviation: 18.26 *m*.

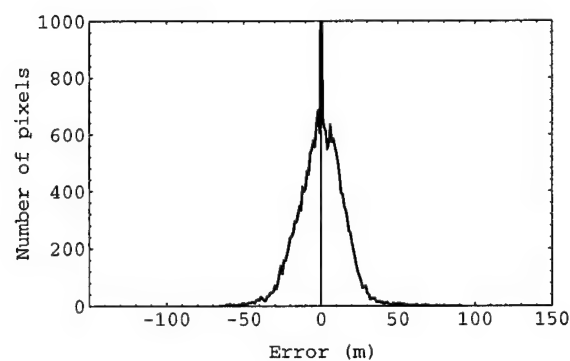


Figure 5-28: Histogram of branch cut height errors (ERS-1 Data Set 1). Standard deviation: 15.15 *m*.

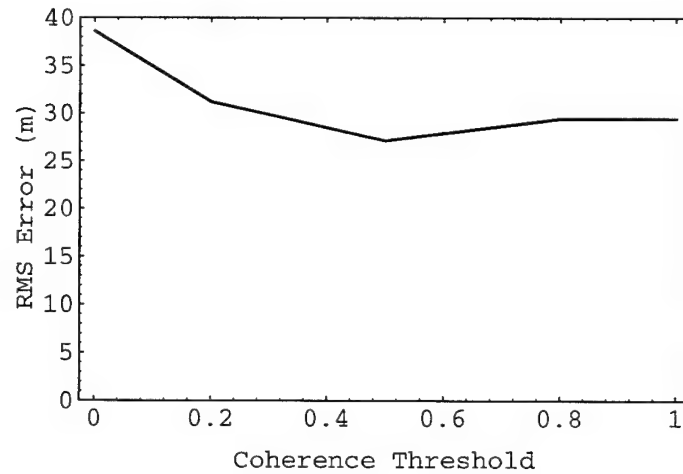


Figure 5-29: Comparison of  $h_{rms}$  error versus  $c_{thr}$  setting of height inverted with weighted least squares with coherence weighting on ERS-1 Data Set 1.

On Data Set 1 data, the branch cut method performed exceptionally well with an error of 15.15 *m*. The straight least squares method has an error of 38.60 *m*. The weighted least squares method with residue weighting has an error of 18.26 *m*. And finally, the weighted least squares with coherence weighting method has an error of 29.47 *m*. It appears that the branch cut method and the hybrid weighted least squares method offered the best performance.

## Data Set 2

In this section another set of ERS-1 data is use to study the various unwrapping techniques. We'll call this data ERS-1 Data Set 2. The interferogram and its corresponding coherence data are shown in Figures 5-31 and 5-32. This data set contains  $256 \times 256$  pixels and the entire image is unwrapped. The corresponding DEM terrain feature can be seen as the mountain peaks at the lower center of the map in Figure 5-14. The residue mask is represented in Figure 5-33. Instead of showing the grayscale error plots, just the height error histograms are shown here. The first histogram represents the height error when the straight least squares method is used,

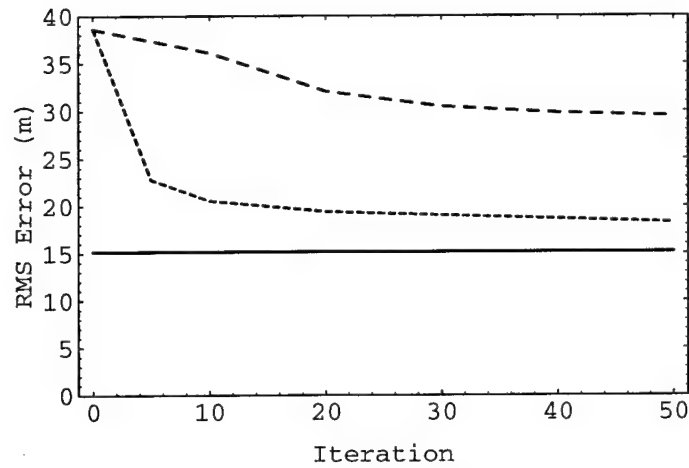


Figure 5-30: Comparison of height error versus iteration on ERS-1 Data Set 1.



Figure 5-31: ERS-1 Data Set 2.



Figure 5-32: Coherence data for ERS-1 Data Set 2.



Figure 5-33: Weighting mask based on residues for ERS-1 Data Set 2.

Method	$h_{error}^{rms} (m)$	Time (s)
LS	74.85	8.43
W-LS (coherence)	39.18	43.64
W-LS (residues)	20.91	38.87
Global optimum BC	22.30	588.98
Local optimum BC	22.40	20.55

Table 5.10: Comparison of rms height error and CPU times for the phase unwrapping methods. LS: least squares, W-LS: weighted least squares and BC: branch cut.

Figure 5-35; the second and third histograms are based on the weighted least squares method using the coherence weighting and residue weighting schemes, Figures 5-36 and 5-37 respectively. The fourth histogram is based on the global optimal branch cut method, Figure 5-38 and the last histogram, Figure 5-39, represents the height errors due to a local optimum branch cut method. Table 5.10 lists the standard deviation, ( $h_{error}^{rms}$ ), for each method used. In addition to the error, the CPU times are provided. These times are meant to show relative times. None of the code was optimized to provide the fastest execution times.

The results of unwrapping ERS-1 Data Set 2 show that the least squares method is not always appropriate for unwrapping SAR interferograms the rms height error is almost twice the next largest error. The weighted least squares method using the coherence data weighting scheme offers great improvement over straight least squares, but as before, the residue scheme offers an still an additional improvement. The residue weighted least squares and the global and local branch cut methods offer the best rms errors of 20.91 m, 22.30 m, and 22.40 m respectively. However, their respective CPU times are 38.87 s, 588.98 s and 20.55 s. The local branch cut method is the fastest followed by the weighted least squares, but the global branch cut method is very slow. The data set contains 2663 residue pairs and finding the optimum takes almost 10 minutes. Figure 5-34 are grayscale pictures of the unwrapped phase of Data Set 2 using the branch cut method with residue connections made with nearest



neighbor, local optimum, and global optimum branch cut algorithms. One can clearly see the effects of long branch cuts in the top image (nearest neighbor). Those phase errors are removed with a local optimum scheme in the center image which is nearly identical to the lower image (global). The center image was unwrapped in less than 4 percent the time necessary to unwrap the lower image with the global algorithm.

As before with ERS-1 Data Set 1, using a weighting least squares method reduces the global error of the unweighted least squares method. The new residue weighting scheme offered considerable improvement over the weighting based on coherence data.

### Data Set 3

In this section another set of ERS-1 data is used to study the various unwrapping techniques. We'll call this data ERS-1 Data Set 3. The interferogram and its corresponding coherence data are shown in Figures 5-40 and 5-41. This data set contains  $256 \times 256$  pixels and the entire image is unwrapped. The corresponding DEM terrain feature can be seen as the horse shoe shaped mountain peak at the center of the map in Figure 5-14. The residue mask is represented in Figure 5-42. The data was selected to show the difficulty even the best methods have with high fringe density compounded with low coherence. Data Set 3 was unwrapped with the hybrid weighted least squares method using the residue mask in Figure 5-42. The results are shown in Figures 5-43 and 5-44. The unwrapping lost most of the height associated the many fringes that wrap around the lower portion of the mountain peak. The result is that the peak height is underestimated by over 120 *m* and the flat portion at the base of the mountain is overestimated. The histogram shows a global error at 15 *m*. The global optimum branch cut method offers similar rms height error, 39.07 *m* versus 39.33 *m* for the hybrid method. Several large portions of the map are over estimated represented by the light patches on lower portion of Figure 5-45. Even with the addition of many *image* residues on the boundary were not able to overcome

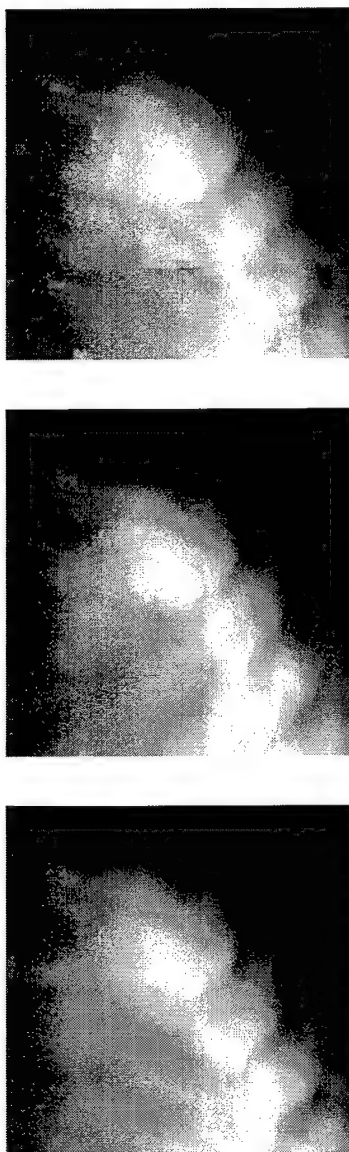


Figure 5-34: Comparison of nearest neighbor (top), local optimum (center) and global optimum (bottom) branch cut phase unwrapping for ERS-1 Data Set 2.

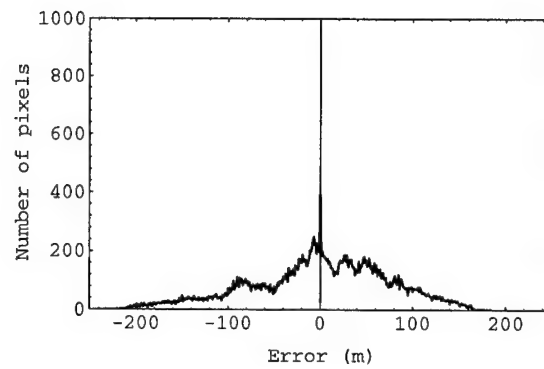


Figure 5-35: Height error histogram for straight least squares method applied to ERS-1 Data Set 2. Standard deviation: 74.85 *m*.

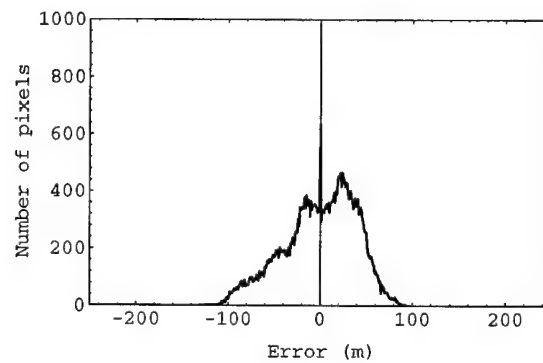


Figure 5-36: Height error histogram for weighted least squares method with coherence weighting applied to ERS-1 Data Set 2. Standard deviation: 39.18 *m*.

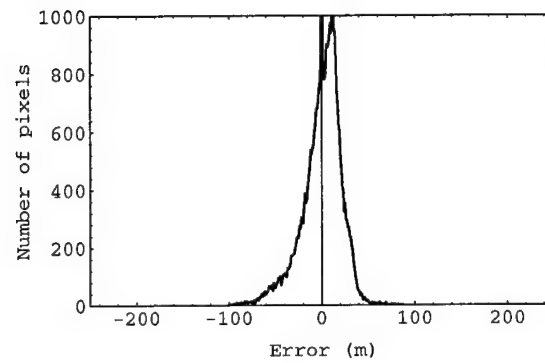


Figure 5-37: Height error histogram for weighted least squares method with residue weighting applied to ERS-1 Data Set 2. Standard deviation: 20.91 *m*.

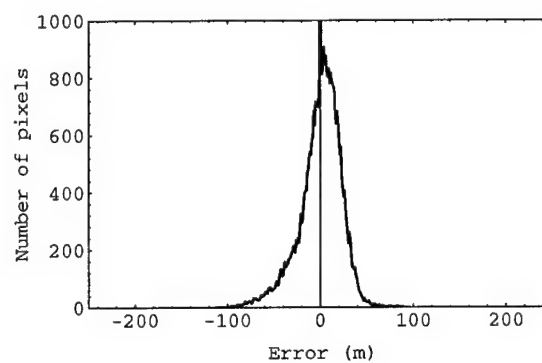


Figure 5-38: Height error histogram for global optimum branch cut method applied to ERS-1 Data Set 2. Standard deviation: 22.30 *m*.

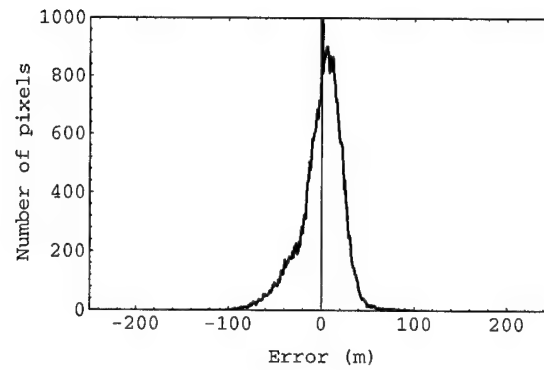


Figure 5-39: Height error histogram for local optimum branch cut method applied to ERS-1 Data Set 2. Standard deviation: 22.40 *m*.



Figure 5-40: ERS-1 Data Set 3.

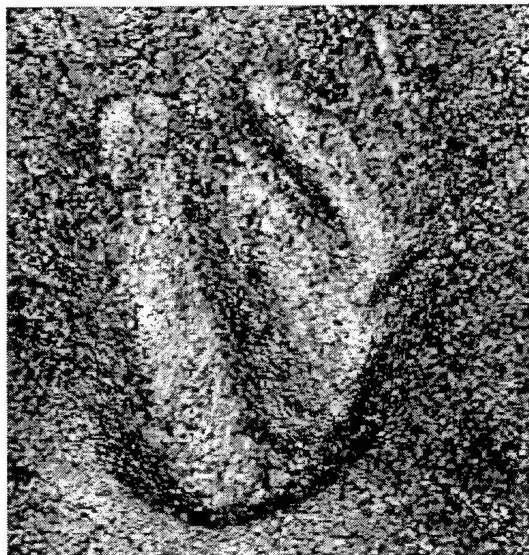


Figure 5-41: Coherence data for ERS-1 Data Set 3.



Figure 5-42: Weighting mask based on residues for ERS-1 Data Set 3.

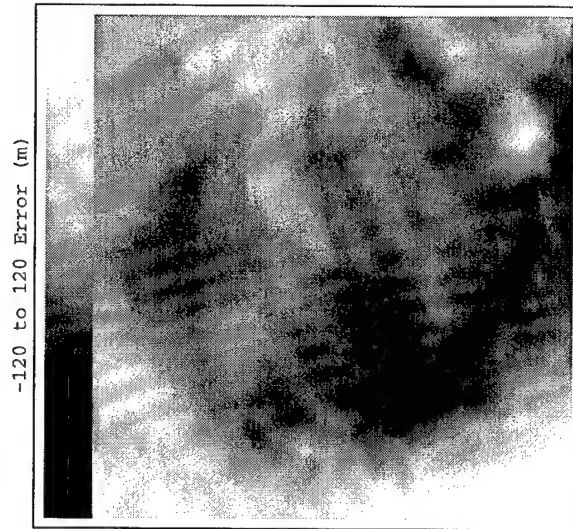


Figure 5-43: Height error for hybrid weighted least squares method applied to ERS-1 Data Set 3. Standard deviation: 39.33 m.

the errors. An *image* residue was placed at the boundary for each *true* residue within 5 pixels from the interferogram's edge.

## 5.10 Summary

In this chapter, different phase unwrapping schemes were described and applied to both simulated and real SAR interferograms. The techniques used were weighted and unweighted least squares and optimal branch cut global and local methods. When no noise is present phase unwrapping is straight forward and uninteresting; however, when noise is present the phase unwrapping process is non-trivial and there is much interest in proper treatment of the noise.

Although the least squares method is very fast because of the Discrete Cosine Transform formulation, it does not treat noisy data very well as shown when attempting to unwrap the simulated interferogram. Once the rms phase noise reached  $35^\circ$ , the least squares method was unable to unwrap the phase data effectively. Up

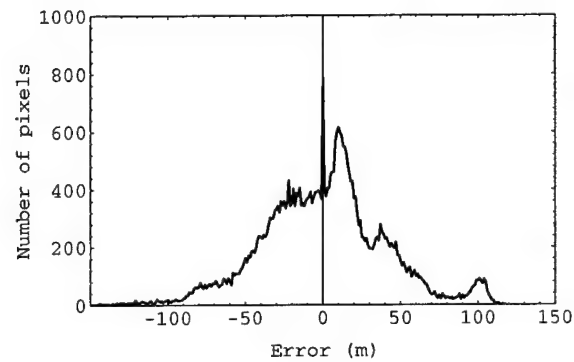


Figure 5-44: Height error histogram for hybrid weighted least squares method applied to ERS-1 Data Set 3. Standard deviation: 39.33 *m*.

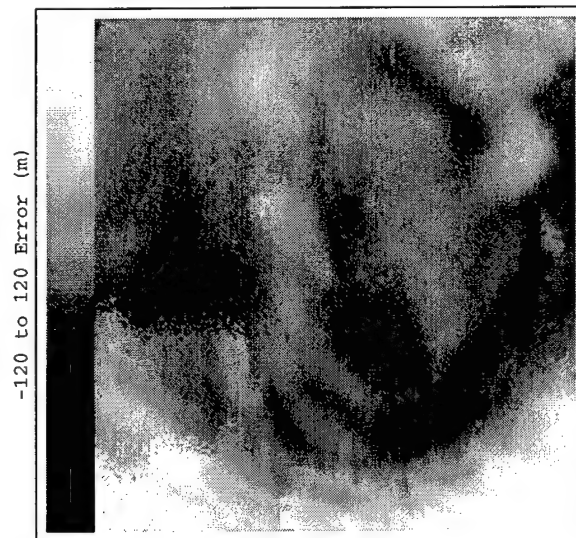


Figure 5-45: Height error for global optimum branch cut method applied to ERS-1 Data Set 3. Standard deviation: 39.07 *m*.



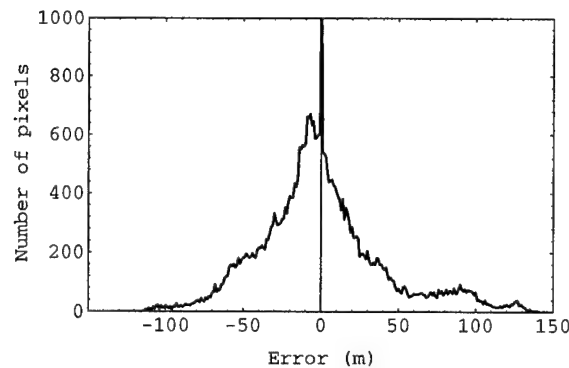


Figure 5-46: Height error histogram for global optimum branch cut method applied to ERS-1 Data Set 3. Standard deviation: 39.07 *m*.

to 35° rms phase noise, all phase unwrapping algorithms performed equally well because the noise was not great enough to produce phase inconsistencies in the form of residues. At 35° rms noise there were only 34 residues in the image of 65536 pixels. However at 55° rms noise there were 4983 residues in the image of 65536 pixels and both the residue (hybrid) weighted least squares and the optimum branch cut methods kept the rms phase error to less than one radian.

Both the hybrid weighted least squares and the optimum branch cut methods offered essentially the same error performance when applied to both simulated SAR interferograms with additive noise and real ERS-1 interferograms. These methods consistently showed improvement over the straight least squares and coherence weighted least squares methods. Specifically, the methods offer over fifty percent reduction in root mean square (rms) height error compared to the straight least squares method and over thirty-five percent reduction in rms height error compared to the weighted least squares method based on coherence data weighting schemes.

The global optimum branch cut method is appropriate when there are not that many residues; however, the local optimum provide near identical results in far less time. The branch cut methods is more likely to produce local errors as shown by the symmetrical error histograms and the hybrid weighted least squares method produces

a fairly symmetrical histogram especially when compared to the straight least squares and coherence weighted least squares methods. In other words, using a weighting scheme greatly reduces the global error introduced by the least squares method.

The hybrid method could be improved by using a different algorithm to solve the weighted least squares problem that guarantees convergence. Although the Picard iteration always converged in this application, simply selecting an iteration number is not the best way to solve the problem. A conjugate-gradient solver as proposed in [170] would guarantee convergence and prevent running unnecessary iterations.

The branch cut method could be improved by characterizing residues by their source. For example, residue pairs due to speckle noise are close to each other and handled quite effectively with the optimum methods. However, residues created by under sampled fringes caused by very steep terrain features can produce residue pairs relatively far apart and are not treated properly in the presence of many other residues. If these residues can be isolated they can be handled separately as proposed in [163]. One way these residues could be found is by using the local optimum branch cut method. When the local optimum algorithm cannot reduce the branch cut length of a long cut, it probably means there is a non-noise produced residue in the vicinity of the long cut. These areas can be flagged and treated with other techniques.



# Chapter 6

## Conclusion

In this thesis, applications of numerical techniques to electromagnetic problems in microelectronic and radar imaging systems were investigated. Dielectric rib waveguide discontinuities were analyzed with the Finite Difference Time Domain (FDTD) method. Within the FDTD framework, two techniques were applied to the study of dielectric rib waveguides. First, Berenger's Perfectly Matched Layer was used to truncate the multi-layered dielectric structure. Second, the rib waveguide's fundamental mode was determined with a two dimensional FDTD simulation for subsequent use in a three dimensional simulation. These numerical techniques were used to study the effect of bend discontinuities in the rib waveguide.

An Impedance Boundary Condition (IBC) was developed for two dimensional FDTD simulations that can replace thin sheets of highly conducting material. The IBC accurately models the conductor loss over a wide frequency range. In this way, the FDTD method is improved by allowing a method to model conductor loss without the need for very large computational domains. The two dimensional IBC was validated through the comparison of resonant cavity quality factors determined with the FDTD simulation data and those calculated with analytical methods.

Phase unwrapping techniques for the inversion of terrain height using Synthetic Aperture Radar Interferometry (InSAR) data were analyzed. A hybrid phase unwrap-

ping technique that combines the weighted least squares method with the residues of the branch cut method was presented. Optimal branch cut methods were also presented: a global one that includes all residues before placing any branch cuts and a local one that uses a subset of residues to fix long branch cuts introduced when using a nearest neighbor connection scheme. These new SAR phase unwrapping methods were used to unwrap simulated and real SAR interferograms and then were compared to straight least squares and other weighted least squares methods.

## 6.1 Analysis of Dielectric Waveguide Discontinuities

A study of the Perfectly Matched Layer showed that the PML conductivities used to absorb the outgoing waves in a multiple dielectric layer simulation must not be assigned independently with the method of normal incidence used by Berenger. Instead, once one of the layer's conductivities is calculated the others must be constructed so that the loss tangents in each layer are equal. With this done, there will be no reflection coefficient singularities in both the normal and tangential directions and the PML will simulate open space to the maximum extent possible under the discretization scheme. If the interdependency of the dielectric layers is ignored even though each layer is perfectly matched, the material differences at the interfaces act as sources for unwanted solutions that contaminate the simulation volume. With the matching conditions determined for multi-layered dielectrics, dielectric rib waveguide structures were terminated with the Berenger Perfectly Matched Layer and each dielectric layer was matched considering all the layers within the simulation volume.

It was shown that the computational domain can be reduced when simulating dielectric rib waveguide with the FDTD numerical technique when the waveguide fundamental mode's spatial distribution is calculated first and used to excite the guide. The better excitation means that shorter distances between the excitation

plane and the discontinuity are needed for the mode to settle. A reduction of twenty percent was shown. This reduction implies bigger problems can be simulated within the same time as those simulations using other excitation techniques, or the same simulations can be run in shorter times.

Although the dielectric rib waveguide provides very low loss for high frequency signals compared to microstrip or coplanar structures, the rib waveguide bend does introduce a significant amount of loss. As the abruptness of the turn is lessened, the rib guides more energy around turn; however, gradual turns require more space on an integrated circuit. With the improvements to the FDTD method presented, rib bend structures can be studied to improve their loss characteristics.

## 6.2 Modeling of Thin Finite Conductivity Sheets

A new Impedance Boundary Condition for good conductors, satisfying  $1 \ll \frac{\sigma}{\omega\epsilon}$ , was extended for use in two dimensional FDTD simulations. The IBC was described in great detail and studied in one dimensional simulations. The influence of FDTD parameters and the number of IBC expansion terms on the accuracy of the IBC was presented. The results showed that the time step constraint is more stringent than the Courant stability limit. The time step must satisfy  $\Delta t \leq \frac{\Delta}{1.82c}$ .

The conductivity range studied spanned four orders of magnitude from  $10^4$  to  $10^8 \Omega^{-1}m^{-1}$ . Two variations of the IBC were investigated: one that approximates the convolution with a piecewise constant magnetic field and another that uses a piecewise linear magnetic field. When a piecewise constant approximation is used for the magnetic field, the amount of computer resources (as measured by number of expansion terms) is directly proportional to the conductivity. Lower conductivities result in larger pole magnitudes and lesser sensitivity to an increased number of terms. The piecewise constant approximation produces an error that cannot be overcome by more expansion terms. The errors from the impedance approximation and the

magnetic field approximation combine to form an optimum number of expansion terms. Using more than the optimum number of terms will result in less accuracy. On the other hand, with a piecewise linear approximation, the error to the magnetic field is greatly reduced and an optimum number of terms is not evident. The more terms used the more accurate the IBC; however, the error quickly levels off.

When extended to two dimensions, the impedance boundary condition works very well over the wide range of skin depths studied,  $3 \rightarrow 185$ . The lowest conductivity,  $\sigma = 5.8 \times 10^4 \Omega^{-1}m^{-1}$ , offered the biggest error of almost 13%, but the error was very small at conductivities near those of the most popular conductors of silver, copper, gold and aluminum. The IBC is an excellent model for thin sheets of good conductors with finite conductivity. The IBC offers the advantage of working over a wide range of frequencies with very little computational overhead. For typical conductors, like copper, 125 terms per tangential electric field component are needed with errors in  $Q$  less than 5%.

### 6.3 Phase Unwrapping of SAR Interferograms

Numerical techniques to unwrap the phase of synthetic aperture radar interferograms were investigated. The foundations of phase unwrapping were described, specifically least squares and optimal branch cut unwrapping. New modifications to these techniques were applied to both simulated and real interferograms. After the application of these techniques to the real SAR data, the phase was used to invert terrain height and the height was compared to ground truth.

Although the least squares method is very fast because of the Discrete Cosine Transform formulation, it does not treat noisy data very well. In simulated SAR interferograms, once the rms phase noise reached  $35^\circ$ , the least squares method was unable to unwrap the phase data effectively. Both the hybrid weighted least squares and the optimum branch cut methods offered essentially the same error performance

when applied to both simulated SAR interferograms with additive noise and real ERS-1 interferograms. These methods consistently showed improvement over the straight least squares and coherence weighted least squares methods. Specifically, the methods offer over fifty percent reduction in root mean square (rms) height error compared to the straight least squares method and over thirty-five percent reduction in rms height error compared to the weighted least squares method based on coherence data weighting schemes.

The global optimum branch cut method is appropriate when there are not that many residues; however, the local optimum method provides near identical results in far less time. The branch cut methods are more likely to produce local errors as shown by the symmetrical error histograms and the hybrid weighted least squares method produces a fairly symmetrical histogram especially when compared to the straight least squares and coherence weighted least squares methods. In other words, using a weighting scheme greatly reduces the global error introduced by the least squares method. In fact, the hybrid method closely approaches the desirable local error distribution of the branch cut method.

## 6.4 Outlook

Although much was accomplished in this work, improvements can always be made and more could be done. The most logical extension of the dielectric waveguides work would be to thoroughly investigate ways to reduce the loss through the turn discontinuity. Different geometries and materials could be tested to reduce the loss while keeping the size small. In the Impedance Boundary Condition work, the IBC could be extended to three dimensions. Finally, the InSAR weighted least squares phase unwrapping technique, in this work, could be improved by replacing the Picard iteration algorithm with another solver that will improve the convergence properties. The optimal branch cut methods could be improved by characterizing the residues by



there most likely source. In this way, residue pairs that may be relatively far apart can be handled separately leaving the optimum algorithm to connect the pairs that should be close together.

Despite the increases in computational power that result from improving computer technology, electromagnetic problems require large amounts of computer resources. Finding better numerical techniques or improving existing numerical techniques will continue to be worthy goals.

# Appendix A

## Mur FDTD Equations

Given a computational domain with boundaries  $x = 0, N_x$ ,  $y = 0, N_y$  and  $z = 0, N_z$ , the tangential electric fields at all six boundary faces must be updated with the ABC equations. For completeness, all the field equations are listed below.

### A.1 1st Order Mur FDTD Equations

$$\begin{aligned} E_x^{n+1}(i + \frac{1}{2}, 0, k) &= E_x^n(i + \frac{1}{2}, 1, k) \\ &+ \frac{c_0 \Delta t - \Delta y}{c_0 \Delta t + \Delta y} [E_x^{n+1}(i + \frac{1}{2}, 1, k) - E_x^n(i + \frac{1}{2}, 0, k)], \end{aligned} \quad (\text{A.1})$$

$$\begin{aligned} E_x^{n+1}(i + \frac{1}{2}, N_y, k) &= E_x^n(i + \frac{1}{2}, N_y - 1, k) \\ &+ \frac{c_0 \Delta t - \Delta y}{c_0 \Delta t + \Delta y} [E_x^{n+1}(i + \frac{1}{2}, N_y - 1, k) - E_x^n(i + \frac{1}{2}, N_y, k)], \end{aligned} \quad (\text{A.2})$$

$$\begin{aligned} E_x^{n+1}(i + \frac{1}{2}, j, 0) &= E_x^n(i + \frac{1}{2}, j, 1) \\ &+ \frac{c_0 \Delta t - \Delta z}{c_0 \Delta t + \Delta z} [E_x^{n+1}(i + \frac{1}{2}, j, 1) - E_x^n(i + \frac{1}{2}, j, 0)], \end{aligned} \quad (\text{A.3})$$

$$\begin{aligned}
E_x^{n+1}(i + \frac{1}{2}, j, N_z) &= E_x^n(i + \frac{1}{2}, j, N_z - 1) \\
&+ \frac{c_0 \Delta t - \Delta z}{c_0 \Delta t + \Delta z} [E_x^{n+1}(i + \frac{1}{2}, j, N_z - 1) - E_x^n(i + \frac{1}{2}, j, N_z)], \quad (A.4)
\end{aligned}$$

$$\begin{aligned}
E_y^{n+1}(0, j + \frac{1}{2}, k) &= E_y^n(1, j + \frac{1}{2}, k) \\
&+ \frac{c_0 \Delta t - \Delta x}{c_0 \Delta t + \Delta x} [E_y^{n+1}(1, j + \frac{1}{2}, k) - E_y^n(0, j + \frac{1}{2}, k)], \quad (A.5)
\end{aligned}$$

$$\begin{aligned}
E_y^{n+1}(N_x, j + \frac{1}{2}, k) &= E_y^n(N_x - 1, j + \frac{1}{2}, k) \\
&+ \frac{c_0 \Delta t - \Delta x}{c_0 \Delta t + \Delta x} [E_y^{n+1}(N_x - 1, j + \frac{1}{2}, k) - E_y^n(N_x, j + \frac{1}{2}, k)], \quad (A.6)
\end{aligned}$$

$$\begin{aligned}
E_y^{n+1}(i, j + \frac{1}{2}, 0) &= E_y^n(i, j + \frac{1}{2}, 1) \\
&+ \frac{c_0 \Delta t - \Delta z}{c_0 \Delta t + \Delta z} [E_y^{n+1}(i, j + \frac{1}{2}, 1) - E_y^n(i, j + \frac{1}{2}, 0)], \quad (A.7)
\end{aligned}$$

$$\begin{aligned}
E_y^{n+1}(i, j + \frac{1}{2}, N_z) &= E_y^n(i, j + \frac{1}{2}, N_z - 1) \\
&+ \frac{c_0 \Delta t - \Delta z}{c_0 \Delta t + \Delta z} [E_y^{n+1}(i, j + \frac{1}{2}, N_z - 1) - E_y^n(i, j + \frac{1}{2}, N_z)], \quad (A.8)
\end{aligned}$$

$$\begin{aligned}
E_z^{n+1}(0, j, k + \frac{1}{2}) &= E_z^n(1, j, k + \frac{1}{2}) \\
&+ \frac{c_0 \Delta t - \Delta x}{c_0 \Delta t + \Delta x} [E_z^{n+1}(1, j, k + \frac{1}{2}) - E_z^n(0, j, k + \frac{1}{2})], \quad (A.9)
\end{aligned}$$

$$\begin{aligned}
E_z^{n+1}(N_x, j, k + \frac{1}{2}) &= E_z^n(N_x - 1, j, k + \frac{1}{2}) \\
&+ \frac{c_0 \Delta t - \Delta x}{c_0 \Delta t + \Delta x} [E_z^{n+1}(N_x - 1, j, k + \frac{1}{2}) - E_z^n(N_x, j, k + \frac{1}{2})], \quad (A.10)
\end{aligned}$$

$$\begin{aligned}
E_z^{n+1}(i, 0, k + \frac{1}{2}) &= E_z^n(i, 1, k + \frac{1}{2}) \\
&+ \frac{c_0 \Delta t - \Delta y}{c_0 \Delta t + \Delta y} [E_z^{n+1}(i, 1, k + \frac{1}{2}) - E_z^n(i, 0, k + \frac{1}{2})],
\end{aligned} \tag{A.11}$$

and

$$\begin{aligned}
E_z^{n+1}(i + \frac{1}{2}, N_y, k) &= E_z^n(i + \frac{1}{2}, N_y - 1, k) \\
&+ \frac{c_0 \Delta t - \Delta y}{c_0 \Delta t + \Delta y} [E_z^{n+1}(i + \frac{1}{2}, N_y - 1, k) - E_z^n(i + \frac{1}{2}, N_y, k)].
\end{aligned} \tag{A.12}$$

## A.2 2nd Order Mur FDTD Equations

The second order Mur equations are substantially more complicated than the first order Mur, they are

$$\begin{aligned}
E_x^{n+1}(i + \frac{1}{2}, j, 0) &= -E_x^{n-1}(i + \frac{1}{2}, j, 1) \\
&+ \frac{c_0 \Delta t - \Delta z}{c_0 \Delta t + \Delta z} [E_x^{n+1}(i + \frac{1}{2}, j, 1) + E_x^n(i + \frac{1}{2}, j, 1)] \\
&+ \frac{2\Delta z}{c_0 \Delta t + \Delta z} [E_x^n(i + \frac{1}{2}, j, 0) + E_x^n(i + \frac{1}{2}, j, 1)] \\
&+ \frac{\Delta z (c_0 \Delta t)^2}{2(\Delta x)^2 (c_0 \Delta t + \Delta z)} [E_x^n(i + \frac{3}{2}, j, 0) - 2E_x^n(i + \frac{1}{2}, j, 0) + E_x^n(i - \frac{1}{2}, j, 0) \\
&\quad + E_x^n(i + \frac{3}{2}, j, 1) - 2E_x^n(i + \frac{1}{2}, j, 1) + E_x^n(i - \frac{1}{2}, j, 1)] \\
&+ \frac{\Delta z (c_0 \Delta t)^2}{2(\Delta y)^2 (c_0 \Delta t + \Delta z)} [E_x^n(i + \frac{1}{2}, j + 1, 0) - 2E_x^n(i + \frac{1}{2}, j, 0) + E_x^n(i + \frac{1}{2}, j - 1, 0) \\
&\quad + E_x^n(i + \frac{1}{2}, j + 1, 1) - 2E_x^n(i + \frac{1}{2}, j, 1) + E_x^n(i + \frac{1}{2}, j - 1, 1)],
\end{aligned} \tag{A.13}$$

$$\begin{aligned}
E_x^{n+1}(i + \frac{1}{2}, j, N_z) &= -E_x^{n-1}(i + \frac{1}{2}, j, N_z - 1) \\
&+ \frac{c_0 \Delta t - \Delta z}{c_0 \Delta t + \Delta z} [E_x^{n+1}(i + \frac{1}{2}, j, N_z - 1) + E_x^n(i + \frac{1}{2}, j, N_z - 1)] \\
&+ \frac{2\Delta z}{c_0 \Delta t + \Delta z} [E_x^n(i + \frac{1}{2}, j, N_z) + E_x^n(i + \frac{1}{2}, j, N_z - 1)]
\end{aligned} \tag{A.14}$$

$$\begin{aligned}
& + \frac{\Delta z(c_0\Delta t)^2}{2(\Delta x)^2(c_0\Delta t + \Delta z)} [E_x^n(i + \frac{3}{2}, j, N_z) - 2E_x^n(i + \frac{1}{2}, j, N_z) + E_x^n(i - \frac{1}{2}, j, N_z) \\
& + E_x^n(i + \frac{3}{2}, j, N_z - 1) - 2E_x^n(i + \frac{1}{2}, j, N_z - 1) + E_x^n(i - \frac{1}{2}, j, N_z - 1)] \\
& + \frac{\Delta z(c_0\Delta t)^2}{2(\Delta y)^2(c_0\Delta t + \Delta z)} [E_x^n(i + \frac{1}{2}, j + 1, N_z) - 2E_x^n(i + \frac{1}{2}, j, N_z) + E_x^n(i + \frac{1}{2}, j - 1, N_z) \\
& + E_x^n(i + \frac{1}{2}, j + 1, N_z - 1) - 2E_x^n(i + \frac{1}{2}, j, N_z - 1) + E_x^n(i + \frac{1}{2}, j - 1, N_z - 1)],
\end{aligned}$$

$$\begin{aligned}
E_x^{n+1}(i + \frac{1}{2}, 0, k) &= -E_x^{n-1}(i + \frac{1}{2}, 1, k) \tag{A.15} \\
& + \frac{c_0\Delta t - \Delta y}{c_0\Delta t + \Delta y} [E_x^{n+1}(i + \frac{1}{2}, 1, k) + E_x^n(i + \frac{1}{2}, 1, k)] \\
& + \frac{2\Delta y}{c_0\Delta t + \Delta y} [E_x^n(i + \frac{1}{2}, 0, k) + E_x^n(i + \frac{1}{2}, 1, k)] \\
& + \frac{\Delta y(c_0\Delta t)^2}{2(\Delta x)^2(c_0\Delta t + \Delta y)} [E_x^n(i + \frac{3}{2}, 0, k) - 2E_x^n(i + \frac{1}{2}, 0, k) + E_x^n(i - \frac{1}{2}, 0, k) \\
& + E_x^n(i + \frac{3}{2}, 1, k) - 2E_x^n(i + \frac{1}{2}, 1, k) + E_x^n(i - \frac{1}{2}, 1, k)] \\
& + \frac{\Delta y(c_0\Delta t)^2}{2(\Delta z)^2(c_0\Delta t + \Delta y)} [E_x^n(i + \frac{1}{2}, 0, k + 1) - 2E_x^n(i + \frac{1}{2}, 0, k) + E_x^n(i + \frac{1}{2}, 0, k - 1) \\
& + E_x^n(i + \frac{1}{2}, 1, k + 1) - 2E_x^n(i + \frac{1}{2}, 1, k) + E_x^n(i + \frac{1}{2}, 1, k - 1)],
\end{aligned}$$

$$\begin{aligned}
E_x^{n+1}(i + \frac{1}{2}, N_y, k) &= -E_x^{n-1}(i + \frac{1}{2}, N_y - 1, k) \tag{A.16} \\
& + \frac{c_0\Delta t - \Delta y}{c_0\Delta t + \Delta y} [E_x^{n+1}(i + \frac{1}{2}, N_y - 1, k) + E_x^n(i + \frac{1}{2}, N_y - 1, k)] \\
& + \frac{2\Delta y}{c_0\Delta t + \Delta y} [E_x^n(i + \frac{1}{2}, N_y, k) + E_x^n(i + \frac{1}{2}, N_y - 1, k)] \\
& + \frac{\Delta y(c_0\Delta t)^2}{2(\Delta x)^2(c_0\Delta t + \Delta y)} [E_x^n(i + \frac{3}{2}, N_y, k) - 2E_x^n(i + \frac{1}{2}, N_y, k) + E_x^n(i - \frac{1}{2}, N_y, k) \\
& + E_x^n(i + \frac{3}{2}, N_y - 1, k) - 2E_x^n(i + \frac{1}{2}, N_y - 1, k) + E_x^n(i - \frac{1}{2}, N_y - 1, k)] \\
& + \frac{\Delta y(c_0\Delta t)^2}{2(\Delta z)^2(c_0\Delta t + \Delta y)} [E_x^n(i + \frac{1}{2}, N_y, k + 1) - 2E_x^n(i + \frac{1}{2}, N_y, k) + E_x^n(i + \frac{1}{2}, N_y, k - 1) \\
& + E_x^n(i + \frac{1}{2}, 1, k + 1) - 2E_x^n(i + \frac{1}{2}, 1, k) + E_x^n(i + \frac{1}{2}, 1, k - 1)],
\end{aligned}$$

$$\begin{aligned}
E_y^{n+1}(0, j + \frac{1}{2}, k) = & -E_y^{n-1}(1, j + \frac{1}{2}, k) \\
& + \frac{c_0 \Delta t - \Delta x}{c_0 \Delta t + \Delta x} [E_y^{n+1}(1, j + \frac{1}{2}, k) + E_y^n(1, j + \frac{1}{2}, k)] \\
& + \frac{2\Delta x}{c_0 \Delta t + \Delta x} [E_y^n(0, j + \frac{1}{2}, k) + E_y^n(1, j + \frac{1}{2}, k)] \\
& + \frac{\Delta x (c_0 \Delta t)^2}{2(\Delta z)^2 (c_0 \Delta t + \Delta x)} [E_y^n(0, j + \frac{1}{2}, k+1) - 2E_y^n(0, j + \frac{1}{2}, k) + E_y^n(0, j + \frac{1}{2}, k-1) \\
& + E_y^n(1, j + \frac{1}{2}, k+1) - 2E_y^n(1, j + \frac{1}{2}, k) + E_y^n(1, j + \frac{1}{2}, k-1)] \\
& + \frac{\Delta x (c_0 \Delta t)^2}{2(\Delta y)^2 (c_0 \Delta t + \Delta x)} [E_y^n(0, j + \frac{3}{2}, k) - 2E_y^n(0, j + \frac{1}{2}, k) + E_y^n(0, j - \frac{1}{2}, k) \\
& + E_y^n(1, j + \frac{3}{2}, k) - 2E_y^n(1, j + \frac{1}{2}, k) + E_y^n(1, j - \frac{1}{2}, k)],
\end{aligned} \tag{A.17}$$

$$\begin{aligned}
E_y^{n+1}(N_x, j + \frac{1}{2}, k) = & -E_y^{n-1}(N_x - 1, j + \frac{1}{2}, k) \\
& + \frac{c_0 \Delta t - \Delta x}{c_0 \Delta t + \Delta x} [E_y^{n+1}(N_x - 1, j + \frac{1}{2}, k) + E_y^n(N_x - 1, j + \frac{1}{2}, k)] \\
& + \frac{2\Delta x}{c_0 \Delta t + \Delta x} [E_y^n(N_x, j + \frac{1}{2}, k) + E_y^n(N_x - 1, j + \frac{1}{2}, k)] \\
& + \frac{\Delta x (c_0 \Delta t)^2}{2(\Delta z)^2 (c_0 \Delta t + \Delta x)} [E_y^n(N_x, j + \frac{1}{2}, k+1) - 2E_y^n(N_x, j + \frac{1}{2}, k) + E_y^n(N_x, j + \frac{1}{2}, k-1) \\
& + E_y^n(N_x - 1, j + \frac{1}{2}, k+1) - 2E_y^n(N_x - 1, j + \frac{1}{2}, k) + E_y^n(N_x - 1, j + \frac{1}{2}, k-1)] \\
& + \frac{\Delta x (c_0 \Delta t)^2}{2(\Delta y)^2 (c_0 \Delta t + \Delta x)} [E_y^n(N_x, j + \frac{3}{2}, k) - 2E_y^n(N_x, j + \frac{1}{2}, k) + E_y^n(N_x, j - \frac{1}{2}, k) \\
& + E_y^n(N_x - 1, j + \frac{3}{2}, k) - 2E_y^n(N_x - 1, j + \frac{1}{2}, k) + E_y^n(N_x - 1, j - \frac{1}{2}, k)],
\end{aligned} \tag{A.18}$$

$$\begin{aligned}
E_y^{n+1}(i, j + \frac{1}{2}, 0) = & -E_y^{n-1}(i, j + \frac{1}{2}, 1) \\
& + \frac{c_0 \Delta t - \Delta z}{c_0 \Delta t + \Delta z} [E_y^{n+1}(i, j + \frac{1}{2}, 1) + E_y^n(i, j + \frac{1}{2}, 1)] \\
& + \frac{2\Delta z}{c_0 \Delta t + \Delta z} [E_y^n(i, j + \frac{1}{2}, 0) + E_y^n(i, j + \frac{1}{2}, 1)] \\
& + \frac{\Delta z (c_0 \Delta t)^2}{2(\Delta x)^2 (c_0 \Delta t + \Delta z)} [E_y^n(i + 1, j + \frac{1}{2}, 0) - 2E_y^n(i, j + \frac{1}{2}, 0) + E_y^n(i - 1, j + \frac{1}{2}, 0)
\end{aligned} \tag{A.19}$$

$$\begin{aligned}
& +E_y^n(i+1, j+\frac{1}{2}, 1) - 2E_y^n(i, j+\frac{1}{2}, 1) + E_y^n(i-1, j+\frac{1}{2}, 1)] \\
& + \frac{\Delta z(c_0\Delta t)^2}{2(\Delta y)^2(c_0\Delta t + \Delta z)} [E_y^n(i, j+\frac{3}{2}, 0) - 2E_y^n(i, j+\frac{1}{2}, 0) + E_y^n(i, j-\frac{1}{2}, 0) \\
& + E_y^n(i, j+\frac{3}{2}, 1) - 2E_y^n(i, j+\frac{1}{2}, 1) + E_y^n(i, j-\frac{1}{2}, 1)],
\end{aligned}$$

$$\begin{aligned}
E_y^{n+1}(i, j+\frac{1}{2}, N_z) &= -E_y^{n-1}(i, j+\frac{1}{2}, N_z-1) \tag{A.20} \\
& + \frac{c_0\Delta t - \Delta z}{c_0\Delta t + \Delta z} [E_y^{n+1}(i, j+\frac{1}{2}, N_z-1) + E_y^n(i, j+\frac{1}{2}, N_z-1)] \\
& + \frac{2\Delta z}{c_0\Delta t + \Delta z} [E_y^n(i, j+\frac{1}{2}, N_z) + E_y^n(i, j+\frac{1}{2}, N_z-1)] \\
& + \frac{\Delta z(c_0\Delta t)^2}{2(\Delta x)^2(c_0\Delta t + \Delta z)} [E_y^n(i+1, j+\frac{1}{2}, N_z) - 2E_y^n(i, j+\frac{1}{2}, N_z) + E_y^n(i-1, j+\frac{1}{2}, N_z) \\
& + E_y^n(i+1, j+\frac{1}{2}, N_z-1) - 2E_y^n(i, j+\frac{1}{2}, N_z-1) + E_y^n(i-1, j+\frac{1}{2}, N_z-1)] \\
& + \frac{\Delta z(c_0\Delta t)^2}{2(\Delta y)^2(c_0\Delta t + \Delta z)} [E_y^n(i, j+\frac{3}{2}, N_z) - 2E_y^n(i, j+\frac{1}{2}, N_z) + E_y^n(i, j-\frac{1}{2}, N_z) \\
& + E_y^n(i, j+\frac{3}{2}, N_z-1) - 2E_y^n(i, j+\frac{1}{2}, N_z-1) + E_y^n(i, j-\frac{1}{2}, N_z-1)],
\end{aligned}$$

$$\begin{aligned}
E_z^{n+1}(0, j, k+\frac{1}{2}) &= -E_z^{n-1}(1, j, k+\frac{1}{2}) \tag{A.21} \\
& + \frac{c_0\Delta t - \Delta x}{c_0\Delta t + \Delta x} [E_z^{n+1}(1, j, k+\frac{1}{2}) + E_z^n(1, j, k+\frac{1}{2})] \\
& + \frac{2\Delta x}{c_0\Delta t + \Delta x} [E_z^n(0, j, k+\frac{1}{2}) + E_z^n(1, j, k+\frac{1}{2})] \\
& + \frac{\Delta x(c_0\Delta t)^2}{2(\Delta z)^2(c_0\Delta t + \Delta x)} [E_z^n(0, j, k+\frac{3}{2}) - 2E_z^n(0, j, k+\frac{1}{2}) + E_z^n(0, j, k-\frac{1}{2}) \\
& + E_z^n(1, j, k+\frac{3}{2}) - 2E_z^n(1, j, k+\frac{1}{2}) + E_z^n(1, j, k-\frac{1}{2})] \\
& + \frac{\Delta x(c_0\Delta t)^2}{2(\Delta y)^2(c_0\Delta t + \Delta x)} [E_z^n(0, j+1, k+\frac{1}{2}) - 2E_z^n(0, j, k+\frac{1}{2}) + E_z^n(0, j-1, k+\frac{1}{2}) \\
& + E_z^n(1, j+1, k+\frac{1}{2}) - 2E_z^n(1, j, k+\frac{1}{2}) + E_z^n(1, j-1, k+\frac{1}{2})],
\end{aligned}$$

$$\begin{aligned}
E_z^{n+1}(N_x, j, k + \frac{1}{2}) &= -E_z^{n-1}(N_x - 1, j, k + \frac{1}{2}) \\
&+ \frac{c_0 \Delta t - \Delta x}{c_0 \Delta t + \Delta x} [E_z^{n+1}(N_x - 1, j, k + \frac{1}{2}) + E_z^n(N_x - 1, j, k + \frac{1}{2})] \\
&+ \frac{2\Delta x}{c_0 \Delta t + \Delta x} [E_z^n(N_x, j, k + \frac{1}{2}) + E_z^n(N_x - 1, j, k + \frac{1}{2})] \\
&+ \frac{\Delta x (c_0 \Delta t)^2}{2(\Delta z)^2 (c_0 \Delta t + \Delta x)} [E_z^n(N_x, j, k + \frac{3}{2}) - 2E_z^n(N_x, j, k + \frac{1}{2}) + E_z^n(N_x, j, k - \frac{1}{2}) \\
&\quad + E_z^n(N_x - 1, j, k + \frac{3}{2}) - 2E_z^n(N_x - 1, j, k + \frac{1}{2}) + E_z^n(N_x - 1, j, k - \frac{1}{2})] \\
&+ \frac{\Delta x (c_0 \Delta t)^2}{2(\Delta y)^2 (c_0 \Delta t + \Delta x)} [E_z^n(N_x, j + 1, k + \frac{1}{2}) - 2E_z^n(N_x, j, k + \frac{1}{2}) + E_z^n(N_x, j - 1, k + \frac{1}{2}) \\
&\quad + E_z^n(N_x - 1, j, k + \frac{1}{2}) - 2E_z^n(N_x - 1, j, k + \frac{1}{2}) + E_z^n(N_x - 1, j - 1, k + \frac{1}{2})],
\end{aligned} \tag{A.22}$$

$$\begin{aligned}
E_z^{n+1}(i, 0, k + \frac{1}{2}) &= -E_z^{n-1}(i, 1, k + \frac{1}{2}) \\
&+ \frac{c_0 \Delta t - \Delta y}{c_0 \Delta t + \Delta y} [E_z^{n+1}(i, 1, k + \frac{1}{2}) + E_z^n(i, 1, k + \frac{1}{2})] \\
&+ \frac{2\Delta y}{c_0 \Delta t + \Delta y} [E_z^n(i, 0, k + \frac{1}{2}) + E_z^n(i, 1, k + \frac{1}{2})] \\
&+ \frac{\Delta y (c_0 \Delta t)^2}{2(\Delta z)^2 (c_0 \Delta t + \Delta y)} [E_z^n(i, 0, k + \frac{3}{2}) - 2E_z^n(i, 0, k + \frac{1}{2}) + E_z^n(i, 0, k - \frac{1}{2}) \\
&\quad + E_z^n(i, 1, k + \frac{3}{2}) - 2E_z^n(i, 1, k + \frac{1}{2}) + E_z^n(i, 1, k - \frac{1}{2})] \\
&+ \frac{\Delta y (c_0 \Delta t)^2}{2(\Delta x)^2 (c_0 \Delta t + \Delta y)} [E_z^n(i + 1, 0, k + \frac{1}{2}) - 2E_z^n(i, 0, k + \frac{1}{2}) + E_z^n(i - 1, 0, k + \frac{1}{2}) \\
&\quad + E_z^n(i + 1, 1, k + \frac{1}{2}) - 2E_z^n(i, 1, k + \frac{1}{2}) + E_z^n(i - 1, 1, k + \frac{1}{2})],
\end{aligned} \tag{A.23}$$

and

$$\begin{aligned}
E_z^{n+1}(i, N_y, k + \frac{1}{2}) &= -E_z^{n-1}(i, N_y - 1, k + \frac{1}{2}) \\
&+ \frac{c_0 \Delta t - \Delta y}{c_0 \Delta t + \Delta y} [E_z^{n+1}(i, N_y - 1, k + \frac{1}{2}) + E_z^n(i, N_y - 1, k + \frac{1}{2})] \\
&+ \frac{2\Delta y}{c_0 \Delta t + \Delta y} [E_z^n(i, N_y, k + \frac{1}{2}) + E_z^n(i, N_y - 1, k + \frac{1}{2})]
\end{aligned} \tag{A.24}$$



$$\begin{aligned}
& + \frac{\Delta y (c_0 \Delta t)^2}{2(\Delta z)^2 (c_0 \Delta t + \Delta y)} [E_z^n(i, N_y, k + \frac{3}{2}) - 2E_z^n(i, N_y, k + \frac{1}{2}) + E_z^n(i, N_y, k - \frac{1}{2}) \\
& \quad + E_z^n(i, N_y - 1, k + \frac{3}{2}) - 2E_z^n(i, N_y - 1, k + \frac{1}{2}) + E_z^n(i, N_y - 1, k - \frac{1}{2})] \\
& + \frac{\Delta y (c_0 \Delta t)^2}{2(\Delta x)^2 (c_0 \Delta t + \Delta y)} [E_z^n(i + 1, N_y, k + \frac{1}{2}) - 2E_z^n(i, N_y, k + \frac{1}{2}) + E_z^n(i - 1, N_y, k + \frac{1}{2}) \\
& \quad + E_z^n(i + 1, N_y - 1, k + \frac{1}{2}) - 2E_z^n(i, N_y - 1, k + \frac{1}{2}) + E_z^n(i - 1, N_y - 1, k + \frac{1}{2})].
\end{aligned}$$

## Appendix B

### FDTD PML Difference Equations

The the difference equations for the twelve PML fields are listed below.

$$\begin{aligned}
 E_{xy}^{n+1}(i + \frac{1}{2}, j, k) &= C_1^{ye}(i + \frac{1}{2}, j, k) E_{xy}^n(i + \frac{1}{2}, j, k) \\
 &+ C_2^{ye}(i + \frac{1}{2}, j, k) \left[ H_z^{n+\frac{1}{2}}(i + \frac{1}{2}, j + \frac{1}{2}, k) - H_z^{n+\frac{1}{2}}(i + \frac{1}{2}, j - \frac{1}{2}, k) \right]
 \end{aligned} \tag{B.1}$$

$$\begin{aligned}
 E_{xz}^{n+1}(i + \frac{1}{2}, j, k) &= C_1^{ze}(i + \frac{1}{2}, j, k) E_{xz}^n(i + \frac{1}{2}, j, k) \\
 &- C_2^{ze}(i + \frac{1}{2}, j, k) \left[ H_y^{n+\frac{1}{2}}(i + \frac{1}{2}, j, k + \frac{1}{2}) - H_y^{n+\frac{1}{2}}(i + \frac{1}{2}, j, k - \frac{1}{2}) \right]
 \end{aligned} \tag{B.2}$$

$$\begin{aligned}
 E_{yx}^{n+1}(i, j + \frac{1}{2}, k) &= C_1^{xe}(i, j + \frac{1}{2}, k) E_{yx}^n(i, j + \frac{1}{2}, k) \\
 &- C_2^{xe}(i, j + \frac{1}{2}, k) \left[ H_z^{n+\frac{1}{2}}(i + \frac{1}{2}, j + \frac{1}{2}, k) - H_z^{n+\frac{1}{2}}(i - \frac{1}{2}, j + \frac{1}{2}, k) \right]
 \end{aligned} \tag{B.3}$$

$$\begin{aligned}
 E_{yz}^{n+1}(i, j + \frac{1}{2}, k) &= C_1^{ze}(i, j + \frac{1}{2}, k) E_{yz}^n(i, j + \frac{1}{2}, k) \\
 &+ C_2^{ze}(i, j + \frac{1}{2}, k) \left[ H_x^{n+\frac{1}{2}}(i, j + \frac{1}{2}, k + \frac{1}{2}) - H_x^{n+\frac{1}{2}}(i, j + \frac{1}{2}, k - \frac{1}{2}) \right]
 \end{aligned} \tag{B.4}$$

$$\begin{aligned}
E_{zx}^{n+1}(i, j, k + \frac{1}{2}) &= C_1^{xe}(i, j, k + \frac{1}{2})E_{zx}^n(i, j, k + \frac{1}{2}) \\
&+ C_2^{xe}(i, j, k + \frac{1}{2}) \left[ H_y^{n+\frac{1}{2}}(i + \frac{1}{2}, j, k + \frac{1}{2}) - H_y^{n+\frac{1}{2}}(i - \frac{1}{2}, j, k + \frac{1}{2}) \right]
\end{aligned} \tag{B.5}$$

$$\begin{aligned}
E_{zy}^{n+1}(i, j, k + \frac{1}{2}) &= C_1^{ye}(i, j, k + \frac{1}{2})E_{zy}^n(i, j, k + \frac{1}{2}) \\
&- C_2^{ye}(i, j, k + \frac{1}{2}) \left[ H_x^{n+\frac{1}{2}}(i, j + \frac{1}{2}, k + \frac{1}{2}) - H_x^{n+\frac{1}{2}}(i, j - \frac{1}{2}, k + \frac{1}{2}) \right]
\end{aligned} \tag{B.6}$$

where the two constants,  $C_1^{\alpha e}$  and  $C_2^{\alpha e}$   $\alpha = x, y, z$ , are given by

$$C_1^{\alpha e}(i, j, k) = e^{-\sigma_{\alpha}^e(i, j, k)\Delta t/\epsilon(i, j, k)} \tag{B.7}$$

and

$$C_2^{\alpha e}(i, j, k) = \frac{(1 - C_1^{\alpha e}(i, j, k))}{\sigma_{\alpha}^e(i, j, k)\Delta\alpha}. \tag{B.8}$$

Similarly, the the difference equation for the magnetic fields used in the PML region of the computational domain are

$$\begin{aligned}
H_{xy}^{n+\frac{1}{2}}(i, j + \frac{1}{2}, k + \frac{1}{2}) &= C_1^{ym}(i, j + \frac{1}{2}, k + \frac{1}{2})H_{xy}^{n-\frac{1}{2}}(i, j + \frac{1}{2}, k + \frac{1}{2}) \\
&- C_2^{ym}(i, j + \frac{1}{2}, k + \frac{1}{2}) \left[ E_z^n(i, j + 1, k + \frac{1}{2}) - E_z^n(i, j, k + \frac{1}{2}) \right]
\end{aligned} \tag{B.9}$$

$$\begin{aligned}
H_{xz}^{n+\frac{1}{2}}(i, j + \frac{1}{2}, k + \frac{1}{2}) &= C_1^{zm}(i, j + \frac{1}{2}, k + \frac{1}{2})H_{xz}^{n-\frac{1}{2}}(i, j + \frac{1}{2}, k + \frac{1}{2}) \\
&+ C_2^{zm}(i, j + \frac{1}{2}, k + \frac{1}{2}) \left[ E_y^n(i, j + \frac{1}{2}, k + 1) - E_y^n(i, j + \frac{1}{2}, k) \right]
\end{aligned} \tag{B.10}$$

$$\begin{aligned}
H_{yx}^{n+\frac{1}{2}}(i + \frac{1}{2}, j, k + \frac{1}{2}) &= C_1^{xm}(i + \frac{1}{2}, j, k + \frac{1}{2})H_{yx}^{n-\frac{1}{2}}(i + \frac{1}{2}, j, k + \frac{1}{2}) \\
&+ C_2^{xm}(i + \frac{1}{2}, j, k + \frac{1}{2}) \left[ E_z^n(i + 1, j, k + \frac{1}{2}) - E_z^n(i, j, k + \frac{1}{2}) \right]
\end{aligned} \tag{B.11}$$

$$\begin{aligned}
H_{yz}^{n+\frac{1}{2}}(i+\frac{1}{2}, j, k+\frac{1}{2}) &= C_1^{zm}(i+\frac{1}{2}, j, k+\frac{1}{2})H_{yz}^{n-\frac{1}{2}}(i+\frac{1}{2}, j, k+\frac{1}{2}) \\
&- C_2^{zm}(i+\frac{1}{2}, j, k+\frac{1}{2}) \left[ E_x^n(i+\frac{1}{2}, j, k+1) - E_x^n(i+\frac{1}{2}, j, k) \right]
\end{aligned} \quad (B.12)$$

$$\begin{aligned}
H_{zx}^{n+\frac{1}{2}}(i+\frac{1}{2}, j+\frac{1}{2}, k) &= C_1^{xm}(i+\frac{1}{2}, j+\frac{1}{2}, k)H_{zx}^{n-\frac{1}{2}}(i+\frac{1}{2}, j+\frac{1}{2}, k) \\
&- C_2^{xm}(i+\frac{1}{2}, j+\frac{1}{2}, k) \left[ E_y^n(i+1, j+\frac{1}{2}, k) - E_y^n(i, j+\frac{1}{2}, k) \right]
\end{aligned} \quad (B.13)$$

$$\begin{aligned}
H_{zy}^{n+\frac{1}{2}}(i+\frac{1}{2}, j+\frac{1}{2}, k) &= C_1^{ym}(i+\frac{1}{2}, j+\frac{1}{2}, k)H_{zy}^{n-\frac{1}{2}}(i+\frac{1}{2}, j+\frac{1}{2}, k) \\
&+ C_2^{ym}(i+\frac{1}{2}, j+\frac{1}{2}, k) \left[ E_x^n(i+\frac{1}{2}, j+1, k) - E_x^n(i+\frac{1}{2}, j, k) \right]
\end{aligned} \quad (B.14)$$

where the two constants,  $C_1^{\alpha m}$  and  $C_2^{\alpha m}$  are given by

$$C_1^{\alpha m}(i, j, k) = e^{-\sigma_\alpha^m(i, j, k)\Delta t/\mu_0} \quad (B.15)$$

and

$$C_2^{\alpha m}(i, j, k) = \frac{(1 - C_1^{\alpha m}(i, j, k))}{\sigma_\alpha^m(i, j, k)\Delta\alpha}. \quad (B.16)$$

The PML coefficients are a function of position, direction and the field type. They are functions of position because both the permittivity and the PML conductivity are functions of position. They are functions of direction since the spatial derivative approximations are functions of grid size which in general are different for each direction. Finally, they are functions of field type since electric and magnetic field equations depend on electric and magnetic conductivities respectively.

As previously stated the PML conductivities are derived by the continuous equation,

$$\sigma_\alpha^{e,m} = \sigma_{\alpha max}^{e,m} \left( \frac{\alpha}{d} \right)^n, \quad \alpha = x, y, z. \quad (B.17)$$

where  $\sigma_{\alpha max}$  is the maximum conductivity and  $d$  is the PML thickness such that  $d = n_{layers}\Delta\alpha$  ( $n_{layers}$  is the number of discretized PML layers). The discretized electric conductivity (in the  $y$  direction for example) is calculated by

$$\sigma_y^e(j\Delta y) = \int_{(j-\frac{1}{2})\Delta y}^{(j+\frac{1}{2})\Delta y} \sigma_{y max}^e \left(\frac{y}{d}\right)^n dy. \quad (B.18)$$

Since the magnetic conductivities are shifted by half a grid space compared to the electric fields, the magnetic conductivities are also shifted so that

$$\sigma_y^m\left(\left(j + \frac{1}{2}\right)\Delta y\right) = \int_{(j-1)\Delta y}^{(j+1)\Delta y} \sigma_{y max}^m \left(\frac{y}{d}\right)^n dy. \quad (B.19)$$

As equations (B.18) and (B.19) show, the discretized conductivities are calculated as the average conductivity over one grid dimension centered at the field location.

With a uniform grid, the coefficient direction dependency is removed. In a single media environment, the coefficients are just a function of the PML layer and the field type. For example,  $C_1^{\alpha e}$ ,  $C_2^{\alpha e}$ ,  $C_1^{\alpha m}$ , and  $C_2^{\alpha m}$  become

$$C_1^e(l) = e^{-\sigma_{max}^e g(l)\Delta t/\epsilon_0}, \quad (B.20)$$

$$C_2^e(l) = \frac{(1 - C_1^e(l))}{\sigma_{max}^e g(l)\Delta}, \quad (B.21)$$

$$C_1^m(l) = e^{-\sigma_{max}^m g(l)\Delta t/\mu_0}, \quad (B.22)$$

and

$$C_2^m(l) = \frac{(1 - C_1^m(l))}{\sigma_{max}^m g(l)\Delta}, \quad (B.23)$$

where  $l$  is the index of the PML layer and  $g(l)$  is a grid factor defined as

$$g(l) = g(l\Delta) = \int_{(l-\frac{1}{2})\Delta}^{(l+\frac{1}{2})\Delta} \left(\frac{\alpha}{d}\right)^n d\alpha, \quad \alpha = x, y, \text{ or } z. \quad (B.24)$$

Since one of the PML matching conditions is

$$\frac{\sigma^m}{\mu_0} = \frac{\sigma^e}{\epsilon_0} \quad (\text{B.25})$$

the first coefficient is field independent, *i.e.*  $C_1^e = C_1^m = C_1$ .

Furthermore, if there is another media with  $(\epsilon_1, \mu_0)$  then

$$C_{11}^e(l) = e^{-\sigma_{1\max}^e g(l) \Delta t / \epsilon_1}, \quad (\text{B.26})$$

$$C_{12}^e(l) = \frac{(1 - C_{11}^e(l))}{\sigma_{1\max}^e g(l) \Delta}, \quad (\text{B.27})$$

Since the PML matching conditions between two dielectrics is

$$\frac{\sigma_1^e}{\epsilon_1} = \frac{\sigma_0^e}{\epsilon_0} \quad (\text{B.28})$$

we see that the first coefficient is media independent, *i.e.*  $C_{01}^e = C_{11}^e$ .

Now let there be  $N$  different dielectrics defined by their permittivities,  $\epsilon_\gamma, \gamma = 0, 1, 2, \dots, N$  using freespace as a baseline ( $\alpha = 0$ ) then the final equations for the formulation of FDTD PML coefficients are

$$C_{\gamma 1}(l) = C_{01}(l) \quad (\text{B.29})$$

and

$$C_{\gamma 2}^e(l) = \frac{(1 - C_{01}(l))}{\sigma_{0\max}^e \frac{\epsilon_\gamma}{\epsilon_0} g(l) \Delta}. \quad (\text{B.30})$$

The magnetic coefficients are defined by

$$C_{\gamma 2}^m(l) = \frac{(1 - C_{01}(l))}{\sigma_{0\max}^e \frac{\mu_0}{\epsilon_\gamma} g(l) \Delta}, \quad (\text{B.31})$$

which simplifies to

$$C_{\gamma^2}^m(l) = \frac{(1 - C_{01}(l))}{\sigma_{0max}^e \frac{\mu_0}{\epsilon_0} g(l) \Delta}, \quad (\text{B.32})$$

becoming media independent. Note that when  $\sigma^e = 0$  then the PML explicit exponential equations become standard Maxwell's difference equations, where

$$C_{01} = 1, \quad (\text{B.33})$$

$$C_{\gamma^2}^e = \frac{\Delta t}{\epsilon_\gamma \Delta}, \quad (\text{B.34})$$

and

$$C_{\gamma^2}^m = \frac{\Delta t}{\mu_0 \Delta}. \quad (\text{B.35})$$

# Appendix C

## Transportation Problem

The transportation problem is used to construct a solution to the optimal set of branch cuts that minimizes the total branch cut length.

### C.1 Introduction

The transport problem is a specific example of a wide class of linear programming problems [181]. Essentially the problem is to minimize the cost of transporting goods to  $m$  locations with  $n$  supply vehicles. Mathematically the transportation problem minimizes the total cost defined by

$$z = \sum_{i=1}^m \sum_{j=1}^n c_{i,j} x_{i,j}, \quad (\text{C.1})$$

within the constraint that a supplier (supply node),  $i$ , can supply no more than  $a_i$  units,

$$\sum_{j=1}^n x_{i,j} \leq a_i, \quad i = 1, 2, \dots, m, \quad (\text{C.2})$$

and each receiver (demand node)  $j$  must receive at least  $b_j$  units,

$$\sum_{i=1}^m x_{i,j} \geq b_j, \quad j = 1, 2, \dots, n \quad (\text{C.3})$$



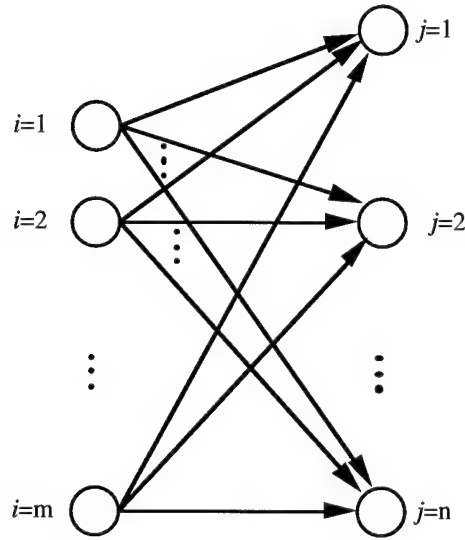


Figure C-1: Transportation network.

and no units are shipped from demand nodes to supply nodes,

$$x_{i,j} \geq 0, \quad i = 1, 2, \dots, m \quad j = 1, 2, \dots, n \quad (\text{C.4})$$

and the cost of shipping one unit from the  $i$ th supply node to the  $j$ th demand node is  $c_{i,j}$ . The values  $a_i$ ,  $b_j$ , and  $c_{i,j}$ , are nonnegative integers.

This problem can be constructed as a *directed network* with a set of nodes,  $V$ , and a set of *edges*,  $E$ . A directed edge is a connection between two nodes that has a defined flow direction. The network is *bipartite* and *complete*. Bipartite means that the nodes can be divided into two distinct groups; in this case the supply nodes ( $i = 1, 2, \dots, m$ ) and the demand nodes ( $j = 1, 2, \dots, n$ ). Completeness implies all the nodes are somehow connected to each other. In the transport problem each supply node has an edge to each of the  $n$  demand nodes and each edge has a unit cost,  $c_{i,j}$ , associated with using it. So the whole problem boils down to finding the shipping amounts,  $x_{i,j}$ , that minimize the total cost  $z$ . Figure C-1 is a graph of the transportation problem.

The problem can be solved only if there are enough units in supply to meet the demand,

$$\sum_{i=1}^m a_i \geq \sum_{j=1}^n b_j,$$

where the  $b_j$  is the demand at node  $j$ . All the deliveries to demand node  $j$  should add up to the total demand,

$$\sum_{i=1}^n x_{i,j} = b_j.$$

If there are exactly enough units in supply to meet the total demand,

$$\sum_{i=1}^m a_i = \sum_{j=1}^n b_j,$$

then every solution will satisfy the inequalities (C.2) and (C.3). So, to solve the problem an additional demand node,  $n + 1$ , may be added with a demand equal to the excess supply,

$$b_{n+1} = \sum_{i=1}^m a_i - \sum_{j=1}^n b_j$$

that costs nothing to deliver *i.e.*  $c_{i,n+1} = 0$ .

The solution approach is to transform the problem into finding the *maximum flow* through a network.

## C.2 Maximum Flow Through a Network

Given a network,  $N = (V, E)$ , there is a source node,  $s$ , and a sink node,  $t$ . Each edge has a capacity,  $k_{i,j}$ . The flow through any edge,  $x_{i,j}$ , must satisfy  $0 \leq x_{i,j} \leq k_{i,j}$ . Furthermore, all the nodes other than  $s$  and  $t$  must obey a conservation of flow given by

$$\sum_i x_{i,j} - \sum_l x_{j,l} = 0,$$

where  $i$  are the edges flowing into node  $j$  and  $l$  are the edges flowing out of node  $j$ . If we define  $f(t)$  as the flow into the sink node  $t$ , then we want to find the set of  $x_{i,j}$

such that  $f(t)$  is a maximum.

To find the maximum flow in a network, we look for any path from  $s$  to  $t$  that can *augment* the flow. As we search possible edges for inclusion into an augmenting path, if the  $(i, j)$ th edge is in the direction of the flow, then  $x_{i,j}$  must be less than  $k_{i,j}$  for this edge to be included; if the edge is in the direction opposing the flow then  $x_{i,j}$  must be nonzero to be included.

To find a path from  $s$  to  $t$  that augments the flow, a systematic process of *labeling* and *scanning* the nodes, starting at  $s$  and ending at  $t$ , is performed. At any give time in the search, a node can be in one of three states: 1.) unlabeled and unscanned; 2.) labeled and unscanned; or 3.) labeled and scanned.

Each edge has a capacity,  $k_{i,j}$ , and a flow  $x_{i,j}$ . The capacities are fixed and the flows are varied to achieve the maximum flow. All flows are initially set to zero ( $x_{i,j} = 0$ ). Thus, in the beginning, any path with positive flow from  $s$  to  $t$  will be an augmenting path. The labeling of a node,  $j$ , assigns two numbers to it: 1.) a source node,  $i$ , (not necessarily  $s$  and 2.) the maximum augmentation flow possible,  $f_j$ , from that source node.

All nodes start as unlabeled and unscanned. We start by labeling  $s$  with  $(-, \infty)$ . There is no source node feeding  $s$  since it is the first node in the path and it has an infinite capacity to augment the flow. Node  $s$  is now considered labeled and unscanned.

Next, for *any* node  $j$  that is labeled with  $(i, f_j(\text{or } -f_j))$  and unscanned, the node is scanned by labeling all of its adjacent nodes,  $l$ , that are currently unlabeled. If an edge is directed from node  $j$  to node  $l$  and the edge has excess capacity (*i.e.*  $x_{i,j} \leq k_{i,j}$ ), then we label node  $l$  with  $(j, f_l)$  where  $f_l$  is the maximum amount of the flow that node  $j$  can augment to node  $l$  through edge  $(j, l)$ . The amount that the flow can be augmented is the minimum between  $f_j$  (the amount at node  $j$  available to augment) and  $k_{i,j} - x_{i,j}$  (the excess capacity available to augment).

If the edge is directed from node  $l$  to node  $j$  and the edge has nonzero flow (*i.e.*

$x_{i,j} > 0$ ) then we label node  $l$  with  $(j, -f_l)$  where  $f_l$  is the maximum amount of the flow that node  $j$  can augment to node  $l$  through edge  $(j, l)$  which is the minimum between  $f_j$  (the amount at node  $j$  it can take from  $l$ ) and  $x_{i,j}$  (the most the flow can be reduced through the edge).

The labeling and scanning continues until the  $t$  node is labeled with  $(l, f_t)$  or no path can be found to  $t$  to augment the flow. If no path is found, the flow is maximized and the problem is solved. If an augmenting path is found, then the edge flows  $(x_{i,j})$  through the path are reassigned to increase the flow from  $s$  to  $t$  by  $f_t$ . Next all the labels are removed and the process starts over.

There is a theorem in Graph Theory called Ford-Fulkerson that states when the labeling algorithm terminates the flow is optimal. Furthermore, if the algorithm always uses the shortest augmenting path (*i.e.* fewest edges) the time to solve the problem is on the order of  $nm^2$  where  $n$  is the number of nodes and  $m$  is the number of edges.

## C.3 Transportation and the Maximum Flow Problem

The transportation problem can be transformed into a maximum flow problem so that the algorithm above can be used.

First, we insert a source node  $s$  to the left of the  $m$  supply nodes  $s_i$ ,  $i = 1, 2, \dots, m$ . A directed edge with capacity  $a_i$  is drawn from  $s$  to  $s_i$ . Next, we insert a sink node  $t$  to the right of the  $n$  demand nodes  $t_j$ ,  $j = 1, 2, \dots, n$ . A directed edge with capacity  $b_j$  is drawn from  $t_j$  to  $t$ . Figure C-2 is a representation of the network used to solve the transportation problem. Unlike the original graph not all edges between the source and demand nodes are allowed.

By duality in Graph Theory, we may assign dual variables  $u_i$  and  $v_j$  to the constraints of the transportation problem, and where the old problem minimizes a quan-

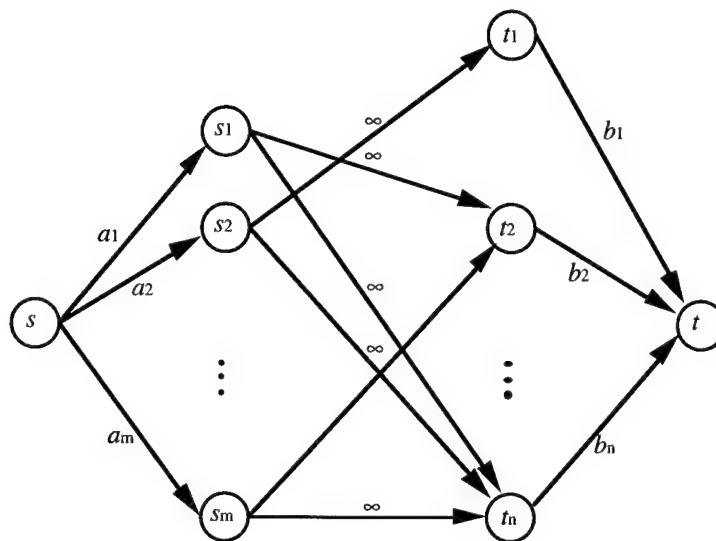


Figure C-2: Transportation as a maximum flow network.

tity, the new problem maximizes a new quantity based on the old constraints. In this case, the quantity

$$-\sum_{i=1}^m u_i a_i + \sum_{j=1}^n u_j b_j$$

is maximized within the constraints

$$-u_i + v_j \leq c_{i,j}$$

and

$$u_i, v_j \geq 0.$$

Now the edges from  $s_i$  to  $t_j$  are allowed if the dual variables satisfy  $-u_i + v_j = c_{i,j}$ . Each of these edges has infinite capacity. Given a set of  $u_i$  and  $v_j$ , a network is constructed and the maximum flow is found. However, the original transportation problem demand constraints must be checked to see if they are satisfied *i.e.*

$$\sum_{i=1}^m \geq b_j?$$

The original supply constraints are inherently satisfied by setting the capacity between the source node  $s$  and the supply node  $s_i$  to  $a_i$ .

If the demand constraint is met the problem is done; otherwise, a new set of  $u_i$  and  $v_j$  is found that does not change the current edge flows. In other words new edges must be established. To create new edges we define a flow increment,  $\delta$ ,

$$\delta = \min[c_{i,j} + u_i - v_j : i \in I, j \in \bar{J}]$$

where  $I$  is the set of labeled supply nodes and  $\bar{J}$  is the set of unlabeled demand nodes. In this step we're looking for the lowest cost path that is not currently being used. Then the new dual variables are  $u_i = u_i$  if node  $s_i$  is labeled and  $u_i = u_i + \delta$  if  $s_i$  is unlabeled, and  $v_j = v_j$  if node  $t_j$  is labeled and  $v_j = v_j + \delta$  if  $t_j$  is unlabeled.

Then the maximum flow algorithm is run and the demand constraints are examined again. The process repeats until the demand constraints are met.

## C.4 Application to Branch Cut Connections

The connection of positive and negative residues to form branch cuts is a very special case of the transportation problem. We can consider the positive residues as the supply nodes,  $i$ , and the negative residues as the demand nodes,  $j$ . Since there are an equal number of positive and negative residues,  $m = n$ . Furthermore, since a single positive residue can connect to exactly one negative residue, we have  $a_i = 1$  and  $b_j = 1$ . Finally, the cost,  $c_{i,j}$ , of transporting one unit from supply node  $i$  to demand node  $j$ , is the distance (by pixel location) between the corresponding residue pair defined as  $l_{i,j}$ .

Solving the transportation problem with

$$a_i = 1, \quad i = 1, 2, \dots, m,$$

$$b_j = 1, \quad j = 1, 2, \dots, n,$$

and

$$c_{i,j} = l_{i,j}$$

is equivalent to finding the set of branch cut connections that minimizes the sum of all branch cut lengths.

# Bibliography

- [1] K. S. Yee. Numerical solution of initial boundary value problems involving Maxwell's equations in isotropic media. *IEEE Trans. Antennas Propagat.*, 14(4):302–307, 1966.
- [2] A. Taflove and M. E. Brodwin. Numerical solution of steady-state electromagnetic scattering problems using the time-dependent Maxwell's equations. *IEEE Trans. Microwave Theory Tech.*, MTT-23(8):623–630, 1975.
- [3] A. Taflove. Application of the finite-difference time-domain method to sinusoidal steady-state electromagnetic-penetration problems. *IEEE Trans. Electromagn. Compat.*, EMC-22(2):191–202, 1980.
- [4] G. Mur. The modeling of singularities in the finite-difference approximation of the time-domain electromagnetic-field equations. *IEEE Trans. Microwave Theory Tech.*, MTT-29(10):1073–1077, 1981.
- [5] L. T. Simpson, R. Holland, and S. Arman. Treatment of late time instabilities in finite-difference EMP scattering codes. *IEEE Trans. Nuclear Sci.*, 29(6):1943–1948, 1982.
- [6] R. Holland. Finite difference solutions of Maxwell's equations in generalized nonorthogonal coordinates. *IEEE Trans. Nucl. Sci.*, NS-30(6):4589–4591, 1983.
- [7] R. Holland. THREDS: A finite-difference time-domain EMP code in 3D spherical coordinates. *IEEE Trans. Nucl. Sci.*, NS-30(6):4592–4595, 1983.
- [8] R. Holland and J. W. Williams. Total-field versus scattered-field finite-difference codes: A comparative assessment. *IEEE Trans. Nucl. Sci.*, NS-30(6):4583–4588, 1983.
- [9] D. H. Choi and W. J. R. Hoefer. A graded mesh FD-TD algorithm for eigenvalue problems. In *17th European Microwave Conference*, pages 413–417, 1987.
- [10] I. S. Kim and W. J. R. Hoefer. A local mesh refinement algorithm for the time domain-finite difference method using Maxwell's curl equations. *IEEE Trans. Microwave Theory Tech.*, 38(6):812–815, 1990.



- [11] D. M. Sheen. *Numerical Modeling of Microstrip Circuits and Antennas*. PhD thesis, Massachusetts Institute of Technology, Cambridge, MA, 1991.
- [12] S. S. Zivanovic, K. S. Yee, and K. K. Mei. A subgridding method for the time-domain finite-difference method to solve Maxwell's equations. *IEEE Trans. Microwave Theory Tech.*, 39(3):471–479, 1991.
- [13] K. Li, M. A. Tassoudji, R. T. Shin, and J. A. Kong. Simulation of electromagnetic radiation and scattering using a finite difference-time domain technique. *Computer Applications in Engineering Education*, 1(1):45–62, 1992.
- [14] K. S. Kunz and R. J. Luebbers. *The Finite Difference Time Domain Method for Electromagnetics*. CRC Press, Boca Raton, FL, 1993.
- [15] R. Gillard, J.-H. Corre, M. Drissi, and J. Citerne. A general treatment of matched terminations using integral equations-modeling and applications. *IEEE Trans. Microwave Theory Tech.*, 42(12):2545–2553, 1994.
- [16] R. Holland. Finite-difference time-domain (FDTD) analysis of magnetic diffusion. *IEEE Trans. Electromagn. Compat.*, 36(1):32–39, 1994.
- [17] K. L. Shlager, S. L. Ray, J. G. Maloney, and A. F. Peterson. Conditions for the equivalence of the Chen and Yee FDTD algorithms. *IEEE Microwave Guided Wave Lett.*, 4(2):48–49, 1994.
- [18] V. Varadarajan and R. Mittra. Finite-difference time-domain (FDTD) analysis using distributed computing. *IEEE Microwave Guided Wave Lett.*, 4(5):144–145, 1994.
- [19] A. Bahr, A. Lauer, and I. Wolff. An efficient source formulation for the analysis of microwave circuits using the FDTD. In *IEEE Antennas and Propagat. Soc. Int. Symposium*, volume 1, pages 244–247, Newport Beach, CA, June 1995.
- [20] K. Li. *Finite Difference Time Domain Analysis of Electromagnetic Interference and Radiation Problems*. PhD thesis, Massachusetts Institute of Technology, Cambridge, MA, 1995.
- [21] P. Mezzanotte, L. Roselli, and R. Sorrentino. A simple way to model curved metal boundaries in FDTD algorithm avoiding staircase approximation. *IEEE Microwave Guided Wave Lett.*, 5(8):267–269, 1995.
- [22] A. Taflov. *Computational Electrodynamics: The Finite-Difference Time-Domain Method*. Artech House, Boston, MA, 1995.

- [23] M. Celuch-Marcysiak and W. K. Gwarek. A novel variable source impedance technique for emulating unperturbed eigenmodes in the FD-TD method. In *Proc. 3rd IEE Conference on Computation in Electromagnetics*, Bath, England, April 1996.
- [24] C. H. Durney, W. Sui, D. A. Christensen, and J. Zhu. A general formulation for connecting sources and passive lumped-circuit elements across multiple 3-D FDTD cells. *IEEE Microwave Guided Wave Lett.*, 6(2):85-87, 1996.
- [25] T.-W. Huang, B. Houshmand, and T. Itoh. Efficient modes extraction and numerically exact matched sources for a homogeneous waveguide cross-section in a FDTD simulation. In *IEEE MTT-S Int. Microwave Symposium*, volume 1, pages 31-34, San Diego, CA, May 1994.
- [26] J. De Moerloose and D. De Zutter. Poynting's theorem for the finite-difference time-domain method. *Microwave Opt. Technol. Lett.*, 8(5):257-260, 1995.
- [27] W. K. Gwarek and M. Celuch-Marcysiak. A differential method of reflection coefficient extraction from FDTD simulations. *IEEE Microwave Guided Wave Lett.*, 6(5):215-217, 1996.
- [28] M. Celuch-Marcysiak, A. Kozak, and W. K. Gwarek. A universal method of accurate S-parameter extraction from FD-TD simulations applicable to oblique ports. In *IEEE MTT-S Int. Microwave Symposium*, volume 2, pages 593-569, San Francisco, CA, June 1996.
- [29] G. Mur. Absorbing boundary conditions for the finite-difference approximation of the time-domain electromagnetic-field equations. *IEEE Trans. Electromagn. Compat.*, EMC-23(4):377-382, 1981.
- [30] J. E. Roy and D. H. Choi. The application of a simple absorbing boundary algorithm to cylindrical waveguide. In *IEEE Antennas and Propagat. Soc. Int. Symposium*, pages 58-61, San Jose, CA, 1989.
- [31] K. K. Mei and J. Fang. Superabsorption—A method to improve absorbing boundary conditions. *IEEE Trans. Antennas Propagat.*, 40(9):1001-1010, 1992.
- [32] T. W. Huang, B. Houshmand, and T. Itoh. The FDTD wide-band absorbing boundary conditions for the excitation plane. In *IEEE Antennas and Propagat. Soc. Int. Symposium*, volume 1, pages 2-5, Ann Arbor, MI, June 1993.
- [33] K. Naishadham and X. P. Lin. Application of spectral domain Prony's method to the FDTD analysis of planar microstrip circuits. *IEEE Trans. Microwave Theory Tech.*, 42(12):2391-2398, 1994.

- [34] C. J. Railton, E. M. Daniel, and J. P. McGeehan. Use of second-order absorbing boundary conditions for the termination of planar waveguides in the FDTD method. *Electron. Lett.*, 29(10):900–902, 1993.
- [35] K. Naishadham and X. P. Lin. Application of the spectral estimation techniques to correct the reflection from imperfect absorbing boundaries in the FDTD simulation of microwave circuits. In *IEEE MTT-S Int. Microwave Symposium*, volume 1, pages 361–364, San Diego, CA, May 1994.
- [36] E. A. Navarro, L. Gallart, J. L. Cruz, B. Gimeno, and V. Such. Accurate absorbing boundary conditions for the FDTD analysis of H-plane waveguide discontinuities. *IEE Proc. H, Microw. Antennas Propag.*, 141(1):59–61, 1994.
- [37] T. Ozdemir and J. L. Volakis. A comparison study of an absorbing condition and an artificial absorber for truncating finite element meshes. *Radio Science*, 29(5):1255–1263, 1994.
- [38] P.-Y. Zhao, J. Litva, and K.-L. Wu. A new stable and very dispersive boundary condition for the FD-TD method. In *IEEE MTT-S Int. Microwave Symposium*, volume 1, pages 35–38, May 1994.
- [39] C. Eswarappa and W. J. R. Hoefer. Treatment of instabilities of one-way equation absorbing boundary conditions using digital filters. In *IEEE MTT-S Int. Microwave Symposium*, volume 1, pages 39–42, Orlando, FL, 1995.
- [40] T. G. Jurgens. A broadband absorbing boundary condition for the FDTD modeling of circular waveguides. In *IEEE MTT-S Int. Microwave Symposium*, volume 1, pages 35–38, Orlando, FL, 1995.
- [41] J. Ritter, V. J. Brankovic, D. V. Krupezevic, and F. Arndt. A wide-band S-parameter extraction procedure for arbitrarily shaped inhomogeneous structures using time domain numerical techniques. In *IEEE MTT-S Int. Microwave Symposium*, volume 1, pages 273–276, Orlando, FL, 1995.
- [42] C. Spillard, S. R. Pennock, and P. R. Shepherd. Absorbing boundary conditions for the modeling of scatterers in parallel-plate transmission media. *IEEE Microwave Guided Wave Lett.*, 5(8):241–242, 1995.
- [43] M. I. Aksum and G. Dural. Comparative evaluation of absorbing boundary conditions using Green's functions for layered media. *IEEE Trans. Antennas Propagat.*, 44(2):152–156, 1996.
- [44] K. Naishadham and X. P. Lin. Minimization of reflection error caused by absorbing boundary condition in the FDTD simulation of planar transmission lines. *IEEE Trans. Microwave Theory Tech.*, 44(1):41–47, 1996.

- [45] M. Mrozowski, M. Niedzwiecki, and P. Suchomski. Improved wideband highly dispersive absorbing boundary condition. *Electron. Lett.*, 32(12):1109–1111, 1996.
- [46] J.-P. Berenger. A perfectly matched layer for the absorption of electromagnetic waves. *J. Comput. Phys.*, 114(1):185–200, 1994.
- [47] D. S. Katz, E. T. Thiele, and A. Taflove. Validation and extension to three dimensions of the Berenger PML absorbing boundary condition for FD-TD meshes. *IEEE Microwave Guided Wave Lett.*, 4(8):268–270, 1994.
- [48] C. E. Reuter, R. M. Joseph, E. T. Thiele, D. S. Katz, and A. Taflove. Ultrawideband absorbing boundary condition for termination of waveguiding structures in FD-TD simulations. *IEEE Microwave Guided Wave Lett.*, 4(10):344–346, 1994.
- [49] W. V. Andrew, C. A. Balanis, and P. A. Tirkas. A comparison of the Berenger perfectly matched layer and the Lindman higher-order ABC's for the FDTD method. *IEEE Microwave Guided Wave Lett.*, 5(6):192–194, 1995.
- [50] A. Bahr, A. Lauer, and I. Wolff. Application of the PML absorbing boundary condition to the FDTD analysis of microwave circuits. In *IEEE MTT-S Int. Microwave Symposium*, volume 1, pages 27–30, Orlando, FL, 1995.
- [51] M. Cai and H. Zhou. Proof of perfectly matched layer conditions in three dimensions. *Electron. Lett.*, 31(19):1675–1676, 1995.
- [52] B. Chen, D. G. Fang, and B. H. Zhou. Modified Berenger PML absorbing boundary condition for FD-TD meshes. *IEEE Microwave Guided Wave Lett.*, 5(11):399–401, 1995.
- [53] J. De Moerloose and M. A. Stuchly. Behavior of Berenger's ABC for evanescent waves. *IEEE Microwave Guided Wave Lett.*, 5(10):344–346, 1995.
- [54] R. Mittra and Ü. Pekel. A new look at the perfectly matched layer (PML) concept for the reflectionless absorption of electromagnetic waves. *IEEE Microwave Guided Wave Lett.*, 5(3):84–86, 1995.
- [55] Ü. Pekel and R. Mittra. An application of the perfectly matched layer (PML) concept to the finite element method frequency domain analysis of scattering problems. *IEEE Microwave Guided Wave Lett.*, 5(8):258–260, 1995.
- [56] J. Bernabeu Verdu, R. Gillard, K. Moustadir, and J. Citerne. An extension of the PML technique to the FDTD analysis of multilayer planar circuits and antennas. *Microwave Opt. Technol. Lett.*, 10(6):323–327, 1995.

- [57] C. Wu, E. A. Navarro, P. Y. Chung, and J. Litva. Modeling of waveguide structures using the nonorthogonal FDTD method with a PML absorbing boundary. *Microwave Opt. Technol. Lett.*, 8(4):226–228, 1995.
- [58] Z. Wu and J. Fang. Numerical implementation and performance of perfectly matched layer boundary condition for waveguide structures. *IEEE Trans. Microwave Theory Tech.*, 43(12):2676–2683, 1995.
- [59] J.-P. Bérenger. Perfectly matched layer for the FDTD solution of wave-structure interaction problems. *IEEE Trans. Antennas Propagat.*, 44(1):110–117, 1996.
- [60] W. C. Chew and J. M. Jin. Perfectly matched layers in the discretized space: An analysis and optimization. *Electromagnetics*, 16:325–340, 1996.
- [61] J. De Moerloose and M. A. Stuchly. Reflection analysis of PML ABC's for low-frequency applications. *IEEE Microwave Guided Wave Lett.*, 6(4):177–179, 1996.
- [62] J. Fang and Z. Wu. Closed-form expression of numerical reflection coefficient at PML interfaces and optimization of PML performance. *IEEE Microwave Guided Wave Lett.*, 6(9):332–334, 1996.
- [63] Y. C. Lau, M. S. Leong, and P. S. Kooi. Extension of Berenger's PML boundary condition in matching lossy medium and evanescent waves. *Electron. Lett.*, 32(11):974–976, 1996.
- [64] K. Naishadham. Stability considerations in the application of PML. In *IEEE MTT-S Int. Microwave Symposium*, volume 2, pages 581–584, San Francisco, CA, June 1996.
- [65] D. M. Sullivan. A simplified PML for use with the FDTD method. *IEEE Microwave Guided Wave Lett.*, 6(2):97–99, 1996.
- [66] J. C. Veihl and R. Mittra. An efficient implementation of Berenger's perfectly matched layer (PML) for finite-difference time-domain mesh truncation. *IEEE Microwave Guided Wave Lett.*, 6(2):94–96, 1996.
- [67] J. R. Wait. On the PML concept: A view from the outside. *IEEE Antennas Propagat. Magazine*, 38(2):48–51, 1996.
- [68] Z. Wu and J. Fang. High-performance PML algorithms. *IEEE Microwave Guided Wave Lett.*, 6(9):335–337, 1996.
- [69] W. C. Chew and W. H. Weedon. A 3D perfectly matched medium from modified Maxwell's equations with stretched coordinates. *Microwave Opt. Technol. Lett.*, 7(13):599–604, 1994.

- [70] M. A. Gribbons, W. P. Pinello, and A. C. Cangellaris. A stretched coordinate technique for numerical absorption of evanescent and propagating waves in planar waveguiding structures. In *IEEE MTT-S Int. Microwave Symposium*, volume 1, pages 31–34, Orlando, FL, 1995.
- [71] C. M. Rappaport. Perfectly matched absorbing boundary conditions based on anisotropic lossy mapping of space. *IEEE Microwave Guided Wave Lett.*, 5(3):90–92, 1995.
- [72] Z. S. Sacks, D. M. Kingsland, R. Lee, and Jin-Fa Lee. A perfectly matched anisotropic absorber for the use as an absorbing boundary condition. *IEEE Trans. Antennas Propagat.*, 43(12):1460–1463, 1995.
- [73] L. Zhao and A. C. Cangellaris. A general approach for the development of unsplit-field time-domain implementations of perfectly matched layers for FDTD grid truncation. *IEEE Microwave Guided Wave Lett.*, 6(5):209–211, 1996.
- [74] L. Zhao and A. C. Cangellaris. GT-PML: Generalized theory of perfectly matched layers and its application to the reflectionless truncation of finite-difference time-domain grids. In *IEEE MTT-S Int. Microwave Symposium*, volume 2, pages 569–572, San Francisco, CA, June 1996.
- [75] T. S. Bird. Propagation and radiation characteristics of rib waveguide. *Electron. Lett.*, 13(14):401–403, 1977.
- [76] C. W. Yeh. Optical waveguide theory. *IEEE Transactions on Circuits and Systems*, CAS-26(12):1011–1019, 1979.
- [77] E. Schweig and W. B. Bridges. Computer analysis of dielectric waveguides: A finite-difference method. *IEEE Trans. Microwave Theory Tech.*, MTT-32(5):531–541, 1984.
- [78] K. Bierwirth, N. Schulz, and F. Arndt. Finite-difference analysis of rectangular dielectric waveguide structures. *IEEE Trans. Microwave Theory Tech.*, MTT-34(11):1104–1114, 1986.
- [79] M. Tsuji and H. Shigesawa. An accurate analysis of discontinuities in dielectric rectangular waveguide and its application to grating filters. In *IEEE MTT-S Int. Microwave Symposium*, volume 2, pages 785–788, Las Vegas, NV, 1987.
- [80] S.-T. Chu and S. K. Chaudhuri. A finite-difference time-domain method for the design and analysis of guided-wave optical structures. *J. Lightwave Technol.*, 7(12):2033–2038, 1989.

- [81] T. M. Benson, P. C. Kendall, M. A. Matin, and M. S. Stern. Polarised modes of semiconductor rib waveguides. *Electron. Lett.*, 27(16):1488–1489, 1991.
- [82] T. Rozzi, G. Cerri, M. N. Husain, and L. Zappelli. Variational analysis of dielectric rib waveguide using the concept of 'transition function' and incoming edge singularities. *IEEE Trans. Microwave Theory Tech.*, 39(2):247–257, 1991.
- [83] J. Schmidtchen, A. Splett, B. Schuppert, and K. Petermann. Low loss single-mode optical waveguides with large cross-section in silicon-on-insulator. *Electron. Lett.*, 27(16):1486–1488, 1991.
- [84] T. Rozzi, L. Zappelli, and M. N. Husain. Radiation modes and step discontinuities in dielectric rib waveguide. *IEEE Trans. Microwave Theory Tech.*, 40(10):1879–1888, 1992.
- [85] N. I. Dib and L. P. B. Katehi. Analysis of the transition from rectangular waveguide to shielded dielectric image guide using the finite-difference time-domain method. *IEEE Microwave Guided Wave Lett.*, 3(9):327–329, 1993.
- [86] A. Erdmann, M. Shamonin, P. Hertel, and H. Dotsch. Finite difference analysis of gyrotropic waveguides. *Optics Communications*, 102:25–30, 1993.
- [87] W. P. Huang and C. L. Xu. Simulation of three-dimensional optical waveguides by the full-vector beam propagation method. *IEEE Journal of Quantum Electronics*, 29(10):2639–2649, 1993.
- [88] P.-L. Liu and B. J. Li. Full-vectorial mode analysis of rib waveguided by iterative lanczos reduction. *IEEE Journal of Quantum Electronics*, 29(12):2859–2863, 1993.
- [89] Z. Lu, R. Bansal, and P. K. Cheo. Radiation losses of tapered dielectric waveguides: A finite difference analysis with ridge waveguide applications. *Journal of Lightwave Technology*, 12(8):1373–1377, 1994.
- [90] R. Magnusson, S. S. Wang, T. D. Black, and A. Sohn. Resonance properties of dielectric waveguide gratings: Theory and experiments at 4-18 GHz. *IEEE Trans. Antennas Propagat.*, 42(4):567–569, 1994.
- [91] C. W. Trueman, S. R. Mishra, C. L. Larose, and R. K. Mongia. Resonant frequencies and Q factors of dielectric parallelepipeds by measurement and by fdtd. In *Conference on Precision Electromagnetic Measurements*, pages 61–62, 1994.
- [92] L. Cascio, T. Rozzi, and L. Zappelli. Radiation loss of Y-junction in rib waveguide. *IEEE Trans. Microwave Theory Tech.*, 43(8):1788–1797, 1995.

- [93] E.-B. El-Sharawy and P. A. Tirkas. A novel design to reduce losses at dielectric waveguide discontinuities. In *IEEE MTT-S Int. Microwave Symposium*, volume 2, pages 841–844, Orlando, FL, 1995.
- [94] M. Taira and N. Morita. Analysis of frequency characteristics of dielectric waveguide discontinuities using finite difference -time difference method. *Electronics and Communications in Japan, Part 2*, 78(5):102–111, 1995.
- [95] K. S. Chiang and W. P. Wong. Rib waveguides with degenerate polarised modes. *Electron. Lett.*, 32(12):1098–1099, 1996.
- [96] N. Dib and L. P. B. Katehi. Characterization of three-dimensional open dielectric structures using the finite-difference time-domain method. *IEEE Trans. Microwave Theory Tech.*, 44(4):513–518, 1996.
- [97] U. Fischer, T. Zinke, J. R. Kropp, F. Arndt, and K. Petermann. 0.1 db/cm waveguide losses in single-mode SOI rib waveguides. *IEEE Photonics Technology Letters*, 8(5):647–648, 1996.
- [98] R. Moosburger, G. Fischbeck, C. Kostrzewa, and K. Petermann. Digital optical switch based on 'oversized' polymer rib waveguides. *Electron. Lett.*, 32(6):544–545, 1996.
- [99] S. J. Polychronopoulos and N. K. Uzunoglu. Propagation and coupling properties of integrated optical waveguides—an integral equation formulation. *IEEE Trans. Microwave Theory Tech.*, 44(5):641–650, 1996.
- [100] G. E. Ponchak, N. I. Dib, and L. P. B. Katehi. Design and analysis of transitions from rectangular waveguide to layered ridge dielectric waveguide. *IEEE Trans. Microwave Theory Tech.*, 44(7):1032–1040, 1996.
- [101] J.-M. Guan and C.-C. Su. Analysis of metallic waveguides with rectangular boundaries by using the finite-difference method and the simultaneous iteration with the Chebyshev acceleration. *IEEE Trans. Microwave Theory Tech.*, 43(2):374–382, 1995.
- [102] X. Zhang, J. Fang, K. K. Mei, and Y. Liu. Calculations of the dispersive characteristics of microstrips by the time-domain finite difference method. *IEEE Trans. Microwave Theory Tech.*, 36(2):263–267, 1988.
- [103] X. Zhang and K. K. Mei. Time-domain finite difference approach to the calculation of the frequency-dependent characteristics of microstrip discontinuities. *IEEE Trans. Microwave Theory Tech.*, 36(12):1775–1787, 1988.
- [104] G.-C. Liang, Y.-W. Liu, and K. K. Mei. Full-wave analysis of coplanar waveguide and slotline using the time-domain finite-difference method. *IEEE Trans. Microwave Theory Tech.*, 37(12):1949–1957, 1989.



- [105] A. Reineix and B. Jecko. Analysis of microstrip patch antennas using finite difference time domain method. *IEEE Trans. Antennas Propagat.*, 37(11):1361–1369, 1989.
- [106] D. M. Sheen, S. M. Ali, M. D. Abouzahra, and J. A. Kong. Application of the three-dimensional finite-difference time-domain method to the analysis of planar microstrip circuits. *IEEE Trans. Microwave Theory Tech.*, 38(7):849–857, 1990.
- [107] D. L. Paul, E. M. Daniel, and C. J. Railton. Fast finite difference time domain method for the analysis of planar microstrip circuits. In *21st European Microwave Conference*, pages 303–308, Stuttgart, Germany, September 1991.
- [108] Q. Chen and V. F. Fusco. Three dimensional finite-difference time-domain slot-line analysis of a limited memory personal computer. *IEEE Trans. Microwave Theory Tech.*, 43(2):358–362, 1995.
- [109] R. Holland, L. Simpson, and K. Kunz. Finite-difference analysis of EMP coupling to lossy dielectric structures. *IEEE Trans. Electromagn. Compat.*, EMC-22(3):203–209, 1980.
- [110] R. Luebbers. FDTD formulation for frequency dependent permittivity. In *IEEE Antennas and Propagat. Soc. Int. Symposium*, pages 50–53, San Jose, CA, 1989.
- [111] R. J. Luebbers, F. Hunsberger, K. S. Kunz, R. B. Standler, and M. Schneider. A frequency-dependent finite-difference time-domain formulation for dispersive materials. *IEEE Trans. Electromagn. Compat.*, 32(3):222–227, 1990.
- [112] D. J. Riley and C. D. Turner. The inclusion of wall loss in finite-difference time-domain thin-slot algorithms. *IEEE Trans. Electromagn. Compat.*, 33(4):304–311, 1991.
- [113] R. J. Luebbers and F. Hunsberger. FDTD for  $N$ th-order dispersive media. *IEEE Trans. Antennas Propagat.*, 40(11):1297–1301, 1992.
- [114] D. M. Sullivan. A frequency-dependent FDTD method for biological applications. *IEEE Trans. Microwave Theory Tech.*, 40(3):532–539, 1992.
- [115] O. P. Gandhi, B. Q. Gao, and J. Y. Chen. A frequency-dependent finite-difference time-domain formulation for general dispersive media. *IEEE Trans. Microwave Theory Tech.*, 41(4):658–665, 1993.
- [116] R. J. Luebbers. Lossy dielectrics in FDTD. *IEEE Trans. Antennas Propagat.*, 41(11):1586–1588, 1993.

- [117] K. Chamberlin and L. Gordon. Deriving a synthetic conductivity to enable accurate prediction of losses in good conductors using FDTD. In *10th Annual Review of Progress in Applied Computational Electromagnetics*, volume 2, pages 46–52, Monterey, CA, March 1994.
- [118] J. L. Young, A. Kittichartphayak, Y. M. Kwok, and D. Sullivan. On the dispersion errors related to  $(FD)^2$ -TD type schemes. *IEEE Trans. Microwave Theory Tech.*, 43(8):1902–1910, 1995.
- [119] D. F. Kelley and R. J. Luebbers. Piecewise linear recursive convolution for dispersive media using FDTD. *IEEE Trans. Antennas Propagat.*, 44(6):792–797, 1996.
- [120] D. M. Sullivan. Z-transform theory and the FDTD method. *IEEE Trans. Antennas Propagat.*, 44(1):28–34, 1996.
- [121] P. A. Tirkas and K. R. Demarest. Modeling of thin dielectric structures using finite-difference time-domain technique. *IEEE Trans. Antennas Propagat.*, 39(9):1338–1344, 1991.
- [122] J. G. Maloney and G. S. Smith. The efficient modeling of thin material sheets in the finite-difference time-domain (FDTD) method. *IEEE Trans. Antennas Propagat.*, 40(3):323–330, 1992.
- [123] J. J. Boonzaaier and C. W. I. Pistorius. Scattering by thin lossy dielectric plates — A finite-difference time-domain approach. *Microwave Opt. Technol. Lett.*, 6(5):326–332, 1993.
- [124] J. G. Maloney and G. S. Smith. A discussion of efficient methods for including thin material sheets in the FDTD technique. In *IEEE Antennas and Propagat. Soc. Int. Symposium*, volume 3, pages 1666–1669, Chicago, IL, July 1992.
- [125] J. G. Maloney and G. S. Smith. A comparison of methods for modeling electrically thin dielectric and conducting sheets in the finite-difference time-domain (FDTD) method. *IEEE Trans. Antennas Propagat.*, 41(5):690–694, 1993.
- [126] J. H. Beggs, R. J. Luebbers, K. S. Kunz, and K. S. Yee. Wideband finite difference time domain implementation of surface impedance boundary conditions for good conductors. In *IEEE Antennas and Propagat. Soc. Int. Symposium*, volume 1, pages 406–409, London, Ontario, 1991.
- [127] C. F. Lee, R. T. Shin, and J. A. Kong. Time domain modeling of impedance boundary condition. *IEEE Trans. Microwave Theory Tech.*, 40(9):1847–1850, 1992.

- [128] M. A. Tassoudji. *Electromagnetic Interference in Electronic Circuits and Systems*. PhD thesis, Massachusetts Institute of Technology, Cambridge, MA, 1994.
- [129] B. Z. Wang. Time-domain modeling of the impedance boundary condition for an oblique incident perpendicular-polarization plane wave. *Microwave Opt. Technol. Lett.*, 7(8):355–359, 1994.
- [130] K. S. Oh and J. E. Schutt-Aine. An efficient implementation of surface impedance boundary conditions for the finite-difference time-domain method. *IEEE Trans. Antennas Propagat.*, 43(7):660–666, 1995.
- [131] H. Jin, R. Vahldieck, and S. Xiao. A full-wave analysis of arbitrary guiding structures using a two dimensional tlm mesh. In *21st European Microwave Conference*, pages 205–210, Stuttgart, Germany, September 1991.
- [132] C. J. Railton and J. P. McGeehan. The use of mode templates to improve the accuracy of the FD-TD method. In *European Microwave Conference*, volume 21, pages 1278–1283, Stuttgart, Germany, 1991.
- [133] V. J. Branković, D. V. Krupežević, and F. Arndt. An efficient two-dimensional graded mesh finite-difference time-domain algorithm for shielded or open waveguide structures. *IEEE Trans. Microwave Theory Tech.*, 40(12):2272–2277, 1992.
- [134] A. Asi and L. Shafai. Multiple mode analysis of waveguides using compact FDTD. In *IEEE Antennas and Propagat. Soc. Int. Symposium*, volume 1, pages 360–363, Ann Arbor, MI, June 1993.
- [135] A. C. Cangellaris, M. Gribbons, and G. Sohos. A hybrid spectral/FDTD method for the electromagnetic analysis of guided waves in periodic structures. *IEEE Microwave Guided Wave Lett.*, 3(10):375–377, 1993.
- [136] D.-L. Paul, N. M. Potheary, and C. J. Railton. Calculation of the dispersive characteristics of open dielectric structures by the finite-difference time-domain method. *IEEE Trans. Microwave Theory Tech.*, 42(7):1207–1212, 1994.
- [137] J. A. Kong. *Electromagnetic Wave Theory*. John Wiley and Sons, New York, NY, 1990.
- [138] D. H. Staelin, J. A. Kong, and A. W. Morgenthaler. *Electromagnetic Waves*. Prentice Hall, Eaglewood Cliffs, NJ, 1994.
- [139] R. F. Harrington. *Time-Harmonic Electromagnetic Fields*. McGraw-Hill, New York, NY, 1961.

- [140] D. E. Johnson, J. L. Hilburn, and J. R. Johnson. *Basic Circuit Analysis*. Prentice-Hall, Eaglewood Cliffs, NJ, 1978.
- [141] M. Abramovitz and I. A. Stegun. *Handbook of Mathematical Functions*. Dover Publications, New York, NY, 1965.
- [142] N. S. Kapany and J. J. Burke. *Optical Waveguides*. Academic Press, New York, NY, 1972.
- [143] W. H. Press, S. A. Teukolsky, W. T. Vetterling, and B. P. Flannery. *Numerical Recipes in FORTRAN The Art of scientific computing*. Cambridge University Press, New York, NY, 1992.
- [144] H. Hirosawa and N. Kobayashi. Terrain height measurements by synthetic aperture radar with an interferometer. *International Journal of Remote Sensing*, 7(3):339–348, 1986.
- [145] A. K. Gabriel and R. M. Goldstein. Crossed orbit interferometry: Theory and experimental results from SIR-B. *International Journal of Remote Sensing*, 9(5):857–872, 1988.
- [146] F. K. Li and R. M. Goldstein. Studies of multibaseline spaceborne interferometric synthetic aperture radars. *IEEE Trans. Geosci. and Remote Sensing*, 28(1):88–96, 1990.
- [147] C. Prati and F. Rocca. Limits to the resolution of elevation maps from stereo SAR images. *International Journal of Remote Sensing*, 11(12):2215–2235, 1990.
- [148] A. Currie and M. A. Brown. Wide-swath SAR. *IEE Proceedings-F*, 139(2):122–135, 1992.
- [149] E. Rodriguez and J. M. Martin. Theory and design of interferometric synthetic aperture radars. *IEE Proceedings-F*, 139(2):147–159, 1992.
- [150] R. Bamler and D. Just. Phase statistics and decorrelation SAR interferometry. In *International Geoscience and Remote Sensing Symposium*, volume 3, pages 980–984, Tokyo, Japan, August 1993.
- [151] E.-A. Herland. SAR interferometry with ERS-1 in forested areas. In *International Geoscience and Remote Sensing Symposium*, volume 1, pages 202–204, Firenze, Italy, July 1995.
- [152] H. Kimura. Method to estimate baseline and platform altitude for SAR interferometry. In *International Geoscience and Remote Sensing Symposium*, volume 1, pages 199–201, Firenze, Italy, July 1995.

- [153] N. Marechal. Tomographic formulation of interferometric SAR for terrain elevation mapping. *IEEE Trans. Geosci. and Remote Sensing*, 33(3):726–739, 1995.
- [154] J. Moreira, M. Schwabisch, G. Fornaro, R. Lanari, R. Bamler, D. Just, U. Steinbrecher, H. Breit, M. Eineder, G. Franceschetti, D. Geudtner, and H. Rinkel. X-SAR interferometry: First results. *IEEE Trans. Geosci. and Remote Sensing*, 33(4):950–956, 1995.
- [155] R. Gens and J. L. van Genderen. SAR interferometry-issues, techniques, and applications. *International Journal of Remote Sensing*, 17(10):1803–1835, 1996.
- [156] D. Massonnet, H. Vadon, and M. Rossi. Reduction of the need for phase unwrapping in radar interferometry. *IEEE Trans. Geosci. and Remote Sensing*, 34(2):489–497, 1996.
- [157] V. Mrstik, G. VanBlaricum, G. Cardillo Jr., and M. Fennell. Terrain height measurement accuracy of interferometric synthetic aperture radars. *IEEE Trans. Geosci. and Remote Sensing*, 24(1):219–228, 1996.
- [158] H. Wakabayashi and K. Arai. A method of speckle noise reduction for SAR data. *International Journal of Remote Sensing*, 17(10):1837–1849, 1996.
- [159] H. A. Zebker and R. M. Goldstein. Topographic mapping from interferometric synthetic aperture radar observations. *Journal of Geophysical Research*, 91(B5):4993–4999, 1996.
- [160] D. Just, N. Adam, M. Schwaebisch, and R. Bamler. Comparison of phase unwrapping algorithms for SAR interferograms. In *International Geoscience and Remote Sensing Symposium*, volume 3, pages 767–769, Firenze, Italy, July 1995.
- [161] H. Lim, W. Xu, and X. Huang. Two new practical methods for phase unwrapping. In *International Geoscience and Remote Sensing Symposium*, volume 1, pages 196–198, Firenze, Italy, July 1995.
- [162] Mark D. Pritt. Multigrid phase unwrapping for interferometric SAR. In *International Geoscience and Remote Sensing Symposium*, volume 3, pages 562–564, Firenze, Italy, July 1995.
- [163] M. T. Chiaradia, L. Guerriero, G. Pasquariello, A. Refice, and N. Veneziani. Absolute phase determination in SAR interferometry. In *International Geoscience and Remote Sensing Symposium*, volume 4, pages 2060–2062, Lincoln, Nebraska, July 1996.

- [164] M. Datcu. Maximum entropy solution for interferometric SAR phase unwrapping. In *International Geoscience and Remote Sensing Symposium*, volume 4, pages 2054–2056, Lincoln, Nebraska, July 1996.
- [165] G. W. Davidson and R. Bamler. A multiresolution approach to improve phase unwrapping. In *International Geoscience and Remote Sensing Symposium*, volume 4, pages 2050–2053, Lincoln, Nebraska, July 1996.
- [166] T. J. Flynn. Consistent 2-D phase unwrapping guided by a quality map. In *International Geoscience and Remote Sensing Symposium*, volume 4, pages 2057–2059, Lincoln, Nebraska, July 1996.
- [167] G. Fornaro, G. Franceschetti, R. Lanari, and E. Sansosti. Theoretical analysis on the robust phase unwrapping algorithms for SAR interferometry. In *International Geoscience and Remote Sensing Symposium*, volume 4, pages 2047–2049, Lincoln, Nebraska, July 1996.
- [168] C. R. Guarino. Weighted two-dimensional phase unwrapping. In *International Geoscience and Remote Sensing Symposium*, volume 1, pages 193–195, Firenze, Italy, July 1995.
- [169] W. Xu and I. Cumming. A region growing algorithm for InSAR phase unwrapping. In *International Geoscience and Remote Sensing Symposium*, volume 4, pages 2044–2046, Lincoln, Nebraska, July 1996.
- [170] D. G. Ghiglia and L. A. Romero. Robust two-dimensional weighted and unweighted phase unwrapping that uses fast transforms and iterative methods. *J. Opt. Soc. Am. A*, 11(1):107–117, 1994.
- [171] D. Kerr, G. H. Kaufmann, and G. E. Galizzi. Unwrapping of interferometric phase-fringe maps by the discrete cosine transform. *Applied Optics*, 35(5):810–816, 1996.
- [172] D. Gusfield, C. Martel, and D. Fernandez-Baca. Fast algorithms for bipartite network flow. *SIAM Journal of Computing*, 16(2):237–251, 1987.
- [173] R. M. Goldstein, H. A. Zebker, and C. L. Werner. Satellite radar interferometry: Two-dimensional phase unwrapping. *Radio Science*, 23(4):713–720, 1988.
- [174] J. M. Huntley. Noise-immune phase unwrapping algorithm. *Applied Optics*, 28(15):3268–3270, 1989.
- [175] J. R. Buckland, J. M. Huntley, and S. R. E. Turner. Unwrapping noisy phase maps by use of a minimum-cost-matching algorithm. *Applied Optics*, 34(23):5100–5109, 1995.

- [176] P. G. Charette and I. W. Hunter. Robust phase-unwrapping method for phase images with high noise content. *Applied Optics*, 35(19):3506–3513, 1996.
- [177] C. De Veuster, P. Slangen, Y. Renotte, L. Berwart, and Y. Lion. Disk-growing algorithm for phase-map unwrapping: Application to speckle interferograms. *Applied Optics*, 25(2):240–247, 1996.
- [178] P. Ettl and K. Creath. Comparison of phase-unwrapping algorithms by using gradient of first failure. *Applied Optics*, 35(25):5108–5114, 1996.
- [179] M. Servin, D. Mallacara, and F. J. Cuevas. Path-independent phase unwrapping of subsampled phase maps. *Applied Optics*, 35(10):1643–1649, 1996.
- [180] B. Strobel. Processing of interferometric phase maps as complex-valued phasor images. *Applied Optics*, 35(13):2192–2198, 1996.
- [181] Maciej M. Syslo, Narsingh Deo, and Janusz S. Kowalik. *Discrete optimization algorithms : with Pascal programs*. Prentice-Hall, Englewood Cliffs, NJ, 1983.